PHASE TRANSFORMATIONS IN Ni-Ti-Hf HIGH TEMPERATURE SHAPE MEMORY ALLOYS

by

Meenu Prasher

(Enrolment No. PHYS01201304044)

Bhabha Atomic Research Centre, Mumbai

A thesis submitted to the
Board of Studies in Physical Sciences
in partial fulfillment of requirements
for the Degree of

DOCTOR OF PHILOSOPHY

of

HOMI BHABHA NATIONAL INSTITUTE

July, 2019

Homi Bhabha National Institute

Recommendations of the Viva Voce Committee

As members of the Viva Voce Committee, we certify that we have read the dissertation prepared by "**Meenu Prasher**", entitled "**Phase Transformations in Ni-Ti-Hf High Temperature Shape Memory Alloys**" and recommend that it may be accepted as fulfilling the thesis requirement for the award of Degree of Doctor of Philosophy.

Chairman	-	Prof. ~~C. K. Dey~~ SAIBAL BASU	**Date:** 13.01.2020
Guide	-	Prof. Debasis Sen	**Date:** 13.01.2020
External Examiner	-	Prof. A. Subramaniam	**Date:** 13 Jan 2020
Member 1	-	Prof. R. Tewari	**Date:** 13. January, 2020
Member 2	-	Prof. A. Biswas	**Date:** 13/1/20
Member 3	-	Prof. V. K. Aswal	**Date:** 13-01-2020

Final approval and acceptance of this thesis is contingent upon the candidate's submission of the final copies of the thesis to HBNI.

I/We hereby certify that I/We have read this thesis prepared under my/our direction and recommend that it may be accepted as fulfilling the thesis requirement.

Date : 13.01.2020
Place: BARC.

Debasis Sen.

Guide

STATEMENT BY AUTHOR

Meenu Prasher

DECLARATION

I, *Meenu Prasher*, hereby declare that the investigation presented in the thesis has been carried out by me. The work is original and has not been submitted earlier as a whole or in part for a degree / diploma at this or any other Institution / University.

Meenu Prasher

Dedicated

to my family....

Acknowledgments

This is the most important part of my dissertation. It gives me great pleasure to acknowledge all those who paved the path to make this dissertation a success. First of all, I would like to convey my deep sense of gratitude to my advisor Dr. Debasis Sen. Without his guidance, continuous support and encouragement throughout my dissertation work, this thesis would not have been possible. In him I found an excellent scientist from whom I learnt the technique of small-angle scattering and Python programming language.

I am grateful to Dr. Madangopal Krishnan, Associate Director Materials Group, Bhabha Atomic Research Centre, whose lab I joined in the year 2008. He introduced me to the fascinating field of shape memory alloys and the martensitic phase transformations. Being from the physics background with limited knowledge of physical metallurgy, in his lab I found an enthusiastic environment to try out new things and his constant encouragement and deep scientific insights helped me throughout.

I am privileged to thank Dr. G. K. Dey, Chairman of the doctoral committee and ex-Director Materials Group, Bhabha Atomic Research Centre for his encouragement and enthusiasm. I would like to express my sincere gratitude to the members of my doctoral committee: Dr. Raghvendra Tewari, Dr. Aniruddha Biswas, and Dr. V. K. Aswal for their precious time for periodic assessment of the work and guidance in improving the quality of the thesis. I also thank Dr. M. Vijayalakshmi, ex-member and Ex-Associate

Director, Physical Metallurgy Group, Indira Gandhi Centre for Advanced Research for her valuable inputs and suggestions.

I also highly acknowledge the help of my other collaborators: Dr. Jitendra Bahadur for carrying out small angle neutron experiments at Oak Ridge National Laboratory, Mr. P. S. R. Krishna and Dr. P. D. Babu for their support for neutron diffraction experiments. I gained a lot from helpful scientific discussions and technical support offered by my colleagues Dr. Bikas C. Maji, Dr. C. B. Basak, Dr. Amit Verma, Dr. Abhijit Ghosh, Dr. P. Sengupta, Dr. Rajeev Kapoor, and Saurav Sunil. I am also grateful to Dr. B. Vishwanadh and Harish Donthula for electron microscopy. I also thank Dr. K. V. Mani Krishna for his help in troubleshooting with LaTeXwhile typing this thesis. The contribution of Santosh Ji, Krishnamohan Ji, Hatwar Ji, Hankare Ji and Shubham from the workshop as well as staff from glass sealing facility cannot be undermined.

I also thank the Materials Group office staff for taking care of many official aspects in the duration of my thesis work. I thank my friends Sudip, Sarita, Dr. Rohini Garg and my training school batch mates for their encouragements and lovely company. I am very grateful to Dr. Param Jeet Singh and Sona Bhabi Ji for being family away from home and always being there for me.

Above all, sincere thanks to my younger brother, Dr. Nitin Kumar, my best friend who has always motivated me to be a good researcher and at the same time an inspiration for me. Thanks to my sister-in-law Dr. Mukta Sharma, who has added colors to our family with her lively and caring nature. I am indebted to my parents for the sacrifices they made for me and always standing by my side in difficult times. Their hard-working and persevering nature has been and will be my guiding light. Last but not least, words are not enough to thank my husband Mr. Kunal Prasher, whose unconditional love and support is my strength. I express my heartfelt gratitude to him for being so understanding and constantly encouraging me when the tasks seemed arduous and insurmountable. I dedicate this humble effort to them.

Abstract

NiTiHf High Temperature Shape Memory Alloys (HTSMAs) are prominent stimuli-responsive smart materials. They demonstrate the capability of remembering their original form when subjected to external thermodynamic stimuli such as temperature, stress etc. due to underlying martensite phase transformation. As a result, they are widely utilized as actuator material in aerospace, aircraft and robotic applications. Since these HTSMAs experience high operating temperatures well above 100°C over prolonged durations, they must meet the stringent criteria of narrow thermal hysteresis as well as high strength for good shape memory response. As these alloys undergo reversible martensite phase transformation, instabilities in the phase transformation temperatures during repeated thermal cycling between martensite and austenite phases over the course of operation also pose a challenge, which must be addressed in order to design high strength NiTiHf HTSMAs with stable functional response.

The present study is aimed at selecting a NiTiHf alloy composition with balanced combinations of high phase transformation temperatures, low thermal hysteresis, high strength, good thermal cyclic stability and achieving an understanding on the correlation between alloy micro-structure and its phase transformation behavior. This work provides an insight into the effect of role of Hf addition and aging treatments on the Ni-rich NiTiHf alloy in terms of their role on phase transformation characteristics and alloy strength.

Various characterization techniques such as differential scanning calorimetry (DSC), vickers micro-hardness (VHN), x-ray diffraction (XRD), neutron diffraction (ND) along with transmission electron microscopy (TEM) and small angle X-ray/neutron scattering etc., were used for the investigations in the present study.

Based on the results obtained by studying substitution of an array of Hf concentrations (5-25 at.%) to $Ni_{50.3}Ti_{49.7}$ alloy wide range of phase transformation temperatures from sub-zero to 280°C were achieved. The hardness of $Ni_{50.3}Ti_{49.7}$ alloy increased linearly with Hf concentration on account of solid solution strengthening effect of Hf. It was established that the $Ni_{50.3}Ti_{49.7}Hf_{20}$ alloy exhibits phase transformation temperature nearly 180°C and lowest thermal hysteresis along with high strength. Aging of the $Ni_{50.3}Ti_{49.7}Hf_{20}$ alloy at 550°C and 650°C further increased its martensite phase transformation temperatures. Further, aging at 550°C resulted in higher strength caused by fine H-phase precipitates, which upon aging at 650°C underwent coarsening vis-a-vis reduction in hardness.

Temporal evolution of H-phase precipitates growth and coarsening kinetics in the $Ni_{50.3}Ti_{49.7}Hf_{20}$ alloy aged at different temperatures was also investigated using correlative TEM and time-resolved small angle neutron scattering. The analysis revealed activation energy for H-phase growth to be 194 $kJmol^{-1}$ and coarsening to be 233±35 $kJmol^{-1}$ and it was established that while the diffusion of Ni atoms in the matrix predominantly governs the growth regime, the coarsening kinetics is primarily controlled by Hf diffusion. Further, relatively sluggish coarsening of the H-phase in this alloy, as compared to Ni_4Ti_3 precipitates in Ni-rich binary NiTi alloys, was attributed to the slow migration of Hf in the matrix. This is an important result from the technological viewpoint, since high coarsening rates of strengthening precipitate phase lead to accelerated loss of strength and shape recovery at high temperatures and hence loss in shape recovery ratios. To study the role of aging on the thermal cyclic stability of martensite transformation in $Ni_{50.3}Ti_{49.7}Hf_{20}$ alloy, stress-free thermal cycling experiments were conducted at fixed, as well as, variable heating/cooling rates, heat-treated at temperatures 300°C-650°C for 3 hours. It was found that the variations in phase transformation temperatures can be minimized to an acceptable range (± 1-2°C) by aging the alloy at 400°C for 3 hours.

List of Publications

Journal Publications:

1. "Influence of Aging on Phase Transformation and Microstructure of $Ni_{50.3}Ti_{29.7}Hf_{20}$ High Temperature Shape Memory Alloy", **Meenu Prasher** and Debasis Sen, *Journal of Alloys and Compounds*, **2014**, 615, 469-474.

2. "Correlative SANS and TEM Investigation on Precipitation Kinetics of H-phase in $Ni_{50.3}Ti_{29.7}Hf_{20}$ High Temperature Shape Memory Alloy", **Meenu Prasher**, Debasis Sen, Jitendra Bahadur, Raghvendra Tewari and Madangopal Krishnan, *Journal of Alloys and Compounds*, **2019**, 779, 630-642.

3. "Tuning the Thermal Cyclic Stability of Martensitic Transformation in the $Ni_{50.3}Ti_{29.7}Hf_{20}$ High Temperature Shape Memory Alloy", **Meenu Prasher**, Debasis Sen, R. Tewari and Madangopal Krishnan (Communicated).

4. "Effect of Hf solute addition on the Phase Transformation Behavior and Hardness of a Ni-rich NiTi Alloy", **Meenu Prasher**, D. Sen, R. Tewari, P. S. R. Krishna , P. D. Babu and Madangopal Krishnan (Communicated).

Conference/ Symposium Proceedings:

1. "Small Angle X-ray Scattering Study of Nano-scale Precipitation in $Ni_{50.3}Ti_{29.7}Hf_{20}$ High Temperature Shape Memory Alloy", **Meenu Prasher**, Debasis Sen, Bikas C. Maji and Madangopal Krishnan, *AIP Conference Proceedings*, **2014**,1591,1691-1694.

2. "Microstructural Investigation in $Ni_{50.3}Ti_{29.7}Hf_{20}$ High Temperature Shape Memory Alloy", **Meenu Prasher**, D. Sen, R. Tewari and Madangopal Krishnan *(presented at Electron Microscopy Society of India-2015)*, 8th-10th July 2015, Mumbai.

3. "Kinetics of Precipitation in $Ni_{50.3}Ti_{29.7}Hf_{20}$ High Temperature Shape Memory Alloy: TEM & SANS Study"; **Meenu Prasher**, Debasis Sen, J. Bahadur, R. Tewari, Madangopal Krishnan, *Oral Presentation at International Conference on Electron Microscopy and Allied Techniques and XXXVC Annual meeting of the Electron Microscopy Society of India (EMSI 2017)*, 17th-19th July 2017, Mahabalipuram.

4. "Phase Transformation in $Ni_{50.3}Ti_{49.7-x}Hf_x$ (x = 0 - 25 at.%) High Temperature Shape Memory Alloy"; **Meenu Prasher**, Debasis Sen, R. Tewari,P. S. R. Krishna, P. D. Babu, Madangopal Krishnan, *Presented at National Seminar on Crystallography (NSC 2019)*, 19th-22nd June 2019, Mumbai.

Meenu Prasher

Contents

List of Figures

List of Tables

List of Abbreviations

AR	Aspect-Ratio
BCC	Body Centered Cubic
BCT	Body Centered Tetragonal
CRSS	Critical Resolved Shear Stress
DFT	Density Functional Theory
DSC	Differential Scanning Calorimetry
EDS	Energy Dispersive Spectrometer
FCC	Face Centered Cubic
HAADF	High Angle Annular Dark Field
HCP	Hexagonal Close Packed
HTSMAs	High Temperature Shape Memory Alloys
JMAK	John Mehl Avrami Kolmogorov
LSW	Lifshitz-Sloyozov-Wagner
ND	Neutron Diffraction
RT	Room Temperature
SANS	Small-angle Neutron Scattering
SAXS	Small-Angle X-Ray Scattering
SE	Super-Elasticity
SEM	Scanning Electron Microscopy
SMAs	Shape Memory Alloys
SME	Shape Memory Effect

STEM	Scanning Transmission Electron Microscope
TEM	Transmission Electron Microscopy
VHN	Vickers Hardness Number
$\mathbf{A}_s$	Austenite start temperature
$\mathbf{A}_f$	Austenite finish temperature
$\mathbf{A}_p$	Austenite peak temperature
$\mathbf{M}_s$	Martensite start temperature
$\mathbf{M}_f$	Martensite finish temperature
$\mathbf{M}_p$	Martensite peak temperature
$\mathbf{A}_f$ **-** $\mathbf{M}_s$	Thermal hysteresis
$\mathbf{R}_G$	Guinier radius
$\mathbf{T}_0$	Thermodynamic equilibrium temperature

CHAPTER 1

Introduction

Shape Memory Effect is the phenomenon of restoring the original shape of a plastically deformed material by simply heating it. The shape memory effect is observed in various materials such as polymers [1, 2], composites [3] and metallic alloys [4]. Being smart materials, they find wide range of applicability in biomedical [5, 6], actuators [7–10], aerospace [11, 12] industries to mention a few. Since the shape memory polymers/composites have quite low yield strength (< 50 MPa) [13, 14], Shape Memory Alloys (SMAs), which are high strength metallic materials, enjoy much wider acceptance in aerospace industry than polymer counterparts.

SMAs can remember their original un-deformed shape under the influence of external stimuli such as temperature or stress due to solid-solid phase transformation known as *Martensitic phase transformation*. This is a first-order diffusion-less, composition invariant, shear-dominated transformation, during which the crystal structure of high temperature phase (known as austenite) becomes thermodynamically unstable during cooling below a certain critical temperature, M_s (martensite start temperature) and transforms to martensite phase with lower crystal symmetry than the austenite. This transformation is thermodynamically reversible in nature and as a result, martensite phase transforms back to the austenite phase upon heating above a critical temperature A_f (austenite finish temperature). Development of SMAs involve several technological challenges which include:

- Stable phase transformation behaviour,
- Low values of hysteresis (defined as A_f - M_s),
- large transformation strains,
- Good mechanical strength over wide range of temperatures,

- Near-complete shape recovery.

These properties are influenced by the interplay between phase transformation characteristics and intrinsic micro-structure of the alloy. Therefore, thorough understanding the phase transformations and their correlation with the mechanical properties of SMAs is essential to tailor them for desired applications.

1.1. Shape Memory Alloys

Shape memory effect has been shown to occur in several alloys systems such as ferrous alloys Fe-Ni [15], Fe-Mn [16] and non-ferrous alloys such as Au-Cd [17], Ni-Ti [18], Cu-Zn-Al [19] etc. Schematic demonstration of the shape memory effect in SMAs is displayed in Figure 1.1. When the phase transformation from austenite to martensite occurs, the

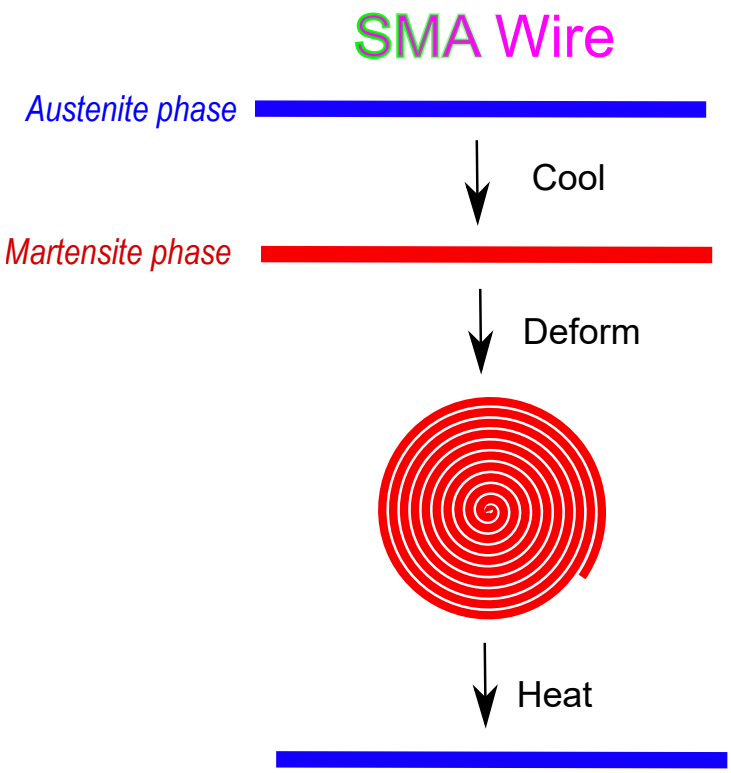

Figure 1.1: Demonstration of shape memory phenomenon.

difference in their crystal structures leads to local elastic strain. This strain is accommodated elastically by producing internally twinned martensite variants. Due to lower symmetry of the martensite phase, it can arrange itself in twin-related multiple orientations, known as variants, which individually can be internally twinned. Each variant is actually martensite phase, which maintains a fixed lattice correspondence as well as

orientation relationship with the austenite crystal lattice. These twin-related martensite variants are also called habit plane variants. Rest of the strain energy can be compensated by forming self-accommodating groups of these twin-related variants.
Depending upon whether the stimulus is temperature or stress, SMAs exhibit unique properties namely Shape Memory Effect (SME) or Super-Elasticity (SE).

1.1.1. Shape Memory Effect (SME)

Martensitic transformation, when induced by cooling the alloy below M_s, results in the formation of twinned martensite micro-structure. When the alloy is deformed in the martensite phase, the externally applied stress causes certain habit plane variants to grow at the expense of other variants in the direction of applied load. This results in detwinning of the martensite and produces a macroscopic shape change, generating macroscopic strain, called transformation strain. This strain does not recover immediately upon unloading the specimen but recovers completely once the specimen is heated above A_f. Thus, the phenomenon in which *the apparent plastic deformation in a SMA in the martensitic state is completely recovered upon heating above A_f is known as Shape Memory Effect (SME).*

1.1.2. Super-Elasticity (SE)

Martensitic transformation in SMAs can also be induced by the application of external stress. When the specimen is deformed in the austenite state *i.e.* above A_f, the applied stress leads to the formation of stress-induced twinned martensite. With an increase in stress, austenite completely transforms to martensite. Once this happens, a further increase in the stress causes de-twinning of the martensite. This means certain habit plane variants start growing at the expense of other variants, in the direction favoured by the applied stress. If enough stress is applied to the specimen such that martensite completely de-twins and is subsequently unloaded, the apparent plastic strain is completely recovered. This phenomenon of *completely recovering the apparent plastic deformation in the SMAs in the austenitie phase upon unloading is known as Super-Elasticity (SE).*

Schematic of shape memory response of SMAs in terms of SME and SE is displayed in Figure 1.2. Amongst wide range of SMAs, the NiTi alloys with near equi-atomic composition stand out as a leading example of SMAs, which were discovered in 1963 by Buehler *et al.* [20]. These alloys have since then gained immense popularity as SMA candidates for

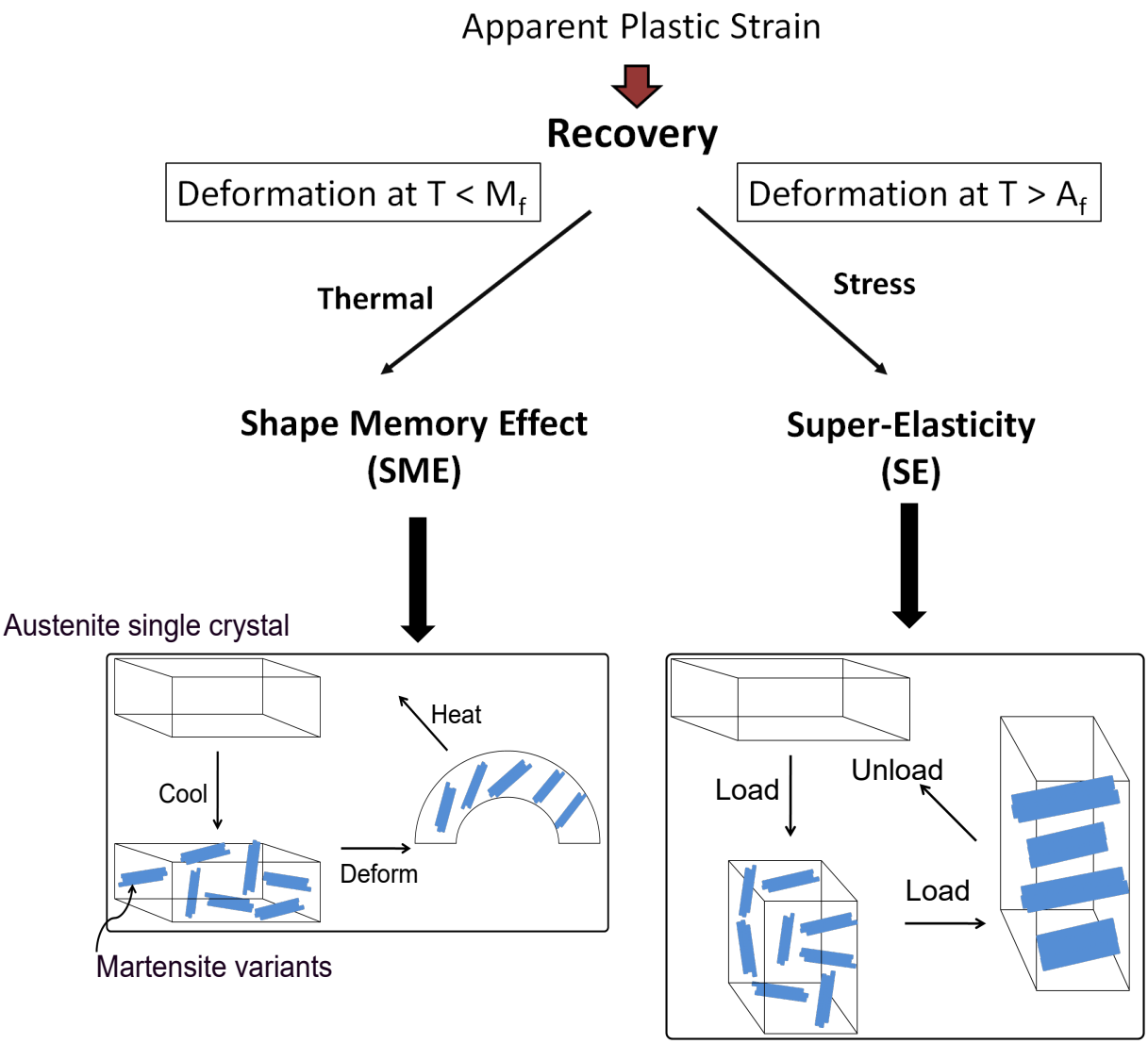

Figure 1.2: Schematic representation of shape memory response of SMA, when deformed at temperatures below M_f (**SME**) and above A_f (**SE**).

broad range of applications [21] covering biomedical [22, 23] to aerospace [24] industries owing to their excellent ductility, high corrosion and wear resistance and near perfect shape memory properties. Since the martensitic phase transformation temperatures in binary and several ternary NiTi SMAs are near or below room temperature [25], their applications are limited to operating temperatures below 100°C [26]. Maximization of the potential of NiTi based SMAs for high temperature applications is the prime motivation behind the development of NiTi based High Temperature Shape Memory Alloys (HTSMAs) which have martensite phase transformation temperatures above 100°C.

1.2. Motivation

In case of NiTi alloys, addition of only few elements such as Pd, Pt, Hf, Zr and Au is known to increase the transformation temperatures above 100°C [26–28]. Studies on the NiTi-based HTSMAs have been actively pursued with the aim of achieving higher phase-transformation temperatures, stable phase transformation behaviour and good mechanical properties including high strength and acceptable shape memory response. Actuation applications of HTSMAs demand a balanced combination of all these properties to utilize their potential to a maximum.

Since HTSMA actuators operate at temperatures significantly above room temperatures, they share several challenges which are common with structural materials; lower yield strength and micro-structural instabilities at high operating temperatures to mention a few. Enhanced dislocation mobility at high temperatures lowers the yield strength of the material, which directly shows up as increased irrecoverable super-elastic strains as well as loss of super-elastic plateau. The alloy strength sets an upper limit on the operating temperatures for these SMAs, since yield strength of metallic alloys behaves negatively with the temperature. Relationship between the alloy yield strength and the SME and SE phenomenon in SMAs can be understood from the temperature-stress diagram [29], shown in Figure 1.3. The figure shows that for temperatures below M_s, the martensite phase is thermodynamically stable, while for temperatures above A_s, martensite is stable only under external applied stress σ^{SIM}, which is stress required to stress induce the martensite. Below A_s, the SMA exhibits only SME while above A_f, only SE is demonstrated. Between A_s and A_f, both the phenomenon co-exist. The extent of super-elasticity in a SMA is decided by the critical stress for plastic deformation, σ_y. For temperatures between A_f and M_d, stress plateau appears due to detwinning of stress induced martensite, giving rise to completely recoverable strain upon unloading, *i.e.* perfect SE. At the temperature M_d, stress induced martensite is no longer possible and plastic deformation of austenite occurs, which results in permanent plastic strain. Figure 1.3 discusses two scenarios:

- Critical stress σ_y^A : In this case, the SE can be observed when the SMA is deformed at temperature above A_f up to M_d.
- Critical stress σ_y^B : In this case, SMA exhibits complete lack of SE. At temperature

just above A_f, stress induced martensite cannot be stabilized due to concomitant plastic deformation.

Thus, for a SMA to exhibit good super-elasticity, the critical stress for plastic deformation of the austenite must be sufficiently high to avoid plastic deformation during straining at temperatures above A_f.

Typically, NiTi-based HTSMAs exhibit transformation temperatures ranging from 200°C-900°C [28, 30]. Elements Hf and Zr are relatively more economic than Pd and Pt and their substitution to NiTi is known to be quite effective in raising phase transformation temperatures [31]. As a result, lot of efforts have been directed towards the development of NiTiHf and NiTiZr HTSMAs, with the two-fold aim of achieving high transformation temperatures and superb shape memory response. However, both these alloy systems have certain issues which must be addressed before putting them into use for HTSMA applications. The chief issues are:

(a) Poor shape memory response: Though both NiTiHf and NiTiZr alloys exhibit high phase transformation temperatures, these alloys are known for their poor workability

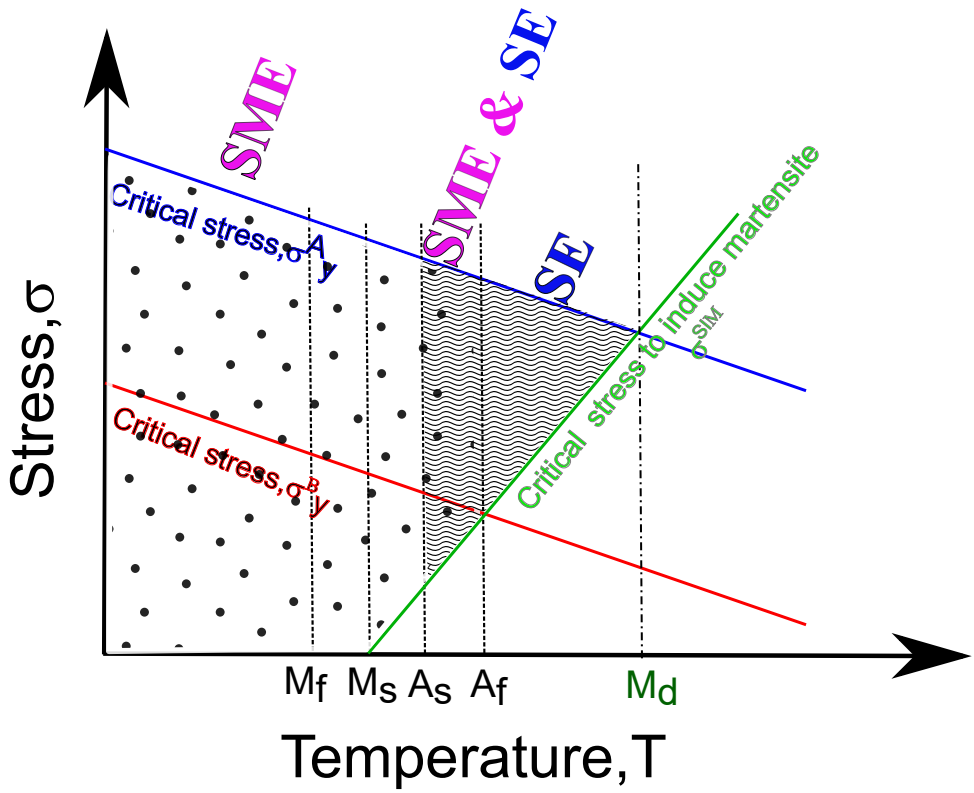

Figure 1.3: Appearance of the SME and SE in the shape memory alloys depicted in the temperature-stress phase space.

[32, 33] and shape memory properties which degrade with Hf and Zr content [34–36]. The NiTiHf alloys, due to their low critical stress for slip [37, 38], exhibit plastic deformation accompanying stress-induced martensite formation and hence non-zero recoverable stains upon unloading. When compared with NiTiHf alloys, the NiTiZr alloys possess poor shape memory properties [39, 40] as well as ductility than NiTiHf alloys, making NiTiHf alloys a more popular HTSMA choice.

(b) Poor thermal cyclic stability: Another issue of concern in front of HTSMA application is the instability of phase transformation behaviour. In case of NiTi SMAs, repeated thermal cycling between austenite and martensite phases leads to accumulation of defects such as dislocations. Consequently, the thermodynamic stability of martensite is lowered with respect to the austenite phase, which manifests itself in the form of lowering of martensite phase transformation temperatures [41]. The rate at which the phase transformation temperatures are lowered with repeated cycling decides the extent of thermal cyclic stability of SMAs. For actuator applications, thermal cycling stability is one of the important aspects of SMA performance. Low critical stress for the slip in NiTiHf alloys results in poor thermal cyclic stability of the alloys [42]. Comparing thermal cyclic stability of NiTiZr alloys with NiTiHf alloys, the former exhibits far lower thermal cyclic stability [39] than the latter.

Considering these factors, the search for low-cost HTSMAs with acceptable shape memory properties concentrated towards NiTiHf alloys and considerable efforts were made to improve their strength. Kockar *et al.* [43] employed thermo-mechanical processing methods such as Equal-Channel Angular Extrusion (ECAE) which lead to increase in transformation strain as well as significantly improved the thermal cyclic stability of $Ni_{49.8}Ti_{42.2}Hf_8$ (at.%) alloys. Later, aging treatments on NiTiHf alloys have been shown to be extremely effective in improving the alloys strength as well as shape memory response [44, 45]. Last few years have seen the emergence of precipitate-strengthened Ni-rich NiTiHf alloys with Hf content 15-20 at.% exhibiting high-temperature super-elastic properties with near-zero irrecoverable strains. Bigelow *et al.* [46] reported super-elasticity with near-zero recoverable strained in aged $Ni_{50.3}Ti_{29.7}Hf_{20}$ alloy. Coughlin *et al.* [47] later reported that yield strength of $Ni_{50.3}Ti_{29.7}Hf_{20}$ alloy can be tuned by aging treatments, which induced ordered precipitates with orthorhombic structure, similar to one

reported by Han *et al.* [48]. Subsequent works demonstrated excellent actuation ability of aged Ni-rich NiTiHf alloys [49].

This has led to several interesting applications of Ni-rich NiTiHf alloys as high-temperature actuator materials in aerospace and spacecraft applications [50–52]. Selection of optimum alloy composition exhibiting best combination of high phase transformation temperatures, low thermal hysteresis, stable phase transformation behaviour is extremely crucial in designing the Ni-rich NiTiHf HTSMA. Since aging treatments involve diffusion-driven precipitation phenomenon, optimization of aging conditions to impart high strength to these alloys is central to the alloy development. An understanding of kinetics of evolution of precipitate phases with time and temperatures plays a key role in this. Further, the role of aging on thermal cyclic stability of martensite transformation in these alloys is equally important to examine. These issues are crucial to the NiTiHf HTSMAs development and must be understood before putting them into use in the practical applications.

1.3. Thesis Overview

Focus of this thesis has been to explore the Ni-rich NiTiHf alloys on account of alloy composition as well as the effect of aging treatments on their phase transformation behaviour and strength.

In this thesis, studies are conducted with the objectives of:

1. Investigation of role of Hf content on the phase transformation characteristics as well as alloy strength in Ni-rich NiTiHf alloys.

2. Studying the role of aging temperatures and durations on the micro-structural evolution and understanding the aging-induced strengthening mechanism in the alloys.

3. Investigating the quantitative precipitation-kinetics of the H-phase precipitates in these alloys and elucidating the underlying mechanism of precipitate growth and coarsening.

4. Tuning the thermal cyclic stability of these alloys by aging treatments and understanding the governing mechanism.

In order to achieve these objectives, Ni-rich $Ni_{50.3}Ti_{49.7-x}Hf_x$ (x = 0, 5, 10, 15, 18, 20, 25 at.%) alloys have been systematically investigated to explore the rate at which Hf con-

tent effects the martensitic phase transformation temperatures, thermal hysteresis and alloy hardness. Next, the role of aging conditions on the martensitic phase transformation characteristics such as phase transformation temperatures, thermal hysteresis and thermal cyclic stability of a Ni-rich $Ni_{50.3}Ti_{29.7}Hf_{20}$ alloy has been elucidated. A systematic investigation of the role of aging temperature and aging duration on the martensitic phase transformation behaviour is carried out and the interplay between precipitate size as well as inter-precipitate spacing on the strengthening effect of H-phase precipitates in these alloys is demonstrated. It needs to be mentioned that kinetics of precipitation in precipitate-strengthened alloys is extremely crucial in adjusting their mechanical properties. Since aging temperature controls the growth rates of the precipitates, the H-phase precipitation kinetics and underlying mechanism behind their growth as well as coarsening has been discussed using complementary electron microscopy and small angle scattering techniques.

1.4. Outline of Thesis

This section presents the organization of the thesis and discusses main theme and major results of each chapter. The thesis is structured as follows:

In **Chapter 2**, detailed survey of the literature relevant to the studies conducted in present thesis is provided. The chapter begins with introduction to martensitic transformation and NiTi SMAs. The martensitic transformations in this alloy system are discussed in view of the crystal structures of the austenite and martensite, with emphasis on factors affecting the transformation behaviour and shape memory properties of these alloys. This is followed by a discussion on the effects of alloying elements and stoichiometry on the phase transformations in NiTi-based HTSMAs. This chapter concludes with discussion on the phase transformation behaviour, mechanical and shape memory properties of the NiTiHf alloys, which are most prominent NiTi based HTSMAs.

In **Chapter 3**, the experimental techniques employed to conduct experiments are presented. This chapter begins with description on the alloys studied and their method of preparation, followed by the techniques used for their characterization. Experimental methodology for the structural and micro-structural characterization via X-ray and

neutron diffraction and Transmission Electron Microscopy (TEM) are described next. The heat-flux Differential Scanning Calorimeter (DSC) set-up utilized to determine phase transformation temperatures and enthalpy of phase transformation is also discussed. The experimental set-up for both Small Angle X-ray Scattering (SAXS) and Small Angle Neutron scattering (SANS), which have been utilized for bulk-scale quantitative micro-structural analysis is described next. This chapter concludes by discussing Vickers micro-hardness as the technique utilized to study mechanical properties of the alloys.

In **Chapter 4**, investigations on the role of Hf content on the phase transformation behaviour in the $Ni_{50.3}Ti_{49.7-x}Hf_x$ (x = 0, 5, 10, 15, 18, 20, 25 at.%) alloys are presented. It is shown that Hf addition to slightly Ni-rich NiTi alloys alters the martensitic phase transformation temperatures (PTTs). For alloys with x < 10, there is an initial decrease in the PTTs values relative to the binary NiTi alloy. For subsequent compositions, there is a linear rise in the values. The dependence of aging temperature on PTTs as a function of Hf content is also explored. It is found that phase transformation in the x = 20 alloy exhibits least thermal hysteresis in comparison to rest of the compositions. This is an important result in view of the fact that since SMA actuation devices must possess near zero response time, large thermal hysteresis values negatively impact the functional capability of these devices. Since x = 20 alloy exhibits sufficiently high PTTs above 100°C and narrow thermal hysteresis, this study paves the way for subsequent part of the thesis, which is focussed on the structure-property correlation in this particular alloy.

In **Chapter 5** the correlation between micro-structure and the mechanical strength of the $Ni_{50.3}Ti_{29.7}Hf_{20}$ alloy as a function of aging temperature is presented. The TEM experiments ascertain that aging the alloy at 550°C and 650°C for a given duration leads to the "H-phase" precipitation. This precipitate phase is compositionally enriched in Ni and Hf, while lean in Ti and possesses an ellipsoidal morphology. The information about precipitate size and morphology obtained directly from TEM is combined with quantitative information on precipitate size-distributions and volume-fraction from SAXS/SANS to elucidate the micro-structural evolution in the alloy with aging. In terms of mechanical properties, H-phase precipitation is found to enhance the alloy hardness on account of precipitation strengthening. Further, lower hardness values of the specimen aged at 650°C

in comparison to one at 550°C has been assigned to precipitate coarsening. The study concluded that aging at 550°C for 3 hours is the peak aging condition for this alloy.

In **Chapter 6**, precipitation-kinetics of the H-phase in aged $Ni_{50.3}Ti_{29.7}Hf_{20}$ alloy has been discussed. In this chapter, analysis done in Chapter 5 is expanded and studies on the micro-structural evolution in the $Ni_{50.3}Ti_{29.7}Hf_{20}$ alloy as a function of both aging temperature as well as aging duration are conducted. Firstly, it is shown that variation of the alloy hardness with aging time is temperature dependent, with the alloy achieving peak hardness at the slowest rate upon when aged at 550°C, in comparison to higher temperatures, *viz.* 600°C and 650°C. The TEM results reveal that aspect-ratio of the ellipsoidal H-phase precipitates is highly dependent upon aging temperature.

Further, *in-situ* and ex-situ SANS experiments enable the determination of temporal evolution of precipitate dimensions as well as volume fraction, which led to the estimation of activation energies for the precipitate growth and coarsening process. This study has established that diffusion of Ni in the alloy matrix governs the early-stage growth kinetics, while diffusion of Hf governs the coarsening kinetics of H-phase. Further, the H-phase coarsening rate is found to be almost eight-time smaller than that of Ni_4Ti_3 precipitates in Ni-rich binary alloys, which has been attributed to slow diffusion of Hf atoms.

In **Chapter 7**, studies on the role of aging on the thermal cyclic stability of the martensitic phase transformation in $Ni_{50.3}Ti_{29.7}Hf_{20}$ alloy are presented. Cyclic stability of the transformation reflects as the variation in associated PTTs and thermal hysteresis. Thermal cyclic stability of the martensitic transformation in present alloy is studied under two scenarios: (a) Thermal cycling at fixed heating/cooling rate and (b) Thermal cycling as a function of heating/cooling rates. It has been observed that aging below 500°C for 3 hours leads to least variation in PTTs as well as thermal hysteresis under both the conditions, while aging at higher temperatures 500°C-650°C degrades the thermal cyclic stability. This dependence has been understood in terms of the activation energy associated with the martensitic transformation.

In **Chapter 8**, the overall results from the present work are summarized and perspective to the future research directions has been laid out.

Finally, **Appendix I** gives a general introduction to basics of precipitation in the alloys. **Appendix II** introduces fundamentals of small-angle scattering, X-ray and neutrons as a probe along with the methodology of data analysis. **Appendices III and IV** give the codes written in python programming language to analyse some of the SAXS/SANS data.

CHAPTER 2

Literature Review

2.1. Martensitic Phase Transformation

When the phase transformation in solids occurs by co-operative atomic movements over distances less than the inter-atomic spacings, crystal structure change materializes without any alteration in composition of the phases. Such transformations are known as *Diffusion-less transformations* and have characteristics very different from the diffusional phase transformations such as precipitation (described in Appendix I). Crystal structure distortion upon diffusion-less transformation leads to volume and shape change of the parent lattice. This introduces elastic strain energy. Further, an interface separating parent and product phase contributes towards the interfacial energy. Based upon relative values of these two energy terms, classification of diffusion-less phase transformations has been done by Cohen *et al.* [53] which is displayed in Figure 2.1.

If strain energy contribution dominates the inter-facial energy and phase transformation between parent and product phases involves shear-dominated atomic displacements, corresponding diffusion-less transformation is known as *Martensite transformation*. The characteristic features of the martensitic transformation are [54, 55]:

- Martensitic transformations is always composition-invariant due to its diffusion-less nature.
- The transformation is of the first-order since it is accompanied with the creation of new interfaces.
- The interface (*Habit plane*) separating parent phase and martensite phases in partially transformed material is un-rotated as well as un-distorted.
- The habit plane has irrational miller indices.

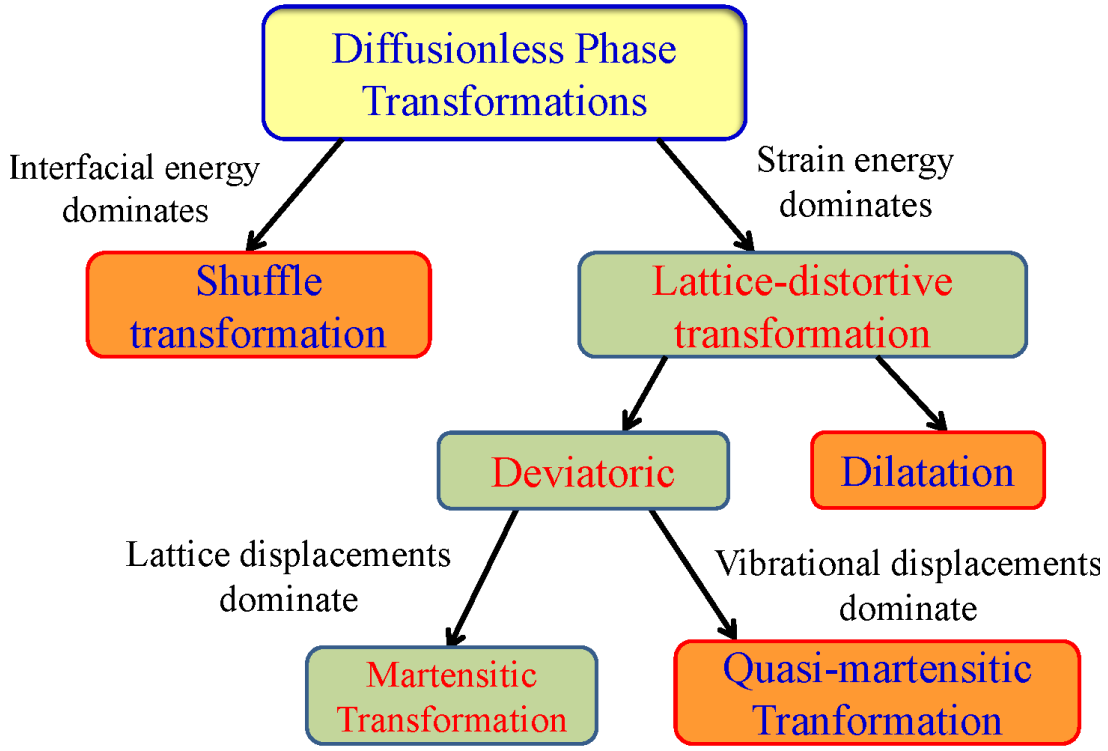

Figure 2.1: Classification scheme for diffusion-less transformations.

- There exists a lattice correspondence between the unit cells of the austenite and martensite phases.
- There is an orientation relationship between the directions and planes of the two phases across the interface.
- The martensite phase exhibits surface features such as plates, laths etc. and fine scale inhomogeneity such as twins, slip or internal faults.

Martensitic transformation occurs by a shear mechanism and begins at a critical temperature M_s during cooling. With further cooling, at temperature M_f, the austenite phase completely transforms to the martensite phase. Upon heating, martensite starts transforming back to austenite at A_s and this reverse transformation completes at A_f. Since the martensitic transformation is of first-order, both austenite and martensite can coexist during cooling within temperature intervals M_s and M_f and during heating between temperature interval A_s and A_f, depicted in Figure 2.2. Martensitic transformations can be further classified into different categories depending upon the nature of nucleation and growth of the transformation.

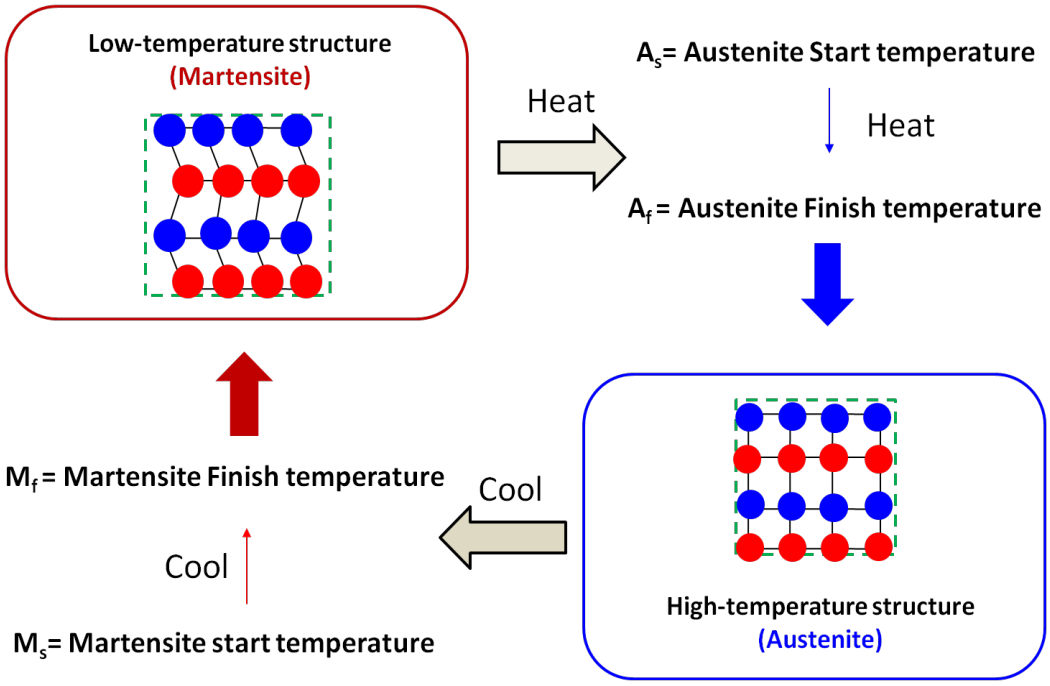

Figure 2.2: Martensitic phase transformation.

Nucleation and Growth of Martensite

Depending upon the nucleation and growth behaviour of martensite, kinetics can be categorized into (a) Athermal and (b) Isothermal martensite [56, 57] .

(a) Athermal: In case of athermal martensite, the transformation progresses with decreasing temperature. In athermal transformation, the martensite nucleation is not thermally-activated. This implies that the transformation fraction is time-independent. In other words, the martensite plates nucleate during lowering of temperature, independent of the cooling rate. As the sample is cooled, the transformation begins at M_s and volume fraction of the martensite increases with further lowering of temperature till the transformation is complete at M_f. Figure 2.3 (a) gives schematic representation of martensite volume fraction as function of temperature.

(b) Isothermal: In case of isothermal martensite transformation, the martensite nucleates in thermally-activated manner at constant temperaturei.e., a critical barrier must be overcome for the nucleation of martensite crystals. As the temperature is maintained below martensite start temperature for certian duration, martensite nucleation becomes favourable and several nuclei appearing due to thermally activated compositional fluctu-

ations become critical, which then grow rapidly in an athermal manner. Therefore, with the increase in temperature, the rate of transformation is dependent on nucleation rate of the martensite. Figure 2.3 (b) gives schematic representation of martensite volume fraction as function of time. Typical examples of alloys which undergo isothermal martensite transformation are Fe-Ni-Mn and Fe-Mn-C [58].

Thus, the major difference between athermal and isothermal martensite can be summa-

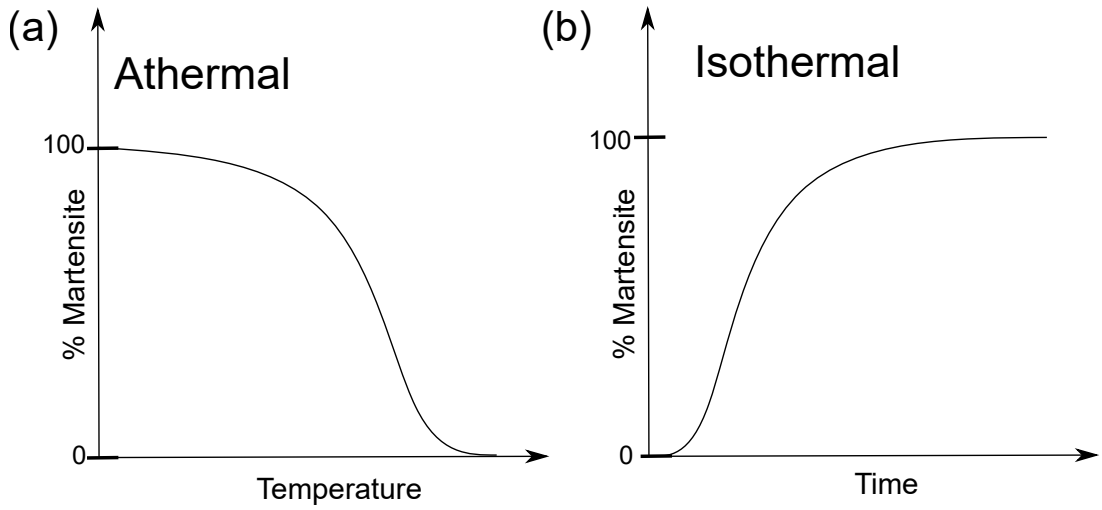

Figure 2.3: Schematic representation of the evolution of martensite volume in (a) athermal martensite and (b) isothermal martensite.

rized in terms of the rate of nucleation of martensite. The nucleation of martensite in the athermal case is not thermally activated and is extremely rapid, while in the isothermal case, the nucleation rate is thermally activated. However, the growth rates exhibit athermal characteristics in both cases.

Thermodynamics of athermal martensitic transformation

In case of athermal martensite, the temperature dependence of free energies of the austenite (G_A) and martensite (G_M) is shown in Figure 2.4. At the crossover point T_0, known as thermodynamic equilibrium temperature, $G_A = G_M$ *i.e.* austenite and martensite are in thermodynamic equilibrium. During forward martensitic transformation from austenite to martensite upon cooling, the change in Gibbs free energy, $\Delta G^{Cooling} = G_A - G_M$. For reverse martensitic transformation during heating, $\Delta G^{Heating} = -\Delta G^{Cooling}$. Upon martensitic transformation, the Gibbs free energy change ΔG^{Total} is given by:

$$\Delta G^{Total} = \Delta G_{chem} + \underbrace{\Delta G_s + \Delta G_{fric}} = \Delta G_{chem} + \Delta G_{nonchem} \tag{2.1}$$

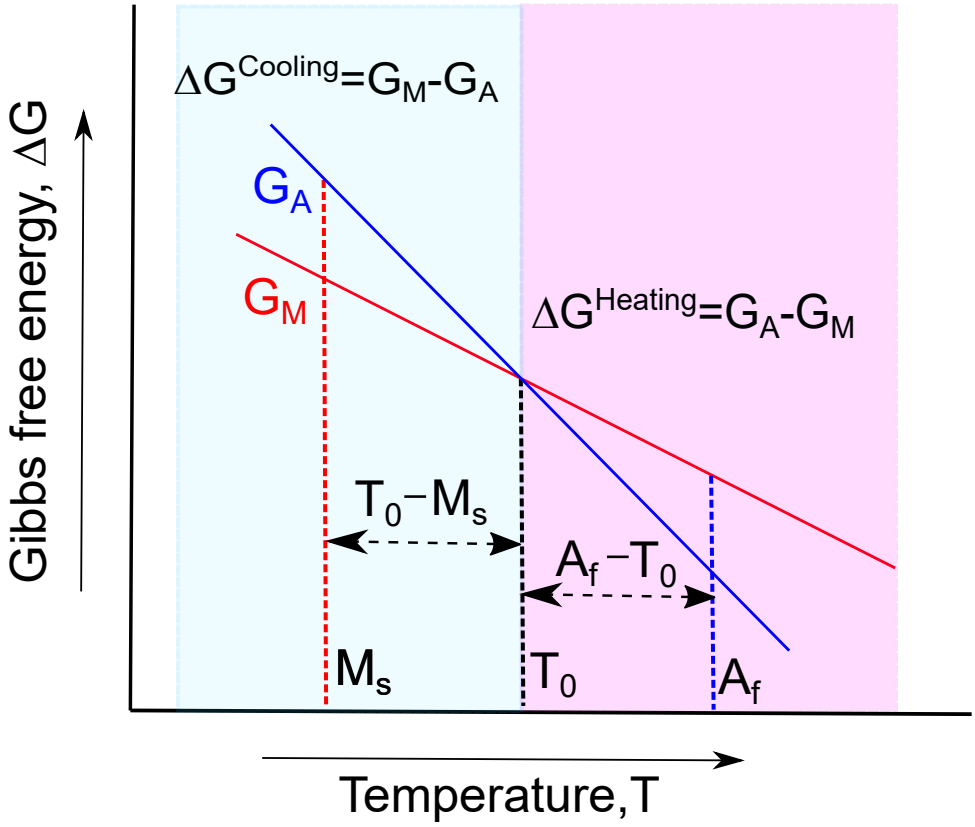

Figure 2.4: Schematic representation of Gibbs free energy of austenite and martensite phases as a function of temperature. The temperature at which martensite structure and austenite structures are stable are labelled as M_s and A_f. The quantity T_0 - M_s and A_f - T_0 are the undercooling and superheating necessary for stabilizing martensite and austenite during cooling and heating, respectively.

which has contributions from:

- ΔG_{chem} ('−' Negative): Chemical driving force arising due to ground state energy difference between austenite and martensite crystal structures.
- ΔG_s ('+' Positive): Strain energy term due creation of austenite-martensite interface.
- ΔG_{fric} ('+' Positive): Dissipative events such as creation of structural defects, acoustic emissions, heat energy etc.

The temperatures at which martensite and austenite structures are thermodynamically stable are labelled as M_s and A_f, respectively. Both are in equilibrium with each other at the thermodynamic equilibrium temperature $T_0 = \frac{M_s + A_f}{2}$. Due to additional contributions from non-chemical term ($\Delta G_{nonchem}$), an *undercooling* of T_0 - M_s is required

for martensite nucleation during cooling and a *superheating* of A_f - T_0 for the austenite nucleation. Further, positive contribution $\Delta G_{nonchem}$ exits as a consequence of strain fields around martensite plates as well as dissipative forces opposing their growth, extra cooling upto martensite finish temperature M_f is necessary for complete transformation to martensite. Similarly, extra heating is required up to A_f till martensite completely transforms to the austenite.

Thermoelastic and Non-thermoelastic Martensite

The athermal martensitic transformations are further classified on the basis of balance between chemical (ΔG_{chem}) and non-chemical ($\Delta G_{nonchem}$) driving forces. If the elastic strain is balanced by the chemical driving forces (thermal energy), martensite is known as thermoelastic, otherwise, it is called non-thermoelastic martensite.

(a) Thermoelastic martensite: In case of thermoelastic martensite, ΔG_{chem} is small in magnitude and is balanced by $\Delta G_{nonchem}$ such that the shape deformation during transformation is elastically accommodated by the parent phase without creating defects or dislocations along the interface. Thus, the austenite-martensite interface is highly coherent and glissile. During heating, the stored elastic energy provides driving force for the reverse transformation. One of the very important characteristics of thermoelastic martensite is that during heating, the martensite will revert back to parent phase in the original orientation *i.e.* crystallographic reversibility is ensured. Due to ease with which back and forth transformation can occur, the thermal hysteresis in alloys undergoing thermoelastic transformation is very small $\approx$ 10-15 K [59]. Non-ferrous alloys such as NiTi and Cu-based alloys belong to thermoelastic martensite category.

(b) Non-thermoelastic martensite: In case of non-thermoelastic martensite, magnitude of ΔG_{chem} is quite large in comparision to $\Delta G_{nonchem}$ and as a result, the martensite grows in a sudden burst. The shape deformation at the austenite-martensite interface in such martensite is accommodated by generating dislocations along the interface, rendering it incoherent as well as immobile. Increase in undercooling enhances the martensite volume fraction, accompanied by increasing defect density till the martensite volume fraction reaches its maximum. The reverse transformation during heating occurs by nucleation of the austenite phase within the martensite plates. Consequently, the non-thermoelastic

martensite is crystallographically not reversible. As a result, non-thermoelastic transformations exhibit wide thermal hysteresis ≈ 100 K [59]. The ferrous alloys such as Fe-Mn, Fe-Mn-Si, Fe-Mn-Si-Cr-Ni etc. belong to category of non-thermoelastic SMAs.

2.1.1. Characteristics of Alloys Exhibiting SME and SE

Smart materials are capable of actuating a device by change in their one or more macroscopic properties brought by external stimuli such as temperature, stress, electric field, magnetic field etc. Development and engineering design of shape memory smart materials involve several technological challenges: attaining low mass-density as cited by Zupan *et al.* [60], small response-time demonstrated by gauthier *et al.* [61] in case of magnetic SMAs, high strength and high work-output efficiency of shape memory alloy actuators over vast range of temperatures discussed by Duerig *et al.* [62] and low in cost [63] to name a few. The SMAs are prominent smart materials and have gained immense popularity as actuator material on account of SME and SE.

For the alloys to display SME and SE, they must possess following characteristics: martensitic transformation should be thermoelastic, both austenite as well as martensite should be ordered and the lattice invariant shear must occur by twinning or stacking faults [64]. Thermoelastic martensite has all the features which are essential for the alloy to exhibit SME and SE namely, small driving force, small volume change, small shear component of the shape strain and low transformation hysteresis. For the alloy to show SME, the plastic accomodation of the strain generated during martensitic transformation must be avoided. As the martensite plate grows into the austenite matrix, accompanying shape deformation tends to cause the matrix to yield plastically. Ling and Owen [65] determined the plastic zone around the growing plate in case of thermoelastic martensite. It was found that ordered alloys have higher yield strength for the same amount of shape strain than the disordered counterparts. As a result, in the case of disordered alloys, the austenite-martensite interface eventually becomes incoherent during growth of martensite. The Table 2.1 below lists few alloy systems and classifies them into two categories namely: *Ferrous* and *Non-ferrous* SMAs.

Amongst ferrous SMAs, the Fe-Mn-Si based alloys alloyed with Cr, Si, Ni undergo non-thermoelastic martensitic transformation and exhibit wide thermal hysteresis as well as lack reasonable SME. Moreover, these alloys have to be thermo-mechanically treated

Table 2.1: Various shape memory alloys categorized into: Non-ferrous and Ferrous SMAs.

Alloy type	Alloy	Alloy composition	Crystal structure		Ordering	Transformation type	Thermal Hysteresis (in K)
			Austenite	Martensite			
Non-Ferrous	**Binary NiTi**	$Ni_{50}Ti_{50}$ [66]	$Pm\bar{3}m$	$P2_1/m$	Ordered	Thermoelastic	40
		$Ni_{50.6}Ti_{49.4}$ [66]					35
		$Ni_{51.1}Ti_{48.9}$ [66]					27
		$Ti_{50.5}Ni_{49.5}$ [67]					32
	Ternary NiTi	$Ni_{46.8}Ti_{50}Fe_{3.2}$ [68]	$Pm\bar{3}m$	$R\bar{3}$	Ordered	Thermoelastic	3
		$Ni_{50-x}Ti_{50}Cu_x$ (x = 8-20 at.%) [69]		Pmmb [70]			~10
		$Ni_{49}Ti_{41}Hf_{10}$ [31]		$P2_1/m$			62
		$Ni_{24.7}Ti_{50.3}Pd_{25}$ [71]		Pmcm [72]			8.5
		$Ni4_{49.5}Ti_{40.5}Zr_{10}$ [73]		$P2_1/m$			75
	Cu-Zn-Al	few at.% Al [74]	B2, $L2_1$	9R, 18R	Ordered	Thermoelastic	10
	Cu-Al-Ni	$Cu_{68.4}Al_{28}Ni_{3.6}$, $Cu_{70}Al_{26.3}Ni_{3.7}$	DO_3	18R or 3H [75]	Ordered	Thermoelastic	10
		$Cu_{68}Al_{28}Ni_4$ [76]		(2H)			30
	Au-Cd	Au-Cd (46.5-48 at.%)	$Pm\bar{3}m$ [77]	Hexagonal	Ordered	Thermoelastic	14 [78], [79]
		Au-Cd (46.5-48 at.%)		Trigonal			
	In-Tl	$In_{77}Tl_{23}$ [80]	FCC	FCT	Disordered	Thermoelastic	5
	Ni-Al	$Ni_{63.2}Al_{36.8}$ [81]	BCC	L10 [82]	Disordered	Thermoelastic	~ 10
		(60-65 at.%)NiAl [83]					
	Ti-Pd	$Ti_{50}Pd_{50}$ [84]	BCC	Orthorohombic (B19)	Ordered	Thermoelastic	46
Ferrous	**Fe-Ni-C**	$Fe_{68.6}Ni_{29.5}C_{1.9}$, $Fe_{71.1}Ni_{25.3}C_{3.6}$ [85]	FCC	BCT	Disordered	Non-Thermoelastic	400-500 [86]
	Fe-Mn-Si	Fe-(21.4-35.6 wt.%)Mn-(1.8-3.1 wt.%)Si [87]	FCC	HCP	Disordered	Non-Thermoelastic	360
	Fe-Mn-Si-Cr-Ni	Fe-15Mn-7Si-9Cr-5Ni (wt.%) [88]	FCC	HCP	Disordered	Non-Thermoelastic	~ 150
	Fe-Ni-Ti-Co	$Fe_{56.9}Ni_{30}Co_{9.3}Ti_{3.8}$ (ausaged) [89]	FCC	BCT	Disordered	Thermoelastic	315
	Fe-Pd	$Fe_{70}Pd_{30}$ [90]	FCC	FCT, BCT [91]	Ordered	Thermoelastic	22 [92]
	Fe-Pt	$Fe_{75}Pt_{25}$ [93]	FCC ($L1_2$)	BCT	Ordered	Thermoelastic	50 [94]

prior to achieve shape recovery which is at the most 3-4% [95]. Occurence of Body Centered Tetragonal (BCT) structure of martensite in Fe-Pd and Fe-Pt thermoelastic ferrous SMAs deteriorates their shape memory properties [96]. In case of Cu-based SMAs such as Cu-Zn-Al alloys, high concentrations of quenched-in vacancies alter the configurational order and affect the relative thermodynamic stabilities of austenite and martensite. For instance, aging of Cu-Zn-Al alloys in martensite phase is known to induce *martensite stabilization* or increase in A_s [97, 98] which, increases with increase in aging time and temperature. Eventually, this leads to complete supression of reverse transformation. High value of $\frac{M_s}{T_m}$ (T_m = melting point of the alloy), typically > 0.2 favours atomic diffusion in martensite [99], which results in rapid martensite aging [100]. Similarly, the In-Tl [99], Au-Cd [101] SMAs exhibit significant martensite aging effects, while it is too slow to be observed in NiTi alloys [99] in comparison to other SMAs. Extremely low ductility and small transformation strains in NiAl SMAs has limited their practical applications [102]. The Ti-Pd SMAs are potential HTSMAs with good ductility, but the shape recovery drastically deteriorates with increase in deformation temperature [84].

The NiTi SMAs, which possess desirable combination of excellent ductility upto 50% elongation, superb corrosion and wear resistance and perfect shape recovery and large super-elastic strains have been most commonly adapted as SMA of choice in the actuator industry.

2.2. History of NiTi SMAs

In the 1890s, the German microscopist *Adolf Martens* found several patterns of the order of few microns on the surface of hard steel, not visible to naked eye. Behind the name of the discoverer, such surface patterns, forming due to diffusion-less solid-solid phase transformations have been known as *Martensite*. This discovery led to the new field of martensitic phase transformations, which were observed to occur in ferrous alloys such Fe-C [103, 104]. The first evidence of martensitic transformation in non-ferrous alloys was provided by Greninger *et al.* [105] in Cu-Zn and Cu-Sn alloys, where they had shown martensite like features, which could be made to appear and vanish with a change in temperature. Later, Chang *et al.* [106] noted diffusion-less phase transformations in the Au-Cd alloys. Subsequently, a lot of other alloys systems such as In-Tl [107], Cu-Al-Be [108], Cu-Zn-Al [109], Ni-Al [81, 110], Fe-based alloys [111] *etc.* were investigated, which

demonstrated SME to varying degrees [112].

In the early 1960s, researchers drew their attention towards the development of lightweight and high strength materials for aerospace applications [113]. During this period, William J. Buehler and co-workers [114] while working at Naval Research Ordnance Laboratory USA on the development of high strength and low weight materials for missiles and space-crafts, demonstrated unique fatigue-resistance property of near equi-atomic NiTi alloy, which they named as **NiTiNOL** (**Ni**ckel **Ti**tanium **N**aval **O**rdnance **L**aboratory) [115].

In the year 1963, Buehler *et al.* [20] reported shape memory phenomenon in near equi-atomic NiTi alloys and a new field of shape memory alloys was born. The NiTi alloys undergo thermoelastic martensite $\rightleftharpoons$ austenite transformation below 100°C and exist at room temperature either as a single phase with ordered BCC CsCl-type (B2) structure or in the two-phase field in equilibrium with Ni_3Ti or $NiTi_2$, depending upon the alloy composition being Ni-rich or Ti-rich. The NiTi binary phase diagram is shown in Figure 2.5.

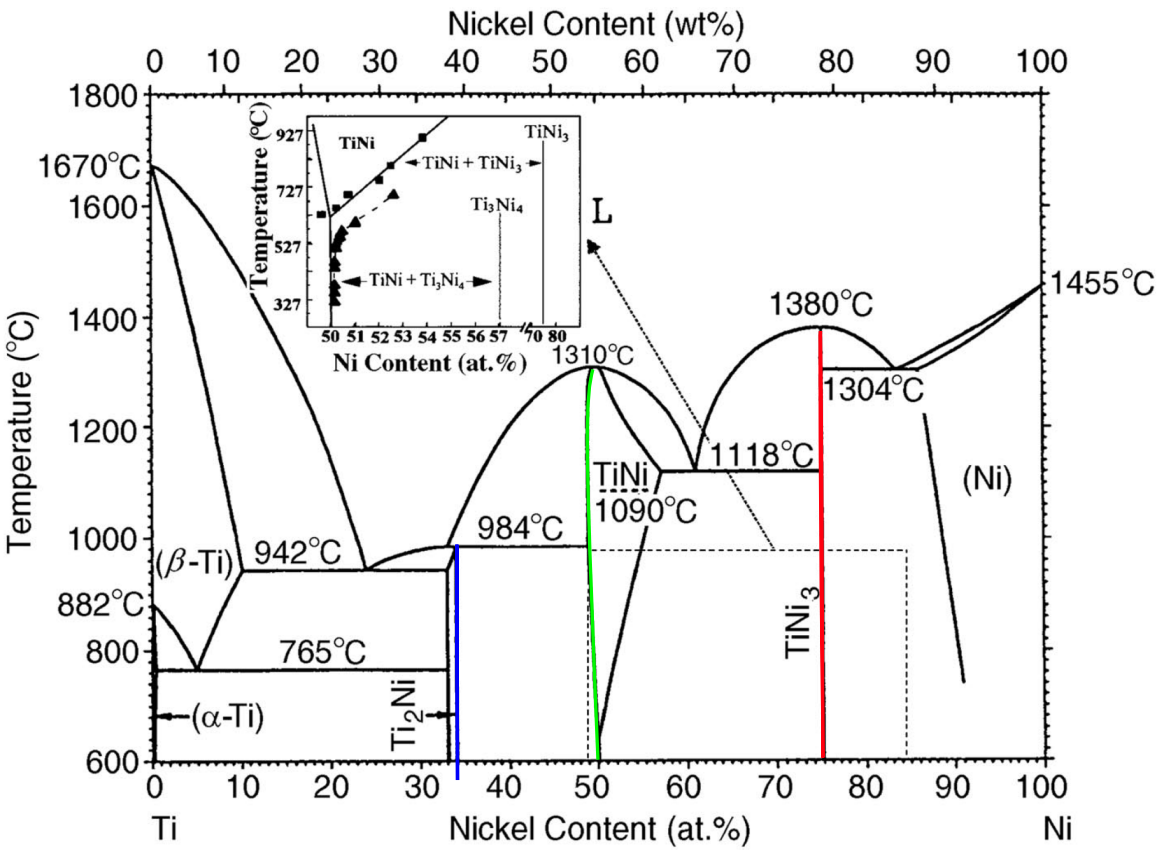

Figure 2.5: Binary NiTi phase diagram [116]. **Figure source:** Otsuka *et al.* [117].

Since then, the NiTi SMAs have drawn significant attention from research fraternity from various point of views including the phase transformation behaviour, mechanical properties, shape memory properties *etc.* Despite being intermetallics, the NiTi alloys are quite ductile (more than 50% elongation) in comparison to the other SMAs, as a result of their low elastic anisotropy ($c_{44}/c^{'} \sim 2$, Table 2.2). Owing to the best combination of large transformation strains [118], high corrosion resistance [119, 120], high wear and tear resistance [121], high damping properties [122] as well as excellent bio-compatiblity [123], development of the NiTi SMAs gained quite an edge over the other SMAs. The Table 2.2 lists physical and mechanical properties of binary NiTi SMA.

Table 2.2: Physical and mechanical properties of Nitinol.

Properties	NiTi Alloys
Density	6.45 gcm^{-3}
Melting point	1310 °C
Magnetic permeability	< 1.002
Coefficient of thermal expansion	10.4×10^{-6} °C^{-1} (24°C - 900°C)
Modulus of non-basal plane shear $\{001\} < 1\bar{1}0 > (c_{44})$	$\sim$ 35 GNm^{-2} [124]
Modulus of basal plane shear $\{110\} < 1\bar{1}0 > (c^{'})$	$\sim$ 17 GNm^{-2} [124]
Transformation temperature range	-100°C - 80°C
Transformation strain	$\sim$ 8%
Ductility	elongation more than 50% [125]
Corrosion resistance	Excellent
Bio-compatibility	Excellent

Engineering applications of NiTi SMA took leap forward with Raychem Corporation's cryofit^{TM} *shrink-to-fit* pipe coupler [115] and since then NiTi SMAs have enjoyed wide acceptance including actuator [126], aerospace and aircraft [24], medical [127] and seismic applications [128].

From the NiTi-phase diagram (Figure 2.5), around 50 at.% Ni concentration, there is negligible solubility on the Ti-rich side while a narrow solubility range exists on the Ni-rich side. Given the narrow Ni-solubility range, the shape memory properties as well as austenite $\rightleftharpoons$ martensite phase transformation temperatures, can be tuned by varying alloy stoichiometry. In solution-treated condition (at 1273 K and water-quenched), NiTi SMAs exhibit poor shape memory effect and complete lack of superelasticity [18] due to

low yield strength of the austenite ($\sim$ 260 MPa) [129]. In order to improve the properties, lots of studies were carried out on NiTi alloys to understand their phase transformation behaviour and shape memory response. The major findings have been [18]:

- Phase transformation temperatures can be tuned by aging as well as ternary additions to NiTi alloys,
- Aging as well as thermo-mechanical treatments on NiTi alloys result in better SME and SE properties.

2.3. Phases in Binary NiTi Alloys

From the phase diagram, presented in Figure 2.5, it can be noticed that near equi-atomic NiTi solid-solution phase field is bounded by $NiTi_2$ inter-metallic phase on the Ti-rich side and Ni_3Ti phase on the Ni-rich side. Further, there is very little solubility for Ni on Ti-rich side of the solid-solution and composition stays close to 50 at.% Ni-50 at.% Ti. These compositions undergo austenite $\rightleftharpoons$ martensite transformation. The crystal structures of austenite as well as martensite phases and precipitate phases in binary NiTi SMAs are discussed below.

2.3.1. Structure of Austenite

From large number of studies on this alloy system, it is generally accepted that phase field between 50.0 at.%Ni to 50.5 at.%Ni has an ordered BCC structure (known as B2) upto 1100°C [130], with lattice parameter of 3.015Å at room temperature [131]. The NiTi B2 unit cell consisting of Ti atoms at the centre of the unit cell and Ni atoms at corners is illustrated in Figure 2.6. As previously mentioned in the section 2.1.1, ordered austenite phase is a necessary condition of alloys undergoing thermoelastic martensitic transformation, martensitic transformation from ordered B2-phase austenite plays crucial role in excellent shape memory properties of this particular alloy system.

2.3.2. Structure of Martensite

The martensite phase in NiTi SMAs can exist in several crystal structures, decided by their relative thermodynamic stabilities. Typically, decided by their crystal symmetries, martensite phase in NiTi SMAs is classified into: Trigonal (R), Orthorhombic (B19) and

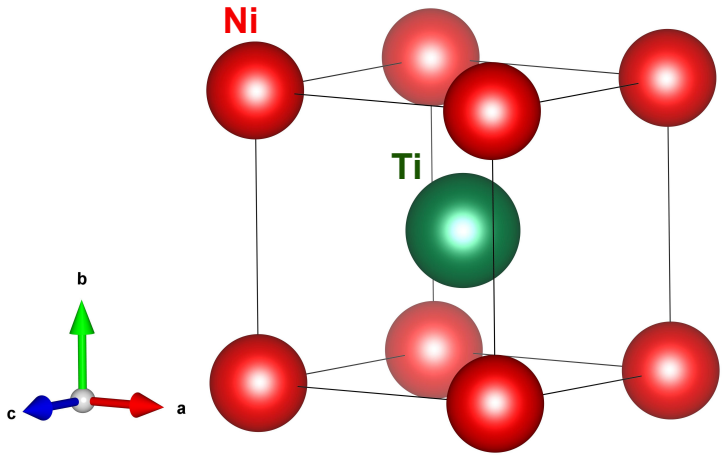

Figure 2.6: Unit cell of NiTi Austenite: B2 (Space group: Pm$\overline{3}$m).

Monoclinic (B19$'$) martensite. Upon quenching, the NiTi SMAs attain stable ground state structure as per following transformation pathway: B2 $\rightarrow$ R $\rightarrow$ B19 $\rightarrow$ B19$'$; monoclinic B19$'$ structure being the ground state [132]. The crystal structures of all three martensite phases are described next.

Trigonal martensite (R-phase): Certain treatments such as aging [133], thermal cycling [134] and thermo-mechanical treatments including annealing after cold working [135–137] stabilize the R-phase martensite prior to B19$'$ martensite in binary NiTi alloys. Further, R-phase is also thermodynamically more stable than B19$'$ in few ternary NiTi SMAs such as NiTiFe [138], NiTiAl [139, 140] etc. The R-phase martensite has trigonal symmetry (space group: P$\overline{3}$) with lattice parameters: a = b = 7.345Å , c = 5.272Å , $\alpha = \beta = 90°$ and $\gamma = 120°$ [141]. The R-phase unit cell of the NiTi martensite is shown in Figure 2.7. Due

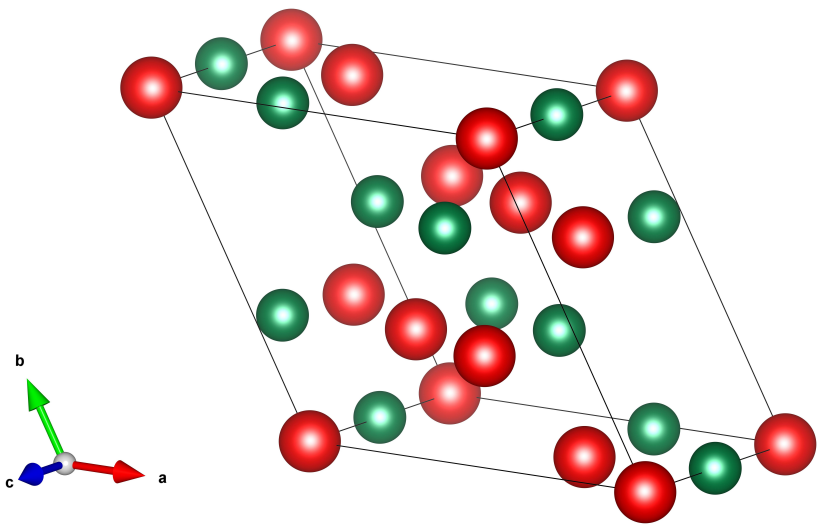

Figure 2.7: Unit cell of NiTi Martensite: R-phase (Space group: P$\overline{3}$).

to small lattice transformation strain associated with B2-trigonal unit cell, transformation barrier for R-phase martensite is lower than B19′ and consequently, R-phase martensitic transformation precedes B2-B19′ martensitic transformation. Further, in comparison to B2 ⇌ B19′, the B2 ⇌ R transformation exhibits narrow thermal hysteresis (∼ 4-5 K) [142], high fatigue life, high thermal cycling stability [143] etc.

Orthorhombic martensite (B19): The orthorhombic martensite is observed in ternary NiTiCu alloys, which for Cu concentration <= 7.5 at.% undergo two-stage reversible martensitic transformation via B2→B19→B19′ and for Cu upto 20 at.% indirectly from B2→B19 [144]. The NiTiPd and NiTiPt high temperature shape memory alloys also undergo B2→B19 martesnitic transformation [145, 146]. Potapov *et al.* [70] proposed Pmmb space group of the B19 martensite in NiTiCu alloys, lattice parameters being a = 2.918Å , b = 4.290Å , c = 4.504Å . The B19 unit cell is illustrated in Figure 2.8.

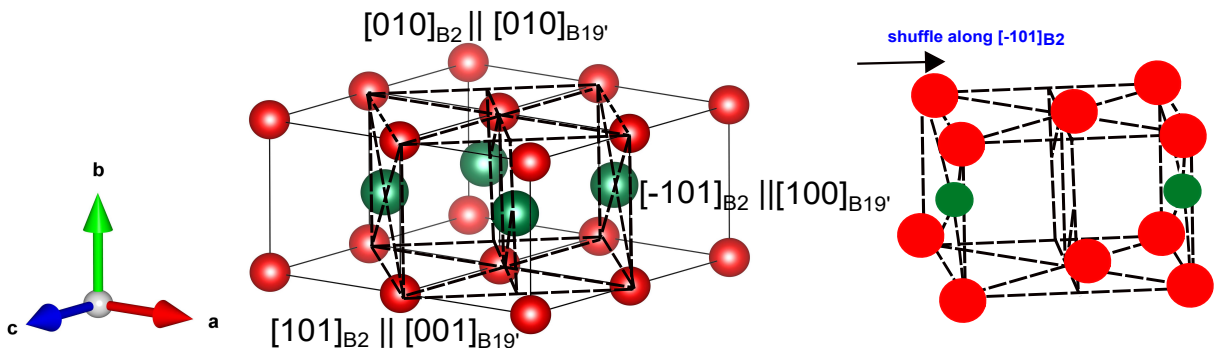

Figure 2.8: Unit cell of NiTi Martensite: B19 (Space group: Pmmb).

The lattice correspondence between B2 and B19 unit cell is [147]:

$$
\begin{aligned}
[001]_{B2} &\rightarrow [100]_{B19} \\
[0\bar{1}1]_{B2} &\rightarrow [010]_{B19} \\
[011]_{B2} &\rightarrow [001]_{B19}
\end{aligned}
\tag{2.2}
$$

Monoclinic martensite (B19′): Kudoh *et al.* [148], using single crystal x-ray diffraction experiments described that NiTi B19′ martensite in $Ni_{49.2}Ti_{50.8}$ at.% alloy has monoclinic symmetry (space group: $P2_1/m$), with unit cell parameters: a = 2.898Å , b = 4.108Å , c = 4.646Å , $\gamma = 97.8°$. The martensite unit cell is formed by distortion of an orthorhombic unit cell delineated from four B2 unit cells involving atomic shuffles. The monoclinic unit

cell delineated from B2 unit cell is shown in Figure 2.9.

The lattice correspondence between B2 and B19′ unit cell is:

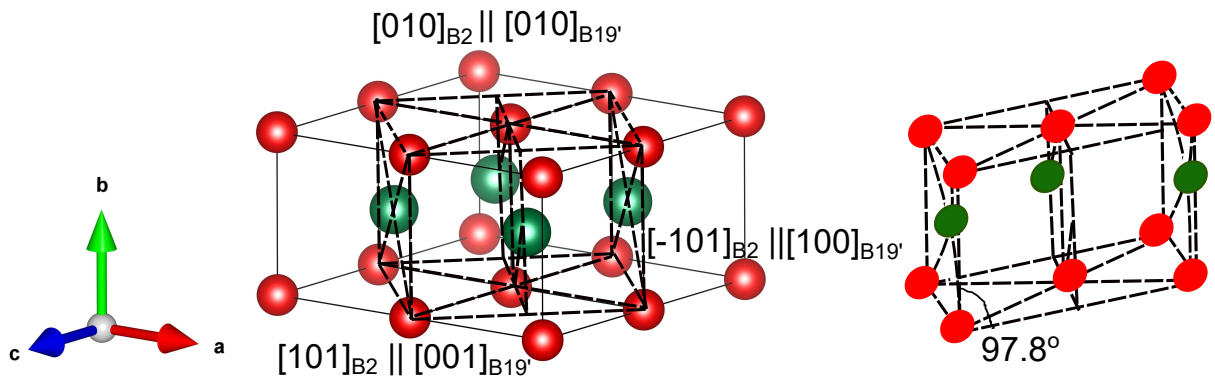

Figure 2.9: Unit cell of NiTi Martensite: B19′ (Space group: $P2_1/m$).

$$
\begin{aligned}
[100]_{B2} &\rightarrow [100]_{B19'} \\
[011]_{B2} &\rightarrow [010]_{B19'} \\
[0\bar{1}1]_{B2} &\rightarrow [001]_{B19'}
\end{aligned}
\tag{2.3}
$$

2.3.3. Precipitate Phases in Binary NiTi Alloys

From the phase diagram, it is established that: (i) Boundary of NiTi-phase on Ti-rich side is almost vertical and (ii) Ni-solubility decreases with lowering of temperature and is nearly zero below 500°C. Since the solid solution has low Ni-solubility, alloy compositions exceeding Ni-content more that 50.5 at.% decompose upon slowly from cooling from high temperatures or aging at temperatures below 700°C. Nishida *et al.* [149] confirmed the presence of Ni_3Ti and Ni_3Ti_2 phases using Scanning Electron Microscopy (SEM) energy dispersive X-ray analysis upon slow cooling of 52 at.%Ni-Ti alloy from 1000°C to room temperature. They derived TTT (Time-Temperature-Transformation) diagram (shown in Figure 2.10) for phase decomposition of the alloy during slow cooling from 1000°C and established that there are three temperature ranges, having decomposition scheme as follows:

1. Aging at temperatures below 953 K (680°C)

$$NiTi \longrightarrow NiTi + Ni_3Ti_4 \longrightarrow NiTi + Ni_3Ti_2 \longrightarrow NiTi + Ni_3Ti \tag{2.4}$$

2. Aging at temperatures between 953 K and 1023 K (680°C and 750°C)

$$NiTi \longrightarrow NiTi + Ni_3Ti_2 \longrightarrow NiTi + Ni_3Ti \tag{2.5}$$

3. Aging at temperatures between 1023 K and 1073 K (750°C and 800°C)

$$NiTi \longrightarrow NiTi + Ni_3Ti \tag{2.6}$$

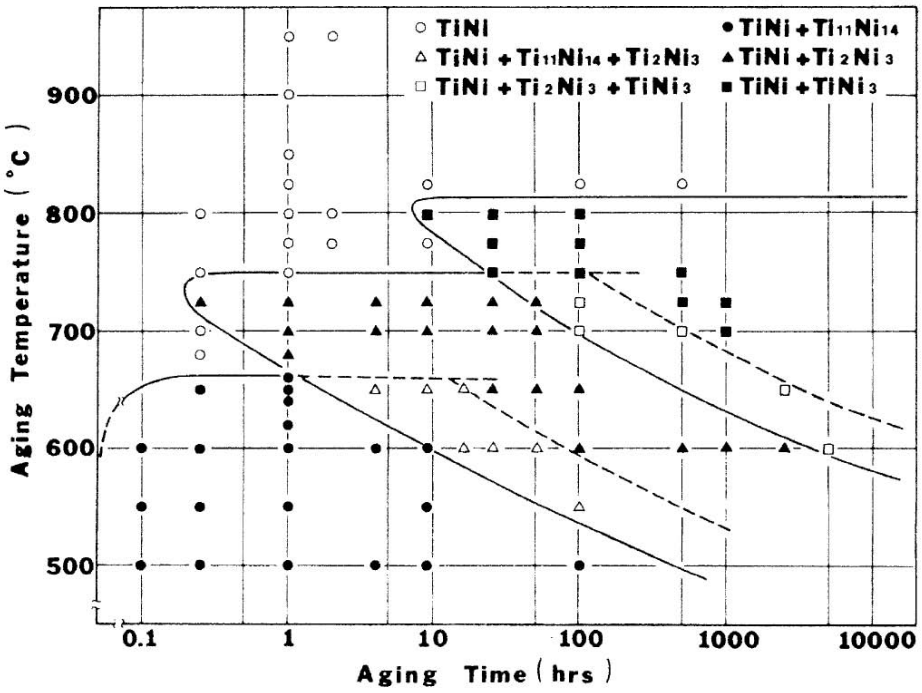

Figure 2.10: Time-Temperature-Transformation(TTT) curve for 52 at.% Ni-Ti alloy. **Figure source:** Nishida *et al.* [149].

The Ni-rich B2-phase decomposes during slow cooling by forming phases which are rich in Ni-content, till it touches the Ni_3Ti inter-metallic phase boundary. Solidus line for the NiTi phase is found to be at 812 ± 22°C [149] for the 52 at.% Ni-Ti alloy. The Ni_4Ti_3 phase appears during early stages of aging at low temperatures in the form of fine platelets, coherent with the matrix [133], [150], [151], [152]. These precipitates are known to significantly improve the shape memory properties of binary NiTi SMAs [153], [154], [155], [156], [157]. The Ni_4Ti_3 phase is an intermediate phase, which precedes the formation of final Ni_3Ti inter-metallic phase.

Crystal Structure of Ni_3Ti phase

The Ni_3Ti inter-metallic compound, as shown in Figure 2.5, melts congruently at 1680°C (1653 K), with Hexagonal Close Packed (HCP) DO_{24} crystal structure. The Ni_3Ti unit cell (space group: $P6_3/mmc$) is composed of 16 atoms, lattice parameters being a = 5.096Å, c = 8.322Å, γ = 120° [158]. Presence of Ni_3Ti phase has deleterious effects on the alloy ductility and shape memory behaviour due to its high hardness [159].

Crystal Structure of Ni_4Ti_3 phase

The Ni_4Ti_3 precipitates forming during aging of Ni-rich NiTi alloys enhance super-elasticity in binary NiTi SMAs. Nishida *et al.* [160, 161] suggested that aging of Ni-rich NiTi alloys lead to precipitation of $Ni_{14}Ti_{11}$ phase, possesses centro-symmetric rhombohedral crystal structure, belonging to space group R3 with unit cell containing total 14 atoms. The lattice parameters of the unit cell were determined as: a = 6.61Å, α = 113.65°. On the basis of electron microscopy and Density Functional Theory (DFT) calculations [150, 162], further research established that the phase is Ni_4Ti_3 and its structure is non centro-symmetric Rhombohedral with space group $R\overline{3}$. Khallil-Allafi *et al.* [163] reported linear increase in the lattice parameters ('a' and 'α') of the Ni_4Ti_3 phase with temperature. These coherent, lenticular disk-like precipitates grow on {111} planes of B2-matrix [164], resulting in eight variants of Ni_4Ti_3 phase. These eight variants fall into four groups and each group includes a pair of conjugate variants which can be obtained from each other by a 180° rotation operation. The orientation relationship between Ni_4Ti_3 rhombohedral unit cell and B2 unit cell is:

$$(111)_{Ni_4Ti_3} \parallel (111)_{B2} \tag{2.7}$$

(*e.g.* $(111)_{Ni_4Ti_3} \parallel (111)_{B2}$ variant and $(111)_{Ni_4Ti_3} \parallel (\overline{1}\ \overline{1}\ \overline{1})_{B2}$ variant). If an initial homogeneous NiTi alloy is aged within the two-phase region of Ni_4Ti_3 and NiTi, without any external constraints, all the differently oriented variants will grow with the equal probability.

The precipitation of Ni_4Ti_3 particles in Ni-rich NiTi alloy compositions occur during aging below 550°C, which significantly enhance the shape memory properties of these alloys. Figure 2.11 shows Ni_4Ti_3 precipitate morphology and improvement in super-elastic response of Ni-rich NiTi alloys upon aging on account of Ni_4Ti_3 precipitation.

Crystal Structure of $NiTi_2$ phase

On the Ti-rich side of the phase diagram, another inter-metallic compound with the stoichiometry $NiTi_2$ is stable. The phase has a complex Face Centered Cubic (FCC) structure (space group: $Fd\bar{3}m$), with unit cell composed of 96 atoms and lattice parameter a = 11.320Å [165]. While the NiTi phase forms congruently from melt at temperature of 1583 K, the $NiTi_2$ phase forms by a peritectic reaction between NiTi compound and the melts at a temperature of 1257 K. The $NiTi_2$ particles are present in the Ti-rich NiTi alloys with typical size ranging from 1-10 μm, typical volume fraction 1-2% [166]. Tadayyaon *et al.* [67, 167] showed that formation of semi-coherent $NiTi_2$ precipitates in Ti-rich $Ni_{49.5}Ti_{50.5}$ alloys lead to increase in transformation temperatures and widening of thermal hysteresis.

The Table 2.3 summarizes the crystal structure information of precipitate phases in binary NiTi SMAs.

Table 2.3: Crystal structures of precipitate phases in binary NiTi SMAs.

Phase	Crystal structure	a(Å)	b(Å)	c(Å)	α(°)	β(°)	γ(°)	Ref.
Ni_3Ti	$P6_3/mmc$	5.096	5.096	8.322	90	90	120	[158]
Ni_4Ti_3	$R\bar{3}$	6.61	6.61	6.61	113.8	90	90	[150, 160–162]
$NiTi_2$	$Fd\bar{3}m$	11.32	11.32	11.32	90	90	120	[165]

2.4. Phase Transformation Behaviour and Shape Memory Properties of NiTi-based HTSMAs

As previously mentioned, binary NiTi SMAs exhibit near or below room temperature phase transformation temperatures, which limits their applicability to the operating temperatures below 100°C. Efforts directed towards raising the transformation temperatures above this limit involve altering alloy stoichiometry, aging treatments and alloying additions. It is well established that M_s temperatures in binary NiTi SMAs decrease at the rate $\sim$ 120 K /at.% Ni, while almost independent of Ti-content in Ti-rich compositions, with values almost equal to that of $Ni_{50}Ti_{50}$ (at.%) alloy [66, 168] (shown in Figure 2.12

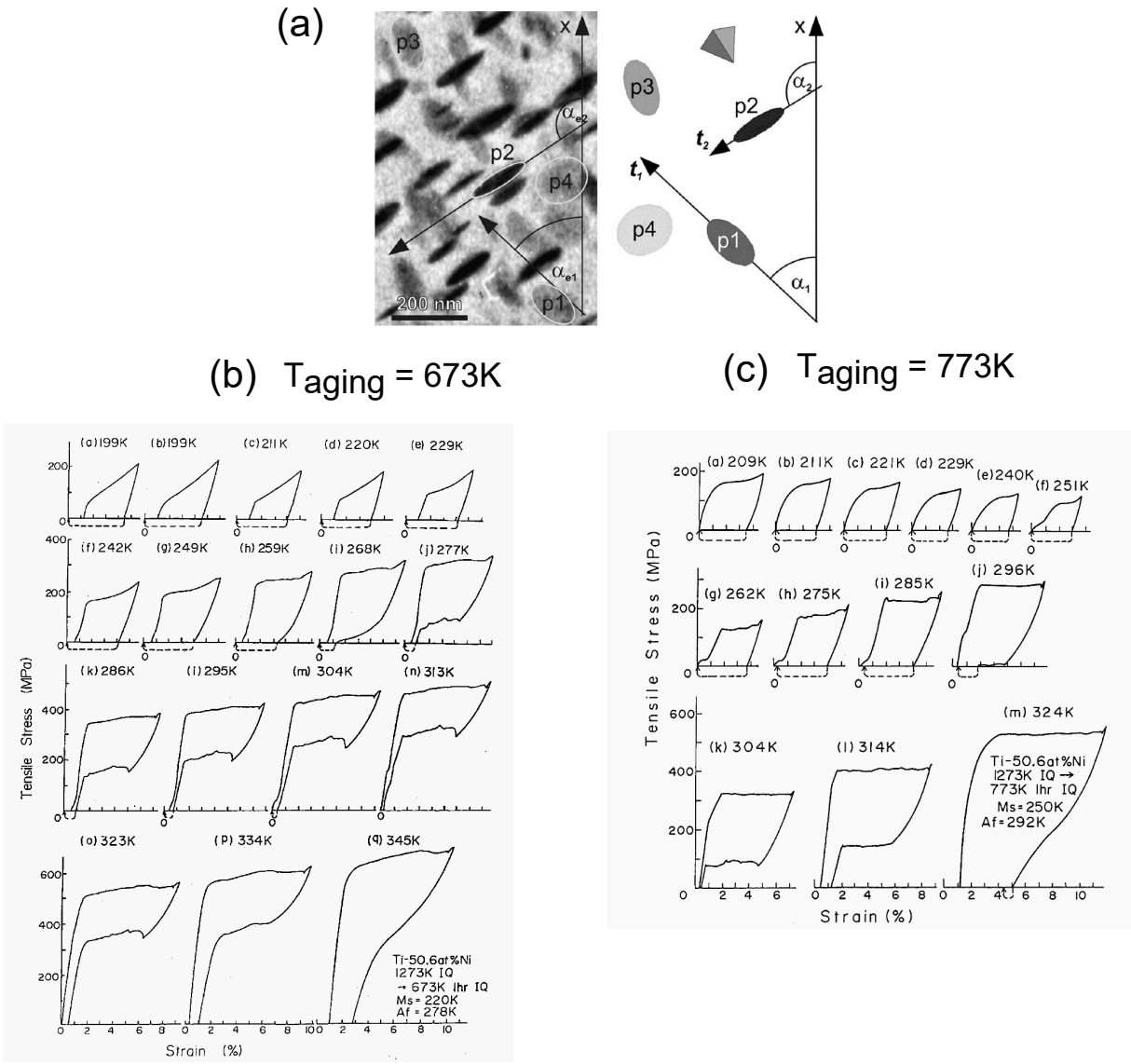

Figure 2.11: (a) Ni_4Ti_3 particles belonging to groups associated with {111} B2 planes in $Ni_{50.7}Ti_{49.3}$ alloy. **Figure source:**Bojda *et al.* [151], stress-strain curves obtained at different temperatures for $Ni_{50.7}Ti_{49.3}$ alloy (b) aged at 773 K for 1 h, (c) aged at 673 K for 1 h. **Figure source:** [18]. Better SE and SME observed in the alloy aged at 673 K for 1 h.

(a)). Aging the Ni-rich compositions induces Ni_4Ti_3 precipitation, which has multi-fold effects including multi-stage martensitic phase transformation [169–171] (shown in Figure 2.12 (b) and (c)). It is the ternary substitution of few elements such as Pt, Pd, Hf and Zr that is known to elevate the phase transformation temperatures of NiTi SMAs above 100°C limit. The ternary NiTi-(Pd, Pt, Hf and Zr) alloys qualify as HTSMAs. This section discusses the phase transformation characteristics and shape memory properties of all the four HTSMAs.

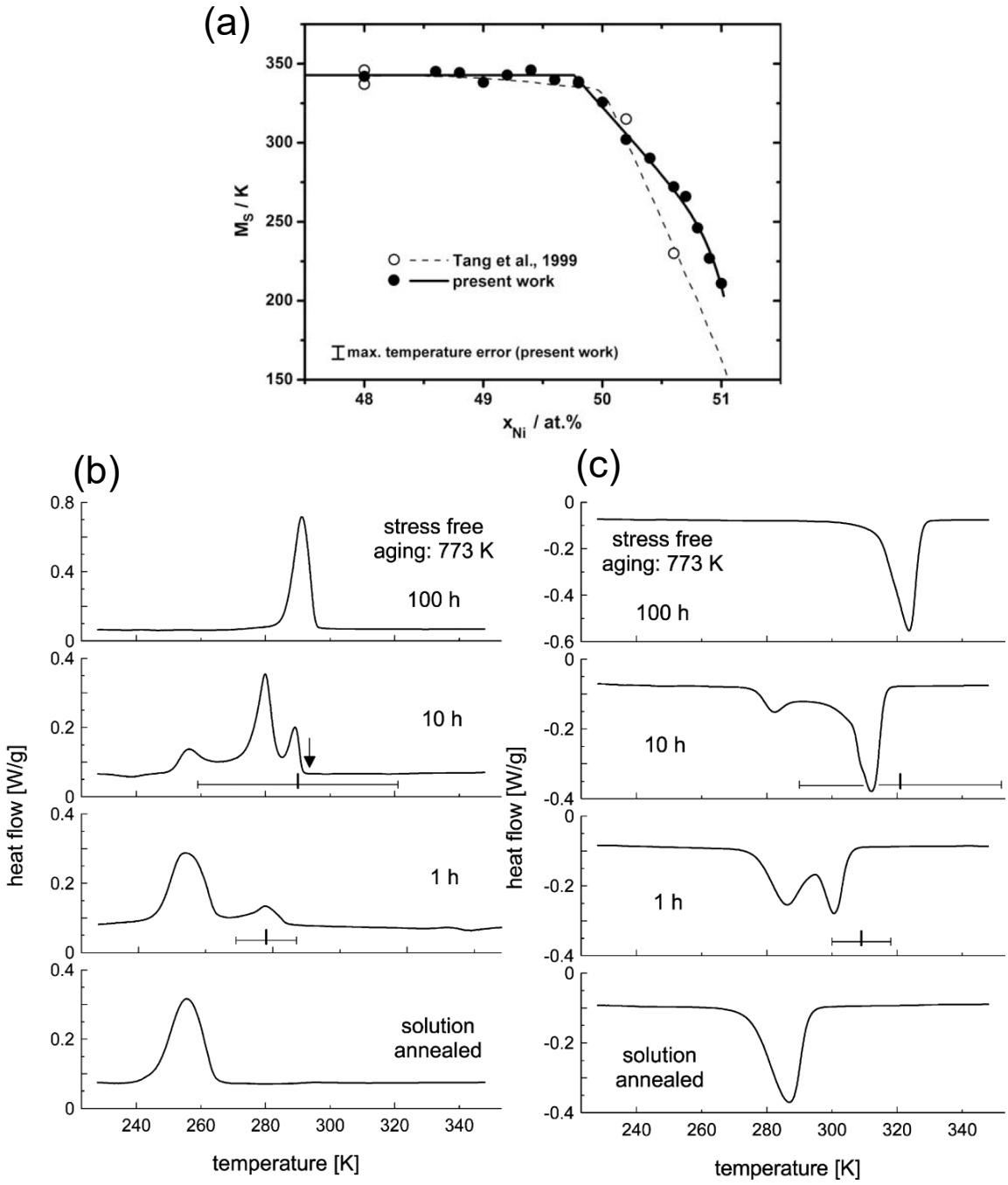

Figure 2.12: (a) Ni-concentration dependence of phase transformation in binary NiTi alloys. Adapted from [66]. DSC plots depicting multi-stage transformation due to aging-induced Ni_4Ti_3 precipitates for (b) B2 → B19′ forward transformation. (c) B19′ → B2 reverse transformation. Figures (b) and (c) adapted from [170].

2.4.1. NiTi-(Pd, Pt, Zr) High Temperature Shape Memory Alloys

NiTiPd and NiTiPt alloys: The phase transformation temperatures of ternary NiTi-(Pd, Pt) alloys alter with the substitution of elements Pd and Pt at the expense of Ni. In

particular, The phase transformation temperatures follow a parabolic trend with the Pd and Pt concentration. Composition dependence of phase transformation temperatures in NiTi-(Pd,Pt) alloys is shown in Figure 2.13 (a) and (b). In terms of martensite transformation pathway, NiTPd and NiTiPt alloys with Pd/Pt concentration < 10 at.% undergo B2 $\rightarrow$ R-phase or B19$'$ transformation [172, 173], while single-stage B2 $\rightarrow$ B19 transformation occurs for higher concentrations [145, 174]. In terms of thermal hysteresis, these HTSMAs exhibit narrow thermal values $\sim$ 10 K [71, 175].

In case of NiTiPd alloys with Ti-content 50 at.%, the transformation temperatures decrease at the rate $\sim$ 4°C/at.% [176] for Pd concentration < 10 at.%. For higher concentrations up to 20 at.% Pd, the transformation temperatures increase at the rate $\sim$ 15°C/at.% [177, 178]. On the other hand, for a fixed concentration of Pd, the transformation temperatures of $Ti_xNi_{70-x}Pd_{30}$ (x = 48.5 to 51.0 at.%) alloys are sensitive to Ti concentration. For Ti concentration > 50 at.%, the transformation temperatures have a plateau value of 250°C, on the other hand for lower Ti-concentration, value drop to 25°C in case of x = 48.5 at.%. Similar parabolic dependence of phase transformation temperatures with Pt concentration exists for NiTiPt alloys, reported by Buccheit *et al.* [175] and Rios *et al.* [179], with transformation temperatures increasing $\sim$ 25°C/at.% Pt for Pt concentration >15 at.%, implying Pt more effective in raising transformation temperatures in comparison to Pd.

In terms of shape memory properties, the NiTiPd and NiTiPt SMAs exhibit poor strain recovery on account of low values of σ^y [180, 181]. In comparison to the equi-atomic compositions (*viz.* $Ni_{50-x}Ti_{50}(Pd,Pt)_x$ alloys), aging in Ti-rich compositions introduced Ti_2(Ni,Pd) [146] and Ti_2(Ni,Pt) [182] precipitates which considerably improved the shape recovery and super-elastic properties [183, 184]. On the other hand, aging of (Ni,Pd) and (Ni,Pt)-rich NiTi(Pd,Pt) alloys introduces P-phase precipitates [185, 186], which raised the transformation temperature considerably upon aging, for alloys with much lower Pt or Pd contents. The P-phase strengthened NiTi-(Pt,Pd) alloy exhibit excellent super-elastic properties by raising the yield strength of austenite [145, 174, 187].

NiTiZr Alloys: Eckelmeyer [188] for the first time reported the phenomenon of increasing the phase transformation temperatures of NiTi alloys with Zr substitution. Alloy compositions with Zr substituted against Ni exhibited much lower transformation tem-

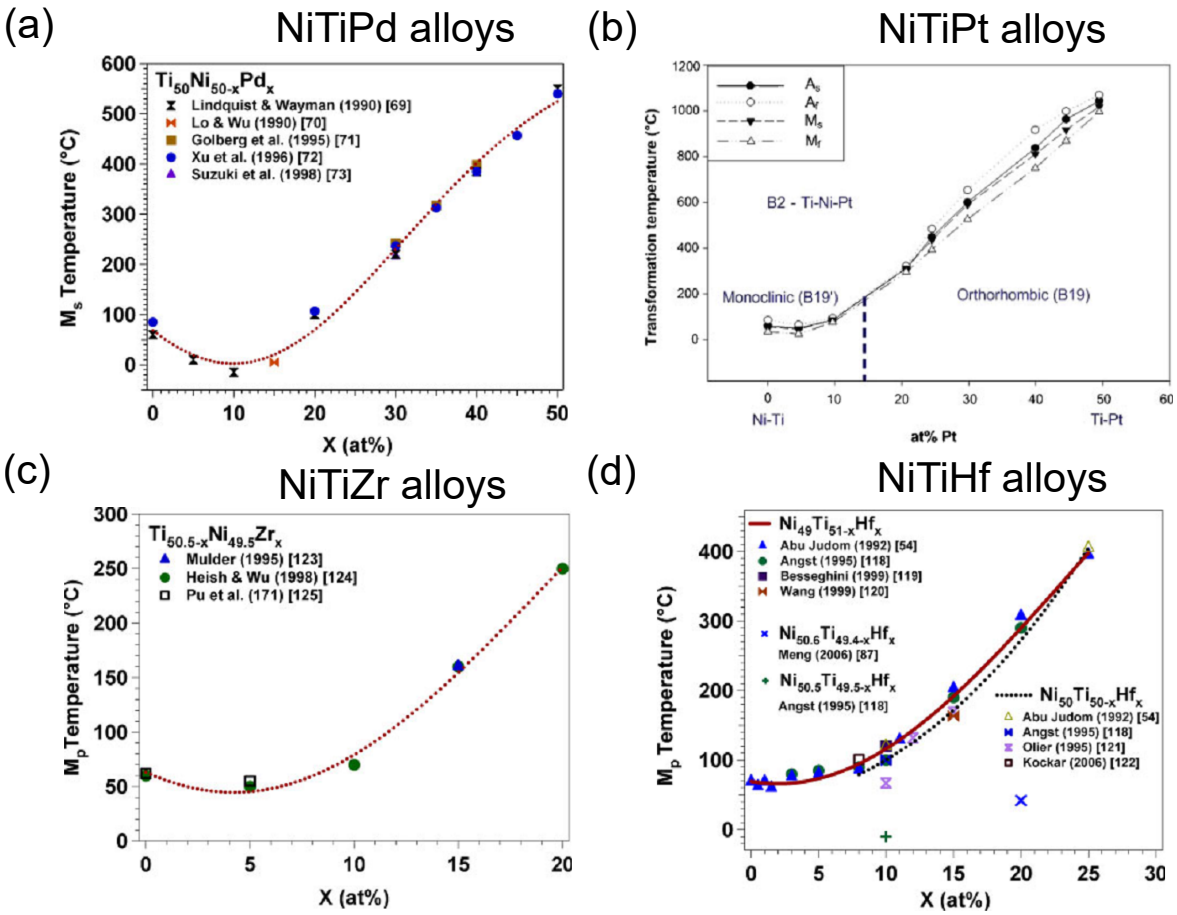

Figure 2.13: Compositional dependence of martensitic phase transformation temperature on the concentration of (a) Pd in NiTiPd alloys, (b) Pt in NiTiPt alloys, (c) Zr in NiTiZr alloys and (d) Hf in NiTiHf alloys. **Figure source:** (a)-(d) [28].

peratures [189] and degrades their ductility. On the other hand, Ti-substituted NiTiZr alloys demonstrate a decreasing trend in transformation temperatures for Zr concentrations < 10 at.% and for higher concentrations, the values rise almost linearly at the rate $\sim 18°$C/at.% Zr [39, 190], shown in Figure 2.13 (c). In terms of martensite transformation pathway, the NiTiZr alloys undergo B2 $\rightarrow$B19$'$ phase transformation for all the Zr concentrations as high as 20 at.% Zr, unlike NiTi-(Pd,Pt) HTSMAs. Although Zr being relatively cheaper than Pd and Pt and significantly raises martensite transformation temperatures, the NiTiZr HTSMAs have certain drawbacks.

The Ti-rich NiTiZr contain large volume fraction of $(Ti,Zr)_2Ni$ precipitates, which negatively affect the mechanical strength and formability of these alloys [190, 191]. In addition to these precipitates, a ternary λ_1 Laves phase [190] also forms, which induces brittleness in the alloys. Low value of σ^y is the major issue behind lack of stress plateau in these alloys [192]. Further, these alloys exhibit of thermal hysteresis $\sim$ 40 K-50 K [39],

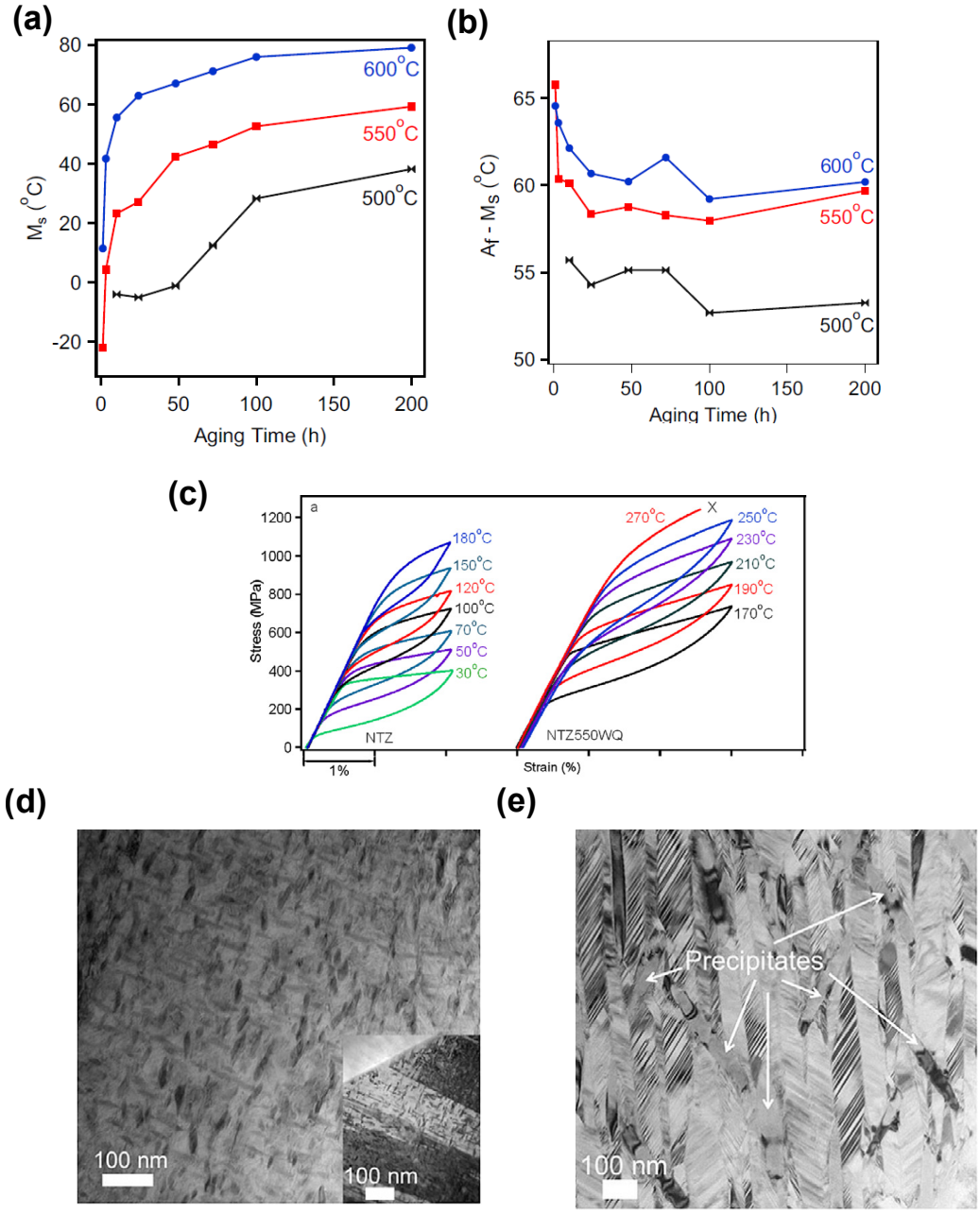

Figure 2.14: (a) Shift in M_s temperature, (b) Thermal hysteresis A_f - M_s in $Ni_{50.3}Ti_{34.7}Zr_{15}$ alloy as a function of aging time and temperature, (c) Temperature dependent super-elastic responses in the $Ni_{50.3}Ti_{29.7}Zr_{20}$ alloy, (d) nano-precipitates in the $Ni_{50.3}Ti_{29.7}Zr_{20}$ alloy aged at 550°C for 100 hours. **Figure source:** (a), (b) adapted from [193], (c) adapted from [194] and (d), (e) adapted from [195].

larger than those of NiTi-(Pd,Pt) HTSMAs.

Sandu *et al.* [196] demonstrated super-elasticity in $Ni_{52}Ti_{42}Zr_6$ (at.%) alloy on account of matrix strengthening by aging induced precipitates with unknown chemistry and structure different from Ni_4Ti_3 precipitates in binary NiTi alloys [197]. Evirgen *et al.* [194, 195] demonstrated near-complete strain recovery in aged $Ni_{50.3}Ti_{29.7}Zr_{20}$ (at.%), in which aging

lead to increase in the yield strength σ^y of the alloy as well tuning the phase transformation temperatures and thermal hysteresis [193, 198] on account of Ni- and Zr-rich precipitate phase with ellipsoidal morphology (shown in Figure 2.14). This precipitate phase has been widely investigated and has been effective in improving super-elastic response in Ni-rich NiTiZr HTSMAs [199, 200]. Carl *et al.* [201] recently showed that the composition of these precipitates is not unique and shifts with Ni-concentration in the alloy.

2.4.2. NiTiHf Alloys

Although poor ductility of the NiTiHf and NiTiZr alloys remains a bigger challenge towards development of these HTSMAs, Hf substitution to NiTi has been most effective in raising transformation temperatures. Particularly for Hf concentration > 10 at.%, the peak martensite transformation temperature, M_p increases at the rate of $\sim$ 20°C/at.% Hf, as shown in Figure 2.13 (d). The trend of decreased transformation temperatures for concentration lower than 10 at.% remains common to substitution of all the elements Pd, Pt, Hf and Zr. In case of binary NiTi alloys, the alloy stoichiometry in other words, the Ni to Ti ratio plays important role in deciding their phase transformations and shape memory characteristics, phase transformation behaviour and properties of Ti-rich and Ni-rich NiTiHf alloys have been discussed next.

Ti-rich NiTiHf Alloys

Majority of studies on NiTiHf alloys involve compositions prepared by substituting Hf at the expense of Ti, with relatively few reporting Hf substitution against Ni [202]. Angst *et al.* [31] studied the Hf-concentration dependence of phase transformation temperatures in Ti-rich $Ni_{49}Ti_{51-x}Hf_x$ (x = 0 - 30 at.%) alloys, by substituting Hf against Ti and found that transformation temperatures can be raised up to 500°C for x = 30 at.%. For constant Hf concentrations, the phase transformation temperatures remain independent of Ti-concentrations > 50 at.% and sharply drop with Ni-concentration > 50 at.% [203], in a manner similar to binary NiTi alloys. Potapov *et al.* [204] also reported an increase in martensite transformation temperatures as well as thermal hysteresis (A_f - M_s) in $Ni_{49.8}Ti_{50.2-x}Hf_x$ (x = 8 - 20 at.%) alloys with increases from 73°C (for x = 8 at.%) to 102°C (for x = 20 at.%). They also observed that B2 lattice parameter increases with Hf content. The B19$'$ lattice parameters *a, c* and β have been found to increase while

parameter b decrease with Hf content [204, 205].

Thermal cyclic stability is an another major factor for SMAs since stable phase transformation temperatures in NiTi SMAs tend to lower with repeated cycling between austenite and martensite phase [41, 206–208]. In case of Ti-rich NiTiHf alloys, the phase transformation temperatures also decrease with number of thermal cycles, but at rate much higher than binary NiTi alloys [209] (shown in Figure 2.15 (a)) and stabilize after 20 thermal cycles. Basseghni *et al.* [210] reported the lowering of phase transformation temperatures by 30°C over 60 thermal cycles, with maximum decrease in A_s values by over 36°C to 40°C. They reported average value of thermal hysteresis as 55°C, which is initially stable upto initial 10 cycles and then slightly decreases with increasing number of cycles. Kockar *et al.* [43] utilized severe plastic deformation in $Ni_{49.8}Ti_{42.2}Hf_8$ alloy to enhance thermal cyclic stability of the alloy. The reason behind poor thermal cyclic stability of NiTiHf alloys their poor strength. Meng *et al.* [211] demonstrated low value of critical shear stress for slip in $Ni_{49}Ti_{36}Hf_{15}$ alloy, as a consequence of which the stress induced martensite formation and plastic deformation occurs simultaneously and stress plateau is completely absent [212]. This results in large irrecoverable plastic strain upon unloading the alloy *i.e.* complete absence of SE (shown in Figure 2.15 (b) and (c)).

The (Ti+Hf)-rich NiTiHf alloys contain $(Ti,Hf)_2Ni$ precipitates [213], whose volume fraction increases with increase in Ni:(Ti+Hf) ratio, make the alloys brittle [210]. Aging the Ti-rich NiTHf alloys is effective in slightly increasing the phase transformation temperatures [210] as well as tuning the volume fraction and size of the $(Ti,Hf)_2Ni$ precipitates [214]. The yield strength of the $Ni_{49}Ti_{36}Hf_{15}$ alloy increases to maximum 550 MPa upon aging at 973 K for 20 hours and then decreases on account of coarsening of the $(Ti,Hf)_2Ni$ precipitates [215]. Aging, however, has deleterious effect on shape recovery ratio in the $Ni_{49}Ti_{36}Hf_{15}$ alloy, with recovery ratio lower than annealed counterpart [214].

Ni-rich NiTiHf Alloys

Above discussion indicates that although Ti-rich NiTiHf alloys exhibit high transformation temperatures, methods such as aging, thermo-mechanical process such as severe plastic deformation, etc. are not quite effective in sufficiently raising the alloy strength and hence improve their shape memory properties. Meng *et al.* [217] demonstrated that aging the Ni-rich $Ni_{50.6}Ti_{29.4}Hf_{20}$ alloy at 823 K up to 30 hours noticeably increase the

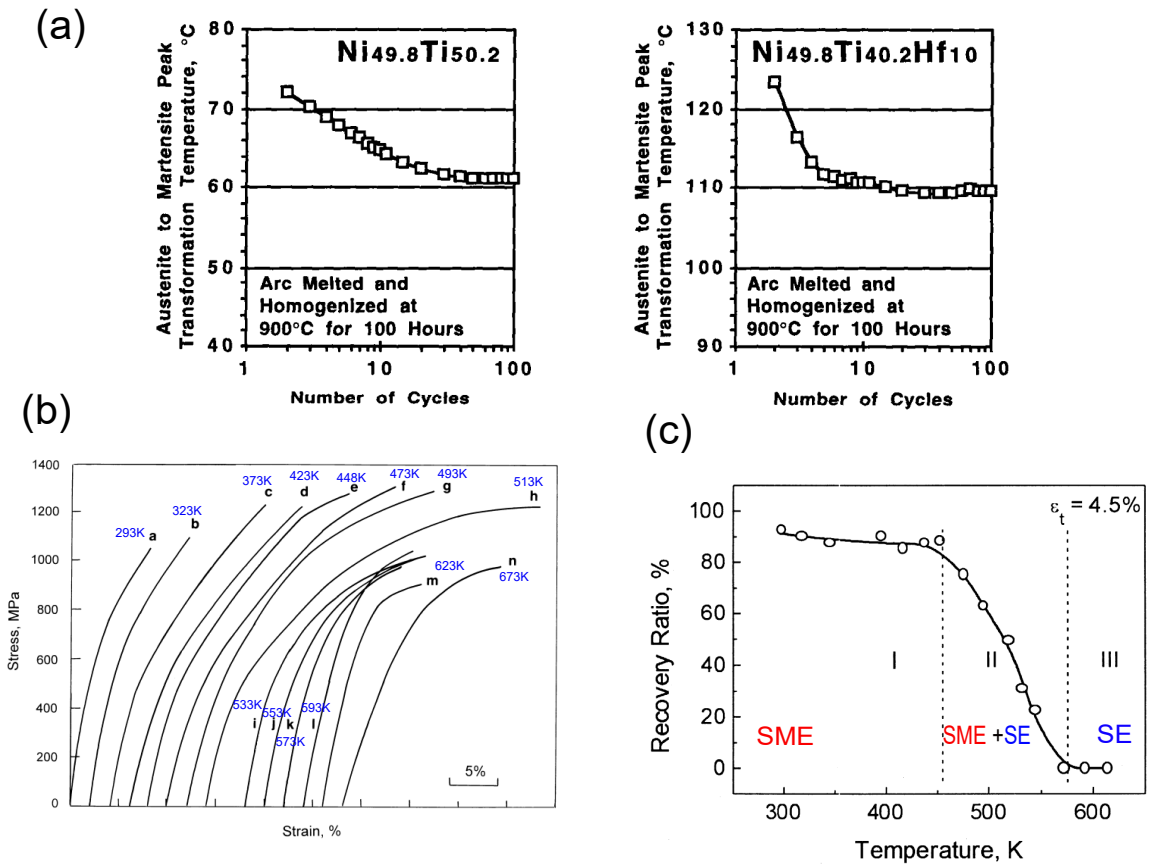

Figure 2.15: (a) Comparison between thermal cyclic stability of $Ni_{49.8}Ti_{50.2}$ and $Ni_{49.8}Ti_{40.2}Hf_{10}$ alloy. **Figure source:** [209], (b) Stress-strain curves for $Ni_{49}Ti_{36}Hf_{15}$ alloy at different temperatures (M_s = 452 K, M_f = 421 K , A_s = 489 K, A_f = 504 K). **Figure source:** [212], (c) Effect of deformation temperature on shape recovery ratio in the $Ni_{49}Ti_{36}Hf_{15}$ alloy. **Figure source:** [211].

phase transformation temperatures and increased the alloy strength, which significantly enhanced the thermal cyclic stability of the alloy, as shown in Figure 2.16 (a) and (b). They accounted the improved properties to the precipitation of lenticular $(Ni+Ti)_4Ti_3$ type precipitates [217], however, a detailed study on the shape memory properties and precipitate structure was not carried out.

Benafan *et al.* [218] have shown that increase of Ni-concentration by 0.7 at.% in as-solutionized $Ni_{50+x}Ti_{30-x}Hf_{20}$ (x = 0 - 1 at.%) lowers the phase transformation temperatures by almost 280°C, at a rate much higher that binary NiTi alloys. Aging these alloys at temperatures 550°C & 650°C has two fold effect: (i) lowering the rate of drop in transformation temperatures, and (ii) raising the transformation temperatures as compared to equivalent as-solutionized compositions. In terms of thermal hysteresis (A_f - M_s), compositions with 50.0 at.% < Ni-concentration < 50.5 at.% exhibit average values

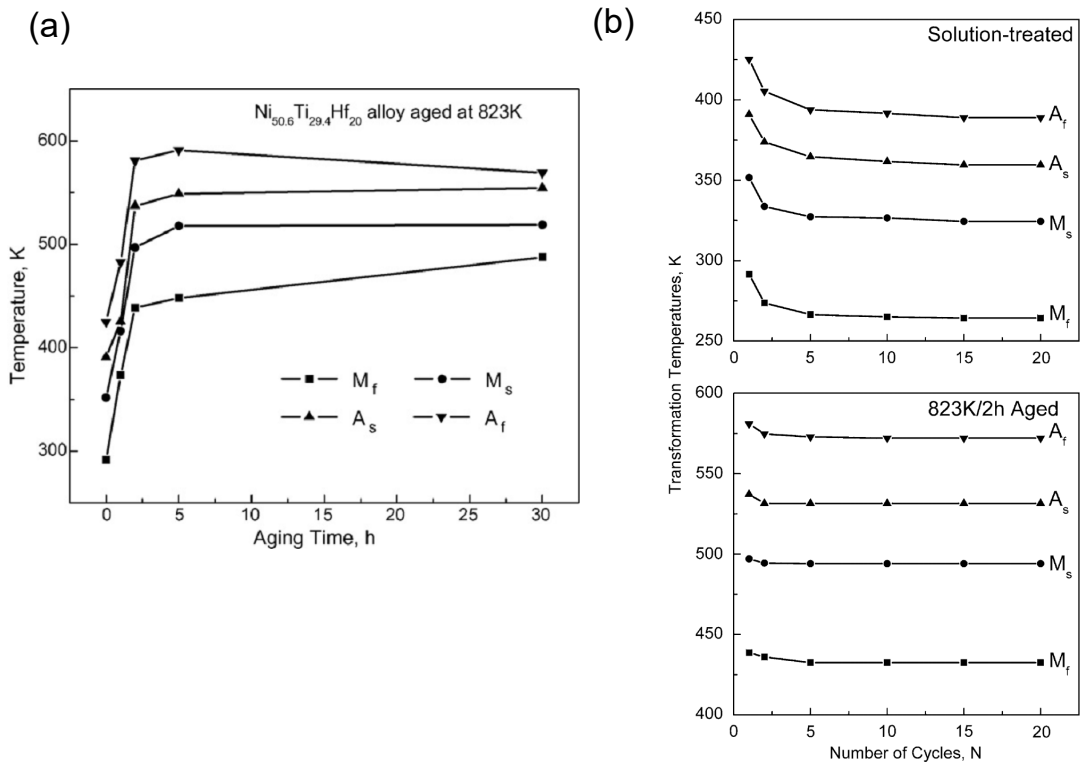

Figure 2.16: (a) Phase transformation temperatures upon aging at 823 K for various durations. **Figure source:** [216], (b) Comparison of thermal cyclic stability in solution-treated and aged condition in the $Ni_{50.6}Ti_{29.4}Hf_{20}$ alloy. **Figure source:** [217]

of nearly 35°C. For higher concentrations, the value rises linearly upto ∼ 70°C for 51 at.% Ni. The hardness of as-solutionized as well the alloy aged at 400°C remains insensitive to Ni-concentration while hardness of the alloys aged at 550°C and 650°C increase for all the compositions in a linear fashion.

2.4.3. Nano-precipitation in Ni-rich NiTiHf Alloys

Aging the Ni-rich $Ni_{50.3}Ti_{29.7}Hf_{20}$ hot-extruded alloy at 550°C for 3 hours leads to precipitation of fine Ni-rich particles and exhibit near perfect tensile super-elasticity in the alloy, as shown in Figure 2.17 (a). The as-solutionized alloy exhibits transformation temperatures M_s = 87°C, M_f = 71°C, A_s = 109°C, A_f = 123°C, which upon aging rise to M_s = 137°C, M_f = 128°C, A_s = 155°C, A_f = 166°C. Further, these alloys exhibit thermal hysteresis of 36°C, much lower than the Ti-rich NiTiHf alloys. The values further decrease with aging to almost 29°C. Coughlin *et al.* [47] revealed that aging of $Ni_{50.3}Ti_{29.7}Hf_{20}$ alloy, prepared by hot-extrusion, significantly raised the alloy critical strength against slip and improved super-elastic response of the material, as shown in Figure 2.17 (b). The alloy exhibits highest yield strength of 1278 MPa, when aged at 550°C for 3 hours. The

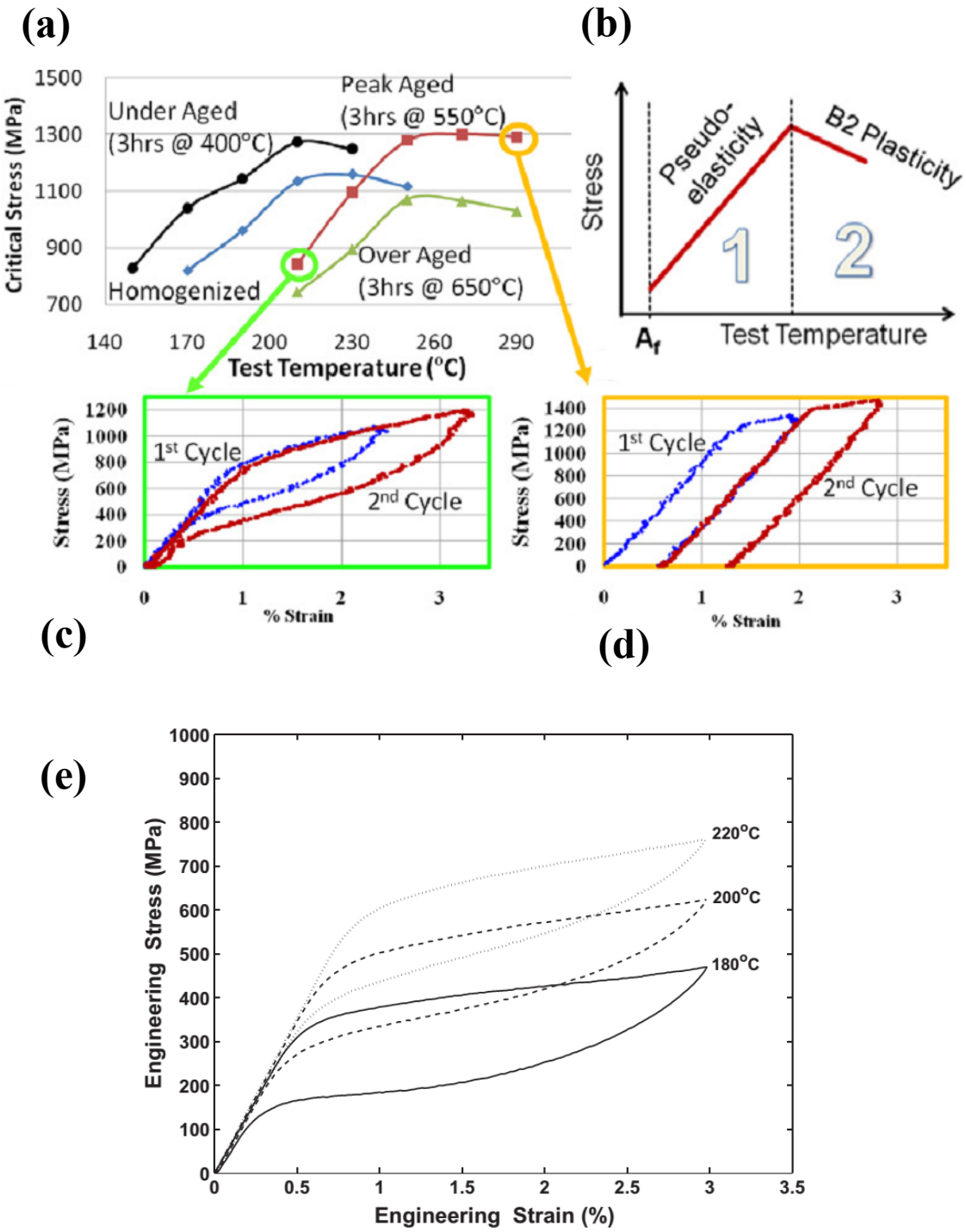

Figure 2.17: (a) Critical stress for slip as a function of temperature in the $Ni_{50.3}Ti_{29.7}Hf_{20}$ alloy aged at three different temperatures under compression mode, (b) Stress-temperature phase space divided into two zones: (i) Super-elastic and (ii) Plastic deformation of B2. For test temperature range within zone-1, alloy aged at 550°C for 3 hours exhibits: (c) Near-perfect SE upto 3%, (d) Absence of stress-plateau and loss of SE for test temperatures lying in zone-2, (e) Near-perfect SE in the $Ni_{50.3}Ti_{29.7}Hf_{20}$ alloy at temperatures A_f + 14°C, A_f + 34°C, A_f + 54°C upto 3% tensile strain. **Figure source:** [47] for (a)-(d) and [46] for (e).

rise in phase transformation temperatures as well as alloy strength has been attributed to strengthening by these precipitates which significantly increase the alloy hardness, phase

transformation temperatures, improved thermal cyclic stability and lower values of thermal hysteresis upon aging at temperature from 400°C to 700°C [219]. On account of aging-induced precipitation strengthening several other Ni-rich NiTiHf HTSMAs demonstrate high strength, superior SE and shape memory response [220–222] in comparison to Ti-rich NiTiHf HTSMAs.

The earliest reference to the precipitation of a new precipitate phase in the Ni-lean $Ni_{48.6}Ti_{36.5}Hf_{15}$ alloy is by Han *et al.* [48], who identified ellipsoidal orthorhombic precipitates with the space group and lattice parameters as a = 12.87 Å , b = 8.74 Å , c = 26.22 Å . Yang *et al.* [223] and Santamarta *et al.* [199] carried out a detailed structural investigations employing electron microscopy and DFT calculations on this precipitate phase, which they labelled as "H-Phase".

It has been found the H-phase precipitates possess an ellipsoidal morphology (as shown in Figure 2.18 (a)) and orthorhombic crystal structure (space group: F d/2 d/2 d/2) and lattice parameters a = 12.64 Å , b = 8.82 Å and c = 26.08 Å . The APT (Atom Probe Tomography) experiments [223–225] reveal that the precipitate phase is lean in Ti and rich in Ni and Hf atomic fractions. The typical composition of precipitate is estimated as: 53.62 ± 0.050 at.% Ni, 20.03 ± 0.027 at.% Ti, and 26.35 ± 0.032 at.% Hf (Morphology of precipitates reconstructed using APT analysis and the precipitate composition profile from APT analysis shown in Figure 2.19 (a) and (b)). The orientation relationship between B2 unit cell and Orthorhombic unit cell of H-phase is [223]:

$$\begin{aligned} [100]_H &\rightarrow [001]_{B2} \\ [010]_H &\rightarrow [110]_{B2} \\ [001]_H &\rightarrow [\bar{1}10]_{B2} \end{aligned} \tag{2.8}$$

Santamarta *et al.* [199] obtained diffraction patterns from H-phase precipitate (length ∼ 200 - 750 nm and width ∼ 50 - 175 nm) in the furnace-cooled $Ni_{52}Ti_{28}Hf_{20}$ alloy along different zone axes as shown in Figure 2.18 (b). Additional spots appearing at $\frac{1}{3} < 110 >^*$ fundamental reflections from B2 phase, indicated as arrows and circles suggest reflections from the H-phase precipitates (refer Figure 2.18 (b)((i)-(iv))). Their study further emphasized on the role of Ni- and Hf-concentrations on the H-phase growth kinetics. It was found that higher the Ni-content of the alloy, faster the growth of the precipitates. Further, the H-phase precipitates coarsen more rapidly in alloys with higher Hf content

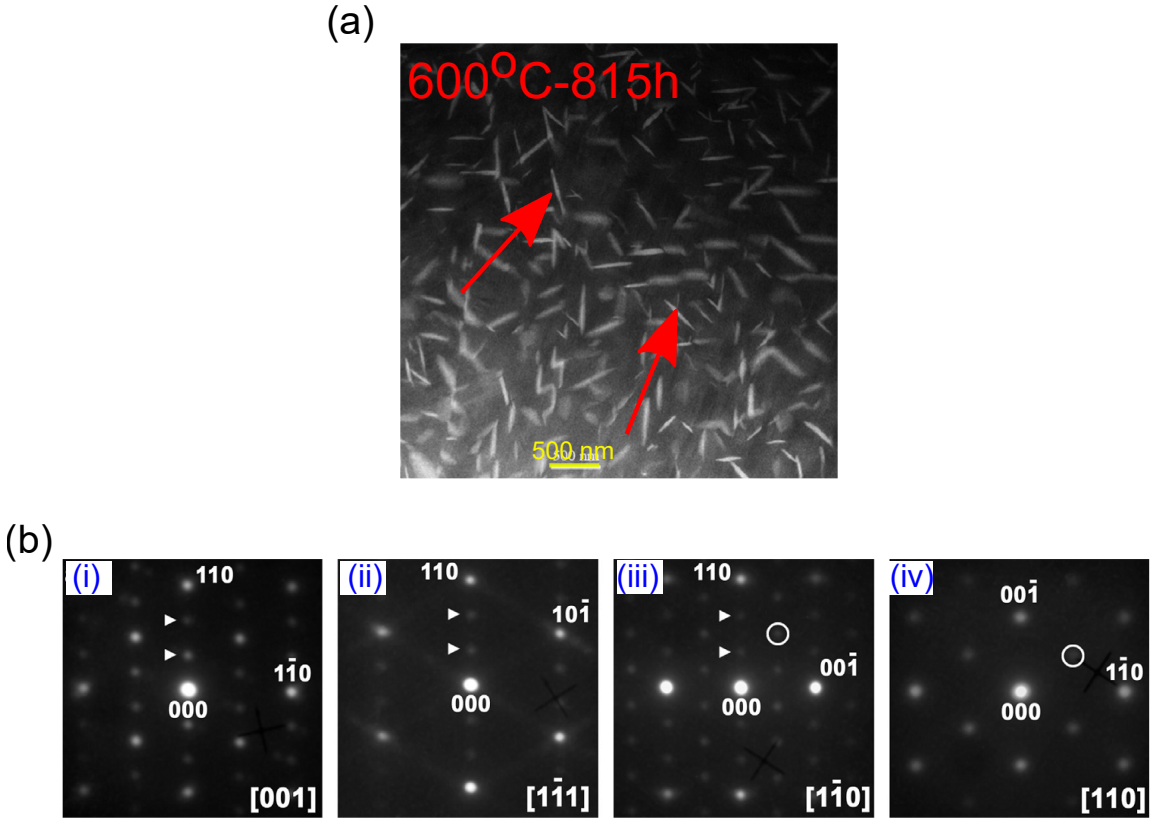

Figure 2.18: (a) Morphology of H-phase precipitates in $Ni_{50.3}Ti_{29.7}Hf_{20}$ alloy as seen in TEM, (b) Diffraction patterns obtained from a H-phase precipitate in the furnace-cooled $Ni_{52}Ti_{28}Hf_{20}$ alloy along (i) $[001]_{B2}$, (ii) $[1\bar{1}11]_{B2}$, (iii) $[1\bar{1}0]_{B2}$ and (iv)$[110]_{B2}$ zone axes. **Figure source:** (a) [223], (b) [199].

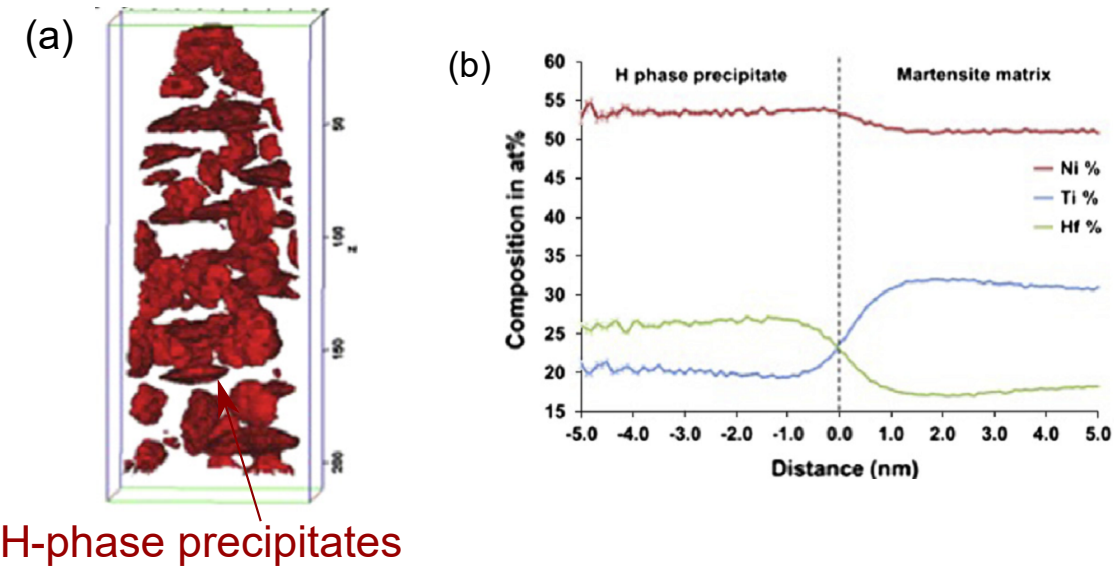

Figure 2.19: (a) Morphology and precipitate distribution of H-phase in the $Ni_{50.3}Ti_{29.7}Hf_{20}$ alloy from the reconstructed volume obtained by APT analysis, (b) Composition profile of matrix and H-phase precipitates from APT analysis. **Figure source:** [223].

for identical Ni-concentrations.

Aging the $Ni_{50.3}Ti_{34.7}Hf_{15}$ alloy at different temperatures over wide range of duration, Evirgen *et al.* [226] demonstrated that the aging induced H-phase dimensions as well as inter-particle spacings play a governing role in deciding the transformation temperatures, thermal hysteresis and shape memory properties. Typically, aging at low temperatures $\leq 550°C$ lead to dense population of fine precipitates $<\sim 20$ nm with small inter-particle spacing, which suppress the transformation temperatures. However, shorter aging duration at relatively higher temperatures coarsen the precipitates, depletes Ni-concentration in the matrix and leads to increase in the martensitic transformation temperatures.
The Table 2.4 summarizes the properties of NiTiHf HTSMAs.

Table 2.4: Comparison between the properties of Ti-rich and Ni-rich NiTiHf HTSMAs.

Properties	Comments	
	Ti-rich NiTiHf alloys	**Ni-rich NiTiHf alloys**
Phase transformation pathway	B2 (Ordered BCC) $\rightleftharpoons$ B19$^{/}$ (Monoclinic)	
Ductility & Workability	Poor [213, 227]	
Phase transformation temperatures	Parabolic increase with Hf concentration $\sim$ 20°C/at.% Hf [28]	
Thermal hysteresis	102°C ($Ni_{49.8}Ti_{30.2}Hf_{20}$ [204])	30°C ($Ni_{50.3}Ti_{29.7}Hf_{20}$ [228])
Precipitation strengthening phase	Ti-rich $(Ti,Hf)_2Ni$ phase [215]	Ni-rich H-Phase [223]
Yield strength	550 MPa; $Ni_{49}Ti_{36}Hf_{15}$ alloy aged at 973K for 20h [215]	1278 MPa; $Ni_{50.3}Ti_{29.7}Hf_{20}$ alloy aged at 823 K for 3h [47]
Shape recovery ratio	Aging treatments deteriorate SME by reducing shape recovery ratio [215]	Aging treatments improve shape memory properties [45]
Superelasticity	Lack of stress plateau and complete lack of SE; $Ti_{36}Ni_{49}Hf_{15}$ alloy [37]	Complete recovery of superelastic strains up to 3%; $Ni_{50.3}Ti_{29.7}Hf_{20}$ [46]

CHAPTER 3

Experimental Methods

A number of experimental techniques have been utilized during course of the current investigations. This chapter describes the methodology followed to prepare and process the NiTiHf alloys studied during thesis work along with general principle behind techniques utilized to characterize them. The crystal structures of the alloy phases were determined by X-ray Diffraction (XRD) and Neutron Diffraction (ND). Phase transformation behaviour was studied by Differential Scanning Calorimetry (DSC) tests. The role of solute addition as well as aging treatments on NiTiHf alloys on the alloy strength has been determined using room temperature Vickers Micro-hardness tests. Correlative Transmission Electron Microscope (TEM) and Small-Angle X-ray Scattering (SAXS)/Small-Angle Neutron Scattering (SANS) analysis was carried out to understand the bulk scale quantitative evolution of the aging-induced precipitates in terms of their morphology, size, inter-precipitate spacings *etc.*

3.1. Materials

In this thesis, several Ni-rich NiTiHf alloys with compositions $Ni_{50.3}Ti_{49.7-x}Hf_x$ (x = 0 - 25 at.%) have been investigated. The chemical compositions and the aging treatments carried out on the alloy samples are described in detail at appropriate sections in the thesis. The alloys were prepared with Nickel, Titanium and Hafnium as starting elements with 99.9% purity. For the alloy preparation, elemental charge was weighed on a weighing balance (accurate upto 0.01 mg) in the respective atomic percentage ratios in an arc-melting furnace, described in the next section.

3.2. Fabrication and Processing of the Alloys

The above mentioned alloy compositions were prepared by arc-melting in an arc-melting furnace using non-consumable tungsten electrode on a water-cooled Copper hearth, under high purity Argon atmosphere maintained at level of $\sim 10^{-3}$ mbar. The alloy ingots were re-melted 7-8 times in order to ensure the chemical homogeneity of the alloy. The solidified ingots were homogenized at 1050°C for 72 hours and water quenched. Meng *et al.* [229] showed that the addition of Hf in range of 5 - 30 at.% to the NiTi alloys leads to unavoidable formation of $Ni(Ti,Hf)_2$ phase. Javadi *et al.* [213] demonstrated that hot-rolling the NiTiHf alloys leads to uniform re-distribution of the $Ni(Ti,Hf)_2$ and improved shape memory properties.

In present work, hot-rolling of the $Ni_{50.3}Ti_{29.7}Hf_{20}$ alloy samples were carried out as follows: the alloy ingot was wrapped in a Tantalum foil and jacketed in a mild steel can under vacuum of 10^{-3} mbar to prevent oxidation while rolling. Typical photograph of the jacketed ingot is shown in figure 3.1. The jacketed ingot was then soaked at 900°C for 30 minutes prior to hot-rolling. Subsequently, it was hot-rolled at 900°C to a sheet $\sim$ 2 mm

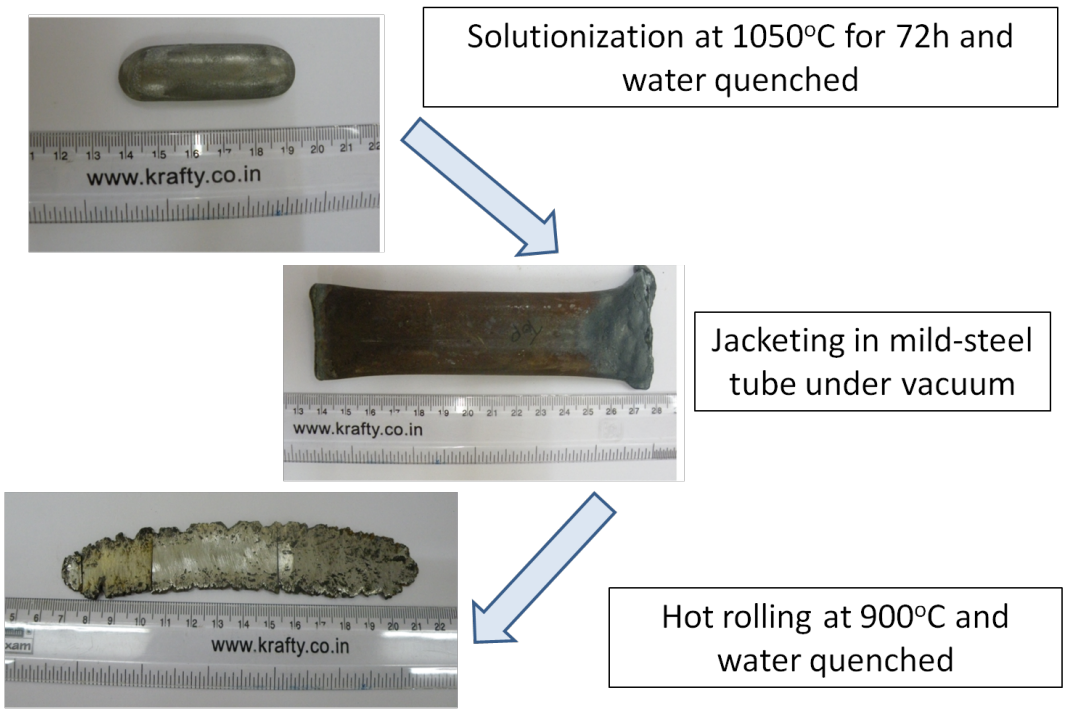

Figure 3.1: Photograph showing processing of the alloy ingot to a hot-rolled sheet.

thick in multiple passes. This sheet was then solutionized at 900°C before quenching in water, resulting in re-crystallized micro-structure with grain size $\sim$ 25 μm.

3.3. Micro-structural Characterization

3.3.1. Optical Microscopy

Optical microscopy was carried out to determine surface morphology of the as-solutionized as well as aged alloy samples. The samples for optical microscopy were mechanically ground on SiC papers of several grades, polished up to 1 μm finish and finally etched using H_2O+HNO_3+HF (5:4:1 vol.%) as an etchant [230]. Optical microscopy was carried out with *Zeiss Axiovert* microscope, using an interference filter with polarized light to enhance the contrast.

3.3.2. Electron Microscopy

Compositional analysis: The chemical composition of all the $Ni_{50.3}Ti_{49.7-x}Hf_x$ (x = 0, 5, 10, 15, 18, 20, 25 at.%) alloys in the as-solutionized alloys was verified using *OXFORD* make Energy Dispersive Spectrometer (EDS) detector attached with the *Ziess* Scanning Electron Microscope (SEM). The composition of the as-solutionized have been determined by SEM-EDS analysis and have been listed in Table 3.1.

Composition	Ni (at.%)	Ti (at.%)	Hf (at.%)
$Ni_{50.3}Ti_{49.7}$	50.4 ± 0.3	49.6 ± 0.2	-
$Ni_{50.3}Ti_{44.7}Hf_{5.0}$	50.0 ± 0.3	45.1 ± 0.3	4.9 ± 0.4
$Ni_{50.3}Ti_{39.7}Hf_{10.0}$	50.2 ± 0.3	39.8 ± 0.3	10.1 ± 0.5
$Ni_{50.3}Ti_{34.7}Hf_{15.0}$	50.5 ± 0.3	34.4 ± 0.4	15.2 ± 0.2
$Ni_{50.3}Ti_{31.7}Hf_{18.0}$	50.5 ± 0.4	31.1 ± 0.3	18.5 ± 0.2
$Ni_{50.3}Ti_{29.7}Hf_{20.0}$	50.3 ± 0.4	29.5 ± 0.3	20.3 ± 0.2
$Ni_{50.3}Ti_{24.7}Hf_{25.0}$	50.6 ± 0.4	25.2 ± 0.3	24.2 ± 0.2

Table 3.1: Compositions of Ni-Ti-Hf alloys selected for the present study.

Transmission Electron Microscopy (TEM): In the current work, Transmission Electron Microscopy was utilized to investigate micro-structural features like precipitates. the TEM samples were prepared by thinning down the bulk samples to 100 μm thick sheets and punching out 3 mm diameter circular discs out of them. The discs were jet-polished

by an electrolyte containing 90% methanol and 10% perchloric acid. During jet polishing, voltage of 20 V and electrolyte temperature of -45°C was maintained. In order to characterize the matrix as well as the precipitate phase, different electron microscopes FEI-TITAN, FEI Technai T20 were utilized. The Selected Area electron Diffraction Patterns (SADP) were obtained for phase identification. The High Angle Annular Dark Field (HAADF) and Bright Field (BF) images were obtained to examine the morphology of the precipitate phase. The EDS detector in the Scanning Transmission Electron Microscope (STEM) mode was employed for the determination of precipitate composition. Precipitate dimensions were estimated by Image analysis using *ImageJ* [231] software.

3.4. Differential Scanning Calorimetery (DSC)

The phase transformation behaviour of the $Ni_{50.3}Ti_{49.7-x}Hf_x$ alloys as a function of alloying addition as well as aging treatments was investigated using DSC.

For any thermodynamic system (mass, m) with specific heat capacity (at constant pressure) C_p, the amount of heat (ΔQ) required to raise its temperature by an amount ΔT is given as:

$$\Delta Q = mC_p\Delta T \tag{3.1}$$

In any DSC, the temperature increase or decrease is scanned over time Δt at a fixed rate $\frac{\Delta T}{\Delta t}$. The heat flow between the sample and reference pan during a first-order phase transformation results in a typical DSC plot as shown in Figure 3.2:

$$\frac{\Delta Q}{\Delta t} = mC_p\frac{\Delta T}{\Delta t} \tag{3.2}$$

The endothermic peak corresponds to heating cycle while an exothermic peak corresponds to cooling cycle. In case of martensitic transformation in current study, the temperatures M_s and M_f are the onset and endset of the forward phase transformation occurring during cooling, with M_p as peak martensite transformation temperature, while A_s and A_f are the onset and endset of the reverse phase transformation occurring during heatng, with A_p as peak austenite transformation temperature. All the four temperatures: M_s, M_f, A_s and A_f were estimated by drawing tangents parallel to the baseline, as per ASTM standards [232]. Further, the area under each peak corresponds to the latent heat associated with the phase transformation, measured in the units of Jg^{-1}.

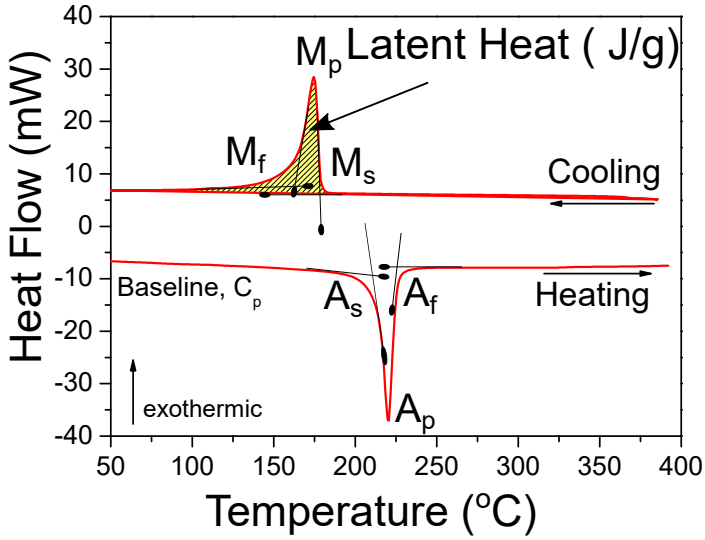

Figure 3.2: Schematic diagram of typical DSC curve for a first-order reversible phase transformation.

The phase-transformation studies in NiTiHf alloys in current work were conducted using the *Mettler-Toledo DSC1* heat-flux DSC equipment. For the DSC tests, specimens of dimensions $\sim$ 2 mm $\times$ 2 mm were cut out of the as-solutionized as well as heat-treated alloy sample, polished on emery paper to ensure flat surfaces and were placed in Aluminium crucibles (40 μl). Both the sample and reference pans, enclosed in a 400 W furnace, were placed on a conducting ceramic HSS7 ceramic sensor plate with thermopile of 120 Gold-Gold/Palladium thermocouples connected in series, sensing both sample (T_S) and reference (T_R) temperatures. This thermopile assembly enabled measuring the heat flow signal with resolution less than 0.04 μW and temperature sensitivity of 11.9°C at 135°C. Since, both the pans are not in direct contact with the sensor, thermal lag ($\Delta T = \Delta T_S - \Delta T_R$) appears, which was corrected by calibrating the measured temperatures to the melting point of In (156.6°C) and Zn (419.6°C) [233, 234], which cover the desired temperature range in the studies. The heat-flow calibration was carried out by comparing the measured enthalpy of fusion with the latent heats of melting of In and Zn standards [235]. DSC measurements were carried out by isochronally heating the samples at heating and cooling rates ranging from 20°C/min to 5°C/min in the temperature range from 25°C to 400°C. The onset and the end temperatures associated with the endothermic and exothermic peaks associated with phase-transformation during heating and cooling of the specimens were determined by drawing tangents parallel to the baselines (refer Figure 3.2). For each DSC experiment, minimum of two heating and cooling cycles were

recorded to ensure the repeatability of the results.

3.5. X-ray Diffraction (XRD)

The XRD patterns were collected and analysed to identify crystal structure of the phases present in the as-solutionzed as well as aged alloys and to estimate their lattice parameters. The samples surface was ensured to be flat by polishing the surface to 1 μm finish. These studies were carried out on a Bruker make D8 Discover power diffractometer in Bragg-Brentano geometry using Cu-K$_\alpha$ wavelength, generated by Cu-target X-ray tube operated at 40 kV and 40 mA. The room-temperature diffraction data was collected on LynxEye position sensitive data offering high count rates over lower data acquisition periods. The high-temperature XRD patterns for the alloys were collected at temperatures at 350°C (ensuring austenite phase) by housing the samples inside a graphite dome under vacuum to avoid high temperature oxidation. The collected XRD data sets were used to determine the lattice parameters of the present phases by *Le Bail* method [236] using *FullProf* [237] software. The optics of the X-ray powder diffractometer employed are tabulated in Table 3.2.

Table 3.2: X-ray optics of the Bruker D8 Discover powder diffractometer.

Description	**Details**
Radiation	Cu-K$_\alpha$
Goniometer Radius	430 mm
Detector Slit	8 mm
Soller Slit	2.5° axial divergence
Filter	Ni (0.012 mm)
2θ range	20° to 100°
Step size	0.02°
Scan rate	1 sec/step

3.6. Neutron Diffraction

In current work Neutron Diffraction (ND) measurements were carried to investigate the role of Hf addition in $Ni_{50.3}Ti_{49.7-x}Hf_x$ (x = 0 - 25 at.%) on the lattice parameters of the crystal structure of as-solutionized alloys in the austenitic state. For the alloys compositions, x = 5 and 10, room temperature ND patterns were collected at the Powder Diffractometer-3 (PD-3) located at the Dhruva Reactor, Bhabha Atomic Research Centre

[238] at wavelength of 1.48 Å. High temperature ND diffraction patterns were collected at temperatures > A_f for the samples x = 0, 15, 18, 20 and 25 at the Powder Diffractometer-2 (PD-2) located at the Dhruva Reactor, Bhabha Atomic Research Centre [239] using neutrons of wavelength 1.244 Å. The optics of the Neutron diffractometers employed in the current studies are tabulated in Table 3.3.

Table 3.3: X-ray optics of the PD-2 and PD-3 Neutron Diffractometers at Dhruva.

Description	**PD-2 diffractometer**	**PD-3 diffractometer**
Wavelength	1.244 Å	1.48 Å
Mono-chromator	Ge (331) crystal	doubly bent Si(511) crystal
Resolution ($\frac{\Delta d}{d}$)	0.8 %	0.3%
Angular range (2θ)	4° - 140°	10° - 123°
Detectors	^3He position sensitive detectors (5 nos.)	^3He position sensitive detectors (3 nos.)
Sample environment	5 K - 2000 K	1.5 K - room temperature

3.7. Small-Angle X-Ray Scattering (SAXS)

In the present study, SAXS experiments were carried out using a conventional laboratory based instrument using Cu-Kα as the incident X-ray radiation in transmission geometry. Scattering intensity was recorded as a function of scattering vector, Q, defined as $Q = \frac{4\pi \sin\theta}{\lambda}$, where 2θ is the scattering angle. In a transmission geometry SAXS instrument, most of the X-rays incident on the sample directly pass through the sample without interacting, with small fraction of the incident intensity elastically scattered over angles upto 2°, which contains structural information about the specimen. Laboratory SAXS instrument is an assembly of three parts: (i) X-ray source, (ii) Collimating optics, and (iii) Detector. In the present study, Cu-K_α radiation was utilized as probe, generated by an micro-focus X-ray tube operating at 1.5 kW. Micro-focus X-ray source geometry consisted of 3 pin-hole collimating system, collimating the monochromatic Cu-K_α X-rays parallel beam with 0.03° divergence. The parasitic scattering by a pin-hole called beam-defining slit is cut-off by another pinhole called anti-scatter slit. This parallel beam exits the X-ray tube through a circular aperture of 400 μm aperture and illuminates the sample. After interacting with the specimen, incident beam directly transmitted through the specimen is blocked by a beam stop (made of a Sb-Pb alloy), while the scattered intensity is collected by a position-sensitive 2D-detector. Schematic of a laboratory SAXS set-up is

displayed in Figure 3.3. Since X-rays interact with matter via electromagnetic interaction

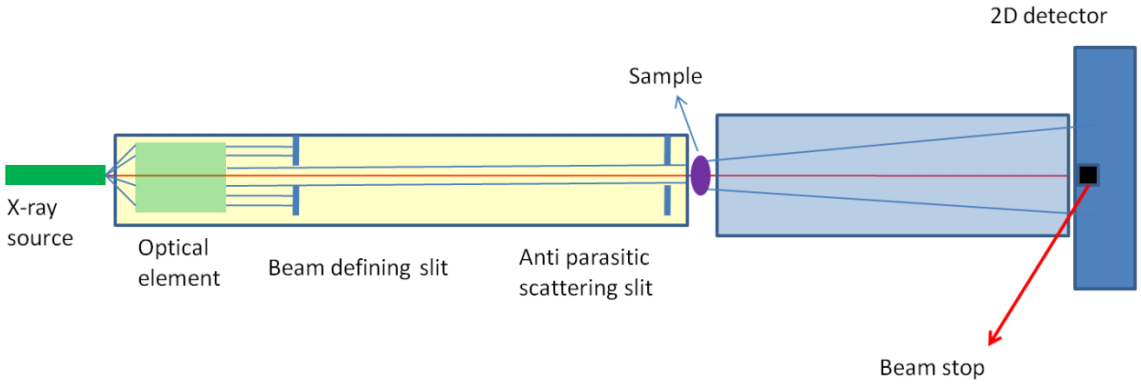

Figure 3.3: Schematic of a laboratory SAXS set-up.

with electrons, the modes of interaction are: (a) elastic scattering, which contributes to scattering intensity collected by the detector; (b) inelastic scattering, electrons weakly bounded to the atoms undergo Compton scattering and contribute to the background and (c) X-ray absorption. The X-ray absorption cross-section depends upon the mass-absorption coefficient of the material at a given wavelength. Typically, the fraction of the incident intensity (I_o) by the specimen varies with its linear mass-absorption coefficient $\frac{\mu}{\rho m}$ (ρ_m is the mass-density of the specimen of thickness x) as:

$$\frac{I_{absorbed}}{I_o} = exp\Big[-(\frac{\mu}{\rho_m})\rho_m x\Big] \tag{3.3}$$

For high quality SAXS data, the sample should have an optimum thickness, x_{opt}, which depends upon linear mass-absorption coefficient as: x_{opt} (cm^{-1})$\propto \frac{1}{(\frac{\mu}{\rho m})}$. Typically for the $Ni_{50.3}Ti_{29.7}Hf_{20}$ alloy, the linear mass-absorption coefficient for Cu-K$_\alpha$ (8 keV) is 125.21 cm^2/g, sets an upper limit on sample thickness $\sim$ 20-25 μm.

In present study, samples for SAXS measurement were prepared by jet-thinning 3 mm discs punched out of a 100 μm sheet, using procedure described in section 3.3.2. The SAXS data was collected over Q range of 0.01 nm^{-1} to 3 nm^{-1}. For X-rays scattered by electrons in an atom with atomic number Z, the scattering length is given as Zr_o; where $r_o = \frac{e^2}{m_e c^2}$, m_e being the mass of electron. The X-ray atomic-form factor (f) is a function of the scattering angle. But at small angles, it can be considered constant and can be taken as equal to the atomic number Z. The scattering length density of X-rays scattered by ensemble of 'n' atoms in phase 'm' (volume V_m) and phase 'p' (volume V_p) are given as

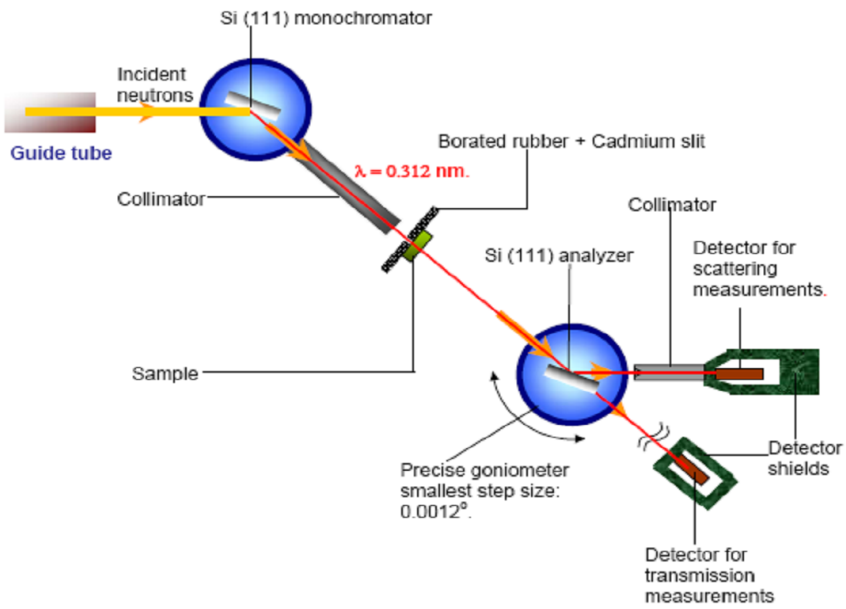

Figure 3.4: Schematic of double-crystal monochromator based MSANS instrument at Guide Tube Laboratory Dhruva reactor, India [242].

$\sum_{i=1}^{n} r_o \frac{f_i^m N_i}{V_m} = \frac{Z_m r_o}{V_m}$ and $\sum_{i=1}^{n} r_o \frac{f_i^p N_i}{V_p} = \frac{Z_p r_o}{V_p}$, where Z_m and Z_p are effective atomic numbers of the each phase and V_m, V_p are their respective average atomic volumes. Then the SAXS "contrast" term becomes:

$$\boxed{\left(\rho_m - \rho_p\right)^2_{SAXS} = r_o^2\left(\frac{Z_m}{V_m} - \frac{Z_p}{V_p}\right)^2} \tag{3.4}$$

The contrast thus increases linearly with Z^2. In present case, the SAXS contrast between $Ni_{50.3}Ti_{29.7}Hf_{20}$ matrix and aging induced precipitates is: 2.61×10^{22} cm^{-4}.

3.8. Small-Angle Neutron Scattering (SANS)

Medium-resolution Small-Angle Neutron Scattering (MSANS) measurements to probe larger length scales in the NiTiHf alloy were carried out using double-crystal monochromator based MSANS facility at the Guide Tube Laboratory of Dhruva reactor, India [240], [241]. The schematic of MSANS instrument at Dhruva is illustrated in Figure 3.4. Technical details of the MSANS instrument are given in Table 3.4.

Major advantage of SANS in case of alloys is realized during small aging times, when the compositional variations are not significant and the distinct signal from SANS provides sufficient intensity to clearly decipher the early stages of precipitation. Further,

Table 3.4: Technical details SANS experiments at the Dhruva MSANS instrument.

Description	Details
Monochromator crystal	Si (111)
Analyser crystal	Si (111)
Neutron Wavelength, λ	3.12 Å
Q-range utilized	0.03 nm^{-1} - 0.15 nm^{-1}
Specimen thickness	$\sim$ 1 mm
Distance between Mono-chromator and sample mount centre	128 cm
Distance between sample and Analyser crystal	100 cm
Distance between sample and detector	55 cm
Detector	BF_3

the possibility of conducting *in-situ* SANS experiments under different environments, to establish the precipitate growth kinetics, provides this technique an additional advantage.

To meet the objective of investigating growth and coarsening kinetics of precipitates in aged $Ni_{50.3}Ti_{29.7}Hf_{20}$ alloys, *in-situ* as well as ex-situ SANS measurements on the alloy samples were carried out at General Purpose-SANS (GP-SANS) instrument at High-Flux Isotope Reactor (HIFR) facility of the Oak Ridge National Laboratory (ORNL) [243]. The schematic of the GP-SANS instrument layout is shown in Figure 3.5.

The samples for *in-situ* as well as ex-situ SANS measurements at GP-SANS instru-

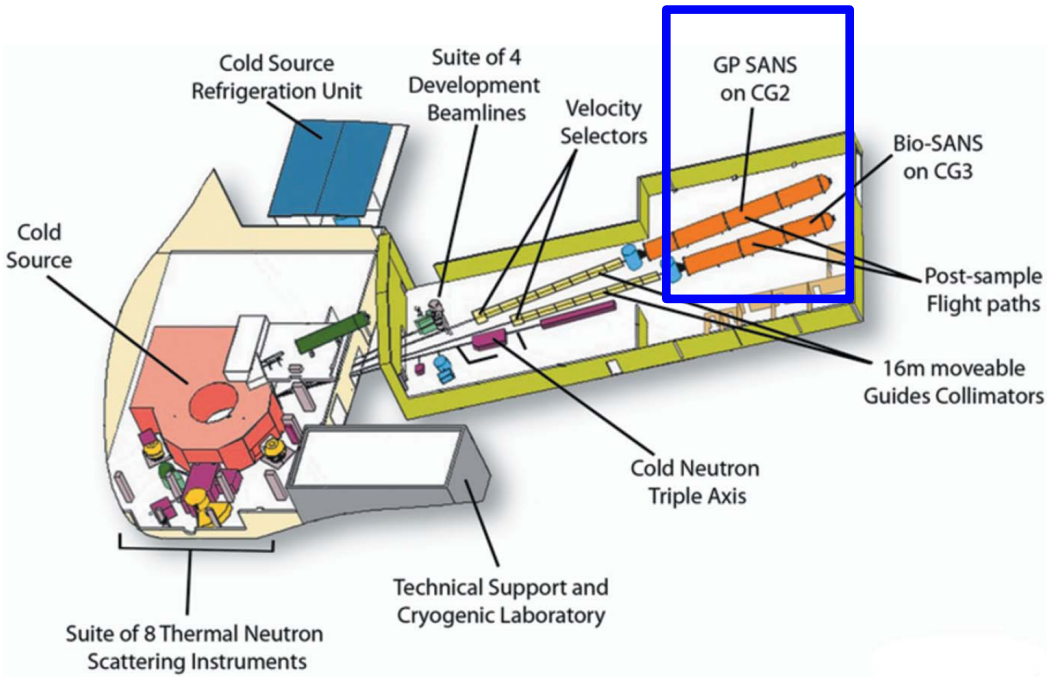

Figure 3.5: The guide-hall of the GP-SANS instrument layout at HFIR-ORNL. The beam-line CG2 utilized is marked in a blue box. **Figure source:** [243]

ment were ∼1 mm thick with cross-sectional area of ∼ 23 mm × 15 mm. The *in-situ* high temperature measurements on the samples at 550°C and 650°C for 800 minutes were carried out using an ILL niobium foil vacuum furnace. The as-solutionized sample was put in the furnace and the temperature was ramped to set temperature in 10 minutes. The sample to detector distance was chosen as ∼ 7 m for the *in-situ* measurements. The neutron wavelength was chosen as 4.75 Å . The accessible Q-range for the kinetics experiment was 0.08 - 1.4 nm^{-1}. The SANS measurements on pre-aged samples have been carried out using two sample detector distances; the accessible Q-range for the ex-situ measurements was ∼ 0.03 - 2.8 nm^{-1}. The specimens for SANS experiments were ground to ensure a flat surface and polished upto 1μm finish using diamond paste.

3.9. Mechanical property Characterization

3.9.1. Micro-hardness Test

The hardness of samples was determined by room-temperature Vickers Micro-hardness tests. During Vickers micro-hardness test, a sharp diamond pyramidal indenter, with angle of 136° between opposite faces is impinged on a sample surface (shown in Figure 3.6 (a)). The Vickers hardness is measured in the units of Vickers Hardness Number (VHN) which is determined by the ratio $\frac{F}{A}$, 'F' being the load applied (in units Nm^{-2}) and 'A' being the surface area of the indention mark (square for a pyramid indenter) l^2, in the units of mm^{-2}. For pyramidal indenter with angle 136°, hardness in units of VHN is:

$$\boxed{VHN = \frac{F}{\frac{l^2}{2\sin(136^\circ/2)}} \approx 0.1891\frac{F}{l^2}} \tag{3.5}$$

where $l = \frac{l_1+l_2}{2}$, l_1 and l_2 are the lengths of two diagonals of the square.

The surface of the sample was polished up to the finish of 1 μm, since surface roughness introduces error in the accurate depth measurement and negatively affects the repeatability of the tests. Samples of about 2 mm thickness polished up to 1 μm finish were used for micro-hardness investigations using pyramidal indenter on a Vickers micro-hardness tester. A constant load of 0.98 N with holding time of 20 seconds was used to measure micro-hardness at room temperature at 10-20 different locations. The standard deviation in the measured data set was calculated by measuring the deviations of the measured values from the average. If for a given specimen 'm' Vickers micro-

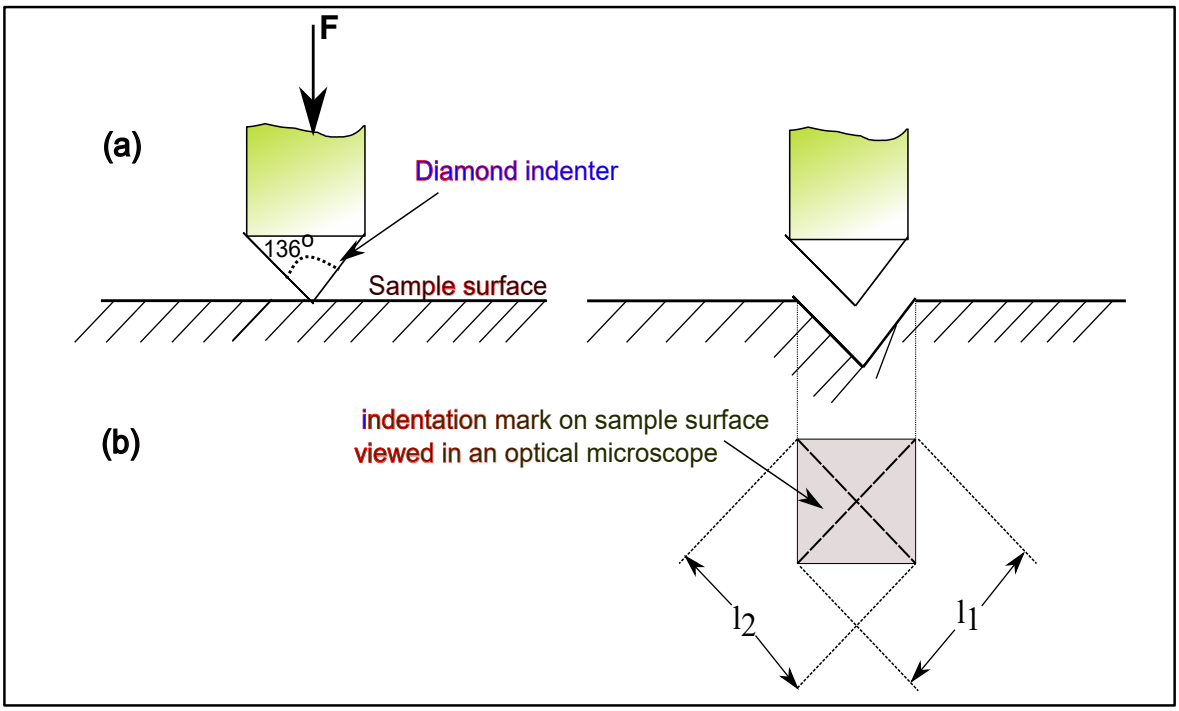

Figure 3.6: Schematic representation of Vickers hardness indentation test (a) load F creating indentation mark on sample surface, (b) cross-section view of the indentation mark

hardness measurements $x_1, x_2, x_3, ..., x_m$ were made, such that average VHN value is $\overline{x} = \frac{x_1+x_2+x_3+.....+x_m}{m}$, then uncertainty ($\Delta$x) in the micro-hardness value was calculated as:

$$\Delta x = \pm\sqrt{\frac{(x_1-\overline{x})^2+(x_1-\overline{x})^2+(x_1-\overline{x})^2+....+(x_m-\overline{x})^2}{m}} \tag{3.6}$$

CHAPTER 4

Effect of Hf Substitution on the Phase Transformation Behaviour, Crystal Structure and Hardness of the $Ni_{50.3}Ti_{49.7-x}Hf_x$ Alloys (x = 0 - 25 at.%)

This chapter presents studies on Ni-rich $Ni_{50.3}Ti_{49.7-x}Hf_x$ (x = 0 - 25 at.%) alloys with regard to their phase transformation characteristics, hardness and crystal structure. For high temperature applications, in addition to PTTs > 100°C, the HTSMAs should exhibit low thermal hysteresis as well as high strength. By keeping Ni-concentration fixed at 50.3 at.%, we optimize the Hf concentration for which the alloy specimen exhibits significantly high transformation temperatures, hardness and lowest thermal hysteresis.

4.1. Introduction

Maximization of the potential of NiTi SMAs over wide range of temperatures prompted the studies on high temperature shape memory alloys. In past, numerous studies have been attempted to tune the phase transformation characteristics of NiTi based HTSMAs with the two pronged aim of achieving:

- High transformation temperatures [28, 244] and,
- High strength [35, 43].

Phase transformation behaviour *viz.* transformation temperatures and thermal hysteresis of the NiTi SMAs can be tuned by either altering Ni/Ti ratio [66, 245] or by ternary additions at the expense of Ni or Ti in the alloys [246]. It is known that excess Ni in binary NiTi alloys lowers the phase transformation temperatures, while the transformation temperatures in alloys with Ti excess are nearly insensitive to the alloy composition [247]. In case of the NiTiHf HTSMAs, several efforts have been made in the past to elevate

the phase transformation temperatures in NiTiHf alloys by substituting Hf against Ti or Ni in the binary NiTi alloys [34, 202, 248]. In both the cases, although the transformation temperature markedly increased with the substitution, alloy ductility and strength reduced dramatically [213, 227].

For instance, Angst *et al.* [31] studied the role of Hf concentration in Ti-rich $Ni_{49}Ti_{51-x}Hf_x$ alloys up to Hf concentration, x = 30 at.%. They found that $Ni_{49}Ti_{21}Hf_{30}$ alloy exhibits the martensite peak temperature, M_p equal to 300°C. Meng *et al.* [35] and Wang *et al.* [212] reported that these alloys however, demonstrate poor ductility and shape memory response due to low values of yield strength. Severe plastic deformation of a Ti-rich composition $Ni_{49.8}Ti_{42.2}Hf_8$ (at.%) on the one hand enhanced the critical resolved shear stress (CRSS) of the alloy on account of increase in the dislocation density, it negatively impacted their phase transformation temperatures and thermal hysteresis.

Tong *et al.* [202] investigated the effect of Hf addition to Ni-rich $Ni_{51-x}Ti_{49}Hf_x$ alloys for x = 3, 5, 7,10 and 15 at.% and found that transformation temperatures linearly increase with Hf concentration, with x = 15 at.% alloy exhibiting M_s = 250°C. The Ni-rich NiTiHf alloys with Hf concentration 15-20 at.% exhibit considerably improved strength as well as phase transformation temperatures [47, 49, 220, 249]. However, limited studies are available on elucidating the role of broad range of Hf concentrations in Ni-rich NiTiHf alloys on their phase transformation temperatures, thermal hysteresis and strength [250, 251].

Here, $Ni_{50.3}Ti_{49.7-x}Hf_x$ (for x = 0, 5, 10, 15, 18, 20 and 25 at.%) alloys are investigated and correlation between the Hf concentration and the phase transformation characteristics *viz.* martensite transformation temperatures, thermal hysteresis and the hardness of the as-solutionized alloys is established.

4.2. Experiments

Total seven alloys with composition $Ni_{50.3}Ti_{49.7-x}Hf_x$ (x = 0, 5, 10, 15, 18, 20 and 25 at.%) were prepared by arc-melting as described in section 3.2. Figure 4.1 shows the alloy compositions (marked black circles) selected for the present study marked on the NiTiHf phase diagram [252]. All the as-melted alloy ingots were sealed in quartz ampoules, back-filled with Argon gas to avoid high temperature oxidation during solutionizing treatment. The alloy with composition corresponding to x = 0 was solutionized at 900°C for 1 hour

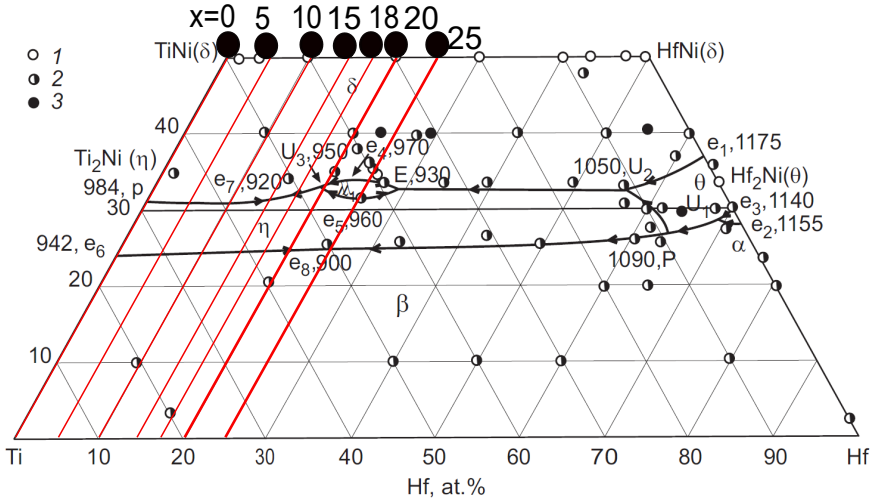

Figure 4.1: (a) The $Ni_{50.3}Ti_{49.7-x}Hf_x$ alloys for x = 0, 5, 10, 15, 18, 20 and 25 at.%. alloy compositions marked on NiTiHf phase digram adapted from [252].

and water quenched. Rest of the compositions with x = 5 - 25 at.% were solutionized at 1050°C for 72 hours and water quenched.

The samples from the as-solutionzed samples were cut in the form of thin slices for DSC experiments in order to determine the phase transformation temperatures. Further, to elucidate the effect of aging temperature on phase transformation characteristics, samples were aged at 500°C, 550°C, 600°C and 650°C for 3 hours each and their phase transformation temperatures were determined using DSC tests. All the DSC test were performed at the heating and cooling rates of 10°C/min on the Mettler Toledo DSC instrument described in section 3.4. High temperature neutron diffraction experiments at temperatures > A_f for each alloy composition were conducted to determine the lattice parameters of the austenite phase in the alloys. The neutron diffraction measurements were conducted on the neutron diffractometer at the DHRUVA facility as described in the subsection 3.6. Room temperature Vickers micro-hardness measurements were conducted to determine the hardness of the alloys using method described in the section 3.9.1.

4.3. Results and Discussion

4.3.1. Phase Transformation Behaviour

In as-solutionized condition

Figure 4.2 (a) shows the DSC plots corresponding to martensitic phase transformations in $Ni_{50.3}Ti_{49.7-x}Hf_x$ alloys for x = 0, 5, 10, 15, 18, 20 and 25 at.%. The forward martensitic

transformation occurring from the austenite phase to the martensite phase during cooling generates an exothermic peak as the temperature is lowered and an endothermic peak vice versa. It can be noticed from the figure that for low Hf-concentration (x = 5 and 10), the DSC plots shift to the left side of DSC curves corresponding to x = 0, indicating decrease in the transformation temperatures. For x > 15 at.%, the DSC plots shift towards right side, implying higher phase transformation temperatures. For x = 0 alloy *i.e.* binary $Ni_{50.3}Ti_{49.7}$ alloys, the forward martensitic transformation from the austenite

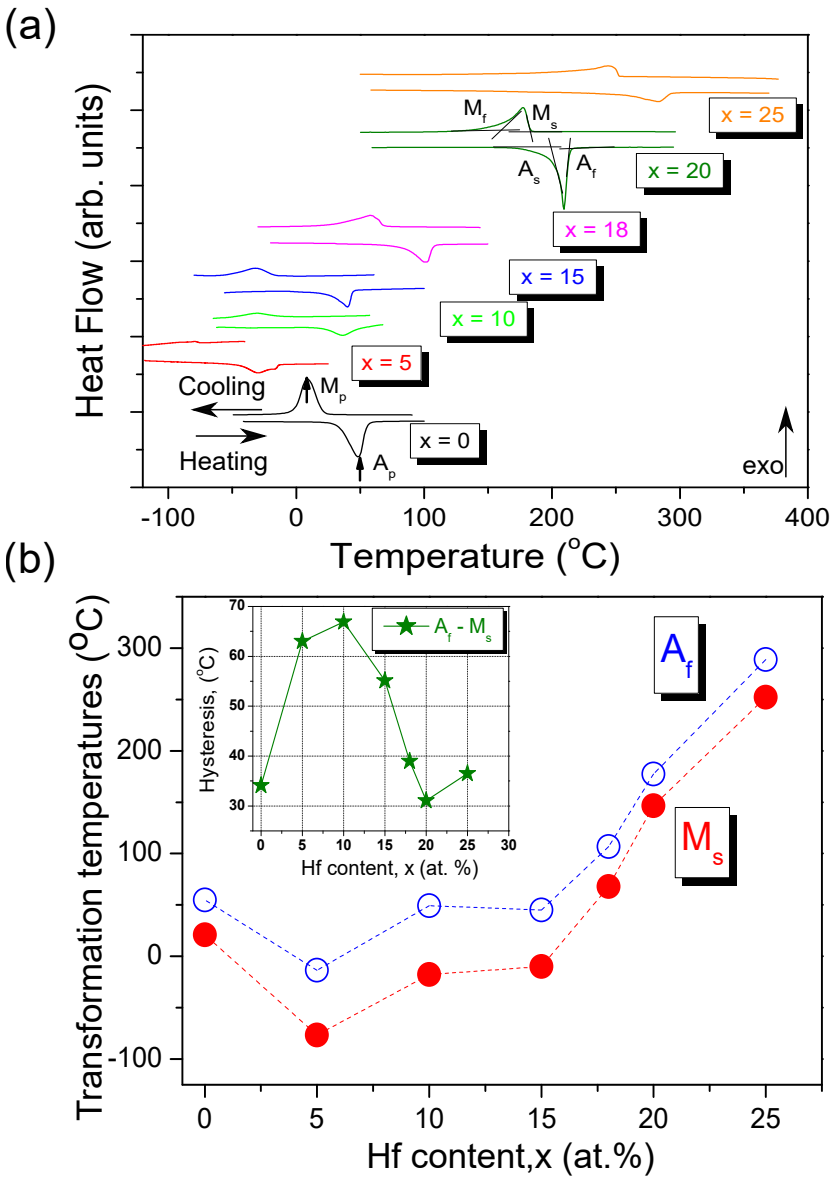

Figure 4.2: (a) DSC plots of the $Ni_{50.3}Ti_{49.7-x}Hf_x$ alloys for x = 0, 5, 10, 15, 18, 20 and 25 at.%. for forward (cooling) and reverse (heating) martensitic phase transformations, (b) Variation in M_s and A_f values of the alloys with Hf concentration, x (in at.%). Inset: Hysteresis modification with Hf concentration.

to the martensite phase begins as M_s = 20.8°C and completes at M_f = -0.8°C , with the exothermic peak at M_p = 9.4°C. The reverse martensitic transformation from the martensite to austenite upon heating commences at A_s = 32.8°C and completes at A_f = 54.9°C, with endothermic peak at A_p = 47.6°C. The phase transformation temperatures of all the compositions along with the thermal hysteresis values (A_f - M_s) and the latent heat associated with reverse transformation ($\Delta H^{Heating}$) are tabulated in Table 4.1.

Two important aspects pertaining to effect of Hf solute addition to $Ni_{50.3}Ti_{49.7}$ alloy martensitic phase transformation behaviour are listed as:

(a) Transformation temperatures, (b) Thermal hysteresis.

It can be seen from the Figure 4.2 (b) that for Hf concentration x = 5 and 10 at.%, there is an initial lowering of the transformation temperatures significantly below room temperatures. For higher concentrations, the transformation temperature exhibit an increasing trend, varying almost linearly with Hf concentration 25°C/at.% for Hf $\geq$ 15 at.%. It can be seen from the Table 4.1 that alloys exhibiting low values of phase transformation temperatures also have lower latent heats of transformation. This interconnection is indicative of difficulty in occurrence of martensitic phase transformation or higher thermodynamic stability of the austenite [253, 254]. The Density Functional Theory (DFT) calculations by Frenzel *et al.* [255] provide a linear relationship between latent heat and M_s for binary NiTi and ternary NiTiCr alloys. However, they found that in Ti-rich NiTiHf alloys, the latent heats are almost constant over wide range of Hf, when substituted against Ti. On the other hand, present experiments establish that in Ni-rich NiTiHf alloys, latent heats

Table 4.1: Phase transformation temperatures, thermal hysteresis and latent heat of transformation associated with $Ni_{50.3}Ti_{49.7-x}Hf_x$ (x = 0, 5, 10, 15, 18, 20 and 25 at.%) alloys.

Hf concentration, x (at.%)	M_s (°C)	M_f (°C)	A_s (°C)	A_f (°C)	M_p (°C)	A_p (°C)	A_f - M_s (°C)	$\Delta H^{Heating}$ (J/g)
x = 0	20.8	-0.8	32.8	54.9	9.4	47.6	34.1	18.3
x = 5	-76.7	-84.3	-43.1	-13.7	-76.8	-43.5	63.0	4.70
x = 10	-17.7	-51.6	23.0	49.2	-31.0	37.0	66.9	5.70
x = 15	-10.0	-18.2	41.5	45.2	-15.0	43.2	55.0	8.50
x = 18	67.9	31.7	84.3	106.9	58.0	102.4	39.0	11.60
x = 20	146.4	116.6	160.4	177.5	177.4	209.4	31.1	8.20
x = 25	252.3	220.1	264.1	288.8	244.3	280.9	36.5	17.2

of transformation are Hf concentration dependent, with low Hf-concentration of 5 at.% showing significantly lower values than rest of the compositions.

The parabolic dependence of transformation temperatures in the present case can also be understood in terms of dependence of shear modulus on the alloy composition. Since martensitic transformation occurs by shear-dominated atomic movements, Ren *et al.* [256] proposed the origin of B19$'$ martensite in NiTi alloys as softening of $011 < 1\bar{1}0 >$ shear modulus, C_{44}. Higher C_{44} values implies lower phase transformation temperatures. For instance, higher C_{44} values in NiTiFe and NiTiCu alloys corroborate low martensite transformation temperatures in these alloys [257]. Although, elements such as Pd, Pt and Zr are known to raise the martensite transformation temperatures, literature on the elastic constants of NiTiX (X = Hf, Zr, Pt and Pd) is rather limited. Hu *et al.* [258] explored Zr concentration dependence in Ni-rich NiTiZr alloys and found that $\frac{\Delta C_{44}}{\Delta C_{44}^{NiTi}}$ increases slightly for low Zr concentrations and for Zr concentration > 6 at.%, the values exhibit a decreasing trend. This observation validates the observed trend in phase transformation temperatures of NiTiZr alloys. A similar dependence of shear modulus C_{44} with Hf concentration could be the possible explanation for initial lowering of the transformation temperatures for x $\leq$ 10 at.% in the present case. Its noteworthy to mention here that, Ni-excess of 0.8 at.% lowers M_s in $Ni_{50.3}Ti_{29.7}Hf_{20}$ alloy drastically by 230°C [259], which suggests that a strict Ni-concentration control in the NiTiHf alloys is extremely important for tuning the phase transformation temperatures.

Inset of Figure 4.2 (b) shows that thermal hysteresis (A_f - M_s) bears a strong Hf concentration dependence. The binary $Ni_{50.3}Ti_{49.7}$ alloy (x = 0) exhibits (A_f - M_s) of 34°C. Atomic radius of the ternary element substituted to NiTi alloys is an important parameter deciding the hysteresis value. For instance in NiTiHf alloys, bigger Hf atoms (1.59 Å) replacing Ti atoms (1.47 Å) in Ni-rich NiTiHf alloys introduce lattice strains, giving rise to larger thermal hysteresis than binary counter parts [30]. For Hf concentration x = 5, thermal hysteresis increases significantly to value of 63°C, significantly larger than the binary alloy. Dalle *et al.* [227] reported thermal hysteresis of 73°C in the $Ni_{49.8}Ti_{42.2}Hf_8$ alloy and attributed this high value to the limited mobility of the austenite-martensite interface due to habit plane distortion. The reduced mobility leads to frictional forces which lead to energy dissipation during interface movement during forward as well as reverse martensitic transformation.

With further increase in Hf concentration, thermal hysteresis increases and then decreases, with maximum value of 67°C for x = 10 and minimum of 31 °C for x = 20 alloy. The hysteresis is found to increase again for x = 25 alloy with the value being 36.5°C. The reduction in thermal hysteresis at x > 10 can be understood in terms of crystallographic compatibility between austenite and martensite lattice. Evirgen *et al.* [260] investigated the correlation between crystallographic compatibility between austenite and martensite with thermal hysteresis in several ternary NiTi based SMAs. In the particular case of NiTiHf alloys, they demonstrated that the volume change during martensitic phase transformation in $Ni_{49.8}Ti_{50.2-x}Hf_x$ (x = 9.5, 15, 20 at.%) alloys is lower at higher Hf concentrations, which reduces the thermal hysteresis. Better lattice compatibility in Ni-rich NiTiHf alloys with higher Hf concentration is a possible explanation to their small thermal hysteresis.

Zarinejad *et al.* [30] described a mechanism based on the valence electrons per atom (e_v) and valence electron concentration (C_v) with ternary and higher order additions to the NiTiHf/Zr HTSMAs, which can serve as useful tool to rationalize M_s dependence on alloy stoichiometry in this alloy system [255]. The valence electrons per atom ($\frac{e_v}{a}$) in ternary NiTiHf alloy are calculated as:

$$\frac{e_v}{a} = x_{Ni}e_v^{Ni} + x_{Ti}e_v^{Ti} + x_{Hf}e_v^{Hf} \tag{4.1}$$

where x_{Ni}, x_{Ti} and x_{Hf} are atomic concentrations of Ni, Ti and Hf , respectively in the alloy. The electronic configuration of Ni (Z = 28): $1s^22s^22p^63s^23p^64s^23d^8$, Ti(Z = 22): $1s^22s^22p^63s^23p^64s^23d^2$, Hf (Z = 72): $1s^22s^22p^63s^23p^64s^23d^{10}4p^64d^{10}5s^25p^64f^{14}5d^26s^2$, and the number of valence electrons in Ni (e_v^{Ni}), Ti (e_v^{Ti}) and Hf (e_v^{Hf}) are 10, 4 and 4 respectively.

The valence electron concentration in the alloys (C_v) is given by the ratio of total valence electrons (e_v) to the total number of electrons (e_t) in the alloy as:

$$C_v = \frac{e_v}{e_t} = \frac{x_{Ni}e_v^{Ni} + x_{Ti}e_v^{Ti} + x_{Hf}e_v^{Hf}}{x_{Ni}Z^{Ni} + x_{Ti}Z^{Ti} + x_{Hf}Z^{Hf}} \tag{4.2}$$

Values of e_v and C_v and the martensite start temperature (M_s) for the $Ni_{50.3}Ti_{49.7-x}Hf_x$ alloys are listed in Table 4.2. Since Ti and Hf atoms have identical number of valence electrons (4 each), the quantity e_v remains independent of Hf concentration. Zarinejad *et al.* [30] found that a wide range of martensite transformation temperatures of the NiTi

Table 4.2: Valence electrons per atom (e_v), valence electron concentration (C_v) and martensite start temperatures of the $Ni_{50.3}Ti_{49.7-x}Hf_x$ (x = 0, 5, 10, 15, 18, 20 and 25 at.%) alloys.

Hf concentration, x (at.%)	**0**	**5**	**10**	**15**	**18**	**20**	**25**
$\frac{e_v}{a}$	7.018	7.018	7.018	7.018	7.018	7.018	7.018
$\mathbf{C_v}$	0.2805	0.255	0.2338	0.2158	0.2063	0.2004	0.1871
$\mathbf{M_s}$**(°C)**	20.8	-76.7	-17.7	-10.0	67.9	146.4	252.3
$\mathbf{A_f}$ **-** $\mathbf{M_s}$ **(°C)**	34.1	63.0	66.9	55.0	39.0	31.1	36.5

based alloys with $e_v = 7$, which holds true for the results from present study as well.

In order to investigate the dependence of thermal hysteresis (A_f - M_s) and the undercooling (T_0 - M_s) needed for martenstic transformation as a function of valence electron concentration in the alloys, a plot depicting dependence of M_s, A_f - M_s and T_0 - M_s with valence electron concentration, C_v is shown in Figure 4.3. As seen from the Figure 4.3 (a), as a general trend, M_s increases with decrease in C_v, a trend observed in several other NiTi based SMAs. An anomalous dip in M_s value with C_v is observed for for x = 5 alloy. Higher values of T_0 - M_s for higher C_v indicates higher thermodynamic stability of austenite, which decreases with lowering of C_v, with a minimum at value corresponding to x = 20. The M_s : C_v and (A_f - M_s) : C_v relationships can serve as important tool for designing new Ni-rich NiTiHf HTSMAs, with desired transformation temperatures and thermal hysteresis.

Effect of aging treatments

In order to understand the effect of aging treatments on the phase transformation behaviour of the $Ni_{50.3}Ti_{49.7-x}Hf_x$ alloys, the alloys were aged at four temperatures namely 500°C, 550°C, 600°C and 650°C for 3 hours each. Figure 4.4 (a)-(d) show the variation in M_s, M_f, A_s and A_f values as a function of aging temperature for all the alloy compositions. It can be inferred from the figure that phase transformation temperatures in the aged alloys vary with Hf concentration in a manner similar to that of the alloys in as-solutionized condition. Interestingly, for all these alloys, aging treatments substantially increase the transformation temperatures relative to the corresponding as-solutionized state.

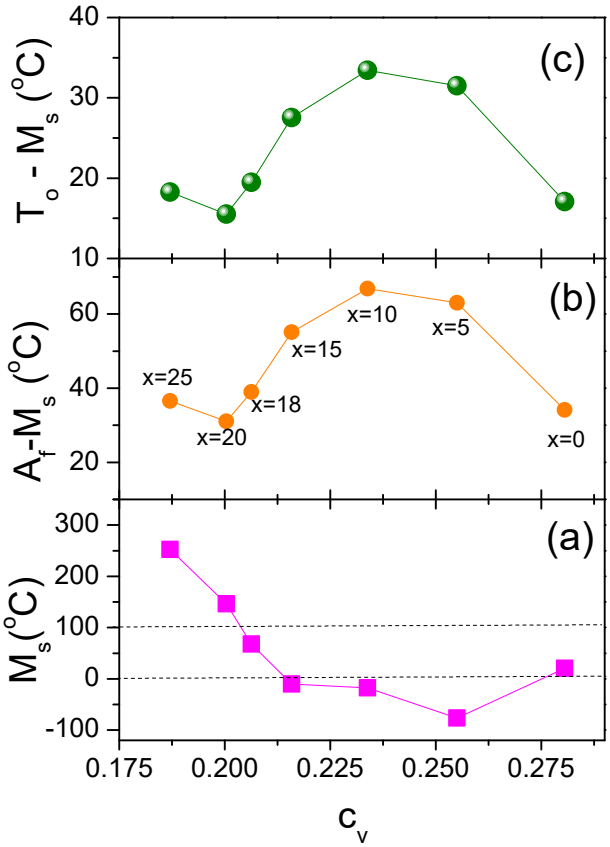

Figure 4.3: (a) Valence electron concentration (C_v) dependence of martensite start temperature (M_s), (b) variation in A_f - M_f values with C_v and (c) thermodynamic stability of austenite phase, indicated by T_0 - M_s as a function of C_v in the $Ni_{50.3}Ti_{49.7-x}Hf_x$ alloys for x = 0, 5, 10, 15, 18, 20 and 25 at.%.

The hysteresis values for all the alloys corresponding to all four aging temperatures were determined and have been listed in Table 4.3 and also plotted in Figure 4.5. Effect of aging on the thermal hysteresis is summarized as follows:

- The alloy x = 20 exhibits lowest thermal hysteresis in as-solutionized as well as after aging amongst rest of the alloys.
- All alloys exhibit higher thermal hysteresis when aged at 650°C, in comparison to respective as-solutionized condition.
- For low Hf concentrations, typically x < 15 at.%, thermal hysteresis values are lower for when the alloys are aged at 500°C, 550°C and 600°C.
- For x = 25 alloy, aging at all the four temperatures increases the thermal hysteresis.

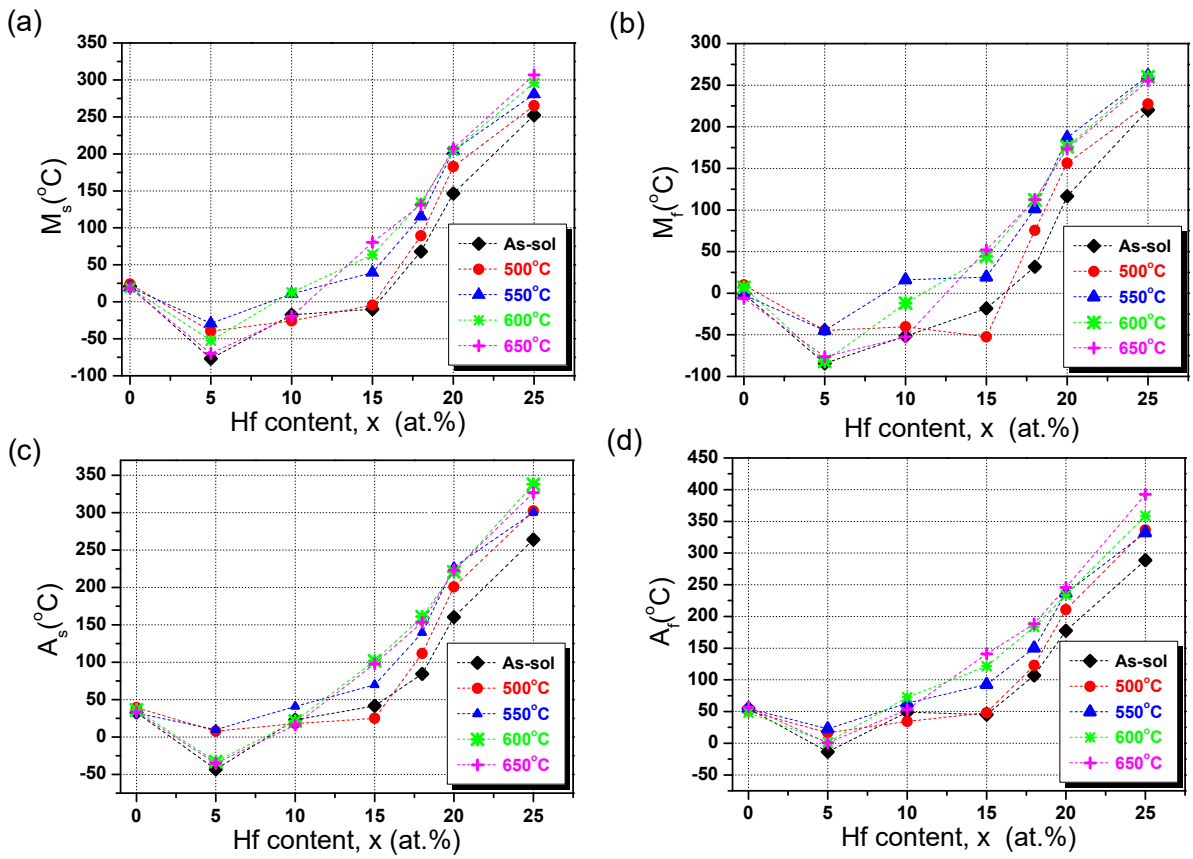

Figure 4.4: (a) Variation of M_s, (b) Variation of M_f, (c) Variation of A_s and (d) Variation of A_f in $Ni_{50.3}Ti_{49.7-x}Hf_x$ alloys for x = 0, 5, 10, 15, 18, 20 and 25 at.%. aged at 500°C, 550°C, 600°C and 650°C for 3 hours each.

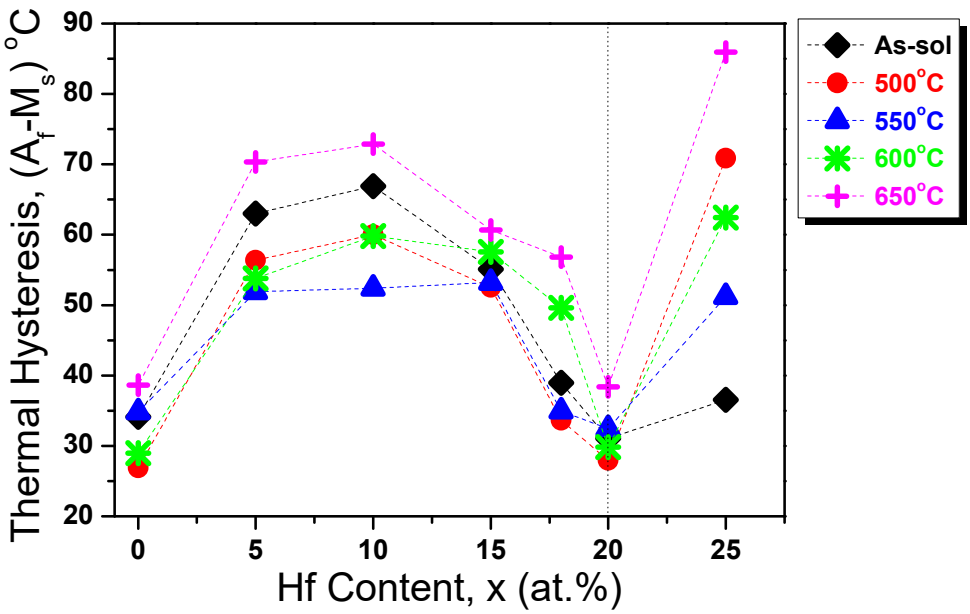

Figure 4.5: Variation of thermal hysteresis (A_f - M_s) of the $Ni_{50.3}Ti_{49.7-x}Hf_x$ alloys for x = 0, 5, 10, 15, 18, 20 and 25 at.% aged at 500°C, 550°C, 600°C and 650°C for 3 hours each.

Table 4.3: Thermal hysteresis (A_f - M_s) of the $Ni_{50.3}Ti_{49.7-x}Hf_x$ (x = 0, 5, 10, 15, 18, 20 and 25 at.%) alloys aged at 500°C, 550°C, 600°C and 650°C for 3 hours each.

Hf concentration, x (at. %)	Thermal Hysteresis (°C)				
	As-sol	500°C	550°C	600°C	650°C
0	34.1	26.9	34.8	29.0	38.6
5	63.0	56.4	51.9	53.8	70.3
10	66.9	60.0	52.4	59.8	72.9
15	55.1	52.5	53.2	57.6	60.7
18	39.0	33.6	34.9	49.6	56.8
20	31.0	27.9	32.5	29.9	38.4
25	36.5	70.9	51.2	62.5	86.0

4.3.2. B2-phase Lattice Parameters

The neutron diffraction patterns for the $Ni_{50.3}Ti_{49.7-x}Hf_x$ alloys for x = 0, 5, 10, 15, 18, 20 and 25 at.%. alloys in the austenite phase are shown in the Figure 4.6 (a). The diffraction patterns for the alloys exhibiting M_s below room temperatures were obtained at ambient conditions, while for the alloys exhibiting transformation temperatures above this limit, diffraction patterns were collected at T > A_f, ensuring the austenite phase. The Bragg peaks in the diffraction patterns validated that all the alloys remain in single phase with B2 crystal structure. Lattice parameters of the austenite unit cell and corresponding cell volumes have been tabulated in Table 4.4 and have been plotted against Hf concentration, x, in Figure 4.6 (b). The calculated B2 lattice parameters of the $Ni_{50.3}Ti_{49.7-x}Hf_x$, a (in Å) follow Vegard's law [261], which can be parametrized in terms of Hf concentration, 'x' as:

$$a_{B2}(x) = 3.005(\pm 0.0017) + 0.0044(\pm 1.57 \times 10^{-4})x \tag{4.3}$$

Single-phase B2 structure and the validity of Vegard's law for all the compositions imply complete solid-solution solubility of Hf in the binary Ni-rich NiTi alloys upto 25 at.%.

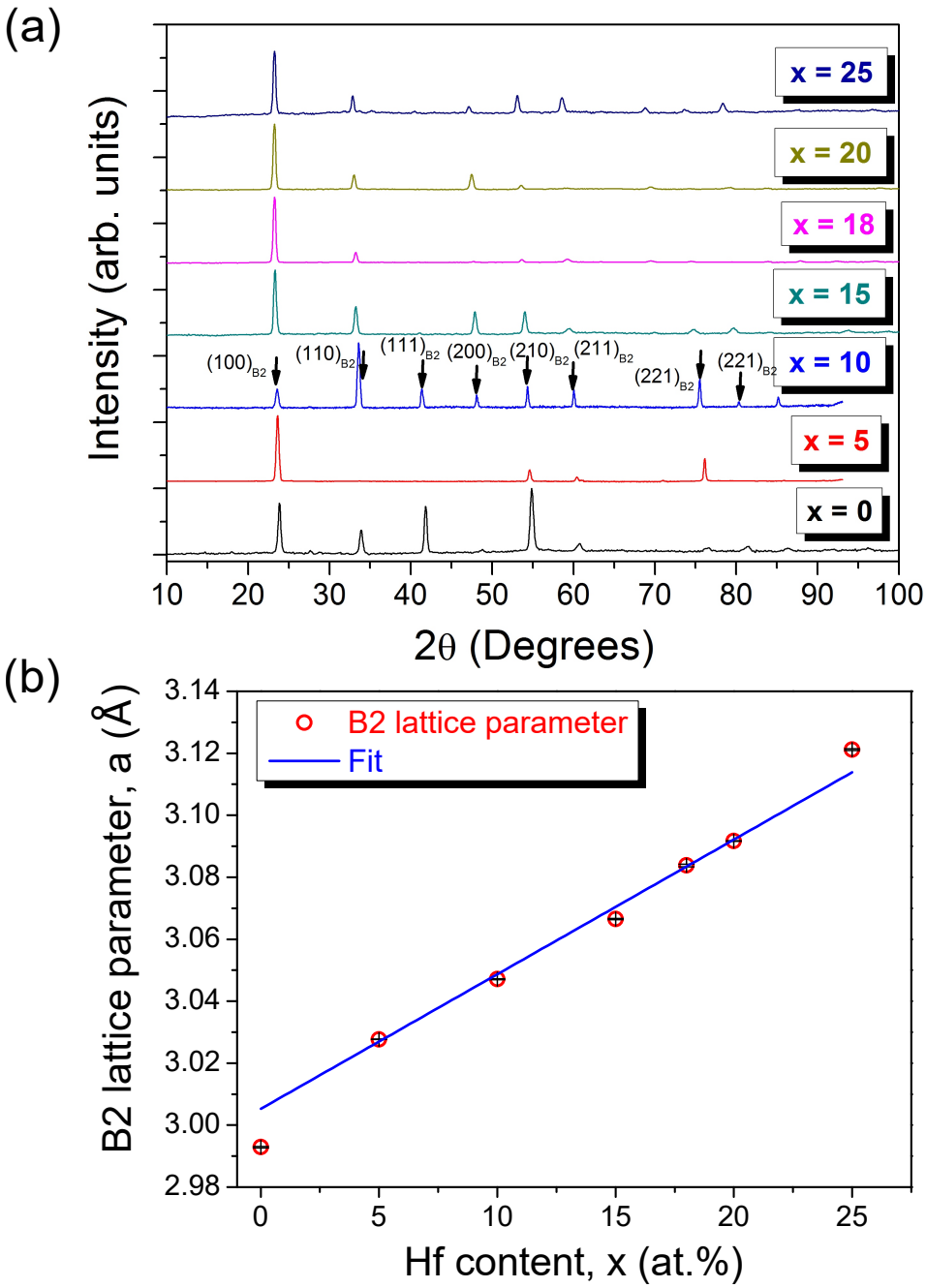

Figure 4.6: (a) Neutron diffraction patterns of the $Ni_{50.3}Ti_{49.7-x}Hf_x$ alloys for x = 0, 5, 10, 15, 18, 20 and 25 at.% alloys obtained in the austenite phase, (b) Lattice parameters of B2 phase with Hf concentration, x (in at.%).

4.3.3. Micro-hardness

Room temperature micro-hardness measurements were conducted on the all the alloy specimens in as-solutionized condition to investigate the effect of Hf concentration on alloy strength. The room temperature Vickers hardness of the alloys as a function of Hf concentration is depicted in Figure 4.7.

These results indicate that the room temperature hardness value for x = 0 alloy is

Table 4.4: Crystal structure, lattice parameters and the unit cell volume of the $Ni_{50.3}Ti_{49.7-x}Hf_x$ (x = 0, 5, 10, 15, 18, 20 and 25 at.%) alloys.

Compositions	Crystal structure	Lattice parameter B2, a (Å)	unit cell volume V_{B2}(Å ^{3})
$Ni_{50.3}Ti_{49.7}$ (x = 0)		2.9929 (4)	26.81 (4)
$Ni_{50.3}Ti_{44.7}Hf_5$ (x = 5)		3.0277 (5)	27.75 (5)
$Ni_{50.3}Ti_{39.7}Hf_{10}$ (x = 10)		3.0471 (4)	28.29 (4)
$Ni_{50.3}Ti_{34.7}Hf_{15}$ (x = 15)	B2	3.0665 (4)	28.84 (4)
$Ni_{50.3}Ti_{31.7}Hf_{18}$ (x = 18)		3.0838 (4)	29.33 (4)
$Ni_{50.3}Ti_{29.7}Hf_{20}$ (x = 20)		3.0917 (5)	29.55 (5)
$Ni_{50.3}Ti_{24.7}Hf_{25}$ (x = 25)		3.1212 (4)	30.41 (4)

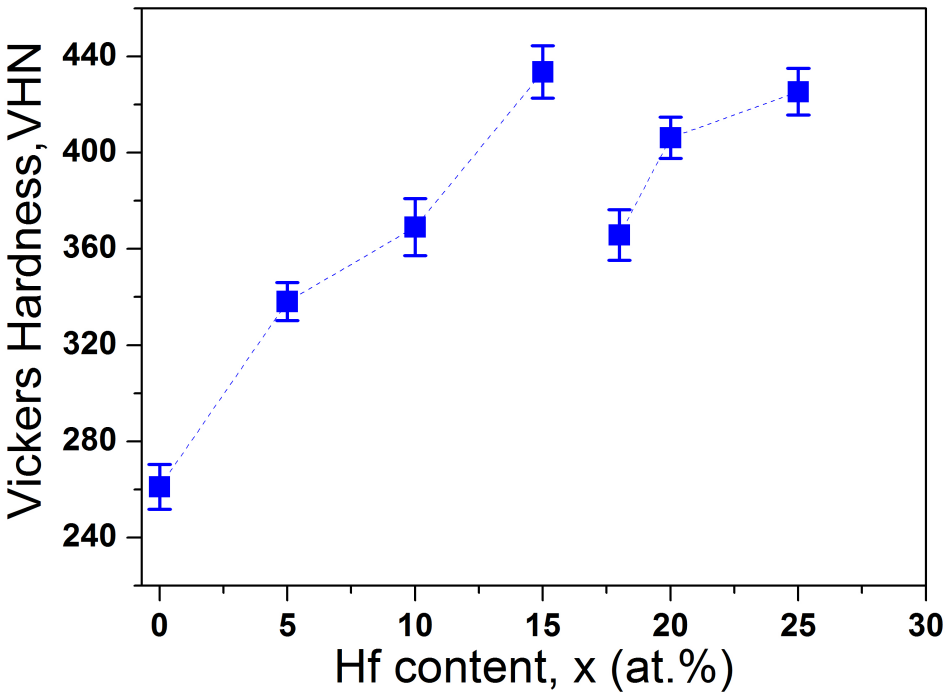

Figure 4.7: Vickers micro-hardness as a function of the Hf concentration for the $Ni_{50.3}Ti_{49.7-x}Hf_x$ alloys (x = 0, 5, 10, 15, 18, 20 and 25 at.%).

261 ± 9 VHN. Substitution of Hf at the expense of Ti in the $Ni_{50.3}Ti_{49.7}$ alloy increases its strength. From the figure it can be inferred that Vickers hardness of $Ni_{50.3}Ti_{49.7-x}Hf_x$ alloys increases linearly with Hf concentration, x. Since the hardness measurements were conducted at room temperature, alloys with x = 18 at.% and above exhibit lower hardness

values than those with x = 15 at.%, due to softer martensite phase. Present results demonstrate the solid solution strengthening effect of substitution of bigger Hf atoms replacing Ti atoms on the Ti sub-lattice.

4.4. Summary

In summary, the Hf concentration dependence of martensitic phase transformation characteristics, lattice parameters and hardness in $Ni_{50.3}Ti_{49.7-x}Hf_x$ (x = 0, 5, 10, 15, 18, 20 and 25 at.%) alloys is demonstrated.

- It has been found that small additions of Hf up to x = 10 at.% lower the phase transformation temperatures with respect to the binary $Ni_{50.3}Ti_{49.7}$ alloy (M_s = 21°C, A_f = 55°C). Further addition of Hf leads to almost linear increase in transformation temperatures, with x = 25 alloy exhibiting M_s = 252°C and A_f = 289°C.

- In terms of thermal hysteresis, NiTiHf alloys with Hf concentration upto 15 at.% exhibit significantly higher thermal hysteresis > 50°C, which drop to minimum value of 31°C for $Ni_{50.3}Ti_{29.7}Hf_{20}$ alloy and subsequently increase to 38°C for the $Ni_{50.3}Ti_{24.7}Hf_{25}$ alloy. Interestingly, $Ni_{50.3}Ti_{29.7}Hf_{20}$ alloy exhibit least thermal hysteresis amongst all the other compositions in as-solutionized as well after aging treatments.

- Substitution of Hf against Ti in these alloys leads to linear increase in alloy hardness on account of solid-solution strengthening by bigger Hf atoms. Further, single-phase B2 structure and the validity of Vegard's law for all the compositions imply complete solid-solution solubility of Hf in Ni-rich NiTi alloys upto 25 at.% Hf.

Since $Ni_{50.3}Ti_{29.7}Hf_{20}$ alloy exhibits best combination of high phase transformation temperatures and significantly lower thermal hysteresis, subsequent studies in the current thesis are focused on this particular alloy composition.

CHAPTER 5

Structure-Property Correlation in Precipitate Strengthened $Ni_{50.3}Ti_{29.7}Hf_{20}$ Alloy

In previous chapter, it was noted that the aging treatments can tune the phase transformation temperatures as well as thermal hysteresis of Ni-rich NiTiHf alloys. This chapter focuses around analysing the alloy micro-structure as a function of aging treatments and understanding the phase transformation behaviour of the $Ni_{50.3}Ti_{29.7}Hf_{20}$ alloy. Further, quantitative rationalization of the effect of aging on the mechanical strength of this alloy has been dealt with.

5.1. Introduction

In case of Ni-rich NiTi alloys, aging results in altering the matrix composition on account of Ni_4Ti_3 precipitates, whose volume fraction is controlled by aging temperature as well as the duration. Since, phase transformation temperatures as well as yield strength of the NiTi SMAs are extremely sensitive to the Ni-concentration of the alloy [154], their shape memory properties *viz.* SME and SE are found to be influenced by the aging treatments. In other words, precipitation phenomenon plays important role in tailoring the shape memory properties of NiTi based SMAs on account of precipitate-strengthening of the alloy matrix. In the Chapter 4, it was seen that Hf addition to the Ni-rich NiTi alloy leads to increase in the phase transformation temperatures as well the alloy strength. The alloy with composition $Ni_{50.3}Ti_{29.7}Hf_{20}$ (at.%) exhibits sufficiently high phase transformation temperatures with sufficiently low thermal hysteresis ($\sim 31°C$) in comparison to the other Ni-rich NiTiHf alloys.

In this chapter, effect of aging treatments on the micro-structure of the $Ni_{50.3}Ti_{29.7}Hf_{20}$ (at.%) alloy has been investigated and is correlated with its phase transformation be-

haviour as well as strength. The aging-induced precipitation is quantitatively investigated using SAXS and SANS as complementary probe to TEM and the mechanism of aging-induced increase in alloy strength is elucidated.

5.2. Experiments

Alloy ingot with nominal composition $Ni_{50.3}Ti_{29.7}Hf_{20}$ (at.%) alloy was fabricated in the form of a sheet by hot-rolling, as described in section 3.2. The specimens from the as-solutionized alloy were aged at 550°C for 3 hours and and 650°C for 3 hours, 6 hours, 144 hours and 256 hours, respectively. For the sake of brevity, these aged specimens have been termed as 550°C-3h alloy, 650°C-3h alloy, 650°C-6h alloy, 650°C-144h alloy and 650°C-256h alloy, respectively, throughout this chapter. XRD patterns of the specimens were collected at room temperature using Cu-Kα radiation. The Vickers micro-hardness tests on the as-solutionized, 550°C-3h and 650°C-3h aged specimens were carried out at room temperature. The phase transformation temperature and latent heat of transformation were determined by carrying out DSC measurements at a heating/cooling rate of 10^0C/min. TEM experiments was carried out on the specimens prepared by methodology as per section 3.3.2. Quantitative micro-structural characterization was conducted using a conventional laboratory scale SAXS instrument (refer section 3.7). SANS experiments were carried out using a double crystal based MSANS instrument at guide tube laboratory, Dhruva reactor, India (refer section 3.8).

5.3. Results

5.3.1. Phase Transformation Behaviour upon Aging

The DSC plots in Figure 5.1 show phase transformation behaviour of the $Ni_{50.3}Ti_{29.7}Hf_{20}$ ialloy in as-solutionized and 550°C-3h and 650°C-3h specimens. It is discernible from the figure that the martensitic phase transformation occurs in single-stage at both the aging temperatures. Further, aging the specimens at 550°C and 650°C tends to shift the DSC plots towards right, which indicates an increase in the martensitic phase transformation temperatures. The phase transformation temperatures (PTTs) after second thermal cycle have been listed in Table 5.1.

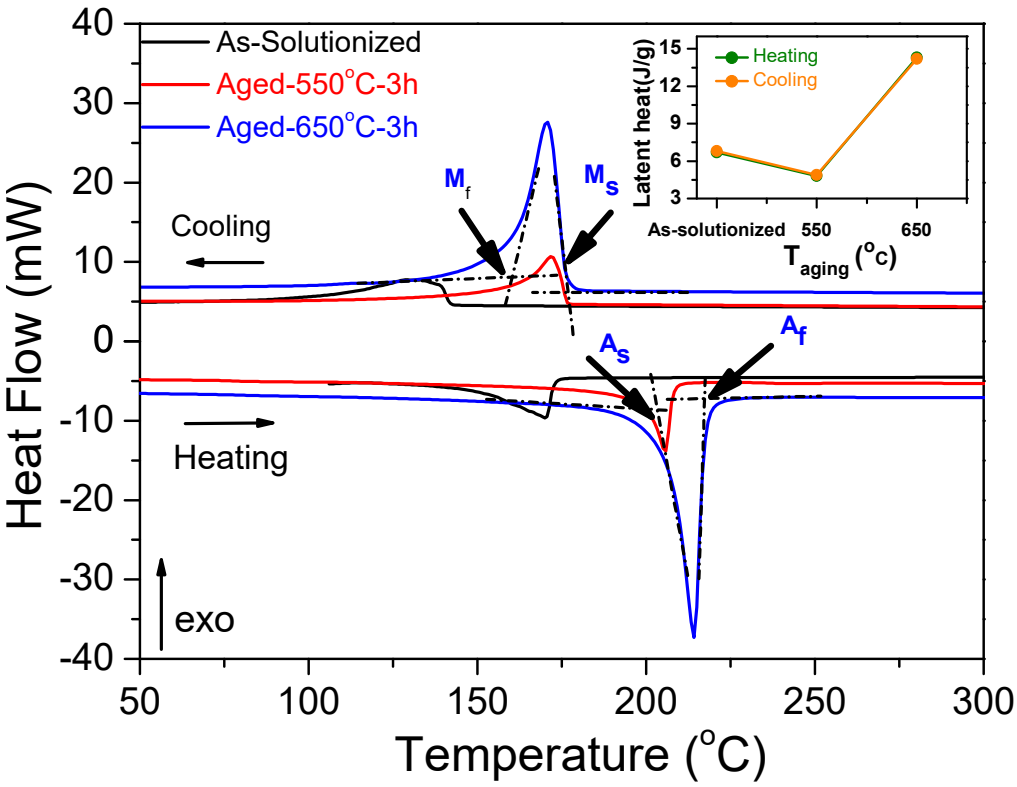

Figure 5.1: (a) Representative DSC scans of the $Ni_{50.3}Ti_{29.7}Hf_{20}$ alloy in as-solutionized condition and after aging at 550°C and 650°C for 3h each, (inset: latent of transformation during cooling and heating cycles).

Table 5.1: Phase transformation temperatures, M_s, M_f, A_s, A_f and the reverse and forward latent heats of transformation, $\Delta H^{B19'-B2}$ and $\Delta H^{B2-B19'}$, respectively of the as-solutionized as well as in as-solutionized condition as well as 550°C-3h, 650°C-3h, 650°C-6h, 650°C-144h and 650°C-240h $Ni_{50.3}Ti_{29.7}Hf_{20}$ alloy specimens.

Alloy	M_s (°C)	M_f (°C)	A_s (°C)	A_f (°C)	$\Delta H^{B19'-B2}$ (J/g)	$\Delta H^{B2-B19'}$ (J/g)
As-solutionized	142	125	152	172	6.7	6.8
550°C-3h	178	163	204	213	4.8	4.9
650°C-3h	177	161	206	217	14.3	14.2
650°C-6h	204	150	207	252	19.4	19.2
650°C-144h	225	171	239	271	15.2	15.3
650°C-256h	223	165	233	262	14.4	14.5

Clearly, PTTs increase significantly after aging the alloy at 550°C for 3 h. However, no appreciable increase in the values is seen upon aging at 650°C for the same duration.

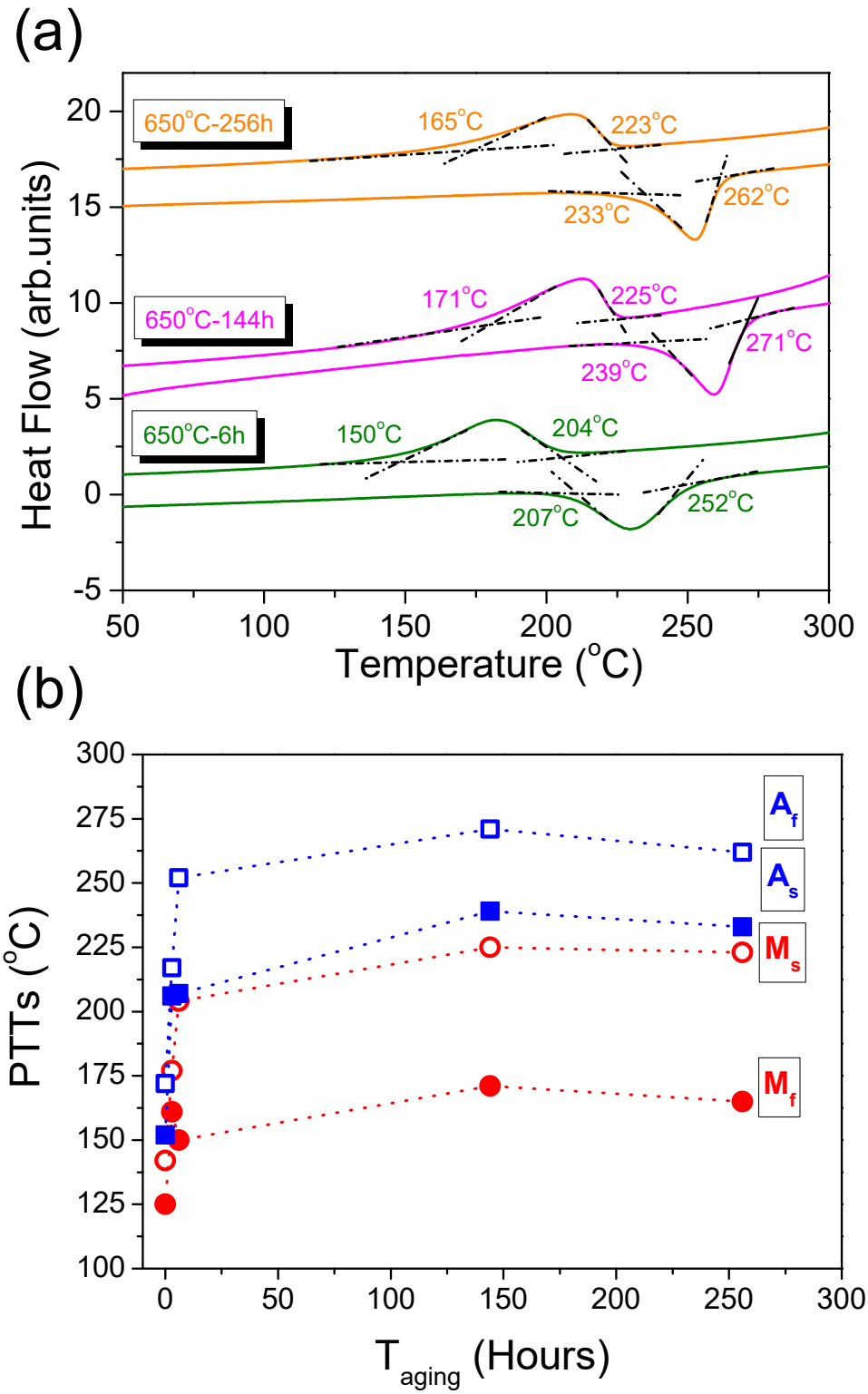

Figure 5.2: (a) DSC scans of the $Ni_{50.3}Ti_{29.7}Hf_{20}$ alloy aged at 650°C for 6 h, 144 h and 256 h, (b) Variation in M_s, M_f, A_s and A_f values with aging time.

The latent heat of transformation ($\Delta H^{B19'-B2}$) while heating and the same while cooling ($\Delta H^{B2-B19'}$) of as-solutionized and aged specimens have been presented in inset of the

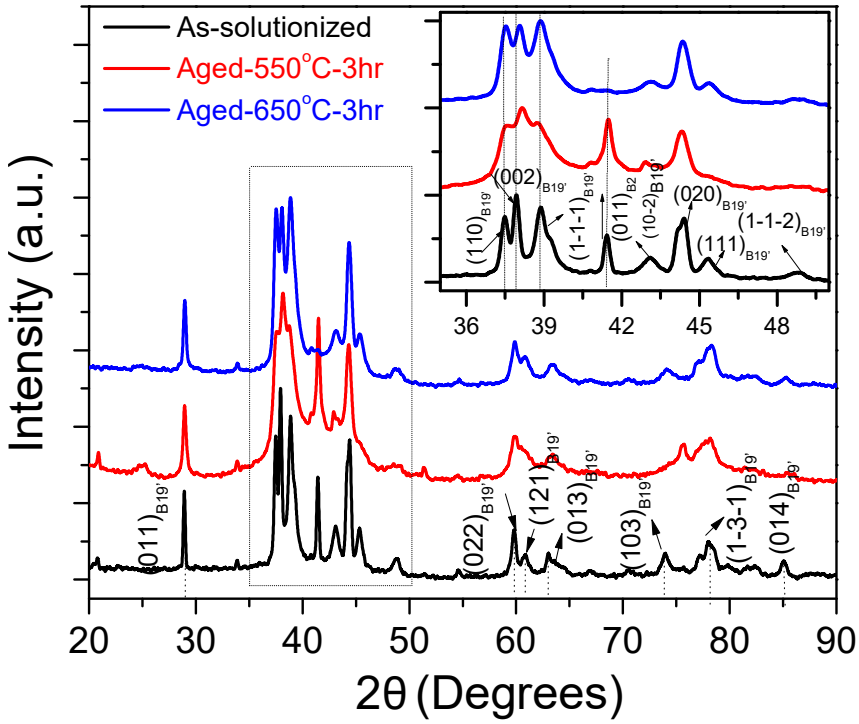

Figure 5.3: X-ray diffraction patterns for $Ni_{50.3}Ti_{29.7}Hf_{20}$ alloy in as-solutionized condition and upon aging at 550°C and 650°C for 3 h; (inset: Decrease in intensity of the (011)B2 reflection and change in peak broadening of B19′ phase upon aging).

Figure 5.1. In order to understand the role of aging time on the PTTs, the alloy specimen was aged at 650°C for longer durations *viz.* 6 h, 144 h and 256 h. The DSC plots obtained after second thermal cycles of the specimens exhibiting reversible martensitic transformation are shown in Figure 5.2. It can be noticed from the figure 5.2 (b) that maximum increase in PTTs values is achieved for aging upto 144 hours. It must be noticed that the change in PTTs values of the samples aged for 144 h and 256 h is smaller in comparison to those obtained by aging for 3 h and 6 h respectively.

5.3.2. Crystal Structure as a Function of Aging

Figure 5.3 illustrates the room temperature XRD patterns of the as-solutionized, 550°C-3h and 650°C-3h specimens. The Bragg peaks in the as-solutionized alloy corroborate to co-existing monoclinic B19′ martensite and B2 austenite structures. Presence of additional Bragg peaks in the XRD patterns of the aged specimens has been observed. These additional peaks originate from face-centred orthorhombic lattice of the H-phase precipitates [223], whose structure belongs to space group F d/2 d/2 d/2. Lattice parameters of the phases are listed in Table 5.2. The presence of fine precipitates in the martensite

Table 5.2: Lattice parameters of B19′ martensite and cell-volume of B2 lattice at room temperature of $Ni_{50.3}Ti_{29.7}Hf_{20}$ alloy in as-solutionized condition and after aging at 550°C and 650°C for 3 h.

Alloy	B19′ Martensite (Space group: $P2_1/m$)				Precipitate phase (Space group: Fd/2d/2d/2)			Cell Volume B2-phase
	a (Å)	b (Å)	c (Å)	β(°)	a (Å)	b (Å)	c (Å)	(Å^3)
As-solutionized	3.05	4.08	4.87	103.15	–	–	–	29.466
550°C-3h	3.04	4.1	4.88	104.41	12.69	8.86	25.98	29.616
650°C-3h	3.01	4.09	4.91	104.76	12.66	8.87	25.94	29.737

matrix leads to significant peak broadening in the B19′ peaks in 550°C-3h specimen. Noticeably, the peaks gets sharp in the 650°C-3h specimen due to increase in precipitate size. It should be noticed that the intensity of (110) reflection from B2 phase in the 650°C-3h aged alloy at $2\theta = 41.5°$ almost disappears. This implies that volume fraction of the martensite phase in the alloy gets enhanced after aging at higher temperature. In other words, thermodynamic stability of martensite increases with aging temperature, which reflects in the form of higher PTTs and latent heats of transformation.

As seen from the Table 5.2, cell volume of B2 phase increases with the increase in aging temperature. It is worth mentioning that Kim *et al.* [262] demonstrated an increase in the lattice parameter of the B2 phase in $Ni_{50.9}Ti_{49.1}$ alloy with increase in aging duration and explained such trend in terms of the reduction of Ni-content in the matrix due of precipitation of the Ni_4Ti_3 phase. In present case also, formation of precipitates in 550°C-3h specimen depletes the amount of Ni in the matrix. At 650°C, increase in the precipitate size results in further reduction of Ni-content in the matrix. The observed increase in cell volume of B2 phase, thus, implies an enhancement of the Ni-depletion in the matrix with increasing aging temperature.

5.3.3. Micro-structural Evolution in the Alloy using TEM

Figure 5.4 depicts micro-structure of the alloy in as-solutionized condition and Figure 5.5 (a), (b) and (c) after aging treatments. The Figure 5.4 illustrates that alloy in as-solutionized condition has internally-twinned micro-structure, typical of martensite phase

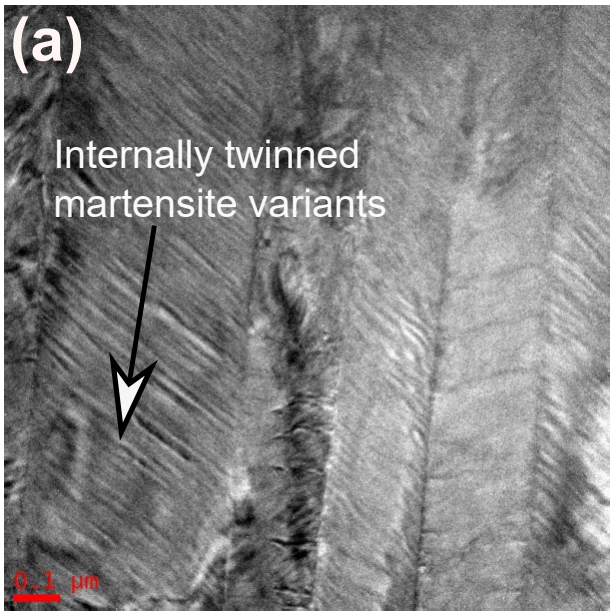

Figure 5.4: TEM micrograph of the as-solutionized $Ni_{50.3}Ti_{29.7}Hf_{20}$ alloy depicting internally-twinned martensite variants.

in NiTi alloys. The HAADF-STEM is an efficient technique to elucidate the chemical contrast in the materials, in which the scattered intensity is approximately proportional to Z^2. In present alloy, the atomic numbers (Z) of Hf being highest among Ni (Z = 28), Ti (Z = 22) and Hf (Z = 72), the phase that is rich in Hf should appear brighter in the micrograph. Figure 5.5 (a) represents HAADF-STEM image of the 550°C-3 h alloy, depicting dense population of nano-precipitates, approximately 5-10 nm in size. In 650°C-3h alloy (shown in Figure 5.5(b)), precipitates attain ellipsoidal morphology with increased inter-precipitate spacing. Furthermore, precipitates are now bigger in dimensions, average length being 60-70 nm and average thickness being 20-30 nm, approximately. Aging the alloy at 650°C for 256 h led to further increase in precipitate size as well as aspect-ratio (length : thickness), as shown in the Figure 5.5 (c). The average length and thickness of precipitates is estimated as 700-1000 nm and 50-60 nm (aspect ratio $\sim$ 15) with wide inter-precipitate spacings.

The composition of precipitates and matrix in 650°C-256h specimen determined by STEM-EDS analysis and listed in Table 5.3. Clearly, the H-phase precipitates are rich in Ni- and Hf-concentration and lean in Ti, making matrix rich in Ti and depleted in Ni, Hf.

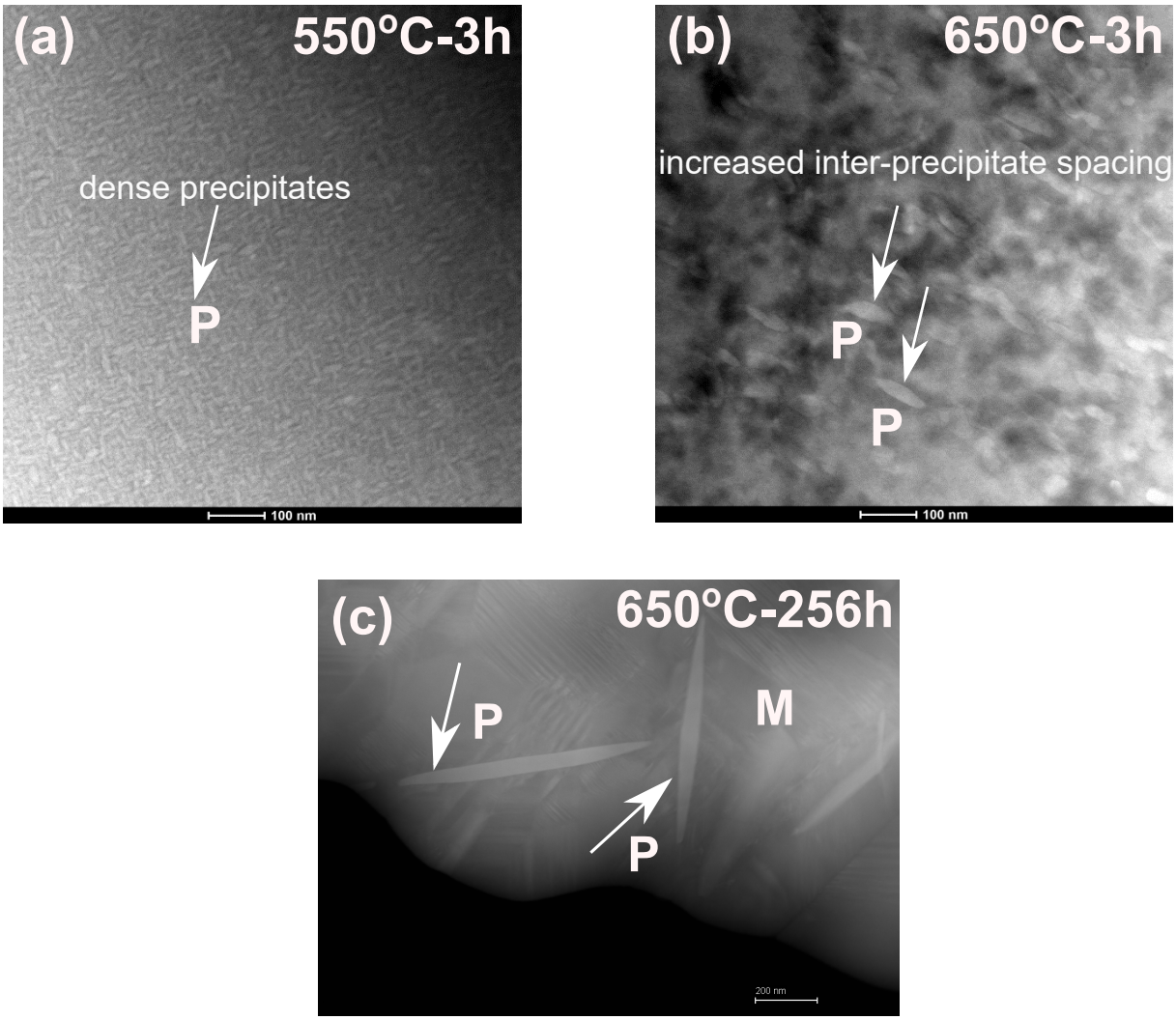

Figure 5.5: HAADF-STEM images of (a) 550°C-3h aged alloy, (b) 650°C-3h aged alloy, and (c) 650°C-256h aged alloy.

5.3.4. Quantitative Analysis of H-phase using SAXS/SANS

Figures 5.6 (a) and (b) represent the combined SAXS and SANS data from the 550°C-3h to 650°C-3h alloy. It is worthy to mention that small-angle scattering is a powerful technique

Table 5.3: STEM-EDS compositional analysis of H-phase precipitates and matrix in the $Ni_{50.3}Ti_{29.7}Hf_{20}$ alloy specimen aged at 650°C for 256 h. (P: Precipitate; M: Matrix)

Phase	Ni (at.%)	Ti (at.%)	Hf (at.%)
Precipitate	52.95 ± 1.59	17.27 ± 0.52	29.78 ± 2.98
Matrix	49.91 ± 1.50	28.29 ± 0.99	21.80 ± 2.18

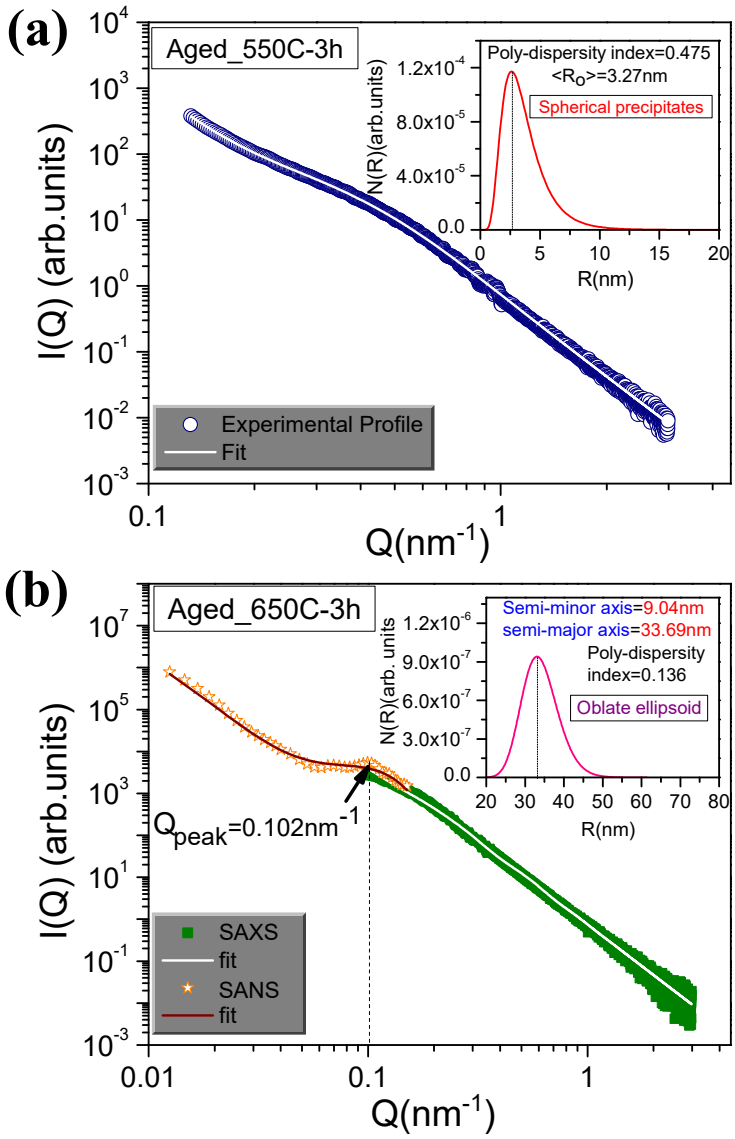

Figure 5.6: (a) SAXS/SANS profiles for specimens aged at (a) 550°C and (b) 650°C for 3 h each. (Inset: number density of precipitates with radius between R and R + ΔR.).

to study mesoscopic inhomogeneities in materials. This technique provides statistically averaged information about the structure, morphology, size distributions, volume fractions etc. of the precipitates from bulk specimens, which directly influence the material properties. It should be noted that scattering measurements are performed in reciprocal space, implying that chemical inhomogeneities with bigger dimensions contribute to scattered intensity at relatively low Q region and vice versa. In present case, both SAXS and SANS have been utilized to probe the micro-structure of alloy over wide Q-range. The scattering profiles have been analyzed in term of scattering from poly-disperse spheres and ellipsoids under local mono-disperse approximation (refer section Appendix II.0.2. The factor P(Q,R) is the single particle form factor, which is function of the precipitate

shape and size. The inter-precipitate interactions S(Q,R) is described in the realm of hard sphere (HS) interaction [263]. The particle form-factor P(Q,R) for spherical precipitates with radius R is given as:

$$P^{spherical}(Q,R) = 9\Big[\frac{sin(QR) - QRcos(QR)}{(QR)^3}\Big] \tag{5.1}$$

For oblate ellipsoidal shaped precipitates, with half axes (R, R, νR) the form factor is given as:

$$P^{ellipsoidal}(Q,r,\nu) = \int_0^{\pi/2} [\psi(Q,R(r,\nu,\gamma)]^2 \sin\gamma d\gamma \tag{5.2}$$

Where, $R(r,\nu,\gamma) = r(\sin^2\gamma + \nu^2\cos^2\gamma)$; γ is the angle between the incident X-ray beam and the major-axis of the ellipsoid.

$$\psi(Q,r) = 3\Big[\frac{(sin(Qr) - Qrcos(Qr))}{(Qr)^2}\Big] \tag{5.3}$$

The precipitate size (number) distribution is fitted to a log-normal distribution (refer Appendix II.1). In order to estimate the quantitative parameters, the SAXS data has been fitted to the above model using spherical particle form-factor for 550°C-3h specimen and ellipsoidal particle form-factor for 650°C-3h specimen, respectively. The spherical particle form-factor is also used to fit SANS data obtained for 650°C-3h alloy. It is interesting to observe that above models agree reasonably well with the experimental observations, as shown in Figures 5.6 (a) and (b).

The scattering intensity in the range Q $\rightarrow$ 0 and Q $\rightarrow$ 1 reveals information about the approximate size and precipitate/matrix interface. In the limit Q $\rightarrow \infty$, the scattered intensity can be approximated by Porod's limit $\lim_{Q\rightarrow\infty} I(Q) \equiv \frac{K}{Q^p}$. The power-law exponent, 'p', provides information about the surface roughness of the precipitates (see Appendix section II.1.2). In present case, value of 'p' obtained after fitting the SAXS profiles from aged specimens is equal to 4. Also, plateaus visible at high Q in Q^4I(Q) *vs.* Q plots in Figure 5.7 (a) indicate that intensities fall as Q^{-4} at high Q. This power-law scattering implies that the precipitates exhibit sharp interface with the matrix. Further, in the limit Q $\rightarrow$ 0, I(Q) can be approximated as I(Q) $\equiv$ I_0 exp$\Big($- $\frac{Q^2R_G^2}{3}\Big)$; where R_G is the Guinier radius. A good estimate of the precipitate dimensions can be obtained from Guinier plots (see Appendix section II.1.1) by plotting Ln I(Q) *vs.* Q^2. Slope of this linear plot is equal to -$\frac{R_G^2}{3}$. The Guinier plots have been presented in Figure 5.7 (b). The value

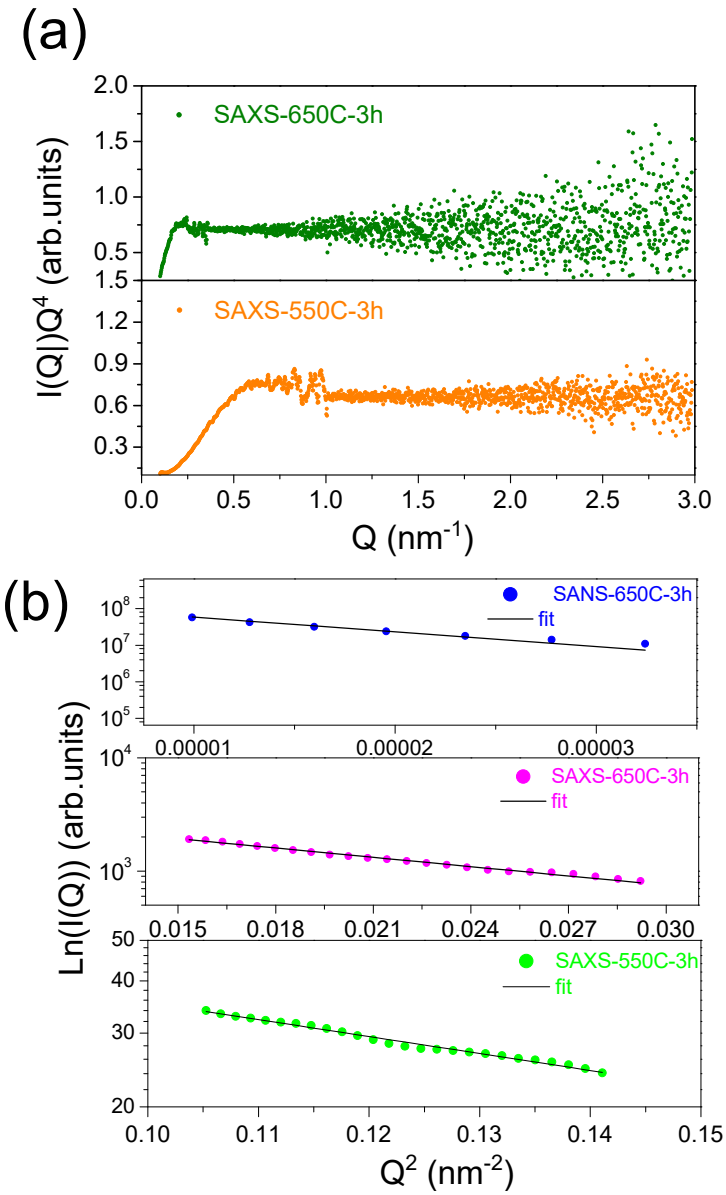

Figure 5.7: (a) Porod plots IQ^4 *vs* Q showing plateau at high Q for SAXS data from 550°C-3h to 650°C-3h alloys, (b) Guinier plots Ln I(Q) vs Q^2 with a linear fit from the SAXS and SANS measurements made on the $Ni_{50.3}Ti_{29.7}Hf_{20}$ alloy aged at 550°C and 650°C for 3 h.

of R_G increases from 5 nm for 550°C-3h alloy to 14 nm for 650°C-3h alloy, respectively. It can be seen that the precipitates in 550°C-3h alloy possess spherical morphology, with typical size of 7 nm. In 650°C-3h alloy, precipitates attain ellipsoidal morphology and are typically 60 nm long and 16 nm wide. Moreover, the poly-dispersity in precipitate size decreases with increase in aging temperature. Further, it has been deduced from SANS data of the 650°C-3h alloy that contribution to scattered intensity at very low Q-range comes from highly poly-disperse (s $\sim$ 0.86) martensite plates, which are approximately 0.1 μm in dimensions. Furthermore, the volume fraction of precipitates decreases in 650°C-3h

Table 5.4: Parameters obtained from fitting the SAXS data obtained from aged specimens.

Alloy Specimen	Morphology	R_G(nm)	Median Size(nm)	Poly-dispersity index(s)	SSA (m^2/g)	Vol. Fraction(%)
550°C-3h	Spherical	5	Diameter: 6.6	0.48	91.4	0.37
650°C-3h	Ellipsoidal	14	Length: 67.4 Width: 18.05	0.11	49.6	0.11

alloy, which is attributed to lesser Ni-depletion from the matrix as the solvus temperature is approached.

The specific surface area (SSA), $\frac{S}{V}$ of the precipitates is also estimated from the SAXS data using equation below:

$$\frac{S}{V} = \left[\pi \frac{\lim_{Q\to\infty} I(Q)Q^4}{\rho \int_0^\infty I(Q)Q^2 dQ}\right] \tag{5.4}$$

where Q is the density of precipitates. The density of precipitates has been evaluated using formula $\rho = \frac{nM_A}{VN_A}$, where, n is no. of atoms of given type in unit cell, M_A is mass of atom (in a.m.u), V is volume of unit cell and N_A is Avogadro's number. Using chemical composition of the precipitates determined by TEM experiments, the density of precipitates is determined to be equal 8.03 g/cm^3. The precipitate size distributions for aged specimens are depicted in insets of Figure 5.6 (a) and (b). It is obvious from the size distribution curves that the radius of the precipitates increases and number of precipitates decreases with aging temperature. Table 5.4 tabulates the quantities obtained after analysing the small angle scattering data from the aged specimens.

5.3.5. Micro-hardness Evolution with Aging

In order to evaluate the effect of aging on the alloy strength, room-temperature Vickers micro-hardness was measured for the as-solutionized as well the aged alloys. Variation in room-temperature Vickers micro-hardness of the alloy with aging temperature is shown in Figure 5.8. Clearly, aging enhances the alloy hardness in comparison to as-solutionized specimen. Hardness value for 550°C-3h alloy is found to be 521 VHN, which is higher than the value (391 VHN) for the as-solutionized alloy. For 650°C-3h alloy, the hardness value decreased to 451 VHN.

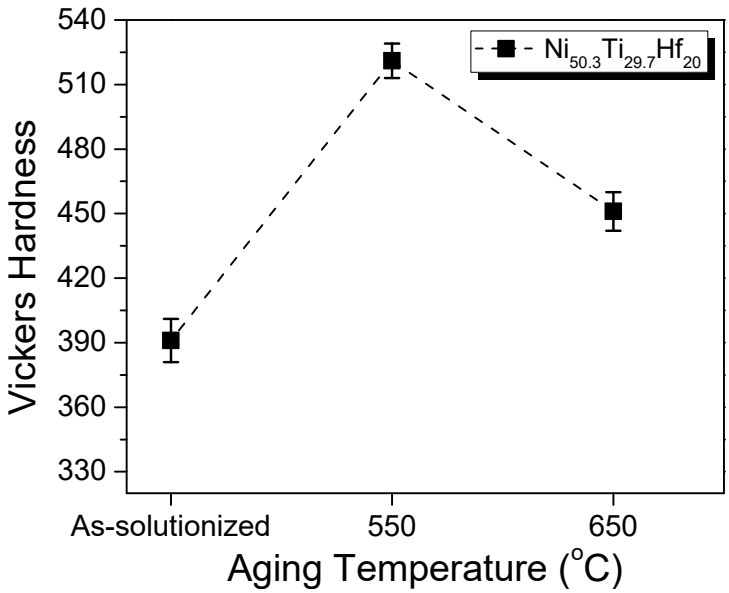

Figure 5.8: Change in Vickers micro-hardness as a function of aging temperature.

5.4. Discussion

Above results clearly reveal that precipitation of the H-phase precipitates strongly govern the phase transfromation characteristics and alloy strength. In case of Ni-rich binary NiTi alloys, precipitation of the Ni_4Ti_3 precipitates reduces the the Ni-concentration in the matrix, which lowers the thermodynamic stability of austenite. This ultimately shows up as increase in phase transformation temperatures. In present case, the precipitate composition obtained from the STEM-EDS analysis reveals that precipitates are rich in Ni-and Hf-concentration, leaving matrix lean in Ni and Hf. Thus, significant increase in the phase transformation temperatures in 550°C-3h specimen is due to lowering of Ni-content in the matrix. In case of 650°C-3h specimen, lower volume fraction of H-phase precipitates results in lesser Ni-depletion from the matrix. It is also interesting to note that higher enthalpy of 650°C aged alloys samples is due to decrease of Ni-concentration in the matrix. This observation corroborates well with the variation of latent heat of transformation with Ni-concentration in binary Ni-Ti alloys [247].

At this juncture, mechanism of hardening in the alloy can be understood in terms of precipitate size and inter-precipitate spacing. The observed change in hardness upon aging can be attributed to the precipitation strengthening. In any metallic alloy, the extent of precipitate strengthening is determined by the precipitate shape, size, their volume fraction and distribution. It can be seen from the TEM and SAXS results that

densely distributed precipitates are formed during aging at 550°C with median radius of approximately, 3 nm. The precipitate dimensions in this case are of the order of typical burger's vector. As a result, the precipitates are sheared by the dislocation cutting and a new region of precipitate matrix interface is produced, which results in an increased inter-facial energy. This contributes towards high strength of the alloy during aging at 550°C for 3h. When the aging temperature is increased to 650°C, the precipitates grow bigger in dimensions. At this point, it is interesting to observe that a hump like feature appears at Q_{peak} = 0.103 nm^{-1} in the SANS data from the 650°C-3h alloy specimen. This indicates inter-particle correlations in the system and gives an estimation of inter-precipitate distance,which is equal to $\frac{2\pi}{Q_{peak}}$.

In 650°C-3h alloy specimen, value of the correlation distance is approximately 61 nm, which is very close to precipitate size determined by SAXS analysis. It can, thus, be argued that the mechanical strengthening in the alloy upon aging at 650°C for 3h is dictated by Orowan's mechanism [264]. According to this mechanism, in case of bigger precipitates with inter-precipitate spacing of the order of their dimensions, it becomes easier for the dislocations to bypass the precipitates by looping around them instead of cutting through them. Further, the stress required to bow a dislocation past the precipitates is relatively less for bigger precipitates with lower volume fraction. Consequently, the hardness of alloy aged at 650°C for 3h is lower than those of aged at 550°C. In addition, since the alloy has M_s above room temperature, mobility of martensite twins under mechanical loading has been shown to affect the mechanical properties of the Ni-Ti alloys [265].

5.5. Summary

In summary, the effect of aging on the phase transformation of $Ni_{50.3}Ti_{29.7}Hf_{20}$ alloy is investigated. Aging at 550°C and 650°C for various durations results in increased phase transformation temperatures. It has been shown that increase in the lattice parameter of B2-phase is caused by Ni-depletion in the matrix due to Ni and Hf-rich H-phase precipitates. Improvement in hardness of the alloy upon aging at 550°C for 3 h is due the formation of dense population of fine precipitates. Lower volume fraction and surface to volume ratio of the precipitates at 650°C indicates coarsening of precipitates. In addition, hardness of the alloy reduces when aged at 650°C for 3 h. This observed reduction is attributed to the dislocation looping around the precipitates, on the basis of Orowan's

mechanism. Evolution of micro-structure of these precipitates with aging adequately explains the observed mechanical behaviour of the alloy. The present investigation is a step towards understanding the correlation between the micro-structure and mechanical strength of the Ni-Ti based HTSMAs,which is of high industrial significance. Further, the peak aging condition for $Ni_{50.3}Ti_{29.7}Hf_{20}$ has been ascertained.

CHAPTER 6

Precipitation Kinetics of H-phase in the $Ni_{50.3}Ti_{29.7}Hf_{20}$ Alloy

Since Ni-rich NiTiHf HTSMAs are H-phase precipitate-strengthened alloys, an optimum size, inter-precipitate spacing and overall volume fraction of these precipitates play a key role in the selection of aging condition for achieving high strength. This makes understanding of the H-phase precipitates growth rates central to the development of Ni-rich NiTiHf HTSMAs, since rapid coarsening of the precipitates can deleteriously affects the alloy strength and hence their functionality. This chapter extends the studies in chapter 5 by elucidating morphological evolution of the H-phase precipitates in the $Ni_{50.3}Ti_{29.7}Hf_{20}$ alloy as function of aging time and temperature. The correlative studies using TEM and *in-situ* SANS analysis enabled the determination of temporal evolution of H-phase precipitate dimensions and volume-fraction, which led to the estimation of activation energies for their growth and coarsening process and establishing mechanism behind the kinetics.

6.1. Introduction

In the previous chapter, it was demonstrated that the alloy strength is a function of interplay between the precipitate dimensions, their volume fraction as well as the inter-particle spacings. Few other authors [47, 222, 266] have also emphasized the effectiveness of the H-phase precipitates in influencing martensitic phase-transformation temperatures and shape memory properties depends upon their size as well as on inter-particle spacing. Evirgen *et al.* [267] have reported that aging the $Ni_{50.3}Ti_{34.7}Hf_{15}$ alloy at 450°C for 10 hours led to the formation of H-phase precipitates with a typical length of 4-7 nm and width of 3-4 nm which exhibited load-biased recoverable strain of 3.3%. However, upon aging the alloy at relatively higher temperature of 550°C for 10 hours, the precipitates grew bigger (10-12 nm long and 7-12 nm wide) and under identical loading conditions, recoverable strain decreased to 2.2%.

In the present work, systemetic evolution of H-phase precipitates with aging teatments is explored by characterizing the evolution of martensitic phase-transformation temperatures, morphology and the volume fraction of H-phase precipitates in $Ni_{50.3}Ti_{29.7}Hf_{20}$ alloy. The H-phase hitherto has been characterized using TEM [199], which primarily provides local information. However, combined usage of electron microscopy along with scattering techniques provides a distinct advantage as far as the quantitative precipitate growth kinetics is concerned. It is re-iterated that SANS is a non-destructive technique, capable of providing statistically averaged bulk sensitive information over a length scale of $\sim$ 1 nm to few hundred nm [268].

In view of the aforementioned comments, a detailed characterization of H-phase precipitates in $Ni_{50.3}Ti_{29.7}Hf_{20}$ alloy as a function of aging temperature and time has been carried out by correlative TEM and SANS experiments. First, TEM is utilized to obtain direct evidence of H-phase precipitation. Next, *in-situ* SANS measurements have been conducted to follow the real-time early-stage growth kinetics. Bulk-scale quantification of H-phase coarsening kinetics by aging the alloy for long durations has been obtained by ex-situ SANS experiments. Present study of H-phase precipitation kinetics, utilizing two complementary techniques, is expected to bring out the growth and coarsening mechanism of H-phase precipitates, which will provide a direction towards tailoring the Ni-rich NiTiHf HTSMAs for technological applications.

6.1.1. John-Mehl-Avrami-Kolmogorov (JMAK) Model

During precipitation reaction, the secondary phase evolves by means of nucleation, growth and finally coarsening (refer Appendix I). For isothermal aging experiments, *i.e.* heat-treating the alloys at a given temperature for certain time duration allows the growth of the precipitate nuclei. This leads to an increase in the precipitate dimensions as well as their volume-fraction. The rate at which the precipitate volume-fraction evolves with aging time or in other words, the *precipitation kinetics* can be modelled in terms of the rates of nucleation and growth of the precipitate phase, which provide a physical insight into the process. One such model is the John-Mehl-Avrami-Kolmogorov (JMAK) model [269–271]. The JMAK model assumes that:

- the reaction proceeds by nucleation and growth,
- the precipitate nucleation occurs randomly throughout the matrix, regardless of its

structure,

- growth occurs isotropically in all directions.

Further, this model takes into consideration the impingement of the growing precipitate particles, which retards and eventually stops the transformation to the β phase, as per the concept of *extended-volume*. If V_α is the real volume fraction of the untransformed phase in the matrix of total volume V, then as per the concept of extended-volume, only those regions will contribute to the volume-fraction, which lie in the previously untransformed region. The, the change in real volume of the α phase dV^α is given as:

$$dV^\alpha = \Big(1 - \frac{V_\alpha}{V}\Big) dV_e^\alpha \tag{6.1}$$

The quantity dV_e^α is the change in extended volume of the matrix and is purely a geometrical factor,which does not account any impingement and $\big(1\text{-}\frac{V_\alpha}{V}\big)$ is the probability of finding an untransformed region in the volume V. For a system with randomly nucleated precipitate particles, the volume fraction of the untransformed α phase matrix is given as:

$$\frac{V_\alpha}{V} = 1 - exp\Big[\frac{V_e^\alpha}{V}\Big] \tag{6.2}$$

In an ξ th order precipitation reaction $\alpha^{'} \rightarrow \alpha + \beta$; the super-saturated $\alpha^{'}$ phase (concentration C_0 at T_1) upon quenching dissociates compositionally into a two-phase field of: β (concentration C_p) and α (concentration C_t after time t such that C_e is the equilibrium composition at T_2)(refer Figure I.1). For such a reaction, the volume fraction f(t) of the untransformed matrix, which is equivalent to the precipitate volume fraction, evolves with time t as:

$$f(t) = \frac{(c_0 - c_t)}{(c_0 - c_e)} = 1 - exp(k_T t^\xi) \tag{6.3}$$

where, C_t is the composition of α phase after time t and k_T is the rate-constant of the reaction. The volume-fraction variation with time typically looks like Figure 6.1. Once the volume-fraction f(t) reaches the value 1.0, growth completely stops and coarsening of the precipitates commences.

The rate-constant k_T is function of nucleation rate and growth rate of the precipitate phase and the quantity ξ is called Avrami exponent. The Avrami exponent is expressed as: $\xi = p \times q + b$. Here, the parameters p, q and b are related to the dimensionality of

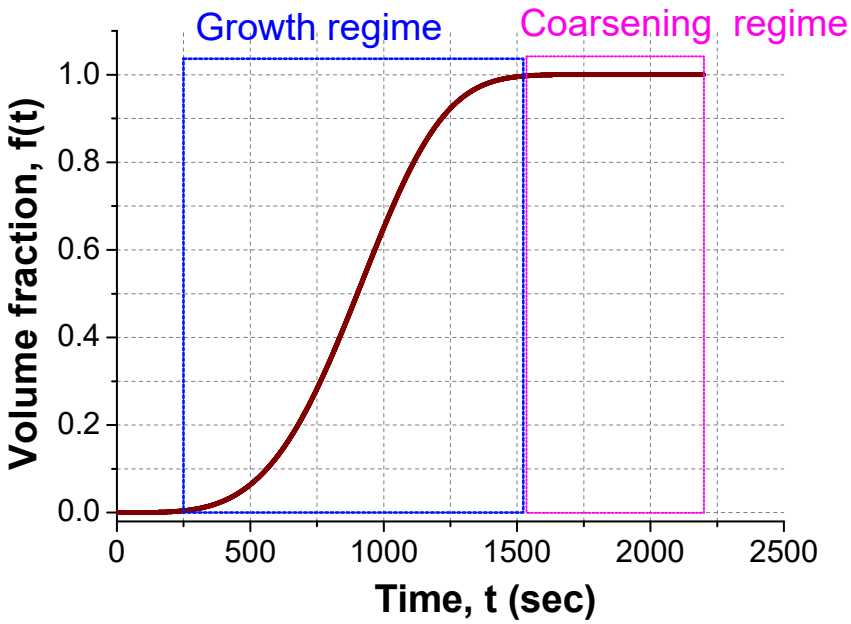

Figure 6.1: Evolution of the precipitate volume-fraction, f(t), with aging time as per eq. 6.3.

the precipitate (p = 1 for 1-D, p = 2 for 2-D and p = 3 for 3-D precipitate), growth-rate of the precipitate (e.g. q = 1/2 for diffusion-controlled parabolic growth) and type of the nucleation (b = 0 for zero nucleation rate, $0 < b < 1$ for diminishing nucleation rate and $b > 1$ for an increasing nucleation rate), respectively.

The JMAK model has been widely employed to determine the precipitation in several alloys systems such as Al-based alloys [272], stainless steels [273], Fe-Cr-Al alloys [274] *etc.*

6.2. Experiments

The hot-rolled as-solutionzed $Ni_{50.3}Ti_{29.7}Hf_{20}$ alloy samples were investigated in as-solutionized as well as aged conditions. The samples were aged isothermally for 3 hours at temperatures ranging from 400°C to 810°C. The role of aging time was investigated by choosing the temperatures 550°C, 600°C and 650°C. The aging conditions selected for the alloy are summarized in Table 6.1. Phase transformation temperatures of the alloy specimens were determined using DSC. Since thermal cycling is known to stabilize martensitic transformation temperatures, two consecutive DSC tests were done at the heating and cooling rate of 10°/min. High temperature XRD data at 350°C was collected for selected samples. Role of aging treatments on the alloy hardness was evaluated using Vickers micro-hardness tests. The *in-situ* SANS experiments at 550°C and 650°C for 13 hours as well as ex-situ

Table 6.1: Isothermal heat treatments carried out on the $Ni_{50.3}Ti_{29.7}Hf_{20}$ alloy.

Aging Temperature, T_{aging}(°C)	Aging time, t (Hours)
550°C	3, 17, 25, 48, 96, 144, 240, 312
600°C	0.5, 3, 8, 16, 24, 48, 72, 96, 144
650°C	0.5, 3, 8, 16, 24, 48, 96, 144

SANS experiments on the samples pre-aged at 550°C, 600°C and 650°C for selected aging durations were conducted at ORNL-HFIR GP-SANS instrument (details described in the section 3.8).

6.3. Results

6.3.1. Phase Transformation Behaviour and Crystal Structure

The martensitic phase-transformation temperatures (henceforth labelled as PTTs) of the as-solutionized samples as well as the samples aged for 3 h at different aging temperatures (T_{aging}) were determined by conducting DSC measurements. The DSC curves for the forward (B2 $\rightarrow$ B19$'$) and reverse (B19$'$ $\rightarrow$ B2) transformations during cooling and heating cycles, respectively are displayed in Figure 6.2 (a).

Appearance of a single DSC peak, both during forward and reverse transformations, irrespective of T_{aging} value, demonstrates a single-stage phase transformation. The peak PTTs for forward and reverse transformation are labelled as M_p and A_p, respectively and tabulated in Table 6.2. The as-solutionized alloy has M_p equal to 177°C and A_p equal to 209°C. Aging of as-solutionized samples appears to shift both M_p and A_p. The variation in the values of M_p and A_p of the samples as a function of aging temperatures has been displayed in Figure 6.2 (b). With increasing aging temperature, both M_p and A_p increase.

Table 6.2: Martensitic phase-transformation temperatures of the $Ni_{50.3}Ti_{29.7}Hf_{20}$ alloy upon isothermal aging for 3 h.

PTTs (°C)		Heat Treatment Temperature (°C)									
	As-solutionized	400	450	500	550	600	650	670	690	750	810
M_p(°C)	177	160	156	178	200	197	198	193	192	174	164
A_p(°C)	209	192	193	207	233	231	237	237	231	208	209

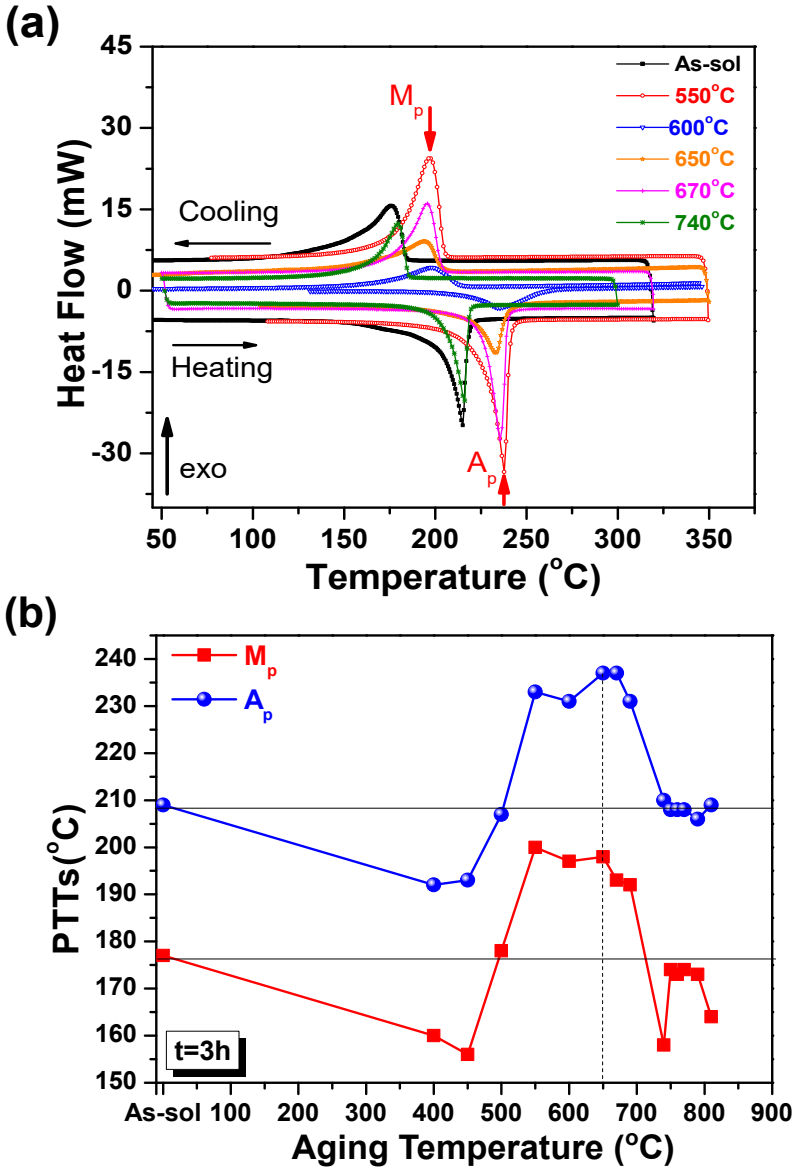

Figure 6.2: (a) DSC plots demonstrating the effect of aging temperature on martensitic phase transformation behaviour in the $Ni_{50.3}Ti_{29.7}Hf_{20}$ alloy aged for 3 h; (b) Variation of values of M_p and A_p of the aged and as-solutionized alloy obtained from (a) are plotted as a function of aging temperature. The maximum values of M_p and A_p are marked as a dotted line.

The maximum values of M_p and A_p reached to 198°C and 237°C respectively, for the sample aged at 650°C (see Table 6.2). The values of M_p and A_p thereafter exhibit a decreasing trend for those samples which were aged at higher temperatures. It is interesting to note that for samples which were aged at 750°C and above, A_p values became nearly constant, equal to that of the as-solutionized alloy. On the other hand, the corresponding values of M_p are lower than that of the as-solutionized alloy.

Considering the fact that aging below 650°C leads to rise in PTTs (M_p and A_p) (marked in Figure 6.2 (b)), samples aged at 550°C, 600°C and 650°C were chosen for

further investigation. It needs to be noted that, in contrast to binary NiTi alloys, where aging results in multiple DSC peaks under certain aging conditions [275, 276], all the samples of $Ni_{50.3}Ti_{29.7}Hf_{20}$ alloy aged at these temperatures have exhibited single-stage martensitic transformations for all the aging durations (presented in Figures 6.3 (a)-(c)). The variation of M_p and A_p as a function of aging time for all the three aging temperatures is shown in Figure 6.3 (d). At all the selected T_{aging} temperatures, M_p and A_p rise sharply for shorter duration and show saturation for longer duration aging. Among all, the samples aged at 550°C exhibited the lowest values of M_p and A_p.

XRD results

In order to determine the effect of aging on the lattice parameters of the austenite phase, XRD diffraction patteren were collected for the as-solutionized samples as well as the samples aged at 550°C for 144 h, aged at 600°C for 96 h, 650°C for 48 h and 740°C for 3 h. The Le Bail fitted profiles for the selected samples have been depicted in Figures 6.4 (a)-(c). It could be observed that the B2 austenite phase (S.G. No. 221: $Pm\overline{3}m$) in all these alloy samples is stable at 350°C and co-exists with another phase identified as the H-phase (S.G. No. 70: F d/2 d/2 d/2). Due to the lower symmetry, a large number of peaks pertaining to the H-phase appeared. Some of these peaks overlapped with each other as well as with the peaks of the B2-phase. The inset of Figure 6.4 (b) shows an expanded view of the broad peak corresponding to several overlapped (hkl) peaks of the H-phase. The refined lattice parameters of the B2-phase for the as-solutionized, 550°C-144 h, 600°C-96 h, 650°C-48 h and 740°C-3 h alloy samples were determined to be: 3.0799±0.0002Å , 3.0834±0.0001Å , 3.0881±0.0001Å , 3.0937±0.0002Å , 3.0861±0.0002Å , respectively. The trend in variation of lattice parameters with aging temperature is presented in Figure 6.4 (d).

The lattice mismatch between precipitates and B2-matrix, determined as for the 550°C-144 h, 600°C-96 h, 650°C-48 h alloys are 2.5%, 2.3% and 2.1% respectively, indicating that although precipitates are still coherent with the matrix [199], contribution of strain energy is decreasing, indicating coarsening. The lattice parameters show an increasing trend with aging temperature up to 650°C and subsequently decrease with aging at 740°C in a similar manner as PTTs. Since increase in B2-lattice parameter is indicative of Ni-depletion from matrix in the Ni-Ti alloys, smaller value of B2-lattice parameter in

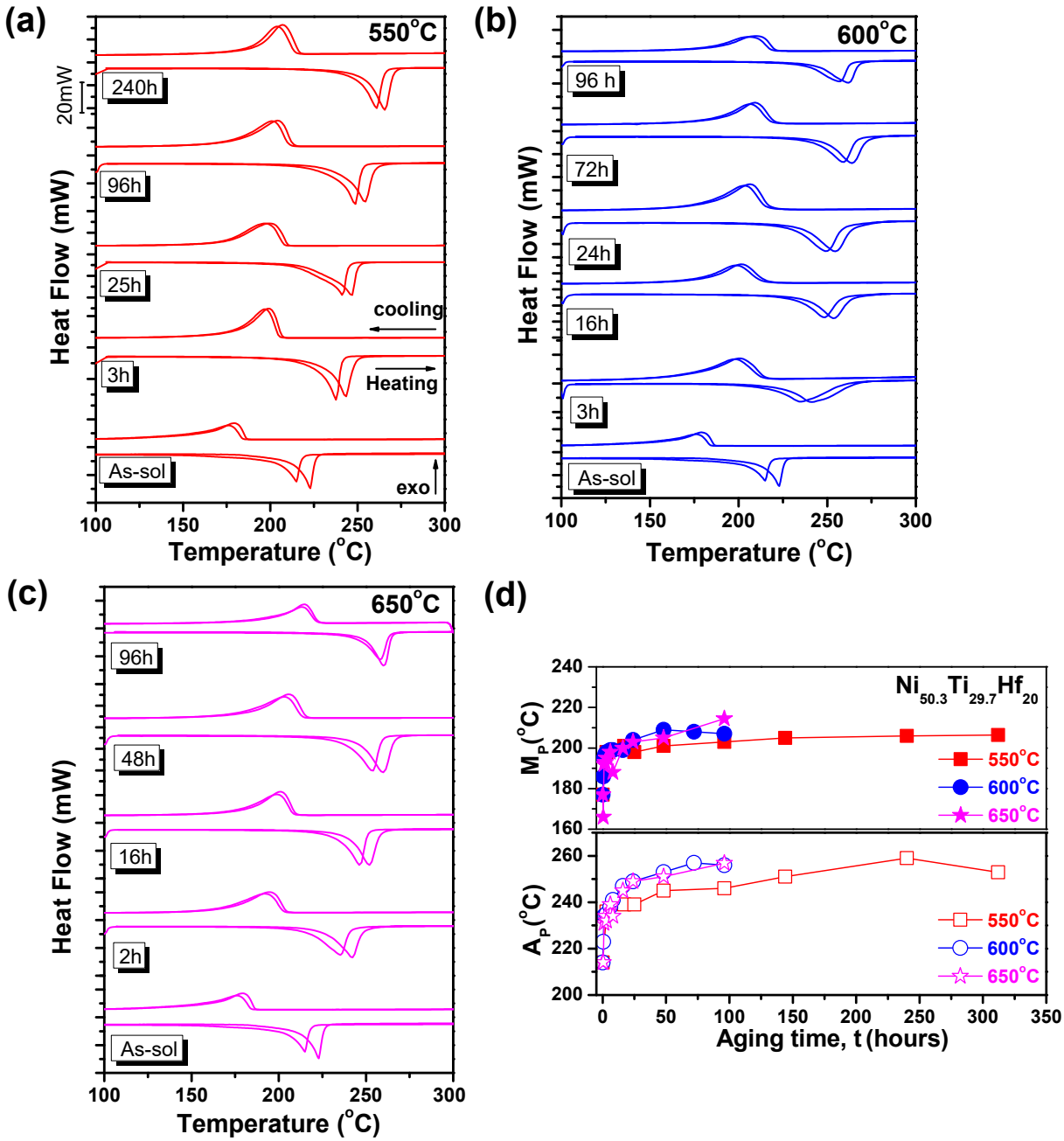

Figure 6.3: DSC curves for the samples aged at (a) 550°C, (b) 600°C and (c) 650°C for various aging durations, (d) dependence of M_p and A_p on aging time for samples aged at 550°C, 600°C and 650°C.

case of aging at 550°C for such a long aging duration in comparison to those of aged at 600°C and 650°C for relatively shorter aging time substantiates the lower Ni-depletion rate during aging at 550°C.

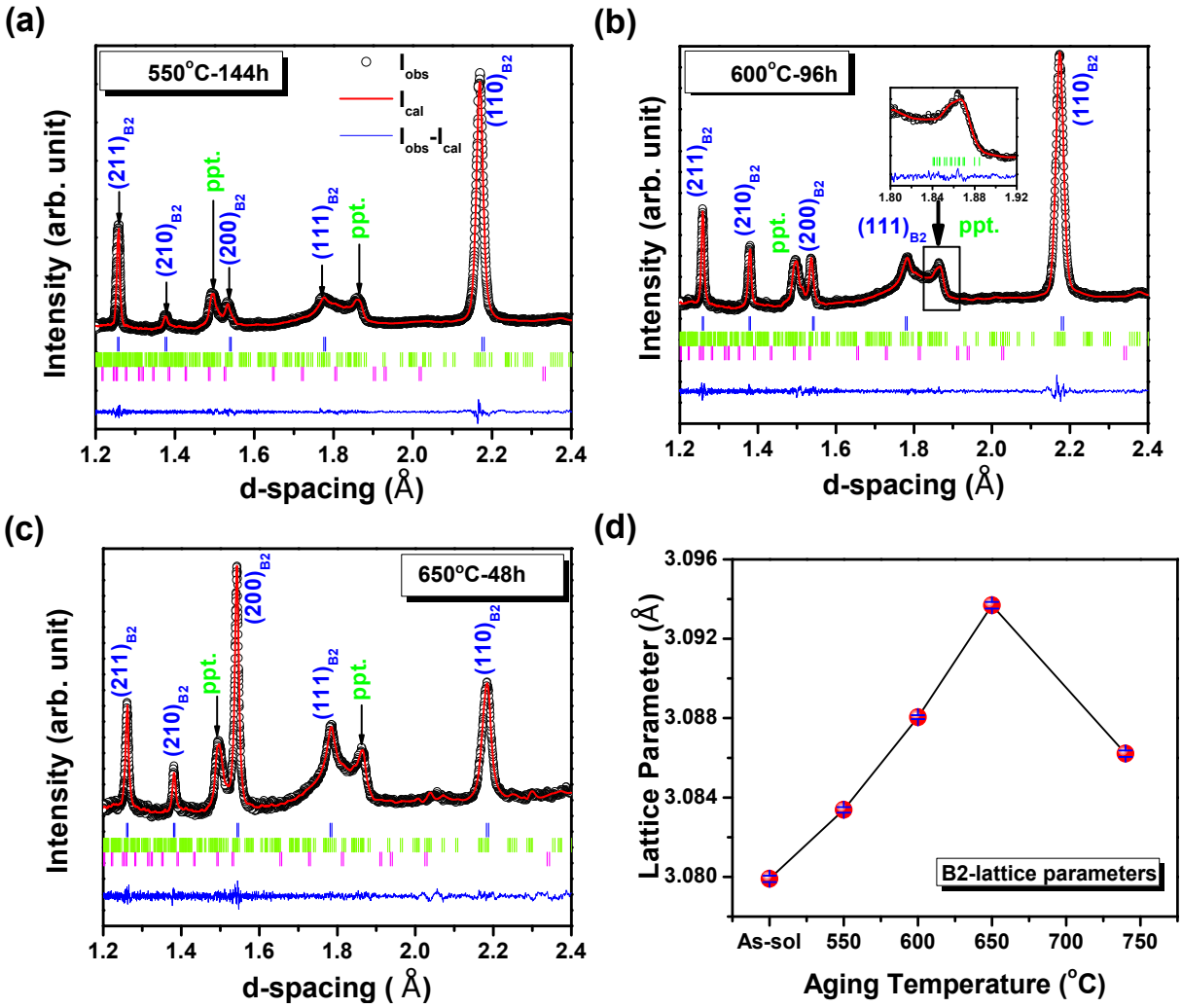

Figure 6.4: High temperature X-ray diffraction patterns obtained at 350°C for the $Ni_{50.3}Ti_{29.7}Hf_{20}$ alloy aged at (a) 550°C for 144 h, (b) 600°C for 96 h and (c) 650°C for 48 h. The H-phase (space group: F d/2 d/2 d/2) co-exists with austenite B2 structure (space group: $Pm\bar{3}m$). (d) Lattice parameter variation of B2 austenite with aging temperature.

6.3.2. Mechanical Properties

Figure 6.5 presents the room temperature micro-hardness evolution of the alloy at the aging temperature, T_{aging} = 550°C, 600°C and 650°C for different aging durations.

Significant effect of aging-induced precipitate strengthening is observed on the hardness as a function of aging time for all the three temperatures. As shown in the previous chapter, H-phase precipitate size, volume fraction and number density play decisive role in the progression of hardness with aging time [228]. Thus, the rate at which this peak hardness is attained is an indicative of the kinetics of the precipitation in an alloy system. The as-solutionized alloy exhibited the hardness of 428 VHN. Upon aging, the hardness of samples increased initially, reached a maximum value and subsequently decreased. In

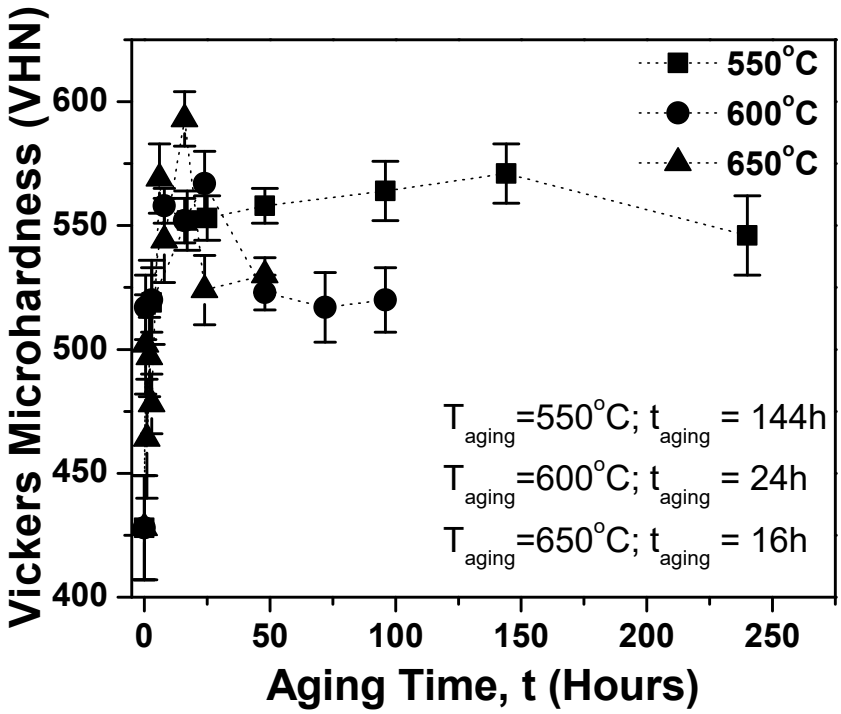

Figure 6.5: Vickers micro-hardness evolution of the $Ni_{50.3}Ti_{29.7}Hf_{20}$ alloy with aging time for samples aged at 550°C, 600°C and 650°C. The peak hardness is achieved in 144 h, 24 h and 16 h at 550°C, 600°C and 650°C, respectively.

samples aged at 550°C, peak hardness was obtained after 144h of aging, while upon aging at 600°C and 650°C; it took 24 h and 16 h, respectively to attain the peak value. The peak hardness values corresponding to the samples aged at 550°C, 600°C and 650°C are: 571±12 VHN, 567±13 VHN and 593±11 VHN, respectively. Further, the decrease in time taken to reach peak hardness (144 h, 24 h and 16 h) suggests that the precipitation kinetics in case of the alloy aged at 550°C is considerably sluggish in comparison to that of aged at 600°C and 650°C.

6.3.3. Micro-structural Investigations

TEM investigations of all those samples subjected to XRD analysis were carried out to directly observe the presence of H-phase precipitates, their morphology as well as the dimensions. Figures 6.6 (a)-(c) present the micro-structures of samples aged at 550°C, 600°C and 650°C for 144 h, 96 h and 48 h, respectively.

The precipitate aspect-ratio (length : thickness ratio) distribution for all the samples, determined using image analysis, has been presented in Figures 6.6 (e)-(f). Dense population of ellipsoid precipitates with an average thickness of 15-20 nm and length of 30-45

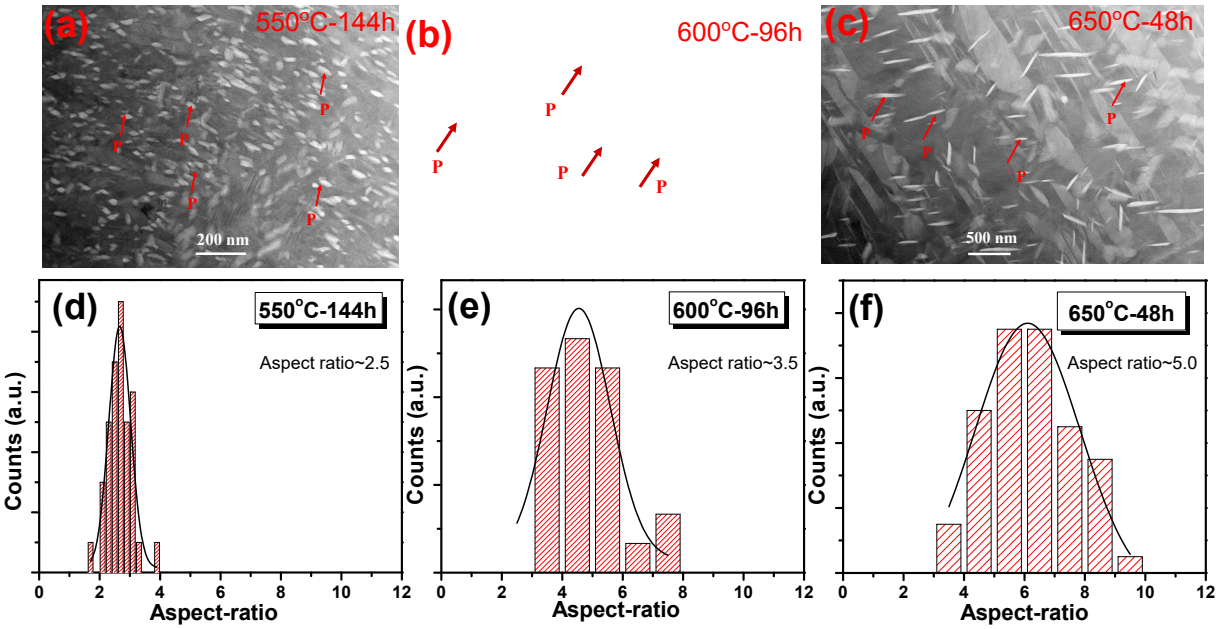

Figure 6.6: TEM micrographs of the alloy samples aged at (a) 550°C for 144 h, (b) 600°C for 96 h and (c) 650°C for 48 h. The precipitate aspect-ratio (length:thickness ratio) distribution profiles determined by image analysis for sample aged at (d) 550°C for 144 h, (e) 600°C for 96 h and (f) 650°C for 48 h, respectively.

nm were observed in specimen aged at 550°C for 144 h (Figure 6.6 (a)). Typical aspect-ratio was determined as $\sim$ 2.5, (Figure 6.6 (d)). Prolonged aging at 600°C for 96 h and at 650°C for 48 h, led to a micro-structure with lower number-density of precipitates, increased inter-precipitate spacing and changing morphology to spindle-like shape with larger aspect-ratios. The average precipitate thickness and length for 600°C-96 h aged alloy are 25-30 nm and 100-125 nm, respectively (shown in Figure 6.6 (b)). The aspect-ratio of the precipitates under these conditions is determined to be $\sim$3.5, as evident from Figure 6.6 (e). The TEM micrographs corresponding to the alloy aged at 650°C for 48 h (shown in Figure 6.6 (c)) exhibited precipitates with a typical thickness of 45-50 nm and length in the range 180-250 nm. Clearly, the precipitate aspect-ratio increased considerably to nearly 5.0 (exhibited in Figure 6.6 (f)). The morphological information of the precipitates obtained from TEM at these aging conditions has been utilized in the SANS data analysis.

6.3.4. SANS Investigations

SANS experiments were carried out in two modes: *in-situ* and ex-situ experiments. The *in-situ* measurements were conducted to probe the aging behaviour for shorter durations

while the samples aged a-priori for longer aging periods were examined in the ex-situ set-up.

In-situ SANS

The real-time *in-situ* SANS profiles at T_{aging} = 550°C and 650°C are presented in Figures 6.7 (a) and (b), respectively. The *in-situ* SANS data was collected up to time, t = 800 min (13 h). The scattering contributions from the grain boundaries and dislocations present in the sample were removed from the SANS profiles by subtracting the scattering profile of as-solutionized sample at t = 0 from those obtained upto t = 800 min. It can be observed from Figure 6.7 (a) that functionality of scattered intensity, I(Q), modifies with time representing growth of the precipitates. In order to obtain the micro-structural parameters related to the precipitate phase, the SANS profiles were analysed in terms of structural models taking into account the morphology observed under TEM. The TEM observations revealed that in the present case, precipitates possess ellipsoid shape with their half-axes defined as r, r, νr; where r is the semi-minor axis and νr is the semi-major axis of the precipitates, ν being the aspect-ratio. The aspect-ratio of ellipsoid precipitates during the early stage of aging were estimated to be $\sim$ 2.3 and 3.5 at 550°C and 650°C, in agreement with values reported in the literature [225, 228]. The intensity I(Q) for the ensemble of poly-disperse ellipsoid particles under is described according to Appendix eq II.7 (see section Appendix II.0.2). The form-factor P(Q, ν, r) for the ellipsoid precipitates averaged over all possible orientations is taken as describe in section Appendix 5.3.4. The evolution of the size-distribution D(r) of the precipitates with aging time was estimated and and the Guinier radius R_G of the precipitates was calculated using Appendix eq. II.12.

Since the H-phase precipitates possess non-spherical morphology, R_G is considered as the effective characteristic precipitate radius in the current analysis. Figure 6.8 (a) shows the time evolution of R_G at 550°C and 650°C. The precipitate radius (R_G) evolution with time is governed by the following power-law:

$$\boxed{R_G^{\alpha}(t) - R_G^{\alpha}(0) = kt} \tag{6.4}$$

Here, R_G (t) and R_G (0) are sizes of the precipitate at time t and at beginning of growth (at t = 0). Power-law exponent, 'α', indicates the precipitate growth rate and 'k' is

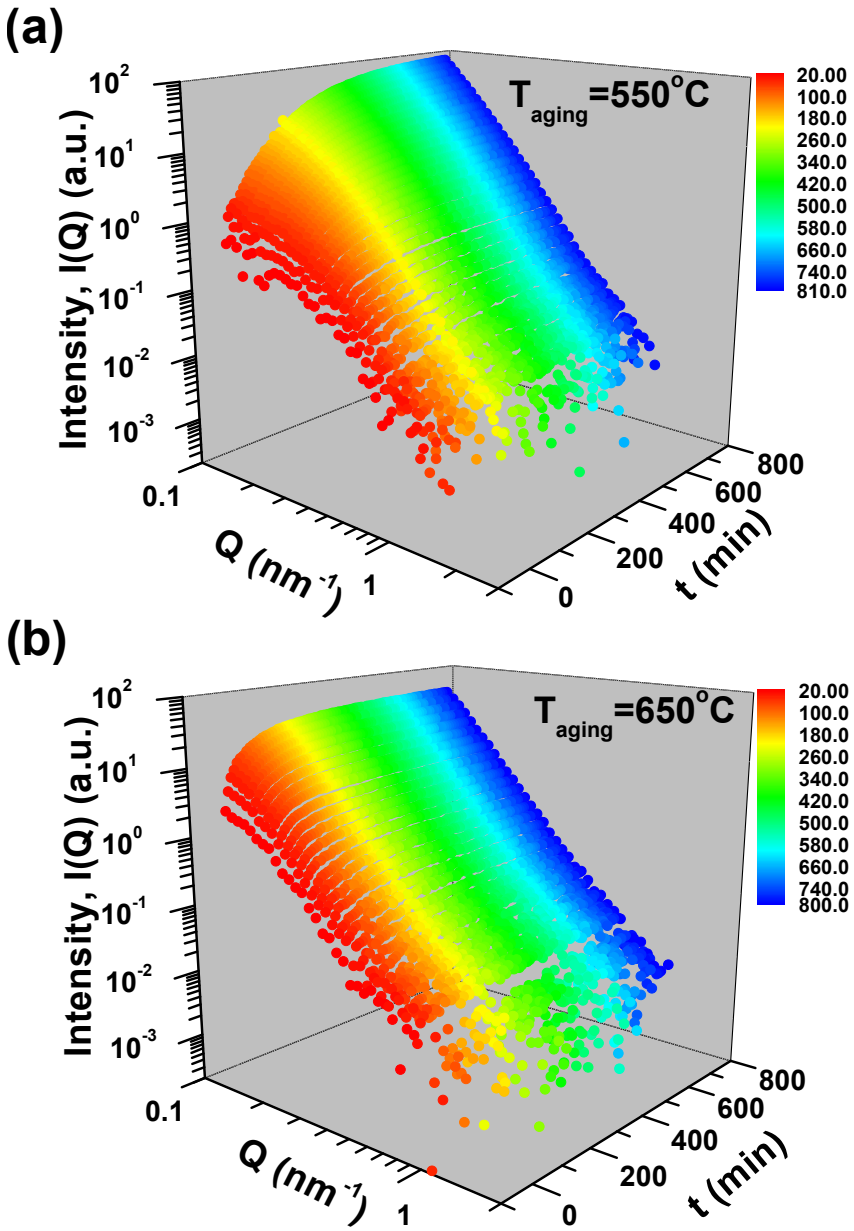

Figure 6.7: The *in-situ* SANS profiles corresponding to the alloy aged at (a) 550°C and (b) 650°C for initial 800 min (13 h).

growth rate-constant. Assuming that in the present case nucleation is already over; the precipitates grow from $R_G \sim 8$ nm - 24 nm during aging at 550°C up to 13 h, whereas in case of aging at 650°C, the R_G increases from $\sim$ 13 nm to 24 nm upon aging up to 13 h. The power-law exponent α for aging temperatures 550°C and 650°C has been obtained by fitting the R_G *vs.* t plot and is exhibited in Figure 6.8 (a). The α-values corresponding to rate-law at 550°C and 650°C are 0.48±0.01 and 0.18±0.01, respectively. Thus, the growth rate at 550°C follows a power-law $\sim t^{\frac{1}{2}}$, while at 650°C, it follows the power-law $\sim t^{\frac{1}{6}}$ functionality. The precipitate volume fraction (ϕ) can be estimated by calculating

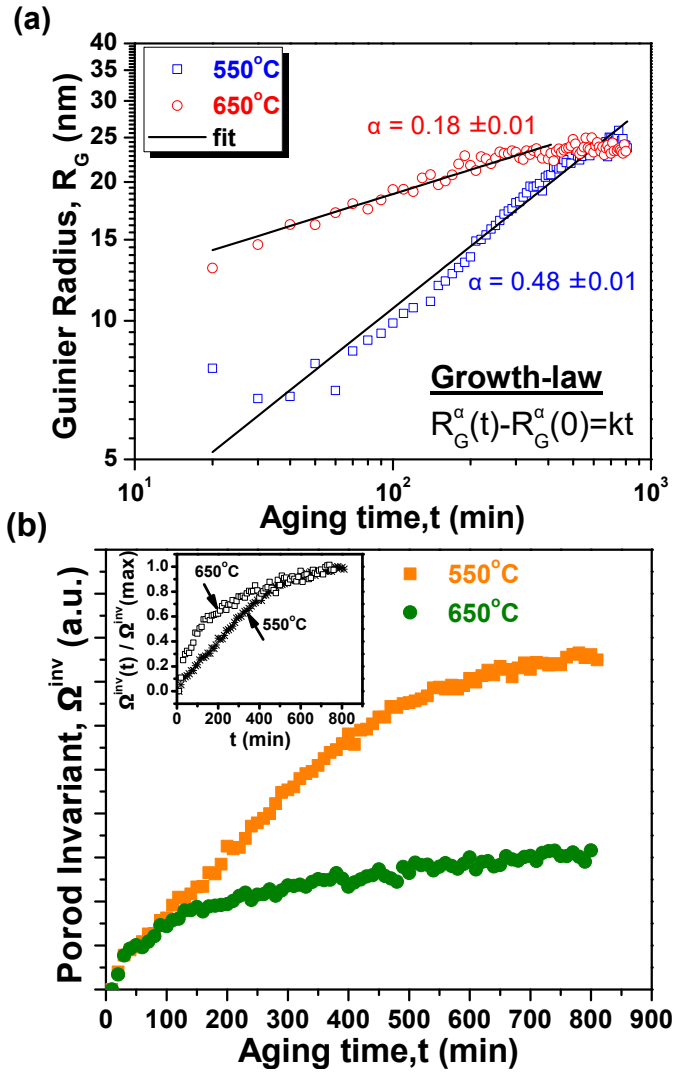

Figure 6.8: (a) Guinier radius (R_G) evolution of the precipitates with aging time during aging at 550°C and 650°C; power-law fitting of the precipitate radius yields the growth law exponent corresponding to both the temperatures; (b) Porod Invariant (Ω^{inv}) evolution with aging time for samples aged at 550°C and 650°C. Inset in (b) shows volume-fraction (ϕ^*(t)) transformed as a function of aging time.

the Porod's Invariant (Ω^{inv}) which is defined as:

$$\boxed{\Omega^{inv} = \int_{Q_{min}}^{Q_{max}} I(Q)Q^2 dQ = 2\pi^2(\Delta\rho)^2\phi(1-\phi)} \tag{6.5}$$

Figure 6.8 (b) displays the time evolution of Porod's Invariant Ω^{inv} for aging temperatures 550°C and 650°C. It can be seen that Ω^{inv} for 550°C aged specimen increases steadily, while for 650°C aged alloy, after an initial increase up to nearly 300 min (5 h), the values tend to saturate. The progression of normalized precipitate volume fraction ($\frac{\phi(t)}{\phi(max)} = \phi^*(t)$) with aging duration is depicted in the inset of Figure 6.8 (b).

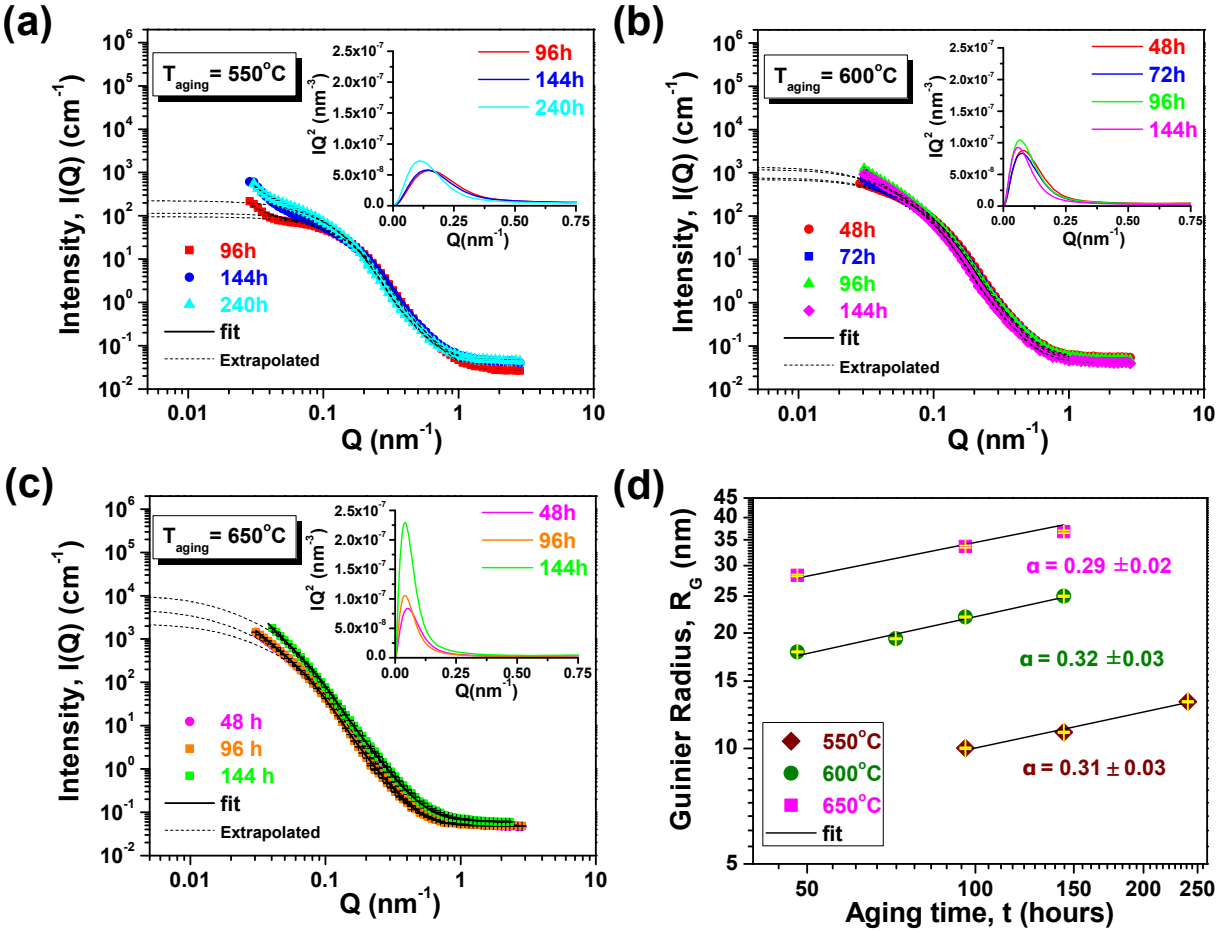

Figure 6.9: Ex-situ SANS profiles for the alloy aged for longer aging times at (a) 550°C, (b) 600°C, (c) 650°C. Inset of all the plots shows the IQ^2 vs. Q plots correspond to each aging time; (d) plot exhibiting least-square fit $R_G(t)$ vs. t obtained from ex-situ SANS data for all the aging conditions. Slopes of the linear fits provide growth-rate exponents at each temperature.

Ex-situ SANS

Ex-situ SANS study was carried out for the samples aged at 550°C, 600°C and 650°C for longer aging periods for which specimens have already achieved the peak micro-hardness. Plots comparing the scattered intensities for the samples aged at 550°C for 96 h, 144 h and 240 h; at 600°C for 48 h, 72 h, 96 h and 144 h and at 650°C for 48 h, 96 h and 144 h have been displayed in Figures 6.9 (a)-(c), respectively. The modelled scattered intensities agree well with the experimental SANS profiles. The thickness and length values of the ellipsoid precipitates obtained by the model dependent fitting and Guinier radii of the precipitates at all aging conditions are listed in Table 6.3. Evidently, the precipitate dimensions obtained by SANS analysis agree quite well with the TEM observations. The growth rates of precipitates in accordance with equation 6.4 during long aging time at all three aging temperatures have been determined by least-squares fitting of the $R_G(t)$ vs.

t plot. The plot displaying the growth exponents is depicted in Figure 6.9 (d). It can be noticed that the growth rate exponents (α) are 0.31±0.04 at 550°C, 0.32±0.03 at 600°C and 0.29±0.02 at 650°C, revealing that the precipitate dimensions grow with time as $\sim t^{\frac{1}{3}}$.

The inset of Figures 6.9 (a)-(c) shows IQ^2 vs. Q plots corresponding to aging at 550°C, 600°C and 650°C for varying aging durations. The contrast term $(\Delta\rho)^2$, which is scattering length density difference between precipitate and matrix in accordance with Appendix eq. II.8. The atomic volume of the matrix phase has been determined from the lattice parameters of the B2-phase for the aged samples, which were estimated from the XRD data presented in the Figure 6.4 (d). The precipitate volume fractions for different aging conditions have been obtained by evaluating the Porod Invariant (Ω^{inv}) for the extrapolated data and are listed in Table 6.4. Low volume fraction of the precipitate phase indicates that precipitate concentration can be considered as sufficiently dilute.

6.4. Discussion

We now discuss the correlation of phase transformation behaviour as a function of aging conditions with the precipitation kinetics of the H-phase in the $Ni_{50.3}Ti_{29.7}Hf_{20}$ alloy.

One noticeable feature which could be observed from Figure 6.3 (a), (b) and (c), is that all the samples exhibit single-stage martensitic transformation during forward as well as reverse transformation. Khallil-Allafi *et al.* [163, 170] and Fan *et al.* [277] in their work on multi-stage transformations in aged Ni-rich NiTi alloy, reasoned that large-scale inhomogeneties such as heterogeneous precipitation of Ni_4Ti_3 precipitates along grain boundaries give rise to multi-stage martensitic transformation. However, Michutta *et al.* [278] argued that multi-stage transformation can occur even in aged Ni-rich NiTi single crystals, with an inter-particle spacing of Ni_4Ti_3 precipitates is more than the critical value of 200 nm. Based on TEM evidence, they suggested that transformation sequence is B2-R (Peak 1) $\rightarrow$ R-B19$'$ (Peak 2 for regions near precipitate/matrix interface experiencing coherency strains) $\rightarrow$ R-B19$'$ (Peak 3 for regions away from precipitate/matrix interface not experiencing coherency strains).

In the present case, an absence of two-stage transformation at all the aging conditions suggests that R-phase does not appear during transformation and hence the role of coherency stresses as well as inter-precipitate spacing on R-B19$'$ transformation (which leads

Table 6.3: The precipitate dimensions obtained by model dependent fitting and Guinier analysis ex-situ SANS data corresponding to the $Ni_{50.3}Ti_{29.7}Hf_{20}$ alloy aged at 550°C, 600°C and 650°C for various aging times.

Precipitate dimensions during aging at 550°C, 600°C and 650°C for different aging durations determined by SANS analysis											
550°C				**600°C**				**650°C**			
Aging time (hours)	R_G (nm)	Length (nm)	Thickness (nm)	**Aging time (hours)**	R_G (nm)	Length (nm)	Thickness (nm)	**Aging time (hours)**	R_G (nm)	Length (nm)	Thickness (nm)
96 h	10.02±0.05	44.6±0.14	17.84±0.05	**48 h**	17.86±0.06	88.28±0.14	25.08±0.04	**48 h**	28.26±0.17	172.7±0.43	34.54±0.09
144 h	11.02±0.05	46.6±0.11	18.64±0.04	**72 h**	19.33±0.07	92.65±0.16	26.32±0.05	**96 h**	33.62±0.24	201.3±0.58	40.26±0.12
240 h	13.24±0.06	51.7±0.12	20.68±0.05	**96 h**	22.03±0.09	97.29±0.19	27.64±0.05	**144 h**	36.74±0.29	215.6±0.15	43.12±0.06
				144 h	24.94±0.12	109.05±0.24	30.98±0.07				

Table 6.4: Volume fraction of the precipitates obtained from analysis of ex-situ SANS data for the $Ni_{50.3}Ti_{29.7}Hf_{20}$ alloy aged at 550°C, 600°C and 650°C for various aging times.

Volume fraction of the precipitates during aging at 550°C, 600°C and 650°C for different aging durations determined by SANS					
550°C		**600°C**		**650°C**	
Aging time (hours)	Volume fraction (%)	**Aging time (hours)**	Volume fraction (%)	**Aging time (hours)**	Volume fraction (%)
96 h	2.29 ± 0.63 %	**48 h**	2.31 ± 0.65 %	**48 h**	1.59 ± 0.63 %
144 h	2.28 ± 1.05 %	**72 h**	2.05 ± 0.80 %	**96 h**	1.68 ± 0.64 %
240 h	2.34 ± 0.85 %	**96 h**	2.37 ± 0.71 %	**144 h**	3.33 ± 0.84 %
		144 h	1.89 ± 0.75 %		

to multiple DSC peaks) can be ruled out. Further, single-stage DSC curves imply that even large-scale inhomogeneties are also absent and H-phase precipitates nucleate homogeneously throughout the matrix. It is relevant to point out here that, Moshref-Javadi *et al.* [279] showed that multi-stage martensite transformation occurs in the $Ni_{50.3}Ti_{34.7}Hf_{15}$ alloy as a result of combined consequences of the appearance of R-phase as well as heterogeneous precipitation of $Ni_4(Ti,Hf)_3$ precipitates. However, Evirgen *et al.* [267] in their work on phase transformations in the same alloy reported the absence of both R-phase as well as the multi-stage martensitic transformation from their DSC experiments. Another feature which could be noticed from Figure 6.3 (d) is that aging samples at the three temperatures (550°C, 600°C and 650°C) lead to increase PTTs (M_p and A_p). Two evidences in support of the linkage between rising PTTs with the precipitation of the H-phase can be provided:

- The values of M_p and A_p increase with the increase in the volume-fraction of the H-phase (compare Figure 6.3 (d) with Figure 6.8 (b)).
- The values of M_p and A_p increase rapidly in the initial stages and tend to saturate when the volume fraction of the H-phase becomes constant for the long duration of aging.

The compositional analysis of H-phase precipiates and the matrix in this alloy depletes the matrix phase in Ni and Hf concentration (refer chapter 5.3)and raises the transformation temperatures. On the contrary, NiTiHf alloys with low Hf content exhibit low values of transformation temperatures, as shown in chapter 4. Considering the opposite roles of Ni and Hf concentrations in the NiTiHf alloys, rise in the martensitic phase-transformation temperatures with aging time for relatively smaller durations suggests the governing role of Ni-depletion. During shorter aging times, volume fraction of the H-phase increases rapidly, leading to the depletion of Ni from the matrix, consequently the PTTs values increase with the duration of aging. However, during prolonged aging, the H-phase undergoes coarsening (Figure 6.9 (d)) and during this period the volume-fraction of the H-phase tends to stabilize. At this stage, the driving force *i.e.* Ni-depletion, which is required to raise the PTTs, reduces drastically and they exhibit saturation.
This suggests that the variation in PTTs as a function of aging conditions is a strong indicator of the kinetics of the H-phase precipitation in the ternary Ni-rich NiTiHf alloys.

It needs to be mentioned here that, although the trend of M_p and A_p as a function of aging duration is alike at all three aging temperatures, the values of M_p and A_p are lowest for the samples aged at 550°C at all the aging durations. This, in turn, suggests that the kinetics of precipitation is slowest at 550°C. This aspect is dealt at detail in the following sections where the kinetics of H-phase precipitation in the $Ni_{50.3}Ti_{29.7}Hf_{20}$ alloy has been estimated quantitatively.

6.4.1. Early-stage Growth Kinetics of H-phase

As mentioned earlier, during early stages of aging (up to 13 h) the precipitates follow two separate growth laws; $\sim t^{\frac{1}{2}}$ at 550°C and $\sim t^{\frac{1}{2}}$ at 650°C, indicating different growth mechanisms are operating at these temperatures (Figure 6.8 (a)). Classical theory of diffusion-controlled precipitation suggests that during early stages of growth, the dimensions of homogeneously nucleated precipitates follow $\sim t^{\frac{1}{2}}$ growth law [280], which during early stage of coarsening regime gradually changes to $\sim t^{\frac{1}{6}}$ growth law [281].

Early-stage growth kinetics of isothermal precipitation occurring homogeneously in the matrix can be described by JMAK kinetic model (refer subsection 6.1.1). Here, the growth rate-constant k_T is the temperature-dependent factor governed by the Arrhenius type relation, $k_T = k_0\ exp(-\frac{E_a}{RT})$, ($k_0$ is rate constant, E_a is the activation energy associated with the growth process in $Jmol^{-1}$ and $R = 8.314\ Jmol^{-1}K^{-1}$).

The Avrami exponent ξ was obtained from the slope of JMAK plot $ln(ln(\frac{1}{(1-\phi^*(t))}))$ *vs.* $ln(t)$. This plot, corresponding to aging temperatures of 550°C and 650°C, is displayed in Figure 6.10 (r^2_{fit} is the adjusted-R squares of the fit, indicating coefficient of correlation [282]). The values of the kinetic parameters, $\ln(k_T)$ and ξ, were extracted by carrying out linear least-squares fitting, providing the nature of the kinetics. From these experiments, we obtain $\xi = 1.24 \pm 0.02$ for aging at 550°C, which is close to the ideal case of the reaction in which a 3-dimensional precipitate undergoes diffusion-controlled parabolic growth with zero nucleation rate (for which $\xi = 1.5$ [283]).

However, in samples aged at 650°C, deviation from the diffusion-controlled parabolic growth was observed ($\xi = 0.76 \pm 0.02$). The low value of ξ has been attributed to the early coarsening [284] and therefore, this deviation could be due to rapid coarsening of the precipitates. Since the coefficient follows an Arrhenius relationship with temperature, the activation energy estimated from the plot of $\ln(k_T)$ vs. $(\frac{1}{T_{aging}})$ is equal to 196

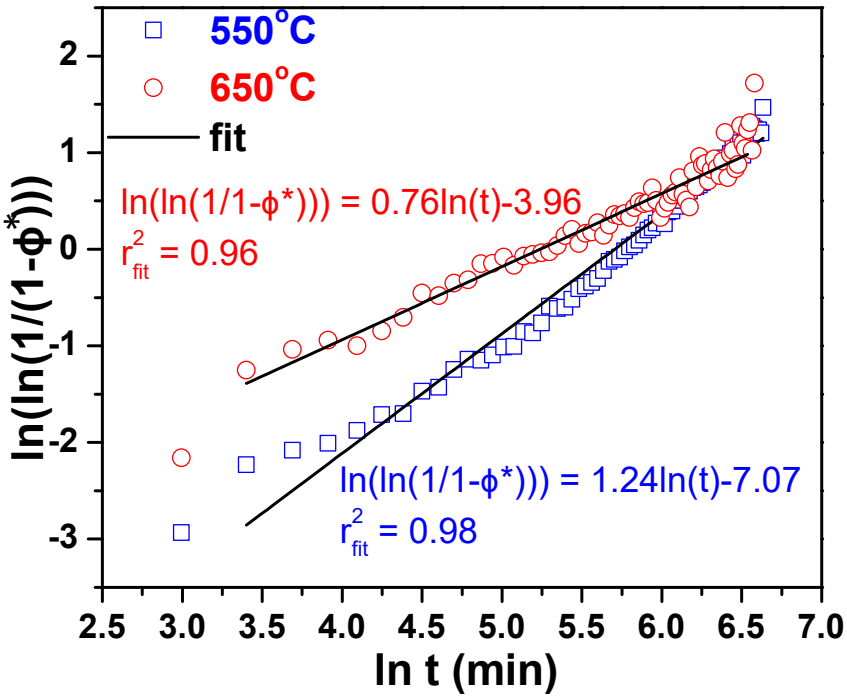

Figure 6.10: Least-squares linear fit of $\ln(\ln(\frac{1}{(1-\phi^*(t))}))$ vs. ln(t) *i.e.* the JMAK plot for aging temperatures 550°C and 650°C. The r^2_{fit} depicts the goodness of fit.

kJmol^{-1}. This value of activation energy is slightly higher than the activation energy required for the diffusion of Ni in NiTi $\sim$ 155 kJmol^{-1} [285, 286]. This implies that though Ni-diffusion in the matrix governs H-phase growth kinetics during early-stages of growth process, diffusion of other elements is also important.

6.4.2. H-phase Coarsening Kinetics

The $t^{\frac{1}{3}}$ dependence of precipitate dimensions upon long aging durations suggest coarsening of the precipitates can be addressed in terms of Lifshitz-Slyozov-Wagner (LSW) model [287]. It needs to be mentioned that the LSW model has quite successfully explained coarsening of the precipitates in several alloy systems [288, 289]. According to LSW theory of coarsening, micro-structure with dilute concentration of spherical precipitates with mean radius undergoes diffusion-controlled volume increase at the expense of smaller precipitates according to following equation:

$$\boxed{R_G^3(t) - R_G^3(0) = K_C t = \frac{8\Gamma V_m C_\infty D_0}{9RT_{aging}} \exp\Big(-\frac{E_{coarsening}}{RT_{aging}}\Big)t} \tag{6.6}$$

Here, K_C is the coarsening rate-constant, which is basically determined by:

Γ = precipitate-matrix specific interfacial energy,

Table 6.5: The experimentally determined coarsening rate constants for the $Ni_{50.3}Ti_{29.7}Hf_{20}$ alloy, along with coefficients of determination corresponding to aging at 550°C, 600°C and 650°C, in conformity with LSW model.

T_{aging}(°C)	Rate constant, K_C ($nm^{-3}s^{-1}$)	Coefficient of determination, r^2_{fit}
550	0.0026	0.985
600	0.0294	0.983
650	0.1023	0.994

V_m = molar volume of the precipitate,

C_∞ = the solid-solubility of solute in matrix,

T_{aging} = aging temperature (in Kelvin),

D_0 = Diffusion-coefficient of solute in the alloy at T_{aging},

$E_{coarsening}$= Activation energy for coarsening of precipitates in the alloy.

In the calculations, R_G was taken as the characteristic length scale of the precipitates. Figure 6.11 (a) shows the R^3_G vs t plot for all the samples aged at 550°C, 600°C and 650°C. The plot shows a linear relationship between R^3_G and t corresponding to aging at 550°C, 600°C and 650°C, with their slopes providing the coarsening rate-constants for each temperature. The K_C values obtained from the linear least-squares fit of the data along with the coefficient of correlation (r^2_{fit}) are listed in Table 6.5. It may be noted from these values of K_C that coarsening rate-constants at 600°C and 650°C are almost 11 times and 39 times that of coarsening rate-constants at 550°C, respectively. The primary cause for this increase in K_C is the higher diffusivity of the solute with increasing temperatures [290, 291].

In the kinetics of the coarsening process, the rate-limiting factor depends on the product of solid-solubility limit of a solute in matrix and its diffusivity. There are few experimental reports on the diffusion of Hf in Ni [290, 292] and Ti [291, 293] available in literature. Assuming linear variation in the solid-solubility of solute with temperature in the range 550°C-650°C *i.e.* $\frac{C_\infty}{T_{aging}}$ remains constant in equation 6.6; the activation energy for the coarsening process, $E_{coarsening}$, can be estimated from the slope of $\ln(K_C)$ vs $\frac{1}{T_{aging}}$ plot, as shown in Figure 6.11 (b). For the present alloy, this value was estimated as equal to 233±35 $kJmol^{-1}$. This value lies in the range ∼ 250-280 $kJmol^{-1}$, which represents the activation energy for diffusion of Hf in Ti between 550°C and 750°C (823K

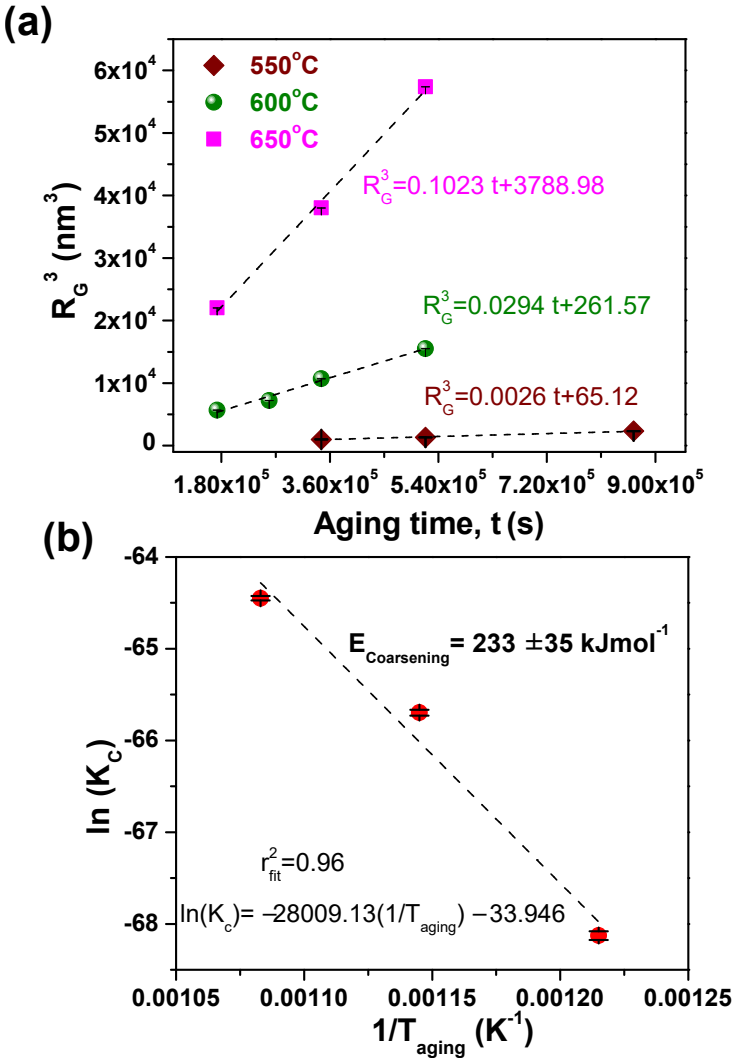

Figure 6.11: (a) Plot of R_G^3(t) vs. aging time (t) at 550°C, 600°C and 650°C. The slopes of least-squares fitted straight line provide the coarsening rate constants (K_C) for each aging temperature, (b) Least-square fit of ln(K_C) vs $\frac{1}{T_{aging}}$ plot derived from (a) provides activation energy for coarsening in the $Ni_{50.3}Ti_{29.7}Hf_{20}$ alloy.

- 1023K) [291, 293] as well as the activation energy for diffusion of Hf in Ni (251 kJmol^{-1}) in the temperature range 750°C-1150°C (1023K - 1423K) [290, 292]. This suggests that coarsening process in Ni-rich NiTiHf alloys is majorly governed by Hf-diffusion in the matrix.

6.4.3. Comparison with Ni_4Ti_3 Precipitates

At this juncture it is pertinent to ask the question that what is the effect of Hf on the precipitation kinetics of precipitate phases in NiTi based SMAs?

To answer this, the coarsening kinetics of Ni_4Ti_3 precipitates in binary NiTi alloys was compared with the H-phase precipitates in ternary $Ni_{50.3}Ti_{29.7}Hf_{20}$ alloy. Using the

data available in literature (listed in Table 6.6) the coarsening rate-constant for Ni_4Ti_3 precipitates at 560°C is analytically estimated by substituting these values in equation 6.6. Upon comparison, it was deduced that the H-phase coarsening rate-constant is nearly 8 times smaller than that of Ni_4Ti_3. Since the H-phase is rich in Ni, Hf, and lean in Ti, this study proposes that sluggish coarsening kinetics of the H-phase in $Ni_{50.3}Ti_{29.7}Hf_{20}$ alloy can be attributed to the high activation energy for the diffusion of Hf in the alloy matrix. This could be rationalized by the fact that during coarsening the larger particles grow at the expense of small particles, the diffusion of the slowest species (Hf) would be the rate controlling step during coarsening. Based on the present study different regions of growth and coarsening can be identified for the $Ni_{50.3}Ti_{29.7}Hf_{20}$ alloy on the time and temperature scale. Figure 6.12 represents a schematic of various regions as a function of time and temperature of aging.

6.5. Summary

In summary, role of thermal aging on the evolution of H-phase precipitates in $Ni_{50.3}Ti_{29.7}Hf_{20}$ high temperature shape memory alloy has been elucidated.

- Complementary informations provided by TEM and SANS revealed the growth kinetics of H-phase precipitates. The *in-situ* neutron scattering measurements showed that the precipitate growth follows a power-law with aging time. The growth rate

Table 6.6: Literature values of Ni_4Ti_3 precipitate interfacial energy, molar volume, diffusion coefficient, solid-solubility and calculated coarsening rate-constant at 560°C, along with coarsening rate-constant of the H-phase precipitates at 550°C (current study).

Precipitate matrix interfacial energy [294, 295] (Jm^{-2})	0.05
Molar volume of Ni_4Ti_3 precipitates [296] (m^3mol^{-1})	1.11×10^{-3}
Diffusion coefficient of Ni in NiTi at 560°C [285] (m^2s^{-1})	3.43×10^{-18}
Solid-solubility of Ni in NiTi at 560°C [297],	0.0004
Calculated K_c^{NiTi} (m^3s^{-1})	1.94×10^{-29}
Measured $K_c^{Ni_{50.3}Ti_{29.7}Hf_{20}}$ at 550°C (m^3s^{-1}) (***this work***)	2.59×10^{-30}

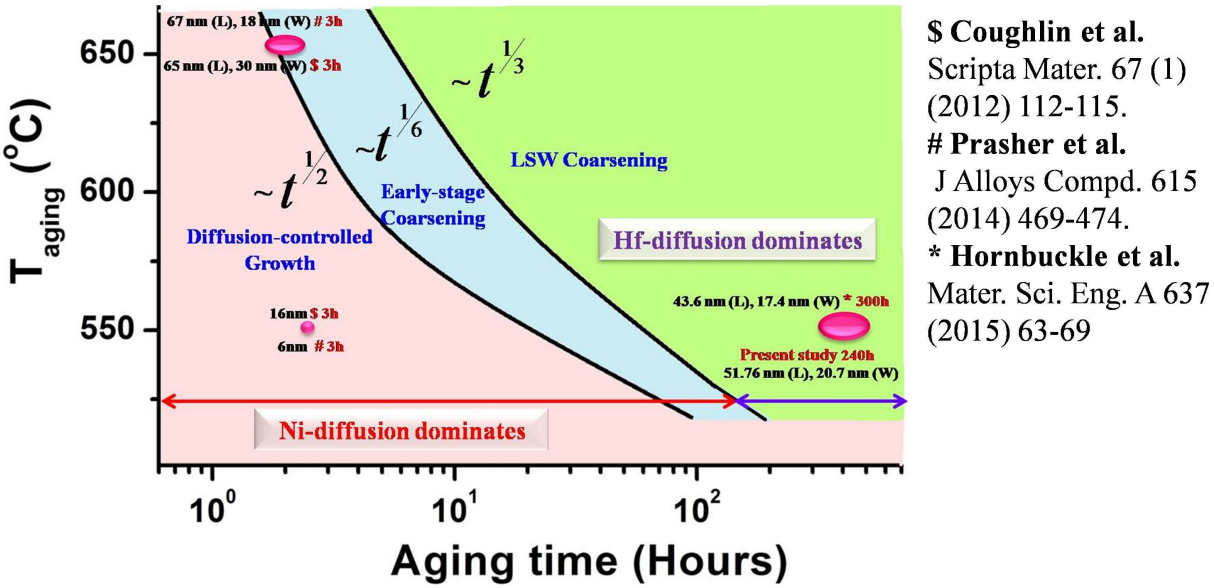

Figure 6.12: Schematic representation of the time-temperature graph depicting growth and coarsening regions of the H-phase in the $Ni_{50.3}Ti_{29.7}Hf_{20}$ alloy.

exponent α remains strongly dependent on the aging temperature with its value of $\sim 1/2$ and $\sim 1/6$ for 550°C and 650°C, respectively. Such dependence pointed towards contrasting growth modes, diffusion-controlled homogeneous growth at lower temperature while an early stage of coarsening for the higher temperature regime.

- Late stage of aging exhibited $\sim 1/3$ power-law behaviour, indicating classical LSW coarsening. The activation energies for the growth and the coarsening processes were estimated to be 196 $kJmol^{-1}$ and 233 $kJmol^{-1}$, respectively.

The present work demonstrated the differential role of Ni and Hf diffusion in deciding the H-phase precipitation kinetics in this alloy. While Ni-diffusion governed the precipitate growth, Hf diffusion remained the rate controlling step for the coarsening process.

CHAPTER 7

Thermal Cyclic Stability of Martensitic Phase Transformation in the $Ni_{50.3}Ti_{29.7}Hf_{20}$ Alloy

This chapter presents the results of study carried out to investigate the effect of aging treatments on the thermal cyclic stability of martensitic phase transformation in $Ni_{50.3}Ti_{29.7}Hf_{20}$ HTSMA. Many practical applications of HTSMAs involve repeated transformation cycling between austenite and martensite phase under different operating conditions. Such processes in NiTi based SMAs lead to thermal fatigue and considering that NiTiHf HTSMAs operate at temperatures significantly above room temperature, the effect may get accentuated over prolonged usage of the device and affect their functionality. Since aging treatments govern the phase transformation behaviour as well as strength of Ni-rich NiTiHf alloys, shown in previous chapters, this chapter elucidates the role of isothermal aging in tuning the thermal cyclic stability of martensitic transformation during thermal cycling at: (i) fixed heating/cooling rate, (ii) variable heating/cooling rates.

7.1. Introduction

Stable phase transformation behaviour during operation is one of the foremost criterion in utilization of SMAs as actuators. In course of their operation, NiTi SMAs undergo repeated cycling between austenite (B2) and martensite (B19$'$) phases, with or without external load. Such repeated cycling without external load is known as thermal cycling and has been shown to affect the thermodynamic stability as well as the properties of binary NiTi SMAs [298–300]. From the perspective of engineering applications of SMAs, variation in PTTs and thermal hysteresis as a function of repeated transformation cycling between austenite-martensite phases can be deleterious to the functional performance of a SMA device.

Thermal cycling leads to *thermal fatigue* in NiTi based alloys by suppressing B2 → B19′ transformation, which manifests in the form of reduction in phase transformation temperatures and induces intermediate R-phase on account of generation of defects such as dislocations [41, 301, 302]. Pelton *et al.* [303] determined that dislocation density in $Ni_{50.5}Ti_{49.5}$ increases from 10^{12} m^{-2} to 5×10^{14} m^{-2} after 100 thermal cycles. Saturation of defect density finally stabilizes the transformation temperatures as well as the B2 → R-phase transformation [299, 304]. Wagner *et al.* [305] elucidated that precipitation of Ni_4Ti_3 phase in $Ni_{50.7}Ti_{49.3}$ alloy prior to stress-free thermal cycling enhances its functional stability.

Cooling rate at which austenite → martensite transformation occurs in NiTi SMAs is also known to influence their phase transformation temperatures, thermal hysteresis, phase transformation behaviour and mechanical properties [306, 307]. Nurveren *et al.* [308] investigated using DSC the phase transformation characteristics in an aged near equi-atomic NiTi alloy as a function of heating/cooling rates and found that phase transformation temperatures in the alloy are strongly sensitive to the heating/cooling rates.

Since, NiTiHf HTSMA have to withstand elevated operating temperatures, high dislocation mobility at those temperatures can lead to significant thermal fatigue in the alloys. As discussed in section 2.4.2, Ti-rich NiTiHf alloys exhibit poor thermal cyclic stability than the binary SMAs on account of their poor strength. Since aging of Ni-rich NiTiHf alloys leads to the formation of the H-phase, which imparts strengthening to the matrix [228, 309], aging Ni-rich NiTiHf alloys can considerably improve. In next sections, the effect of stress-free transformation cycling at fixed as well as varying heating and cooling rates on the phase transformation characteristics of $Ni_{50.3}Ti_{29.7}Hf_{20}$ (at.%) alloy aged at different temperatures has been evaluated.

7.2. Experiments

Samples from the hot-rolled $Ni_{50.3}Ti_{29.7}Hf_{20}$ (at.%) alloy sheet were cut and heat-treated at following aging temperatures (T_{aging}) : 300°C, 400°C, 450°C, 500°C, 550°C, 600°C and 650°C for aging time (t_{aging}) of 3 hours each. Optical microscopy was carried out to determine the micro-structure of the alloy in as-solutionized condition. Specimens for optical microscopy were prepared as described in section 3.3.1.

Martensitic phase transformation behaviour of the as-solutionized as well as the aged

samples was investigated using DSC in the temperature range of 50°C-300°C. Thermal cyclic stability of the martensite phase transformation in the alloy at fixed heating/cooling rate was determined by thermal cycling the sample 20 times at a scanning rate of 10°C/min. The effect of heating and cooling rates on the thermal stability of phase transformation characteristics was probed at following rates: 20°C/min, 15°C/min, 10°C/min, 8°C/min and 5°C/min.

7.3. Results

Figure 7.1 displays surface of the as-solutionized sample under the optical microscope. Clearly visible surface-relief in the micro-structure is indicative of room temperature martensite phase [310, 311].

Figures 7.2 (a) and (b) present DSC response of the as-solutionized and the aged alloy samples, during cooling and heating cycles at the rate of 10°C/min, respectively. The PTTs, M_s, M_f, A_s, A_p, A_f are marked on the DSC curves in the figure and along with latent heats of B2 - B19$'$ transformation ($\Delta H^{B2-B19'}$) and B19$'$ - B2 phase transformation ($\Delta H^{B19'-B2}$) for the first thermal cycle are listed in Table 7.1.

The as-solutionized alloy exhibits $M_s = 161$°C and $A_f = 200$°C. In the low-temperature regime, PTTs show decreasing trend up to T_{aging} of 400°C, and afterwards increase linearly with T_{aging} up to 600°C, with a minimum at 400°C. The trend of A_f and M_s values

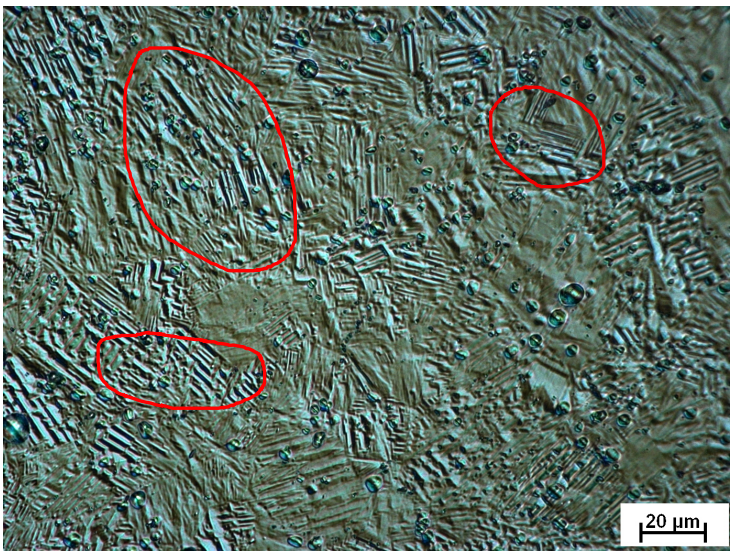

Figure 7.1: Optical micrograph of the $Ni_{50.3}Ti_{29.7}Hf_{20}$ alloy in as-solutionized condition. Surface-relief due to martensite phase marked in red.

with aging temperature is displayed in Figure 7.2 (c). Present results agree well with those of Karaca *et al.* [312], who proposed that initial lowering of PTTs during low-temperature aging can be due to strain energy of the precursor phase to H-phase precipitates, which

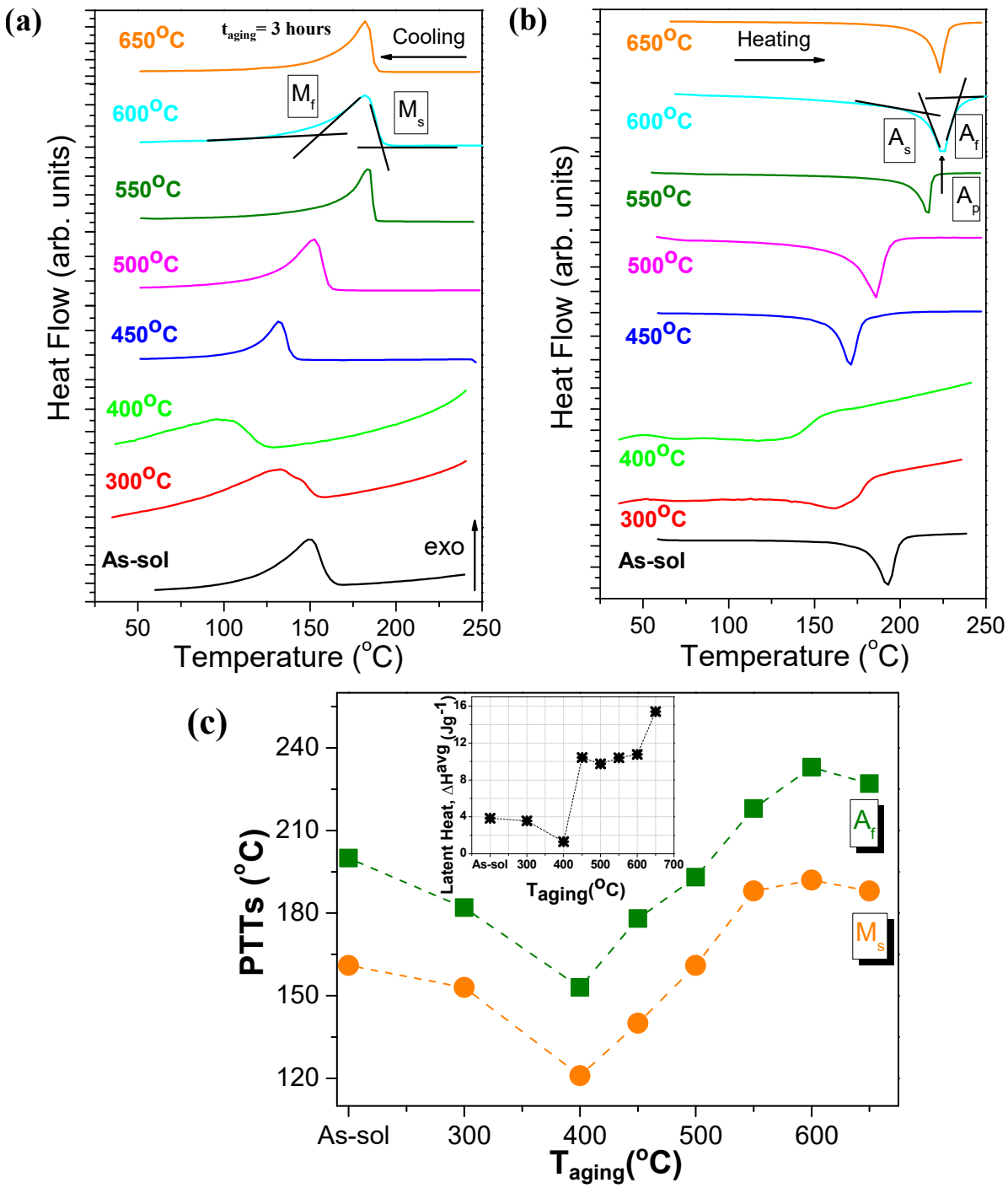

Figure 7.2: DSC plots during (a) Cooling cycle (b) Heating cycle depicting martensitic phase transformation in $Ni_{50.3}Ti_{29.7}Hf_{20}$ alloy aged at different temperatures for 3 hours each (c) T_{aging} dependence of M_s and A_f. Inset of figure (c) depicts the evolution of average latent heat of transformation, ΔH^{avg}, with aging temperature.

Table 7.1: Martensitic Phase transformation temperatures and latent heats of transformation associated with $Ni_{50.3}Ti_{29.7}Hf_{20}$ alloy in as-solutionized and aged conditions.

Aging conditions	Transformation temperatures (°C)							Latent heat of transformation (Jg^{-1})	
	M_s	M_f	A_s	A_f	M_p	A_p	T_0	$\Delta H^{B2-B19'}$	$\Delta H^{B19'-B2}$
As-solutionized	161	121	183	200	150	192	180.5	7.49	7.5
300°C-3h	153	92	138	182	132	162	167.5	3.61	3.48
400°C-3h	121	59	97	153	101	136	137	1.5	1.1
450°C-3h	140	114	161	178	131	169	159	10.11	10.74
500°C-3h	161	128	167	193	151	182	177	10.23	10.56
550°C-3h	188	169	210	218	184	215	203	10.23	10.56
600°C-3h	192	153	224	233	183	224	212.5	10.76	10.76
650°C-3h	188	164	223	227	183	223	207.5	15.03	15.77

makes martensite transformation difficult occur. In other words, low-temperature aging lowers the thermodynamic stability of martensite phase.

Aging above critical temperature of 500°C up to 600°C leads to Ni-depletion in the matrix on account of increase in H-phase volume fraction [199]. Above 600°C, a little drop in PTTs values is noted, which can be attributed to decrease in volume fraction of H-phase precipitates [228]. The inset of Figure 7.2 (c) depicts the average latent heat of transformation ($\Delta H^{avg} = \frac{[\Delta H^{B2-B19'} + \Delta H^{B19'-B2}]}{2}$) variation with T_{aging}.

7.3.1. Thermal Cycling at Fixed Heating/Cooling Rate

Thermal stability of the martensitic transformation in $Ni_{50.3}Ti_{29.7}Hf_{20}$ alloy in as-solutionized as well as in aged conditions is investigated by thermally cycling the samples between austenite and martensite phases, at the scanning rate of 10°C/min, for 20 times. Figures 7.3 (a)-(d) show a comparison of the DSC curves obtained for the cycle #1 and cycle #20 for the as-solutionized alloy, aged at 400°C, 550°C and 650°C for 3 hours each. Insets of the figures depict the DSC curves for 20 thermal cycles correspond to each aging temperature. It can be noted from the inset plots that with increasing number of thermal cycles, DSC peaks drift towards left during cooling cycle and heating cycles, indicating decrease in PTTs. Even after 20 thermal cycles, the phase transformation occurs in a single-stage, contrary to the binary Ni-rich NiTi alloys where R-phase appears during thermal cycling

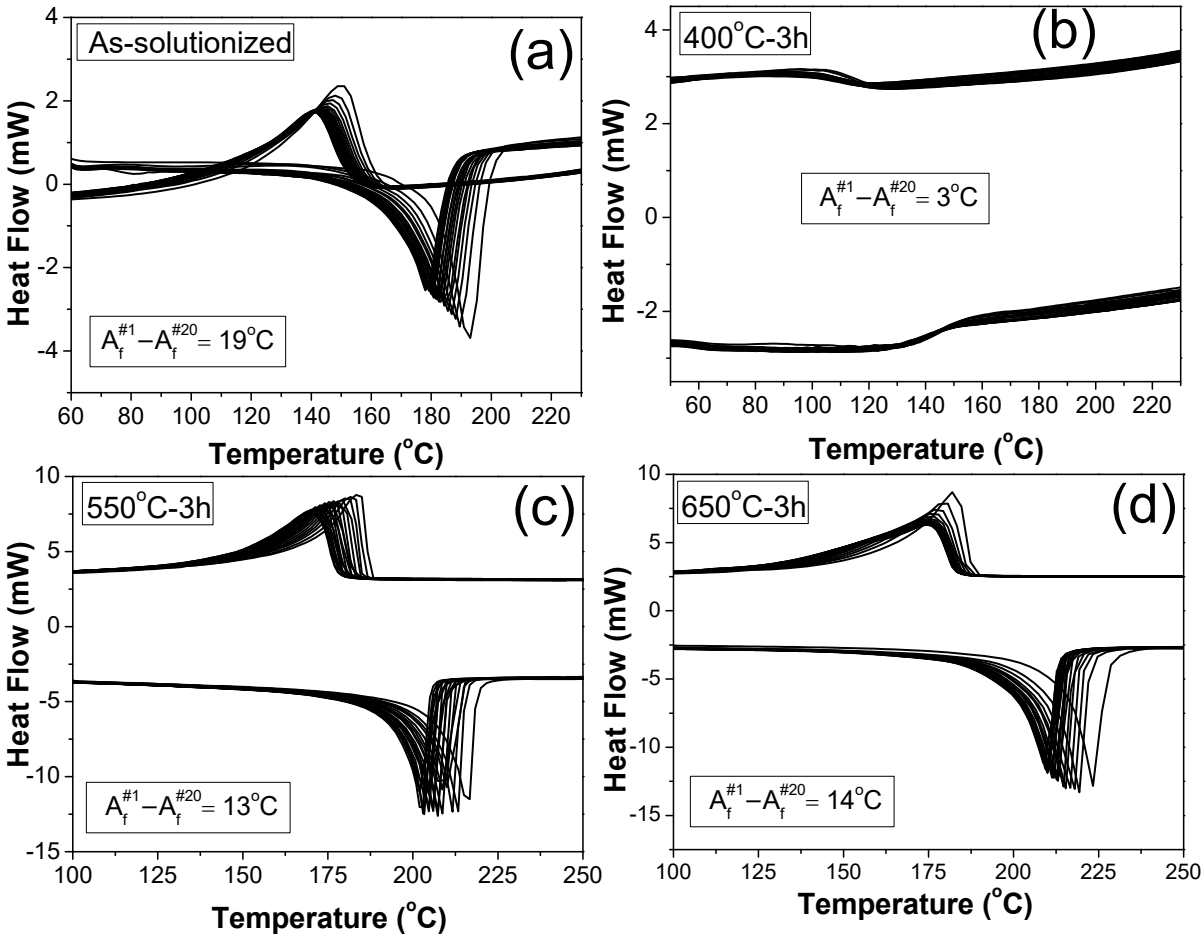

Figure 7.3: DSC plots exhibiting martensitic transformation in the $Ni_{50.3}Ti_{29.7}Hf_{20}$ corresponding to 20 thermal cycles at the rate of 10°C/min for (a) as-solutionized condition, aged at (b) 400°C, (c) 550°C, (d) 650°C.

[313].

Figures 7.4 (a) and (b) depict the decrease in M_s and A_f values with number of thermal cycles as a function of T_{aging}. Interestingly, thermal cycling lowers reverse transformation temperatures more strongly than forward transformation temperatures. In terms of change in PTTs upon thermal cycling at a fixed heating and cooling rate, the decrease in the as-solutionized alloy sample is relatively slower in comparison to binary NiTi alloys, as observed by Miyazaki *et al.* [41]. They reported a decrease of nearly 30°C in first 10 cycles, which is higher than in case of the $Ni_{50.3}Ti_{29.7}Hf_{20}$ alloy, implying higher thermal cyclic stability of martensitic transformation in this alloy. The values of M_s and A_f for cycle #1 and cycle #20 have been tabulated in Table 7.2. The difference between M_s and A_f values for cycle #1 and cycle #20 *i.e.* ($M_s^{\#1}$ - $M_s^{\#20}$) and ($A_f^{\#1}$ - $A_f^{\#20}$) are tabulated in Table 7.2.

Table 7.2: Martensitic transformation temperatures and thermal hysteresis of $Ni_{50.3}Ti_{29.7}Hf_{20}$ alloy after thermal cycle # 1 and # 20 in as-solutionized and after aging treatments.

Alloy	Transformation temperatures and hysteresis (°C)							
	$A_f^{\#1}$	$A_f^{\#20}$	$A_f^{\#1}$-$A_f^{\#20}$	$M_s^{\#1}$	$M_s^{\#20}$	$M_s^{\#1}$-$M_s^{\#20}$	$A_f^{\#1}$-$M_s^{\#1}$	$A_f^{\#20}$-$M_s^{\#20}$
As-solutionized	200	181	19	161	153	8	39	28
300°C-3h	183	177	6	154	150	2	29	27
400°C-3h	153	150	3	121	120	1	32	30
450°C-3h	178	173	5	140	138	2	38	35
500°C-3h	193	181	12	161	154	7	32	27
550°C-3h	218	205	13	188	179	9	30	26
600°C-3h	233	217	16	192	185	7	41	32
650°C-3h	227	213	14	188	183	5	39	30

It is worth noting that while the difference ($M_s^{\#1}$ - $M_s^{\#20}$) is below 10°C for all the T_{aging} values, the values of $A_f^{\#1}$ - $A_f^{\#20}$ is 19°C, which is significantly higher than those of equivalent values at T_{aging} = 300°C and 400°C, values being 6°C and 3°C, respectively. For T_{aging} > 400°C, the difference again started increasing, attaining values nearly as that of the as-solutionized alloy. Due to more prominent effect of thermal cycling on A_f, relative to M_s values, thermal hysteresis defined as (A_f - M_s) lowered after 20 thermal cycles. Also, aging the alloy below 500°C leads to comparatively less change in hysteresis after 20 thermal cycles. The alloy aged below 450°C undergo least change in thermal hysteresis over 20 thermal cycles. This change is found to increase significantly with

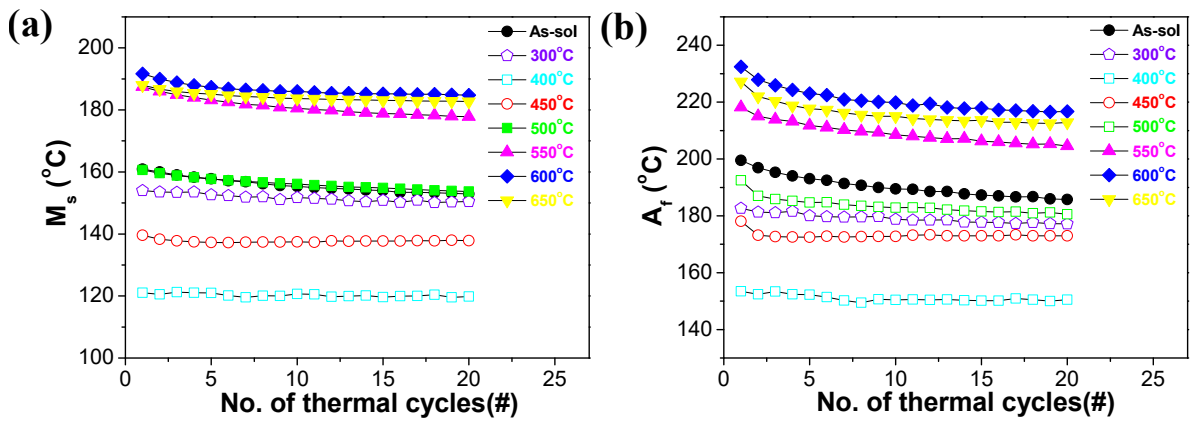

Figure 7.4: Variation in the (a) M_s and (b) A_f values over 20 thermal cycles for the alloy in as-solutionized as well aged condition.

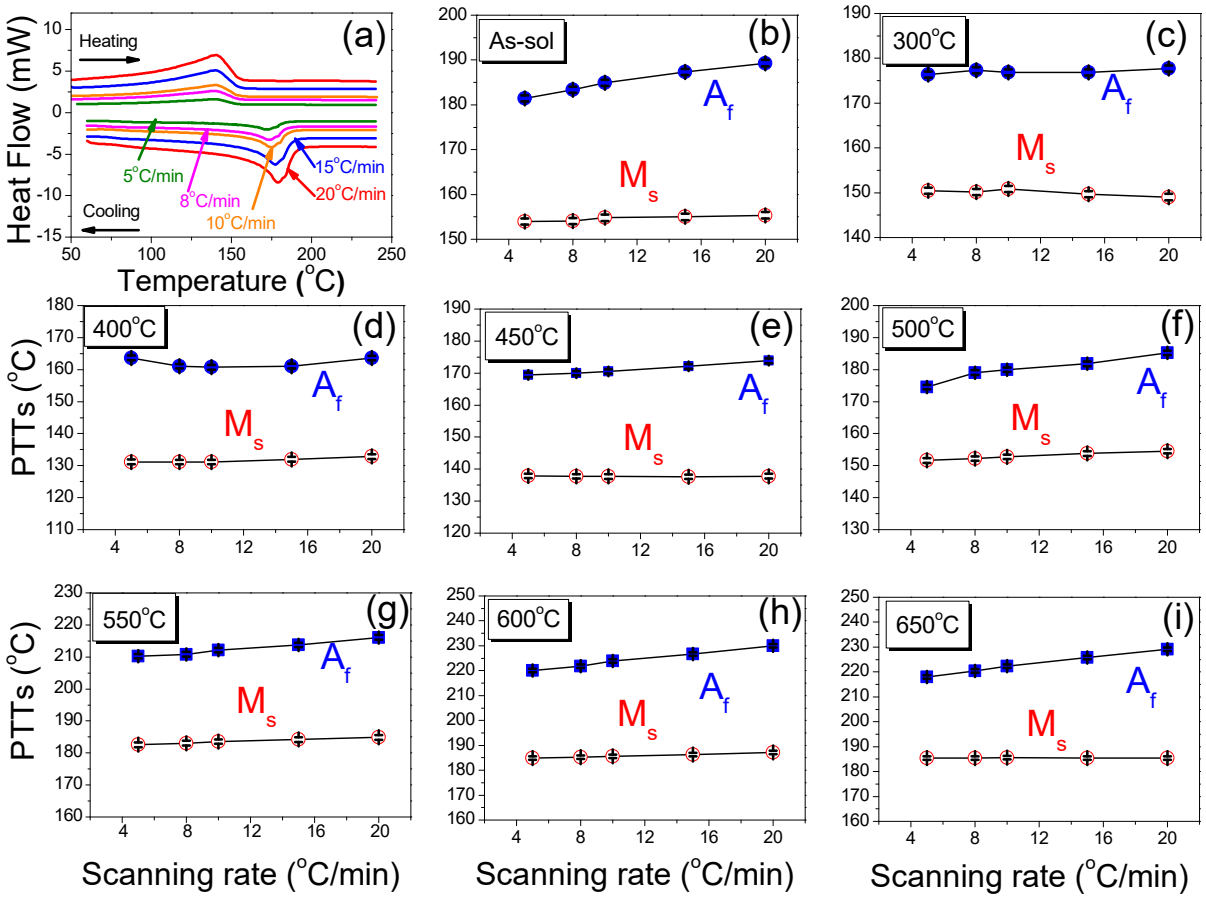

Figure 7.5: (a) DSC plots exhibiting martensitic transformation in the as-solutionized $Ni_{50.3}Ti_{29.7}Hf_{20}$ alloy at different heating and cooling rates. Variation in M_s and A_f with scanning rates for the alloy in (b) as-solutionized condition, aged at (c) 300°C, (d) 400°C, (e) 450°C, (f) 500°C, (g) 550°C, (h) 600°C, (i) 650°C.

increase in aging temperature (Table 7.2).

Above results indicate that the $Ni_{50.3}Ti_{29.7}Hf_{20}$ alloy aged below 500°C for 3 hours exhibits high thermal cyclic stability of martensitic transformation against stress-free thermal cycling at fixed heating and cooling rate.

7.3.2. Role of Heating/Cooling Rates on Thermal Cyclic Stability

DSC tests of the as-solutionized $Ni_{50.3}Ti_{29.7}Hf_{20}$ alloy for varying heating rates (20°C/min-5°C/min) are presented in Figure 7.5 (a). It can be seen that at all the scanning rates, martensitic transformation occurs in a single-stage transformation. The M_s and A_f values obtained from the DSC curves for all specimens are presented in Figures 7.5 (b)-(i). Notice that both M_s as well as A_f values increase linearly with heating and cooling rates, in other words, thermodynamic stability of martensite increases with scanning rate. However,

increase in A_f values is significant in comparison to M_s values. Interestingly, the change in M_s and A_f values of the sample aged below 500°C for 3 hours is least sensitive to scanning rates.

Thermal hysteresis values were also found to increase linearly with scanning rates for all the samples except in the samples which were aged at 300°C and 400°C, which were least affected by scanning rate. The thermal hysteresis dependence on scanning rate is demonstrated in Figures 7.6 (a)-(h). The thermal hysteresis values for the as-solutionized alloy increases linearly from 27°C to 34°C as the cooling rate increased from 5°C/min to 20°C/min at the rate of 0.43°C/°C min^{-1}. However, the thermal hysteresis remained within 30°C ± 1°C for the sample aged at 400°C. The rate of change of thermal hysteresis with scanning rate is relatively higher for aging temperatures exceeding 400°C. It is noteworthy that the phase transformation characteristics of the alloy aged at 400°C for 3 hours are least sensitive to the scanning rate and the alloy aged at this condition exhibits highest thermal cyclic stability of the martensitic phase transformation in terms of transformation temperatures and thermal hysteresis as a function of heating/cooling rates.

7.4. Discussion

The main observations drawn from the results are summarized as follows:

- Initial decrease in PTTs for the samples which were aged below 500°C and subsequent increase in the values for the samples aged at temperatures higher than 500°C suggest that aging treatment modifies the relative thermodynamic stability of the austenite and martensite phases.

- Thermal cycling at fixed heating/cooling rate lowers PTTs and thermal hysteresis with increasing number of cycles. Least variation in PTTs and thermal hysteresis was observed for the specimen aged at 400°C.

- In the case of thermal cycling carried out with variable heating/cooling rates, PTTs as well as thermal hysteresis were observed increasing with increasing the number of cycles. Once again, least variation in PTTs and thermal hysteresis was observed for specimen aged at 400°C.

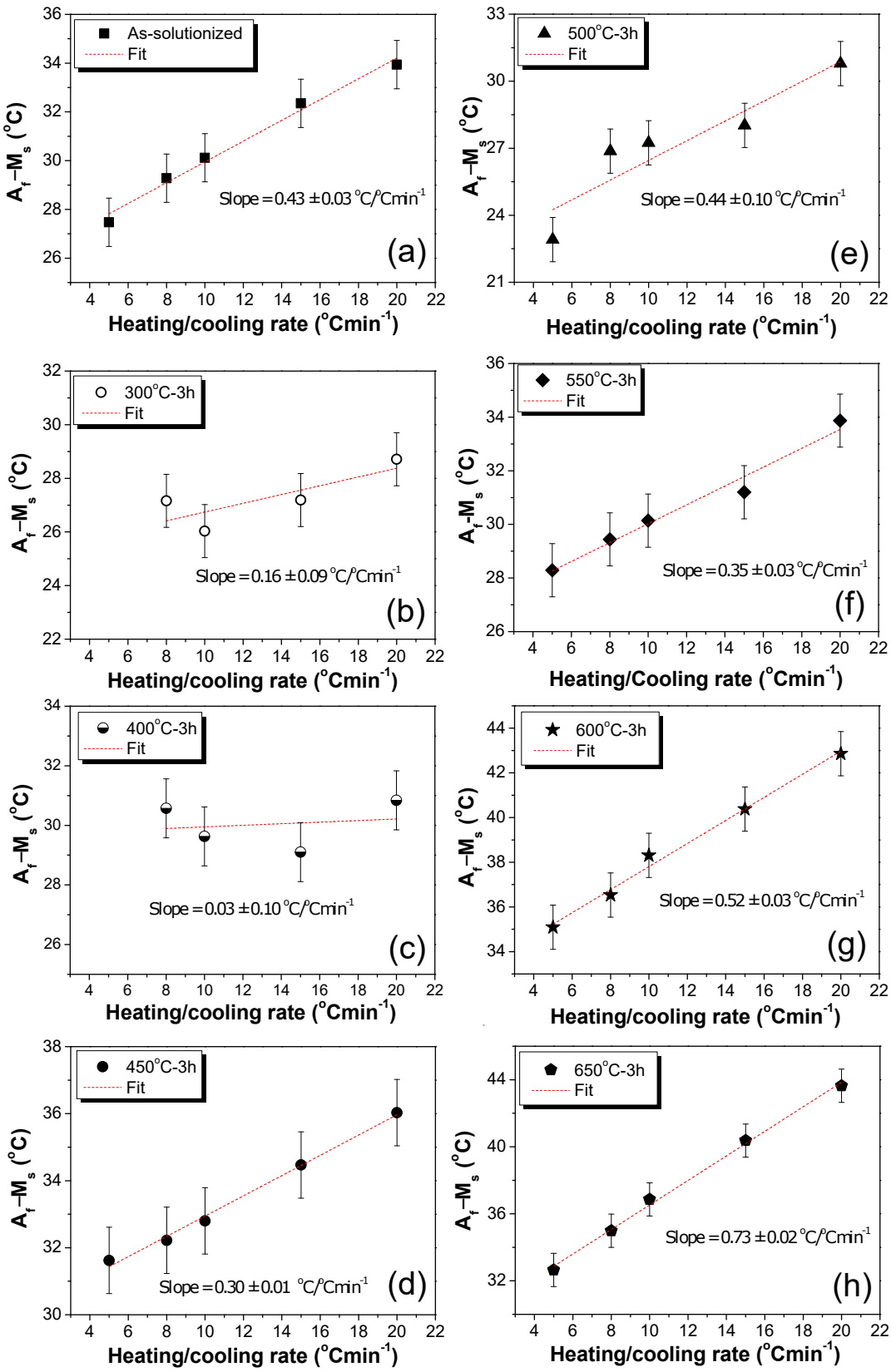

Figure 7.6: Variation in thermal hysteresis (A_f-M_s) as a function of scanning rates for the alloy in (a) as-solutionized condition, aged at (b) 300°C, (c) 400°C, (d) 450°C, (e) 500°C, (f) 550°C, (g) 600°C, (h) 650°C.

As previously mentioned in section 2.1, the change in the total Gibbs free energy (ΔG^{Total}) during phase transformation i.e. driving force for MT, is the sum of "chemical" and "non-chemical" contributions:

$$\Delta G^{Total} = \Delta G_{chem} + \underbrace{\Delta G_s + \Delta G_{fric}} = \Delta G_{chem} + \Delta G_{nonchem} \tag{7.1}$$

While the first term is the undercooling (ΔG^{chem}), which is the difference between ground state energies of austenite and martensite has a net negative magnitude and favors the transformation, the terms ΔG^s (strain energy due to creation of austenite-martensite interface) and ΔG^{fric} (dissipative events such as acoustic emissions, heat losses etc.) are generally net positive in magnitude and oppose the transformation. The thermodynamic driving force is a balance between "chemical" and "non-chemical" contributions to the total free energy change. The decrease in value of T_0 indicates lowering of the thermodynamic stability of martensite.

The values of T_0 for the present alloy aged at different temperatures are shown in Table 7.1. In the present alloys, significant drop in T_0 values and the latent heat of transformation in the specimen aged at 400°C clearly suggests difficulty in the nucleation of martensite. This observation can be rationalized on the basis of reasoning offered by Evirgen *et al.* [226] to explain the tuning of M_s in the $Ni_{50.3}Ti_{34.7}Hf_{15}$ alloy with aging temperature and duration. They attributed the lowering of PTTs in the alloy specimens aged below 500°C to the suppression of nucleation of martensite due to small inter-particles spacing between H-phase precipitates. The increase in T_0 and latent heat values for the present alloy aged at higher temperatures ($T_{aging} > 500$°C), on the other hand, can be attributed to the "compositional" effect [226] where depletion of Ni from the matrix phase, due to higher volume fraction of H-phase [199], stabilizes the martensite phase.

During thermal cycling, repeated movements of martensite-austenite interfaces in NiTi based SMAs create tangled sessile dislocations pinning the coherent or semi-coherent interfaces [157], density of which increases during initial cycles and subsequently saturates [314]. Thermodynamically, the contribution of ΔG^s and ΔG^{fric} to the total free energy change increases with increasing the iteration of cycle. As a result, additional undercooling is needed for the MT to occur, which manifests itself in terms of decrease in PTTs during thermal cycling.

The poor thermal cycling stability of NiTiHf alloys, in comparison to the binary NiTi SMAs, is generally attributed to distorted austenite-martensite interfaces. In these alloys, plastic deformation is accommodated at the interface via (001) mechanical twinning, which causes poor interfacial mobility [227] and hence, poor thermal cyclic stability. In the present case, however, better thermal cyclic stability of the $Ni_{50.3}Ti_{29.7}Hf_{20}$ alloy was observed in those specimens which were aged at temperatures below 500°C. Typically, the specimen aged at 400°C exhibited least variation of 2°C-3°C in PTTs as well as thermal hysteresis. Bucsek *et al.* [315] compared the transformation strains and lattice compatibility in unaged and aged $Ni_{50.3}Ti_{29.7}Hf_{20}$ alloy and found that aged alloys exhibit larger transformation strains and better lattice compatibility between austenite and martensite, resulting in lower thermal hysteresis. Their observation is in agreement with present results. Evirgen *et al.* [260] further investigated the effect of aging temperature on lattice compatibility and demonstrated poor crystallographic compatibility between austenite and martensite lattice in the $Ni_{50.3}Ti_{29.7}Hf_{20}$ alloy aged at higher temperatures. They attributed this to the coarse precipitates [228], which result in larger distortion martensite lattice and bigger change in transformation volume. Better thermal cyclic stability in the present alloy aged at 400°C case, thus, can be associated with the higher degree of atomic order across the interface and mobility of such interfaces, therefore, is least affected by repeated cycling.

Wollants *et al.* [316] interpreted the thermoelastic equilibrium during MT in terms of local equilibrium at the interface separating growing martensite plate and austenite matrix. This equilibrium can be affected by the presence of defects such as point defects, dislocations, precipitates etc., which alter the free energy landscape and the system can attain several metastable states. The energy barriers offered by these metastable states must be overcome for the MT to proceed. The activation energy for MT in the alloy specimens has been determined using the Kissinger method [317], which has been successfully implemented to determine the activation energy barrier for martensitic phase transformations in several shape memory alloys [318–320]. Kinetic parameters of martensitic transformations were determined from isochronal DSC scans in terms of Kissinger's equation employed at four different heating/cooling rates: 20°C/min, 15°C/min, 10°C/min,

and 8°C/min:

$$\boxed{ln\left(\frac{\phi}{A_p^2}\right) = \frac{-1000Q}{RA_p} + C} \tag{7.2}$$

Here, ϕ is the heating rate, A_p is austenite peak temperature (in Kelvin), Q is the activation energy associated with the transformation (in kJmol^{-1}), R is the Universal gas constant (8.314 Jmol^{-1}K^{-1}) and C is a constant.

The plots of $\ln(\frac{\phi}{A_p^2})$ vs. $(\frac{1000}{A_p})$ for the $Ni_{50.3}Ti_{29.7}Hf_{20}$ alloy in as-solutionized and aged condition have been displayed in Figures 7.7 (a)-(h). Slope of the straight line obtained by least square fitting quantifies the activation barrier for martensitic transformation. It can be seen from the plots that activation energy varies with aging temperature T_{aging}. The values of A_p and Q corresponding to the each aging condition are listed in Table 7.3. The activation energy value for the as-solutionized specimen is 289±10 kJmol^{-1}, which is higher than that of binary NiTi alloy 240-263 kJmol^{-1} [321]. Activation energy value then increases to 855±35 kJmol^{-1} for the specimen aged at 400°C and again reduces to 312±10 kJmol^{-1} for the specimen aged at 650°C. The activation energy value variation with aging temperature has been presented in Figure 7.8.

It is worth noting that high activation energy for MT in the present alloy corresponds

Table 7.3: Aging temperature dependence of activation energy (Q) for the martensitic transformation in the $Ni_{50.3}Ti_{29.7}Hf_{20}$ alloy.

Aging condition	**A_p (°C)**				**Q (kJmol^{-1})**
	20(°C/min)	**15(°C/min)**	**10(°C/min)**	**8(°C/min)**	
As-solutionized	178.6	177.2	174.8	173.4	288.7 ± 10.1
300°C-3h	156.8	156.7	155.5	154.9	657.4 ± 126.4
400°C-3h	151.5	151.4	150.4	149.7	855.2 ± 35.1
450°C-3h	169.3	168.5	167.5	167.3	693.4 ± 83.9
500°C-3h	178.0	177.0	176.0	175.9	670.9 ± 101.8
550°C-3h	212.6	210.1	208.8	207.6	356.7 ± 57.7
600°C-3h	220.4	217.8	215.7	213.9	282.5 ± 22.8
650°C-3h	222.7	220.7	218.4	216.9	311.8 ± 9.8

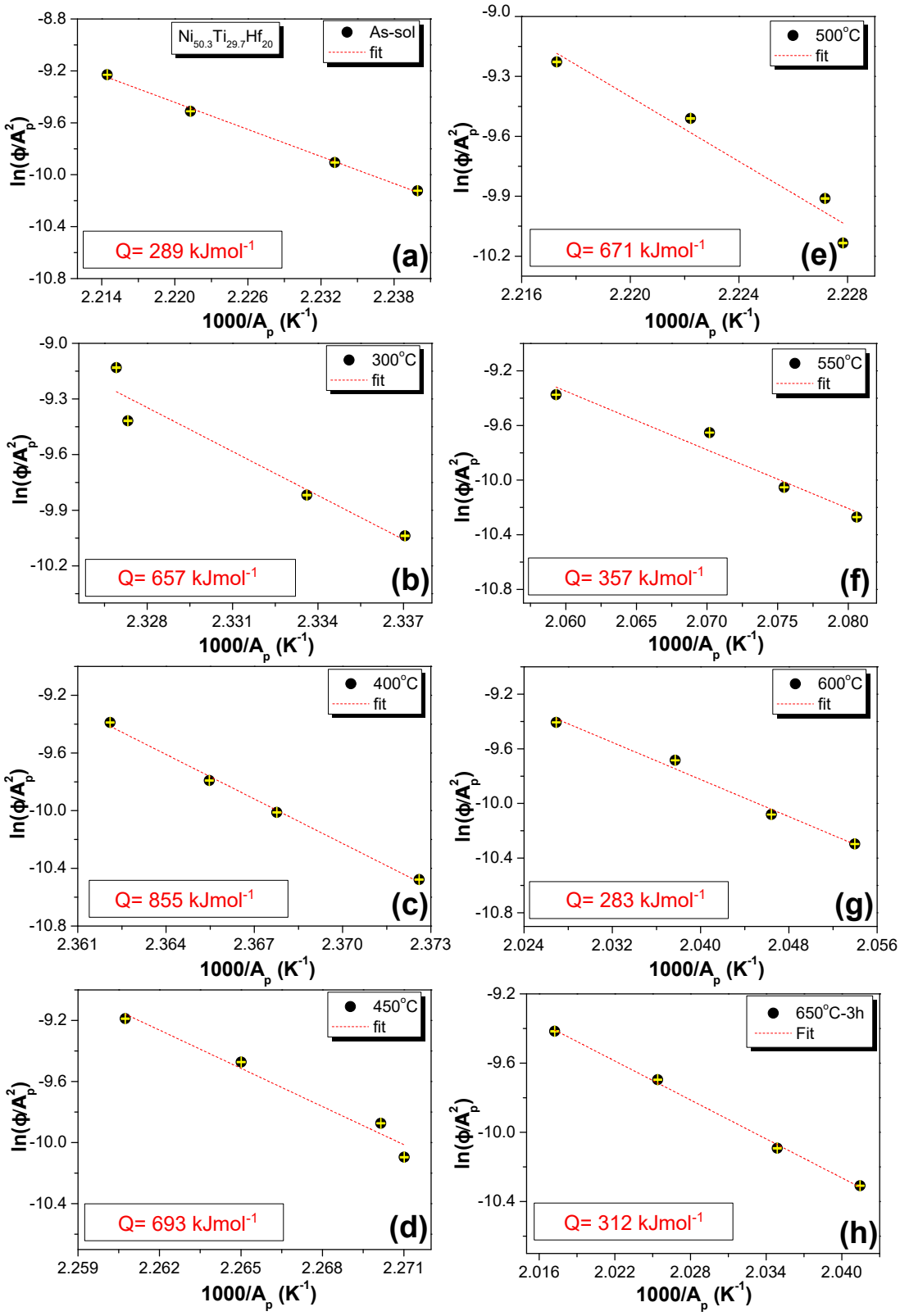

Figure 7.7: Least-squares fitted $\ln\frac{\phi}{A_p^2}$ vs. $(\frac{1000}{A_p})$ Kissinger plots for the alloy in (a) as-solutionized condition, aged at (b) 300°C, (c) 400°C, (d) 450°C, (e) 500°C, (f) 550°C, (g) 600°C, (h) 650°C.

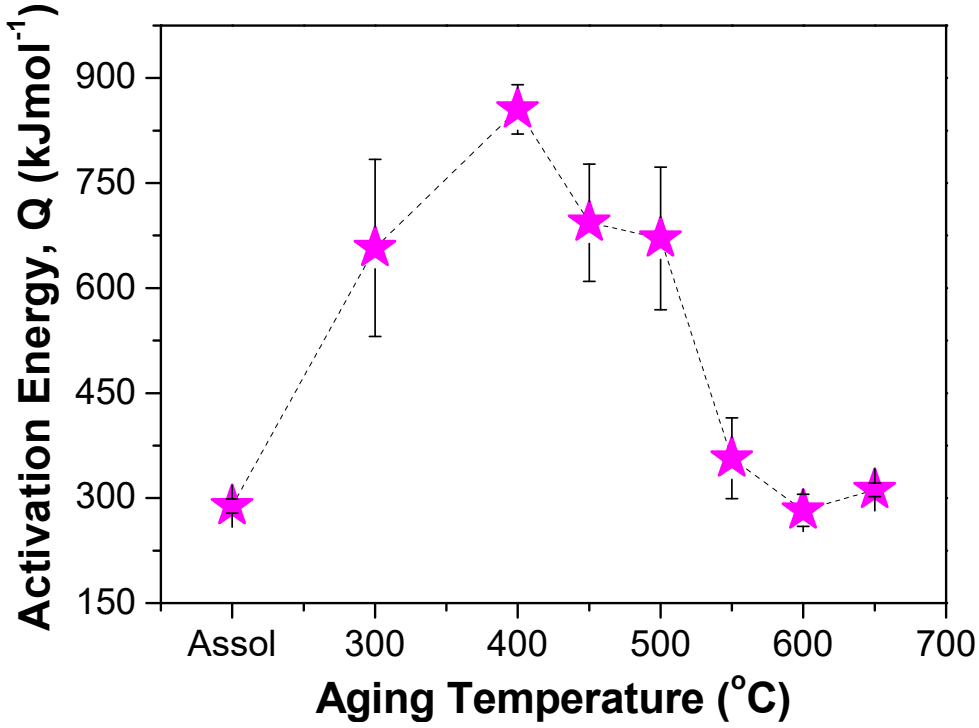

Figure 7.8: Aging temperature dependence of Activation energy for the martensitic transformation in $Ni_{50.3}Ti_{29.7}Hf_{20}$ alloy.

to high thermal cyclic stability of MT and vice-versa. In literature, several authors have emphasized on the correlation between activation energy related to transformation kinetics and thermal cyclic stability of the martensitic transformation. For instance, Ramaiah *et al.* [71] reported highly stable stress-free thermal cyclic response of the $Ni_{24.7}Ti_{50.3}Pd_{25}$ alloy and found that that alloy exhibited high activation energy (1931 $kJmol^{-1}$) for the MT. They ascribed better thermal cyclic stability to high degree of atomic order and perfect atomic match at the austenite-martensite interface. Recently, Yi *et al.* [322] determined activation energy of MT in Pt-doped Ti-Ni-Cu SMAs by Kissinger's equation and associated the high activation energy value of 960 $kJmol^{-1}$ with excellent thermal cyclic stability of the alloy owing to improved lattice geometric compatibility. The observation of high activation energy barrier for MT in the 400°C-3h specimen could be taken as a supportive evidence of the aforementioned argument. High thermal cyclic stability of MT in the $Ni_{50.3}Ti_{29.7}Hf_{20}$ alloy specimen aged at 400°C suggests that with each additional thermal cycles defect density in the specimen is lowest among all other samples. Thus, the PTTs and thermal hysteresis in the specimen are highly stable against number of thermal cycles as well as the rates at which the temperature is swept during cooling/heating cycles. In contrast, low activation energy barriers, in the as-solutionized

alloy specimen as well as those aged at higher aging temperatures imply formation of higher defect density, which degrades the thermal cyclic stability of MT.

7.5. Summary

In summary, stress-free thermal cycling of the isothermally aged $Ni_{50.3}Ti_{29.7}Hf_{20}$ alloys was carried out in DSC at fixed as well as at variable heating/cooling rates.

- Thermal cycling at 10°C/min lowers the phase transformation temperatures and thermal hysteresis. For heating/cooling rates in the range 20°C/min-5°C/min, the transformation temperatures and thermal hysteresis were found to increase.
- The alloy aged at 400°C for 3 hours demonstrates least variation in phase transformation temperatures as well hysteresis under both the conditions and hence, highest thermal cyclic stability of martensitic transformation.
- A concurrence between thermal cyclic stability and activation energy for MT in NiTiHf HTSMAs is demonstrated. Highest thermal cyclic stability of martensitic phase transformation in $Ni_{50.3}Ti_{29.7}Hf_{20}$ upon aging at 400°C for 3 hours, which exhibits high activation energy ($\sim$ 855$\pm$35 kJmol^{-1}) for martensitic transformation.

This work shows that aging of Ni-rich NiTiHf alloys at low temperatures is capable of alloys with stable phase transformation behaviour, which is important for reliable shape memory response. The present study is a step towards development of fundamental knowledge necessary for the optimization and development of reliable and cheap HTSMAs for engineering application

CHAPTER 8

Summary and Future Directions

The main purpose of investigating Ni-Ti-Hf alloys was to develop a NiTi-based HTSMA with good combination of high phase transformation temperatures, low thermal hysteresis, good thermal cyclic stability and high strength. This demands a thorough understanding of the phase transformation behaviour in these alloys and its correlation between the alloy micro-structure and its strength. In this dissertation work, studies were carried out to investigate the effect of alloy composition as well as aging conditions on the evolution of the martensitic phase transformation behaviour, evolution of precipitates with aging time as well as temperatures and alloy strength. In this regard, the use of two complementary techniques: small-angle scattering and electron microscopy has been instrumental in probing the time-resolved bulk-scale micro-structural evolution in a statistically averaged manner.

8.1. Summary

A systematic effect of Hf addition in the $Ni_{50.3}Ti_{49.7-x}Hf_x$ (x = 0, 5, 10, 15, 18, 20, 25 at.%) on transformation temperatures, thermal hysteresis and alloys strength were studied via DSC experiments and room-temperature Vickers micro-hardness tests. The solid-solubility limit of Hf in these alloys was analysed using high temperature ND experiments. The validity of Vegard's law for B2 lattice parameters for all the compositions implies complete solid-solution solubility of Hf in Ni-rich NiTi alloys upto 25 at.% Hf. The Hf-concentration above 15 at.% is required to create viable Ni-rich NiTiHf high temperature shape memory alloys, whose strength increases linearly with Hf-content on account of solid-solution strengthening. The $Ni_{50.3}Ti_{29.7}Hf_{20}$ alloy exhibits least thermal hysteresis amongst all the other compositions. With the selection criteria of high transformation temperature and low hysteresis, $Ni_{50.3}Ti_{29.7}Hf_{20}$ composition was selected as an alloy composition to further investigate the effect of aging on phase transformation behaviour and

alloy strength.

For this, precipitation heat treatments were carried out on this composition at different temperatures for various aging durations. Statistically averaged quantification precipitates using is imperative to correlate the alloy micro-structure with the macroscopic properties. For this, micro-structural evolution of the precipitates with heat treatments was studied in terms of their size, morphology, crystal structure and inter-precipitate spacing using correlative TEM and SAXS/SANS experiments. Aging the $Ni_{50.3}Ti_{29.7}Hf_{20}$ alloy at different temperatures lead to ellipsoidal H-phase precipitates, whose aspect ratio is significantly increases with time at higher aging temperatures. Enhancement of the alloy strength with aging was explained in terms of precipitate size and inter-precipitate spacings. Formation of dense population of fine precipitates in 550°C-3h specimen significantly enhanced alloy strength, while lower volume fraction and surface to volume ratio of the precipitates at 650°C indicates coarsening of precipitates. Coarsening induced reduction in hardness is attributed to the dislocation looping around the widely separated precipitates.

Further, based on real-time SANS experiments in combination with TEM, the mechanism behind precipitate growth and coarsening kinetics was analysed for the first time in literature. The *in-situ* SANS measurements showed that the precipitate growth follows a power-law with aging time. The early-stage growth rate exponent α remains strongly dependent on the aging temperature with its value of $\sim 1/2$ and $\sim 1/6$ for 550°C and 650°C, respectively. Late stage of aging exhibited $\sim 1/3$ power-law behaviour, indicating classical LSW coarsening. The activation energies for the growth and the coarsening processes were estimated to be 196 $kJmol^{-1}$ and 233 $kJmol^{-1}$, respectively. Differential role of Ni and Hf diffusion is deciding factor for the H-phase precipitation kinetics in this alloy. While Ni-diffusion governed the precipitate growth, Hf diffusion remained the rate controlling step for the coarsening.

Repeated transformation cycling of HTSMAs during their operation can lead to thermal fatigue, which shows up as change in phase transformation temperatures as well as thermal hysteresis and degrade the functional performance of the SMA device. A study was taken up to investigate the effect of aging temperature on the thermal cyclic stability of the $Ni_{50.3}Ti_{29.7}Hf_{20}$ alloy under two conditions, normally encountered by HTSMA devices: (i) stress-free cycling at fixed heating/cooling rates, and (ii) stress-free cycling

at variable heating/cooling rates. It has been demonstrated that alloy specimen aged at 400°C for 3 hours exhibits least variation in phase transformation temperatures as well hysteresis under both the conditions *i.e.* highest thermal cyclic stability of martensitic transformation. This observation has been explained in terms of correlation between the thermal cyclic stability and activation energy for MT in NiTiHf HTSMAs. The high value activation energy ($\sim$ 855$\pm$35 kJmol^{-1}) for martensitic transformation in this alloy sample is correlated with better thermal cyclic stability in this alloy aged at 400°C for 3 hours.

8.2. Future Direction

Since their discovery, the NiTi-based shape memory alloys are at the centre of attention as an actuator materials. The versatility in tuning the alloy strength, transformation temperatures etc. are far better in comparison with other alloy systems exhibiting shape memory such as Cu-based SMAs, Fe-based shape memory alloys etc. Being a "smart material", NiTi SMAs are capable of responding to stimuli such as temperature and stress in predictable or controlled manner, these SMAs have revolutionized the sensors and actuator industry, with their application spanning over. More recently, high strength Ni-rich NiTiHf HTSMAs have gained the foremost spot as NiTi-based SMAs, capable of exhibiting shape memory properties at temperatures as high at 300°C. Nonetheless, being functional metallic materials, they face the issue of loss of strength over prolonged usage at high operating temperatures, which directly affects their functional performance. Therefore, comprehensive understanding of the phase transformation behaviour-microstructure-strength relationship is central to the alloy development. The studies presented in this dissertation have shown that amongst NiTiHf alloys with fixed Ni-concentration of 50.3 at.% and Hf concentration over 5-25 at.%, the $Ni_{50.3}Ti_{29.7}Hf_{20}$ HTSMA exhibits lowest thermal hysteresis, whose strength as well as thermal cyclic stability can be appropriately tuned with aging induced H-phase precipitates. Further, these precipitates are quite effective in strengthening the matrix due to their sluggish coarsening kinetics in comparison to Ni_4Ti_3 precipitates in binary NiTi alloys. In addition to observed results, possible future studies on these alloys which can be taken up are listed below:

- Understanding of very early stage clustering phenomenon in Ni-rich NiTiHf alloys still remains a challenge. This may be realized by use of the complementary tech-

niques, such as, APT, TEM and SAXS/SANS.

- Application of elastic stress during the ageing process of precipitate-strengthened alloys affects the resulting micro-structures quite considerably, in particular, the distribution of strengthening precipitates [323]. In case of binary NiTi alloys, this directly shows up as modification in their shape memory properties [324]. In future, studies may be taken up to explore this aspect in Ni-rich NiTiHf alloys in terms of the influence of stress-assisted aging on the phase transformation temperatures, thermal hysteresis and alloy strength.

- Externally applied stress can alter the growth as well as coarsening kinetics of the H-phase precipitates. Combinatorial real-time SANS/SAXS and TEM studies carried out in this thesis can be extend to investigate the H-phase precipitates evolution under externally applied stress.

- The resulting effects of stress-induced aging in NiTiHf alloys on the functional properties such as super-elastic response, super-elastic fatigue of these NiTiHf alloys may be explored.

- Computational thermodynamic studies may be taken up to predict the higher order NiTiHf HTSMAs which can be verified using experimental methods. First principle calculations can be carried out to predict phase stabilities in theses alloys.

These studies can pave the way for designing Ni-rich NiTiHf alloys to interesting applications in industries other than aerospace and aircraft industry such as nuclear sector, where these alloys can be utilized as safety devices for decay heat removal [325], couplings for pipes, centrifugal fans in nuclear reactor ventilation systems [326] etc. However, to ensure the durability of the device, it must be able to withstand the high neutron fluence which can be taken up as a future investigation on the neutron irradiation stability of NiTiHf HTSMAs.

Since our work has shown that by selecting a proper aging condition, the thermal cyclic stability of $Ni_{50.3}Ti_{29.7}Hf_{20}$ HTSMA composition can be significantly enhanced, this alloy can find application as thermal switches [327]. Since SMAs basically convert heat energy to mechanical work, it can simultaneously act as sensor as well as can generate work. Schematic of a thermal conduction switch is shown in Figure 8.1.

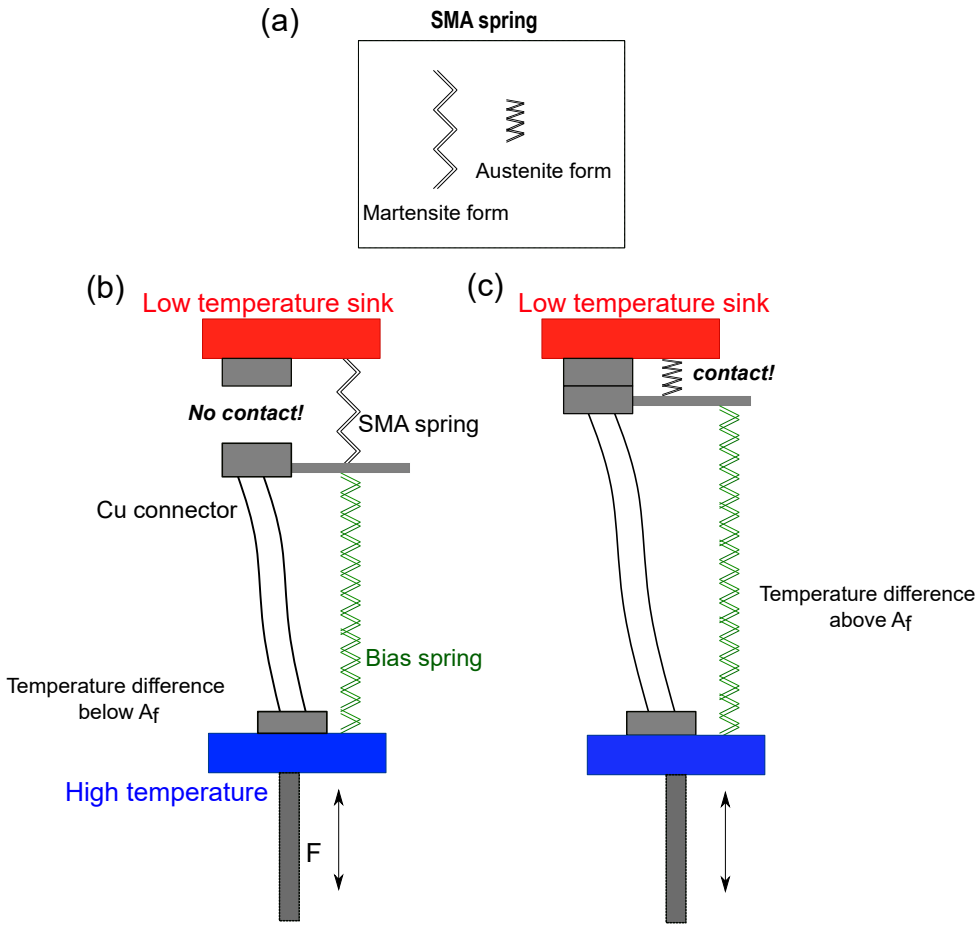

Figure 8.1: Schematic representation of a a HTSMA thermal switch. (a) SMA spring in austenite and martensite forms, (b) when the temperature of the Copper connector below A_f (, (c) when the temperature of the Copper connector above A_f. Back and forth movement of the Bias spring during thermal cycling of the SMA spring gives rise to force F, which can be converted to work.

The figure 8.1(a) shows the macroscopic shapes of the SMA spring in the martensite state (at $T < A_f$) and austenite state (at $T > A_f$). This SMA spring acts as a sensor in a way that when the temperature of the Cu connector is below A_f, the SMA spring expands and attains its martensite form, breaking its contact with the low temperature sink, as seen from figure 8.1 (b), maintained at temperature below M_f for the SMA alloy composition. However, as soon as the temperature reaches above A_f, the contact of Cu connector with sink is enabled (figure 8.1 (c)) due to austenite phase transformation. Therefore, such switches can act as sensor which are capable of connect the equipment to heat sink preventing it from overheating and again disconnect from heat sink, so that a constant operating temperature is maintained. Furthermore, this back and forth movement of the bias spring over repeated thermal cycles generates force F, which can be converted to work.

APPENDIX I

Diffusional Phase Transformation

The diffusional transformations, as the name suggests, involve the diffusion of atomic species in the crystalline solid over distances much larger than the typical lattice spacing of the structure. Generally, the alloy systems which undergo diffusional transformation, lower their free energy by going to a more stable structure via: Nucleation, growth and coarsening of the new phase. Thermal fluctuations lead to long-range atomic diffusion and nuclei of the new phase appear within the matrix. However, due to the creation of new interfaces and consequent strain, there is an increase in the total free energy of the system leading to an energy barrier. This barrier destabilizes nuclei with sizes below a certain critical size. Once that energy barrier is crossed, those nuclei grow into final stable phase and finally coarsen to reduce the interface energy. One type of diffusional phase transformation commonly encountered in metallic alloys is known as *Precipitation*.

I.1. Precipitation: Basic Concepts

When an alloy existing as phase $\alpha^{'}$ with composition C_0 at temperature T_1, is rapidly cooled to temperature T_2 into a two-phase field $\alpha + \beta$, precipitation of β phase occurs from supersaturated $\alpha^{'}$ phase, as shown in Figure I.1.

In next sections, the mechanism of precipitate nucleation, growth and coarsening is discussed.

I.1.1. Classical Nucleation Theory

In case of solid-solid precipitation reaction, the free energy difference between initial and final states is the driving force behind nucleation of the precipitate phase. This process is initiated by the gathering a very small number of solute atoms inside the parent phase, with a fuzzy interface separating the two. However, the nucleated atomic configuration tends to strain the parent matrix. Both the interface as well as strain energy add positive

energy terms to the total free energy and destabilize the system. But, once the size of this nucleated configuration increases up to a certain critical radius such that it overcomes the opposing forces, it grows into *embryo* or *cluster*, with a sharp boundary marking the precipitate-matrix interface. As per the classical nucleation theory, nucleation event can occur in two ways: *Homogeneously* and *Heterogeneously*.

Homogeneous Nucleation: Homogeneous nucleation of precipitate (β-phase) happens uniformly throughout the parent α phase. Change in the total free energy of the system can be written as:

$$\Delta G_{total} = -V\Delta G_v + A\gamma + V\Delta G_s \tag{I.1}$$

where, -VΔG$_v$ is decrease in the volume free energy due to the creation of a more stable β phase inside the parent α phase quenched to a lower temperature T$_2$. Here, γ is the increase in surface energy per unit volume of the system due to creation of the α/β interface with an an area A. The term V ΔG$_s$ is a positive contribution from the strain energy, caused by the β phase crystal lattice trying to fit perfectly inside the crystal lattice of the α phase. When there is exact matching of lattice planes between the precipitate and matrix, in other words, the interface is *coherent*, these nuclei assume a spherical shape. In other cases, where the lattice plane matching is not perfect or totally lacking *i.e.* the interface is *semi-coherent* or *incoherent*, respectively. Under these conditions, anisotropic nuclei(such as platelets or rods) form. For simple case of spherical nuclei, the change in

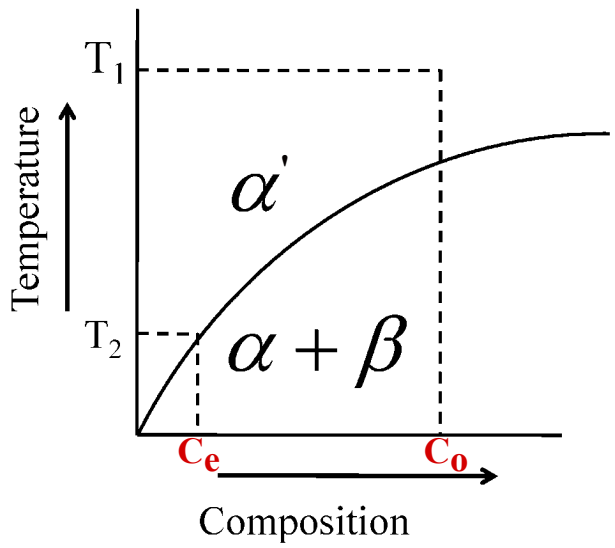

Figure I.1: Precipitation of phase β from solid solution α.

total free energy can be written down as:

$$\Delta G_{total} = -\frac{4}{3}\pi r^3(\Delta G_v - \Delta G_s) + 4\pi r^2 \gamma_{\alpha\beta} \tag{I.2}$$

Figure I.2 depicts the variation of ΔG_{total} as a function of nucleus radius (r). Balance of

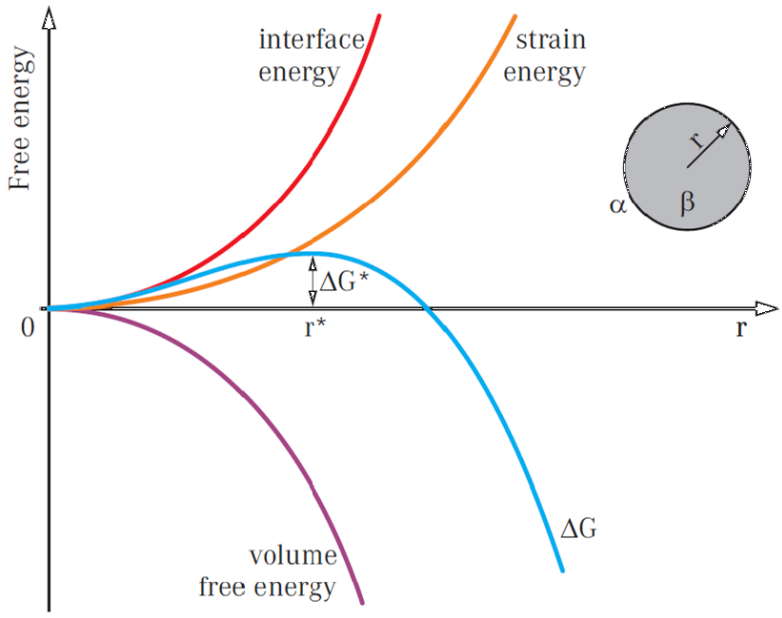

Figure I.2: The free energy barrier ΔG^* and the critical nucleus size r^* according to classical nucleation theory based on hetero-phase fluctuations

all these terms decide the critical radius of an embryo (r^*), which is decided by the radius at which ΔG_{total} has a minimum. Variation of total free energy change is displayed in Figure I.2. Thus, when

$$\frac{d\Delta G_{total}}{dr} = 0; \Rightarrow r^* = \frac{2\gamma_{\alpha\beta}}{(\Delta G_v - \Delta G_s)} \tag{I.3}$$

the free energy barrier or activation energy for nucleation, ΔG^* is:

$$\Delta G^*_{Homo} = \frac{16\pi\gamma^3_{\alpha\beta}}{3(\Delta G_v - \Delta G_s)^3} \tag{I.4}$$

Homogeneous nucleation is a rather difficult process. A large amount of undercooling is required for the nuclei to attain critical radius. Nature generally prefers a site-specific nucleation of the precipitate phase, where certain high energy sites such as grain-boundaries, dislocations *etc.* act as preferential nucleation sites. This results in lowering of the activation barrier and such nucleation is termed as *Heterogeneous nucleation.*

Heterogeneous Nucleation: When the alloy, in its original configuration, contains high-density of defects such as grain boundaries, dislocations *etc.* and is quenched to a two-phase field, the precipitate phase tends to nucleate on these sites to bring down the overall free energy of the system. If -ΔG_d is the reduction the free energy by precipitation on the defect sites, the change in total free energy during heterogeneous nucleation can be written as:

$$\Delta G_{total} = -V\Delta G_v + A\gamma + V\Delta G_s - \Delta G_d \tag{I.5}$$

Assuming: (i) solid nuclei form on the defects as spherical caps, with the contact angle between precipitate and defects as θ and (ii) the surface forces balance each other at the point of contact of precipitate and surface, in the direction parallel to the surface, as shown in Figure I.3 (a). The angle θ is a function of the surface energy terms, shown in Figure I.3 (b) and is given as:

$$\cos\theta = \frac{\gamma_{\alpha s} - \gamma_{\beta s}}{\gamma_{\alpha\beta}} \tag{I.6}$$

The change in free energy associated with heterogeneous precipitation becomes:

$$\Delta G^{hetero}_{total} = -V(\Delta G_v - \Delta G_s) + A_{\alpha\beta}\gamma_{\alpha\beta} - A_{\alpha s}\gamma_{\alpha s} \tag{I.7}$$

Here, $A_{\alpha s}\gamma_{\alpha s}$ is the reduction in free energy due to the formation of precipitate on defect surface in α phase. The activation energy for the heterogeneous and homogeneous nucleation, Δ G^{hetero}_{total} and Δ G^{homo}_{total}, respectively are related as:

$$\Delta G^*_{Hetero} = \Delta G^*_{Homo}\left[\frac{(2 - 3\cos\theta + \cos^3\theta)}{4}\right] \tag{I.8}$$

This means that for all the angles of contact between the β phase and the defect surface in

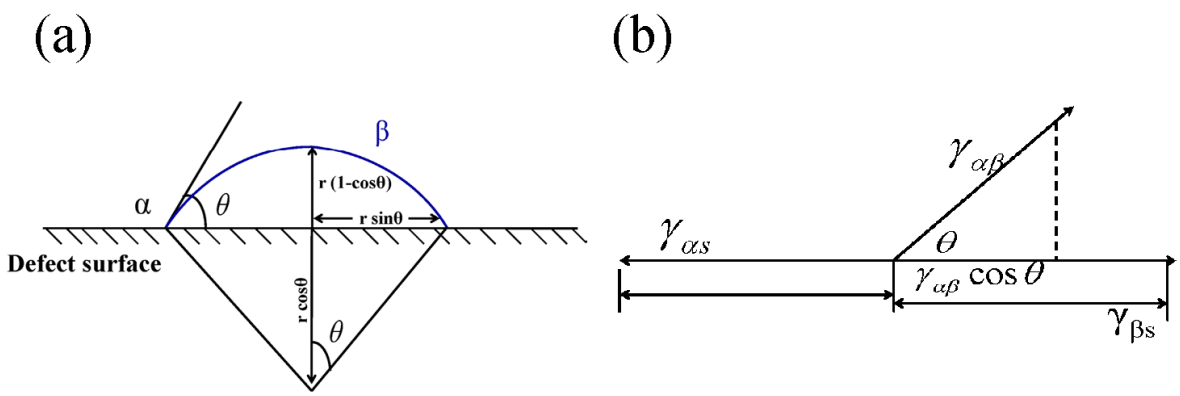

Figure I.3: (a) Spherical cap embryo of β phase, (b) Contact angle θ between α and β phases.

α phase, heterogeneous precipitation causes huge reductions in the the total free energy, for a given embryo radius. Now once these embryos attain critical radius, they tend to grow, if enough time is allowed.

I.1.2. Diffusion-Controlled Growth

During the rapid cooling or quenching, the concentration of solute B in the precipitate is higher than in the matrix and is labeled as C^B_β. Figure I.4 (a) demonstrates the concentrations of solute B atoms at the precipitate-matrix interface and away from the interface. If it is assumed that the time taken for atoms to cross the precipitate-matrix interface is much smaller than the time taken by solute atoms to diffuse up to the matrix, then the process is termed as diffusion controlled. Under such conditions, the concentration of B atoms (C^B_β) in the β phase is always in equilibrium with that of in the α phase C^B_α at the interface. However, at distances far away from the interface, the concentration of solute in matrix rises to C^B_∞, which is the composition of the matrix just before the precipitation started. Now as the α/β interface, with an area $a_{\alpha\beta}$, moves by a distance dx, it has the

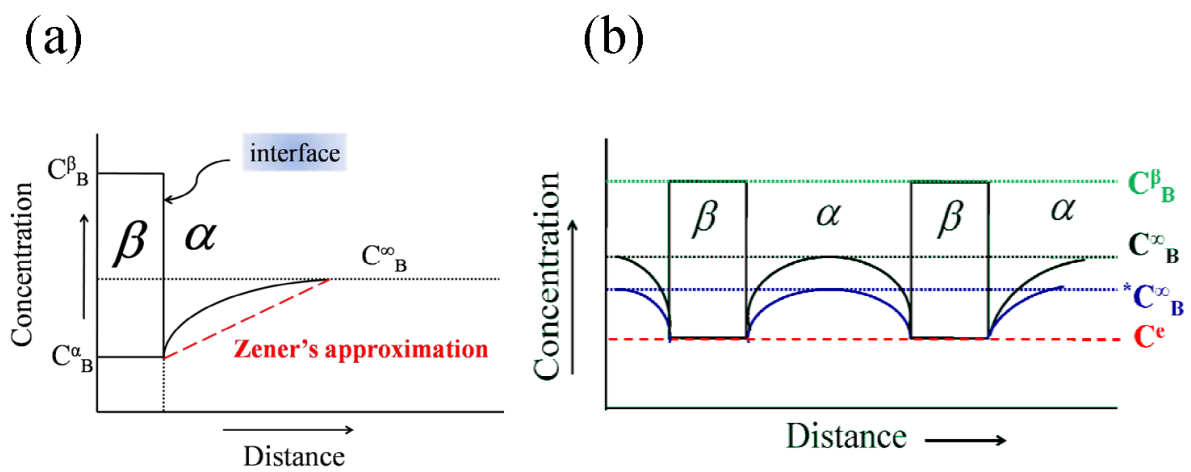

Figure I.4: (a) Concentrations of solute B atoms at the precipitate-matrix interface and away from the interface, (b) Composition variation of solute B in the α matrix with distance.

effect of converting the volume $a_{\alpha\beta}dx$ from the concentration of solute B from C^α_B to C^β_B. For this to happen, $(C^\alpha_B\text{-}C^\beta_B)a_{\alpha\beta}dx$ atoms jump across the interface. By Fick's law, the total number of atoms should remain constant. So, if J is the flux of atoms crossing the interface per second per unit area and D is the diffusion constant of the solute B, then

$$-Jdt = (C^\beta_B - C^\alpha_B)dx = D\Big(\frac{dC^\alpha_B}{dx}\Big)dt \Rightarrow \frac{dx}{dt} = \frac{D}{\Big(C^\beta_B - C^\alpha_B\Big)}\frac{dC^\alpha_B}{dx} \tag{I.9}$$

Now, as per Zener's approximation, the quantity (C^B_∞-C^B_α) varies linearly such that

$$(C^\beta_B - C^\alpha_B)dx = \frac{1}{2}(C^\infty_B - C^\alpha_B)x \tag{I.10}$$

Equating these two equations gives us:

$$\frac{dx}{dt} = \frac{D}{2}\Omega\frac{(C^\infty_B - C^\alpha_B)}{(C^\beta_B - C^\infty_B)}\frac{1}{x} \tag{I.11}$$

where, $\Omega = \frac{\left(C^\infty_B - C^\alpha_B\right)}{\left(C^\beta_B - C^\alpha_B\right)}$ is the degree of super-saturation and is a dimensionless parameter. In most cases, $(C^\beta_B - C^\infty_B) = (C^\beta_B - C^\alpha_B)$. Integration of (eq. I.11) gives:

$$x = \Omega\sqrt{Dt} \tag{I.12}$$

This is *Parabolic diffusion-controlled growth law* for the growth of precipitates controlled by diffusion of the solute atoms across the interface. Figure I.4 (b) presents the concentration of solute atoms (B) in the α matrix as a function of distance from the α/β interface. When these precipitates grow big enough that their diffusion fields start interacting, this will deplete the solute from the matrix by reducing the solute concentration in the matrix from the value prior to precipitation. This lowers C^∞_B to $^*C^\infty_B$. The precipitates keep on growing by the diffusion of the solute across the interface till matrix solute concentration drops to equilibrium solute concentration at that temperature, C_e. Once the C_e is attained, the excess solute in the alloy is uniformly distributed and the growth completely stops.

I.1.3. Precipitate Coarsening

When all the excess solute has emerged in the form of β-phase precipitates with certain size-distribution, the system contains a large number of precipitate-matrix interfaces. Due to the curvature of this interface, there is an excess of solute near smaller precipitates. This is known as *Capillary* or *Gibbs-Thomson effect*. So, once the growth stops, bigger precipitates draw solute from the smaller ones and grow at their expense. This results in the lowering of inter-facial energy and the overall free energy of the system. This process is termed as *precipitate coarsening*.

Gibbs-Thomson Effect: Consider an ideal alloy A_aB_b, existing as α phase, with composition C^α_∞, containing n_A and n_B moles of A type and B-type atoms. The total Gibbs free

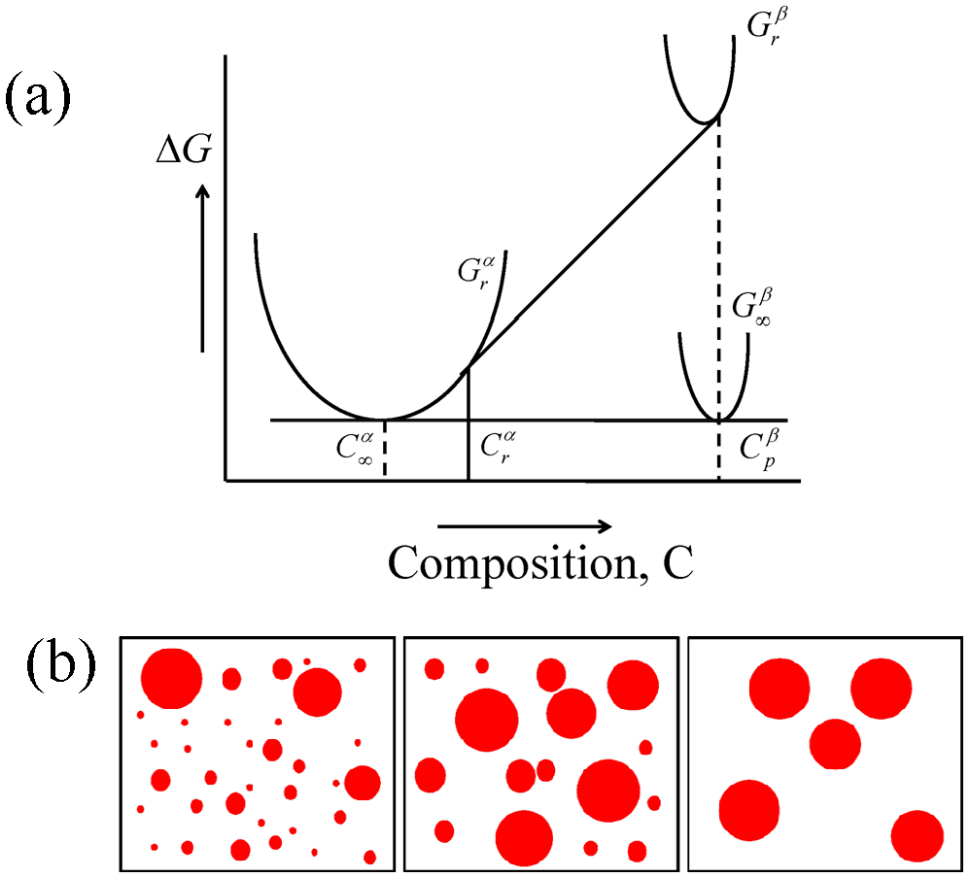

Figure I.5: (a) Free energy curves for α and β phases, (b) Increase in precipitate size and decrease in their number density depicting *precipitate coarsening*.

energy, G^α of this alloy at a temperature T can be written down as:

$$G^\alpha = n_A\Big[G_A + kT\ln\left(n_A\right)\Big] + n_B\Big[G_B + kT\ln\left(n_B\right)\Big] \tag{I.13}$$

G_A and G_B are free energies of pure A and B, respectively and k is Boltzmann constant. Upon quenching this alloy, new solute-rich β phase co-exists with the α phase, with concentration of solute B in β phase as $C_p^\beta = \frac{n_B}{(n_A+n_B)}$. In precipitate-matrix interface has surface area S^β, the free energy of this β phase is given as:

$$G^\beta = n^\beta G_n^\beta + \gamma S^\beta \tag{I.14}$$

where, γ is the inter-facial surface energy. At equilibrium, the transfer of a few atoms of A and B type from the α phase to the β phase will not alter C_∞^α. The free-energy curves for α and β phases are shown in Figure I.5 (a).

According to Gibbs-Duhem equation [328], upon transfer of dn atoms, change in free

energy for α phase is given by:

$$dn(1 - C_p^\beta)\frac{\partial G^\alpha}{\partial n_{A\,|C_\infty^\alpha}} + dnC_p^\beta\frac{\partial G^\alpha}{\partial n_{B\,|C_\infty^\alpha}} = dn\frac{\partial G^\beta}{\partial n} \tag{I.15}$$

Now, if it is assumed that the precipitates are spherical in shape with radius r and atomic volume v_{atomic}^β, such that $\frac{4}{3}\pi r^3 = \mathrm{n}_B \mathrm{v}_{atomic}^\beta$ then, the change in free energy of the β phase becomes:

$$dG^\beta = \frac{\partial G^\beta}{\partial n} = G_n^\beta + \frac{2\gamma v_{atomic}^\beta}{r} \tag{I.16}$$

Similarly, from equation I.13, change in the free energy of α phase upon atom transfer is given as:

$$dG^\alpha = (1 - C_p^\beta)\Big[G_A^\alpha + kT\ln\left(1 - C_\infty^\alpha\right)\Big] + C_p^\beta\Big[G_B^\alpha + kT\ln C_\infty^\alpha\Big] \tag{I.17}$$

Equating equations I.16 and I.17, for extremely dilute solutions such that $\mathrm{C}_p^\beta = 1$, Gibbs-Thomson equation takes the following form:

$$C_r^\alpha = C_\infty^\alpha exp\Big(\frac{2\gamma v_{atomic}^\beta}{rkT}\Big) \tag{I.18}$$

This equation suggests that the presence of an interface between a precipitate of radius r and the matrix tends to increase the solute concentration near the precipitate. However, this enhancement of solute or *capillarity effect* near the precipitates is appreciable only for the precipitates $\sim$ 1 - 50 nm. For larger precipitates, the effect is negligible.

Coarsening: Coarsening is the next step to lower the total free energy. Due to *capillarity effect*, the smaller precipitates have excess solute content near their vicinity, bigger precipitates derive the solute from the smaller precipitates and grow further in size at the expense of smaller ones. As a result, although the volume fraction of the precipitates remain constant, their number density reduces (Figure I.5 (b)). This leads to a considerable reduction in the interfacial energy of the system and hence the overall free energy, making system thermodynamically more and more stable. This process is also known as *Ostwald Ripening*. Lifshitz-Sloyozov-Wagner (LSW) [287] theory is used to describe the Ostwald ripening process in alloys. According to this theory, in the limit of dilute precipitate concentrations such that diffusion field between neighbouring precipitates can be ignored, the characteristic size of the precipitates increases as $\sim \mathrm{t}^{\frac{1}{3}}$ and their number density decreases as $\sim \mathrm{t}^{-1}$. However, for cases such as Ni-based superalloys which have

high volume fractions of precipitates [289], LSW theory has to be modified. For such alloy systems, several modifications to the LSW formulations have been suggested in literature such as Modified-LSW (MLSW) [329], Trans-Interface Diffusion Controlled Coarsening (TIDC) model [330].

APPENDIX II

Basics of Small Angle Scattering

Small-angle scattering is a powerful non-destructive tool to probe the nano-structures (1 nm to several 100 nm) in condensed matter and provides statistically averaged quantitative information from bulk sample. This technique involves elastic scattering of X-rays and neutrons over angles in the range 0.1° to 2°, the angular range much smaller than X-ray and neutron diffraction experiments, hence the name *small-angle*. This technique finds suitability in wide range of fields including condensed matter, polymers, molecular biology and metallurgy. In fact, small-angle studies dates back to the works of Guinier who introduced the concept of *particle scattering* while interpreting the diffuse x-ray streaks appearing in the x-ray Laue diffraction pattern of the aged Al-Cu alloy [331, 332]. This technique provides statistically averaged information about the structure, morphology, size distributions, volume fractions *etc.* of the precipitates from bulk samples, which directly influence the material properties. In case of a system consisting of structural features of colloidal dimensions (R) (1 nm - 1 μm) interacting with X-rays/neutrons of De-Broglie wavelength λ, the path difference between waves scattered by any two atoms will be small for scattering angle $2\theta < \lambda/R$. Typically for Cu-K$_\alpha$ (λ = 1.54 Å), the scattering angle 2θ lies in the range 0.1°-2°. Beyond this range, the waves will interfere destructively and scattered intensity will be zero. In other words, particles much bigger than the incident De-Broglie wavelength act as point scatterers, which scatter incident radiation at small angles.

II.0.1. Small-angle Scattering from a Single Particle

The concept of small-angle scattering can be understood in terms of interference of the the scattered waves. Scattering of incoming plane waves by electrons/nuclei in matter generate secondary waves. These secondary waves superimpose upon each other to generate an interference pattern. For an incoming wave ($\overrightarrow{K}_i$) elastically scattered by a potential

field of strength $\rho(\vec{r})$ brings a momentum transfer $\vec{Q} = \vec{K}_f - \vec{K}_i$. Then the intensity of the scattered wave, A($\vec{Q}$), is the Fourier transform of the potential field $\rho(\vec{r})$:

$$A(\vec{Q}) = \int_V \rho(\vec{r}) \exp(i\vec{Q}.\vec{r}) \tag{II.1}$$

The scattered intensity, I($\vec{Q}$) is then:

$$I(\vec{Q}) = \int_{V1} \int_{V2} \rho(\vec{r_1})\rho(\vec{r_2}) \exp(i\vec{Q}.(\vec{r_1} - \vec{r_2}))dV1dV2 \tag{II.2}$$

Figure II.1 shows the schematic of incoming wave (x-ray or neutron) by a group of point-scatterers distributed in the particle over volume V_p.

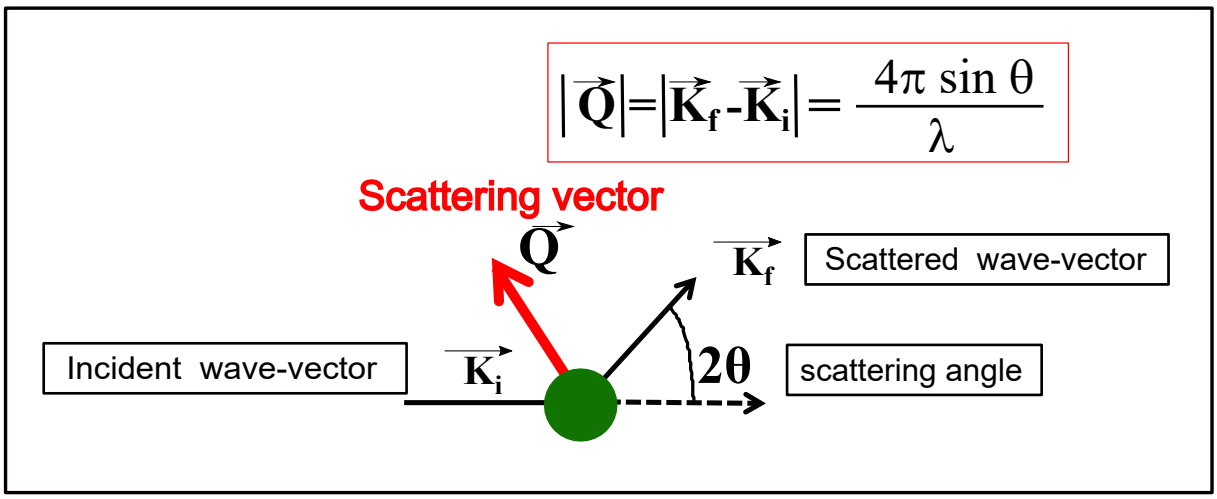

Figure II.1: Schematic of scattering of an incoming plane wave with wave-vector $\vec{K}_i$ by group of point-scatterers over an angle 2θ. The scattered intensity is represented in terms of scattering wave-vector $\vec{Q} = \vec{K}_f$ - $\vec{K}_i$, scattered wave-vector being $\vec{K}_f$

For a macroscopically isotropic system, the the potential field is orientation independent and $< \exp(i\vec{Q}.\vec{r}) >$ upon integration over all the orientations can be approximated as $\frac{\sin Qr}{Qr}$. For such particles, the scattered intensity in equation II.3 becomes:

$$I(Q) = V_p \int_0^\infty 4\pi r^2 \gamma(r) \frac{sinQr}{Qr} dr \tag{II.3}$$

This single-particle scattering intensity is function of electron density-density correlation γ(r) due to finite size of the particle.

II.0.2. Scattering from Two-Phase System

Above eq. II.3 indicates that intensity of the scattered wave is governed by the potential field or scattering length density (SLD) of the scatterers. In case of X-ray scattering, this

potential is essentially the average electron density of the particle. On the other hand, neutrons being electrically neutral, interacts with matter through nuclear interactions and the nuclear potential is expressed in terms of the neutron scattering length density discusses in subsequent sections.

In case of a dilute two-phase system consisting of identical particles (SLD: ρ_1), dimension 'R' (shown in Figure II.2 and volume fraction ϕ_2 dispersed in a homogeneous matrix (SLD: ρ_2) and volume fraction ϕ_2, scattered intensity will be a function of $(\rho_1 - \rho_2)^2$, termed as *contrast*, a particle form-factor P(Q,R) and structure-factor term S(Q,R) which takes into account inter-particle interactions. The total scattered as per equation II.5, the total intensity will be a sum of the individual scattered intensities.

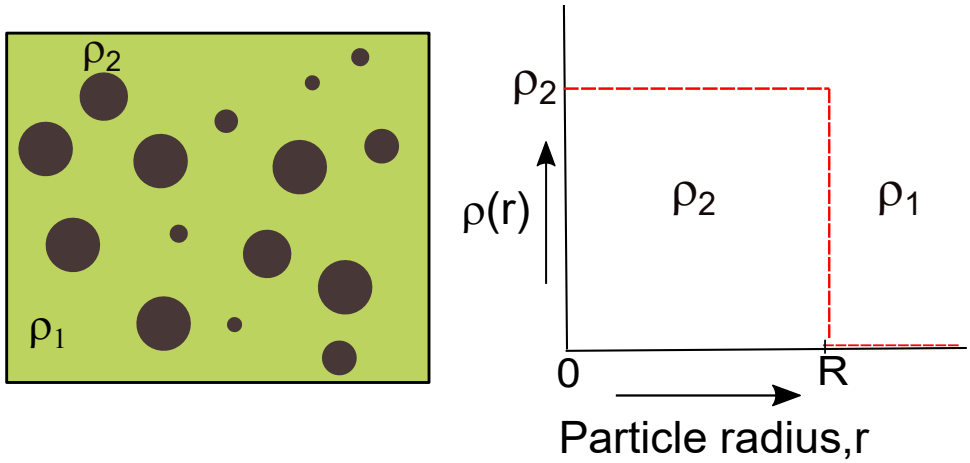

Figure II.2: Schematic of two-phase system with discrete particles embedded in a homogeneous matrix with electron density/scattering length densities ρ_1 and ρ_2

$$I(Q) = (\rho_1 - \rho_2)^2 \int_0^R 4\pi r^2 \gamma(r) \frac{sinQr}{Qr} dr \tag{II.4}$$

$$I(Q) = (\rho_1 - \rho_2)^2 (\frac{4\pi R^3}{3})^2 P(Q,R) = (\rho_1 - \rho_2)^2 V_p^2 P(Q,R) S(Q,R) \tag{II.5}$$

For N identical particles in a sample volume V, such that number-density of particles is $\frac{N}{V}$, the total scattered intensity for a mono-disperse two-phase system is:

$$I(Q) = \frac{N}{V} (\rho_1 - \rho_2)^2 V_p^2 P(Q,R) S(Q,R) \tag{II.6}$$

For a system containing interacting particles with poly-dispersity in size (defined by a poly-dispersity index s), is described by a distribution function D(r) [333], scattered intensity for such a system under local mono-disperse approximation [263] is expressed

as:

$$\boxed{I(Q) = (\Delta\rho)^2 \int_0^\infty D(r)V_p^2(r)P(Q,r)S(Q,R)dr} \tag{II.7}$$

where, $(\Delta\rho)^2 = (\rho_1 - \rho_2)^2$ is the *scattering contrast*. Since both X-rays and neutrons interact differently with matter, combined Small-Angle X-Ray Scattering (SAXS) and Small-Angle Neutron Scattering (SANS) experiments let an in-depth investigation of the system. It needs to be mentioned here that SAXS as well as SANS intensities are a function of the scattering vector, the smaller features scatter at higher Q-values and vice-versa. In present work, both SAXS and SANS have been utilized as probes to investigate the precipitate micro-structure evolution as a function of aging conditions.

II.0.3. Small-Angle Neutron Scattering (SANS)

Due to large neutron scattering length difference between Ni, Ti and Hf, SANS is an ideal technique for quantitative evaluation of meso-scopic chemical heterogeneities such as precipitates in NiTi based alloys. For neutrons, the scattering length of a phase consisting of N atoms is given as $\sum_{i=1}^{n} b_i N_i$, where b_i (in fm) is neutron scattering length of the ith atoms. Since for scattering at small-angles, the observed length scale is much larger than the inter-atomic spacings, the neutron scattering length can be taken as total scattering length of the atoms averaged over the volume of the phase 'm' (V_m) such that neutron Scattering Length Density (SLD) $= \sum_{i=1}^{n} \frac{b_i^m N_i}{V_m} = \frac{b_m}{V_m}$. Similarly, the neutron SLD of phase 'p' $= \sum_{i=1}^{n} \frac{b_i^p N_i}{V_p} = \frac{b_p}{V_p}$. Then the "contrast" term for SANS intensity becomes:

$$\boxed{\left(\rho_m - \rho_p\right)^2_{SANS} = \left[\frac{b_m}{V_m} - \frac{b_p}{V_p}\right]^2} \tag{II.8}$$

In present case, the SANS contrast between $Ni_{50.3}Ti_{29.7}Hf_{20}$ matrix and aging induced precipitates is $\sim 3.7 \times 10^{20}$ cm^{-4}. All SANS instruments consist of three major components:

- Selection a specific De-Broglie λ from the incident thermal neutrons beam using monochromator,
- Collimation of the selected wavelength by two apertures (source and specimen apertures), separated by distance of few meters,

- Sample holder for scattering of monochromatic collimated neutrons, and
- Detection of scattered neutrons by a detector.

The SANS instrument can be categorized into: (i) Pin-hole based SANS instrument and, (ii) Double-crystal based SANS instrument. In the pin-hole collimator based SANS instruments, collimation lengths are quite large, which require long collimating tubes ($\sim$ 1-20 m) need to be employed. Collimator with adjustable lengths is employed in several instruments to access variable Q-ranges. Such pin-hole collimated SANS instruments are much bigger in size, with maximum accessible length scales $\sim$ 100 nm. For larger length-scale in-homogeneities beyond this limit, a double-crystal based SANS instrument is used. In such an instrument, the sample is placed between two perfect crystals known as: Monochromator and Analyser. The scattered intensity is collected by rotating Analyser crystal with respect to the other crystal and scattered intensity pattern is collected by the detector.

II.1. Small-Angle Scattering Data Analysis

The experimental SAXS as well as SANS data were modelled according to equation II.7 using non-linear least squares fitting procedure by SASFIT [334] software, by appropriately choosing the form-factor P(Q,R) as per the particle morphologies obtained by complementary TEM investigations. Fitted data was used to obtain structural information of the system such as particle size, particle/matrix interface, their surface to volume ratio and their volume fraction. In current work, the particle size-distribution D(r) is described in terms of a log-normal distribution:

$$D(r) = \frac{\left(\frac{N}{V}\right)}{sr\sqrt{2\pi}} \exp\left[-\frac{\ln\left(\frac{r}{\mu_o}\right)^2}{2s^2}\right]. \tag{II.9}$$

where, s is the poly-dispersity index, μ_o is median radius and N is the total number of particles. A typical SAXS/SANS profile for poly-disperse spherical particles (Median radius, μ_o = 35 nm), along with their size-distributions D(r) around the median value looks like as shown in Figure II.3. We next introduce the concepts of Guinier's law, Porod's law and Porod invariant.

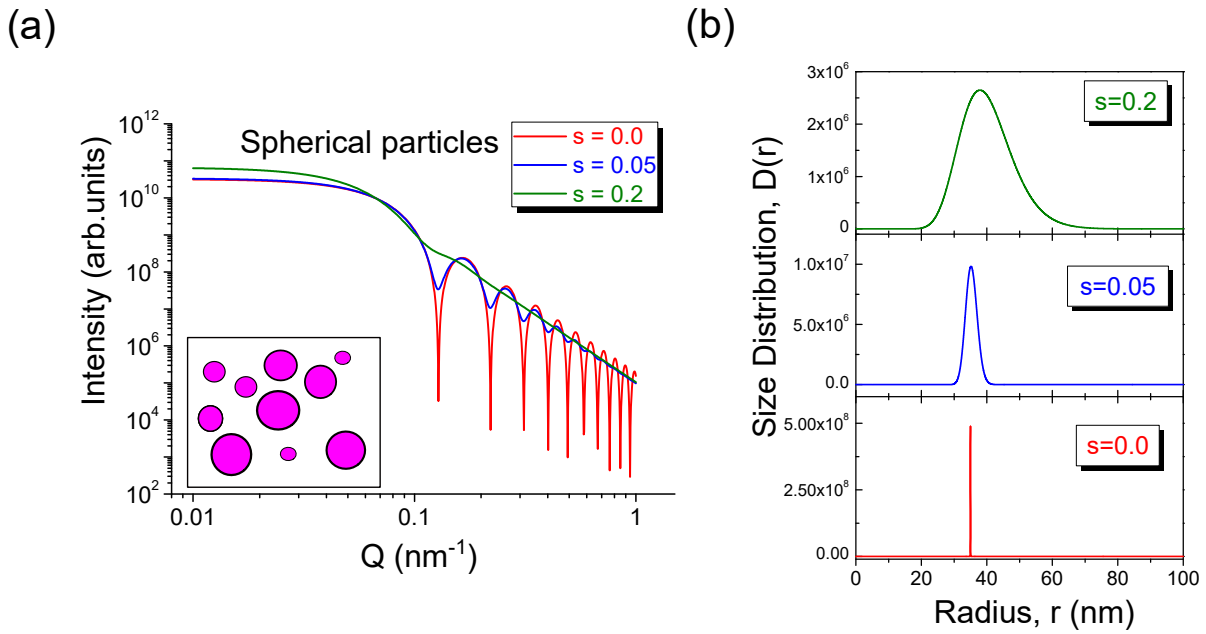

Figure II.3: (a) Small-angle scattering profiles for N spherical particles (median radius of 35 nm) distributed over unit volume with different poly-dispersity index (s = 0, 0.05 and 0.2) (b) Size-distributions corresponding to each poly-dispersity index

II.1.1. Guinier's Law:

Guinier radius of a particle (R_G) is defined as average electron density weighted distance of the scatterers from the centre of mass of the object. The quantity $\frac{\sin Qr}{Qr}$ in eq. II.3 can be expanded as:

$$\frac{\sin Qr}{Qr} = 1 - \frac{Q^2r^2}{6} + \frac{Q^4r^4}{120} + ... \tag{II.10}$$

For the very small scattering angles, in the limit Q $\rightarrow$ 0, intensity scattered by a single particle reduces to:

$$\boxed{I(Q) = I_0 exp(-Q^2R_G^2/3)} \tag{II.11}$$

The Guinier radius of a particle can be obtained from the slope of a straight line fit of the plot between $\log_e(I(Q))$ vs. Q^2, as shown in the Figure II.4.

For a spherical particle of radius R, the Guinier radius $R_G = \sqrt{\frac{3}{5}}R$. Guinier law also holds for dilute concentration of poly-disperse near spherical particles with size-

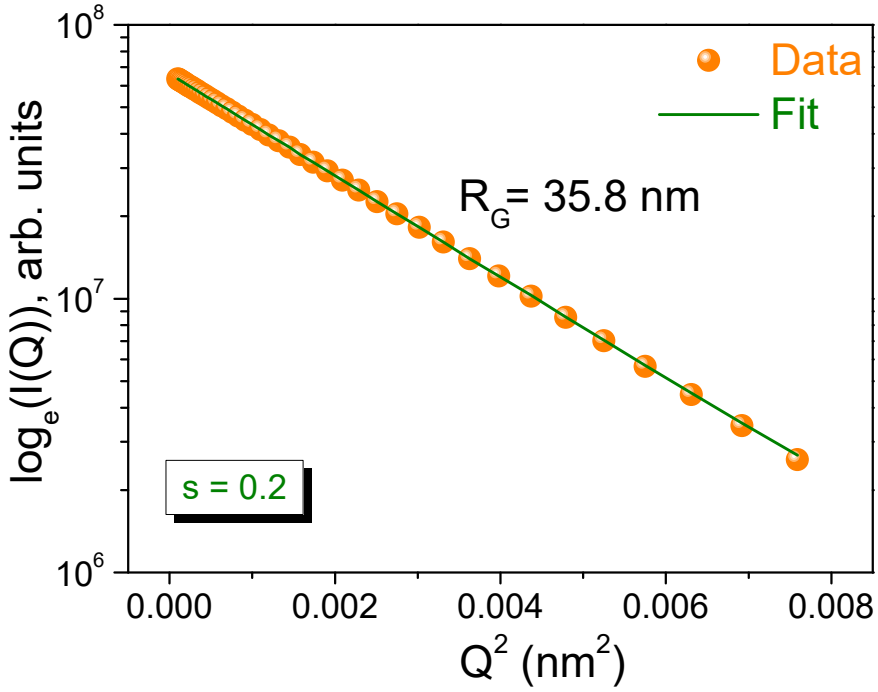

Figure II.4: Slope of a linear least-squares fitted plot of $\log_e$(I(Q)) vs Q^2 provides Guinier radius R_G of the spherical particles

distribution D(r). For such a system, the Guinier radius R_G can be estimated as:

$$\boxed{R_G = \sqrt{\frac{3}{5}}\left(\frac{< r^8 >}{< r^6 >}\right)^{1/2}} \tag{II.12}$$

where, $< r^t >$ is the tth moment of particle size-distribution defined as $< r^t >= \frac{\int D(r) r^t dr}{\int D(r) dr}$. In the present study, we determined the precipitate Guinier radius as a function of aging conditions using both the methods. A code is written in python for determining Guinier radius and can be found in Appendix III.

II.1.2. Porod's Law:

The scattering intensity in the limit $Q \to \infty$ reveals the information of the particle-matrix interface. Typically, in the limiting case of $\lim_{Q\to\infty} I(Q) = \frac{K_p}{Q^p}$, K_p being Porod's constant and 'p' the Porod's exponent. For sharp change in the electron density between particle (ρ_1) and the matrix (ρ_2) at the interface *i.e.* sharp interface, the value of Porod's exponent is equal to 4.0. For particles bearing with sharp interface with matrix, the intensity I(Q)

varies with Q according to *Porod's Law*:

$$\boxed{I(Q) = \frac{K_p}{Q^4}} \tag{II.13}$$

For a system obeying Porod's law, the plot of I(Q)Q^4 vs. Q is a flat plateau for high Q values after initial fluctuations at low Q values, as shown in Figure II.5.

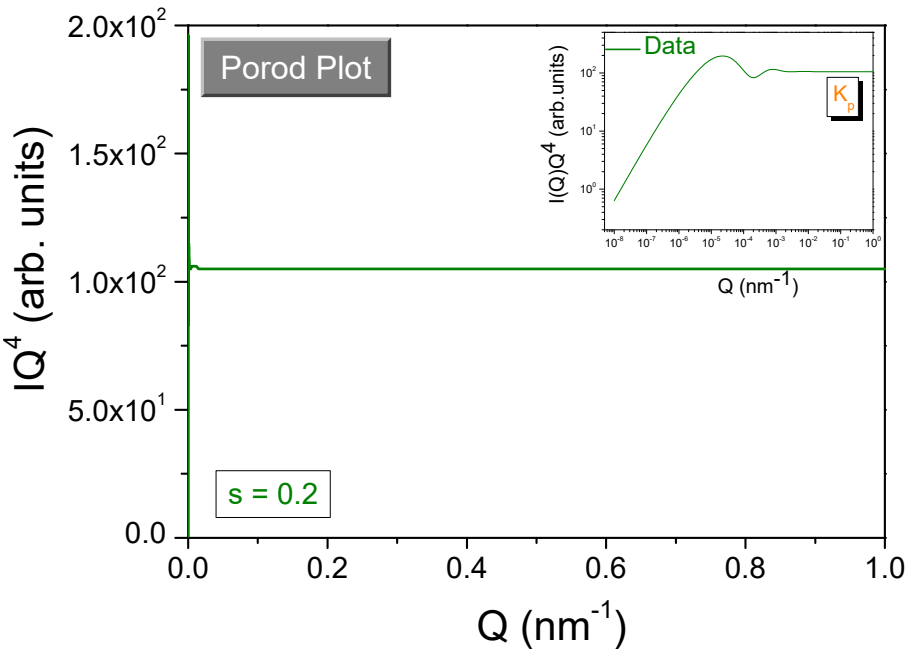

Figure II.5: Porod's plot corresponding to particles bearing sharp interface with the matrix

The ordinate of the plateau provides value of Porod's Constant K$_p$. For the large scattering angles, in the limit Q $\rightarrow \infty$, intensity scattered by particles with surface area S becomes:

$$I(Q) = \frac{2\pi(\rho_1 - \rho_2)^2 S}{Q^4} \tag{II.14}$$

This equation is applicable to two-phase systems with sharp interfaces such as precipitate-matrix interface in alloys. The Porod's constant is determined by plotting I(Q)Q^4 vs. Q plot, which eventually is used to obtain specific surface to volume ratio (S/V) of the precipitate with mass-density ρ_0 as:

$$\boxed{\frac{S}{V} = \pi \left[\frac{\lim_{Q\rightarrow\infty} I(Q)Q^4}{\rho_0 \int_0^\infty I(Q)Q^2 dQ} \right]} \tag{II.15}$$

The quantity $\int_0^\infty I(Q)Q^2 dQ$ is known as Porod's Invariant and is related to the

particle volume-fraction ϕ as

$$\boxed{Porod\ Invariant = \int_0^\infty I(Q)Q^2 dQ = 2\pi^2(\Delta\rho)^2\phi(1-\phi)} \tag{II.16}$$

A code is written in python for surface to volume ratio determination and is given in Appendix IV.

APPENDIX III

Python Program for Determination of Guinier Radius

Part 1

```python

### This Code calculates the Guinier radius from Small-angle scattering profile using Guinier Law

data = np.loadtxt("inputfile.txt", dtype=float)   # Opening input file
f = open("Guinier Radius.csv","w")                # Opening Output file

for line in data:                          # Reading data into an array
q = data[:,0]
I = data[:,1]                              # Data points in the Guinier region
Q = q**2

def exponential(Q,par):                    # Defining exponential function
    I0 = par[0]
    R = par[1]
    fp = I0*exp((-Q*(R**2))/3)
    return fp

def residual(par, y, Q):                   # Defining error function
    errfunc = (y-exponential(Q,par))
    return errfunc
par=[1000.0,5.0]                           # Initial guess value
fit = leastsq(residual, par, args=(I,Q),ftol=1e-10, maxfev=2000)
par = fit[0]

A = np.array(Q)
B = np.array(I)
C = np.array(exponential(Q,par))
out = np.column_stack((A.flatten(),B.flatten(),C.flatten()))

print("Parameters are:\n","I0 = ", par[0],"\n Guinier Radius=", par[1], file=f)
np.savetxt("output.csv", out, delimiter = ',')
f.close()

plt.plot(Q,exponential(Q,par),'-',Q,I,'o')   # Plotting I(q) vs (q**2)
plt.yscale('log')
plt.xlabel('Q**2 (nm-2)', color='b', size=16)
plt.ylabel('Intensity (a.u.)', color='b', size=16)
plt.title('Guinier Radius', color='r', size=32)
plt.show()
```

Part 2

```
### This code calculates the Guinier radius from size-distribution


data = open("inputfile.txt","r")                # Opening an input file
inputdata = data.readlines()
x = arange(0.0001,150,0.5)
for i in range (d):                    # 'd' data points
    AgingTime = eval(str.split(inputdata[i+1])[0])
    N = eval(str.split(inputdata[i+1])[1])      # Median radius, mu
    sigma = eval(str.split(inputdata[i+1])[2]) # Poly-dispersity, sigma
    mu = eval(str.split(inputdata[i+1])[3])

# Distribution Function

    def  SizeDistribution(x):
        distribution=(N/sqrt(2*pi*x*x*sigma*sigma))*exp(-(1.0/2.0)*((log(x)
    -log(mu))/sigma)**2)
        return distribution
    y = zeros(len(x))
    for k in range(len(x)):
     y[k] = SizeDistribution(x[k])

    R8 = sum((x**8)*y)/sum(y)     # Eighth Moment of size-distribution <r8>
    Y1 = array(R8)
    X1 = array(AgingTime)
    out1 = hstack((X1.flatten(),Y1.flatten()))

    R6 = sum((x**6)*y)/sum(y)     # Sixth Moment of size-distribution <r6>
    Y1 = array(R6)
    X1 = array(AgingTime)
    out2 = hstack((X1.flatten(),Y1.flatten()))

#  Guiner Radius
    Rg = sqrt((3.0/5.0)*(R8/R6))
    print(AgingTime,Rg)
```

APPENDIX IV

Python Program to Evaluate Surface to Volume Ratio

```python

data = np.loadtxt("input.txt")
q = data[:,0]                                # Reading data into an array
I = data[:,1]

#  Interpolation of data

f = interp1d(q,I)
def Porodinv_intg(q):
    return f(q)*q*q

###   calculate PorodInvariant

def intg1(fx,i,f,n,flag):                    # Integration subroutine
    h=float((f-i))/float(n)
    s=0
    x=float(i)
    for j in range(n):
        if flag==1:
            s+=h*fx(0.5*(2.*x+h))            # rectangle rule
        elif flag==2:
            s+=0.5*h*(fx(x)+fx(x+h))         # trapezoidal rule
        elif flag==3:
            s+=(1.0/8.0)*h*(fx(x)+3.*fx((3*x+h)/3.0)+3.*fx((3.*x+2.*h)/3.0)
    +fx(x+h))                                # simpson's 3/8 rule
        x+=h
    return s
print(Porodinv_intg(min(q)),Porodinv_intg(max(q)))
PI = intg1(Porodinv_intg,min(q)+0.000001,max(q)-0.00001,1000,3)
print ("Porod Invariant = ", PI)

# Calculating S/V ratio

Kp = float(input('Porod Constant, Kp = '))
rho = float(input('mass-density, rho = '))    #density in g/cc
surfacearea = (pi/rho)*(Kp/PI)*(1.0e3)
print("S/V ratio(m2/g)=", surfacearea)
plt.plot(q,I*q**4,'o')
plt.show()
```

Bibliography

[1] C. Liu, H. Qin, and P. T. Mather, J. Mater. Chem. **17**, 1543 (2007).

[2] A. Lendlein and S. Kelch, Angewandte Chemie International Edition **41**, 2034 (2002).

[3] H. Meng and G. Li, Polymer **54**, 2199 (2013).

[4] W. Huang, Z. Ding, C. Wang, J. Wei, Y. Zhao, and H. Purnawali, Materials Today **13**, 54 (2010).

[5] W. Sokolowski, A. Metcalfe, S. Hayashi, L. Yahia, and J. Raymond, Biomedical Materials **2**, S23 (2007).

[6] L. Machado and M. Savi, Brazilian journal of medical and biological research **36**, 683 (2003).

[7] A. Nespoli, S. Besseghini, S. Pittaccio, E. Villa, and S. Viscuso, Sensors and Actuators A: Physical **158**, 149 (2010).

[8] J. W. Cho, J. W. Kim, Y. C. Jung, and N. S. Goo, Macromolecular Rapid Communications **26**, 412 (2005).

[9] Y. Liu, H. Lv, X. Lan, J. Leng, and S. Du, Composites Science and Technology **69**, 2064 (2009).

[10] A. Lendlein, H. Jiang, O. Jünger, and R. Langer, Nature **434**, 879 (2005).

[11] Y. Liu, H. Du, L. Liu, and J. Leng, Smart Materials and Structures **23**, 023001 (2014).

[12] E. Chau, C. Friend, D. Allen, J. Hora, and J. Webster, Materials Science and Engineering: A **438**, 589 (2006).

[13] T. Ohki, Q.-Q. Ni, N. Ohsako, and M. Iwamoto, Composites Part A: Applied Science and Manufacturing **35**, 1065 (2004), ISSN 1359-835X.

[14] Q.-Q. Ni, C.-s. Zhang, Y. Fu, G. Dai, and T. Kimura, Composite Structures **81**, 176 (2007).

[15] R. Reed, Acta Metallurgica **15**, 1287 (1967).

[16] J.-B. Seol, J. Jung, Y. Jang, and C. Park, Acta Materialia **61**, 558 (2013).

[17] N. Nakanishi, T. Mori, S. Miura, Y. Murakami, and S. Kachi, Philosophical Magazine **28**, 277 (1973).

[18] K. Otsuka and X. Ren, Progress in Materials Science **50**, 511 (2005).

[19] K. Takezawa, T. Shindo, and S. Sato, Scripta Metallurgica **10**, 13 (1976).

[20] W. J. Buehler, J. V. Gilfrich, and R. C. Wiley, Journal of Applied Physics **34**, 1475 (1963).

[21] M. Krishnan, B. C. Maji, and S. Banerjee, Mineral Processing and Extractive Metallurgy Review **22**, 341 (2002).

[22] F. El Feninat, G. Laroche, M. Fiset, and D. Mantovani, Advanced Engineering Materials **4**, 91 (2002).

[23] L. Petrini and F. Migliavacca, Journal of Metallurgy **2011** (2011).

[24] D. J. Hartl and D. C. Lagoudas, Proceedings of the Institution of Mechanical Engineers, Part G: Journal of Aerospace Engineering **221**, 535 (2007).

[25] H. Hosoda, S. Hanada, K. Inoue, T. Fukui, Y. Mishima, and T. Suzuki, Intermetallics **6**, 291 (1998).

[26] G. S. Firstov, J. V. Humbeeck, and Y. N. Koval, Journal of Intelligent Material Systems and Structures **17**, 1041 (2006).

[27] J. V. Humbeeck, Journal of Engineering Materials and Technology **121**, 98 (1999).

[28] J. Ma, I. Karaman, and R. D. Noebe, International Materials Reviews **55**, 257 (2010).

[29] K. Otsuka and K. Shimizu, International Metals Reviews **31**, 93 (1986).

[30] M. Zarinejad and Y. Liu, Advanced Functional Materials **18**, 2789 (2008).

[31] D. Angst, P. Thoma, and M. Kao, Journal de Physique IV **05**, C8 (1995).

[32] S. M. Russell and F. Sczerzenie, MRS Proceedings **360** (1994).

[33] C. C. Wojcik, Journal of Materials Engineering and Performance **18**, 511 (2009).

[34] Z. J. Pu, H.-K. Tseng, and K.-H. Wu, in *Smart Structures and Materials 1994: Smart Materials*, edited by V. K. Varadan (SPIE, 1994).

[35] X. Meng, Y. Zheng, Z. Wang, and L. Zhao, Materials Letters **45**, 128 (2000).

[36] Z. W. Feng, B. D. Gao, J. B. Wang, D. F. Qian, Y. X. Liu, et al., in *Materials Science Forum* (Trans Tech Publications Ltd., Zurich-Uetikon, Switzerland, 2001), vol. 394, pp. 365–368.

[37] Y. Wang, Y. Zheng, W. Cai, and L. Zhao, Scripta Materialia **40**, 1327 (1999).

[38] P. Chowdhury and H. Sehitoglu, Progress in Materials Science **85**, 1 (2017).

[39] Z. J. Pu, H.-K. Tseng, and K.-H. Wu, in *Smart Structures and Materials 1995: Smart Materials*, edited by A. P. Jardine (SPIE, 1995).

[40] P. Olier, J. Brachet, J. Bechade, C. Foucher, and G. Guénin, Journal de Physique IV **05**, C8 (1995).

[41] S. Miyazaki, Y. Igo, and K. Otsuka, Acta Metallurgica **34**, 2045 (1986).

[42] S. Besseghini, E. Villa, and A. Tuissi, Materials Science and Engineering: A **273**, 390 (1999).

[43] B. Kockar, I. Karaman, J. Kim, and Y. Chumlyakov, Scripta Materialia **54**, 2203 (2006).

[44] X. Meng, W. Cai, F. Chen, and L. Zhao, Scripta materialia **54**, 1599 (2006).

[45] X. Meng, W. Cai, Y. Fu, Q. Li, J. Zhang, and L. Zhao, Intermetallics **16**, 698 (2008).

[46] G. Bigelow, A. Garg, S. Padula Ii, D. Gaydosh, and R. Noebe, Scripta Materialia **64**, 725 (2011).

[47] D. Coughlin, P. Phillips, G. Bigelow, A. Garg, R. Noebe, and M. Mills, Scripta Materialia **67**, 112 (2012).

[48] X. Han, R. Wang, Z. Zhang, and D. Yang, Acta Materialia **46**, 273 (1998).

[49] H. Karaca, E. Acar, H. Tobe, and S. Saghaian, Materials Science and Technology **30**, 1530 (2014).

[50] R. N. Saunders, D. J. Hartl, J. G. Boyd, and D. C. Lagoudas, in *Active and Passive Smart Structures and Integrated Systems 2015*, edited by W.-H. Liao (SPIE, 2015).

[51] O. Benafan, R. Noebe, and T. Halsmer, Acta Astronautica **118**, 137 (2016).

[52] O. Benafan and D. Gaydosh, Smart Materials and Structures **26**, 095002 (2017).

[53] M. Cohen, G. Olson, and P. Clapp, in *Proceedings of International Conference on Martensitic Transformations, ICOMAT-79* (1979), p. 1.

[54] R. W. Cahn, *Physical Metallurgy* (North-Holland, Amsterdam New York, 1996), ISBN 0444898751.

[55] J. W. Christian, *The Theory of Transformations in Metals and Alloys : Part I + II* (Elsevier, Burlington, 2002), ISBN 0080440193.

[56] Z. Nishiyama, *Martensitic Transformation* (Academic Press Inc, 1978), ISBN 978-0-12-519850-9.

[57] V. A. Lobodyuk and E. I. Estrin, Physics-Uspekhi **48**, 713 (2005).

[58] C. H. Shih, B. L. Averbach, and M. Cohen, Journal of Materials **7**, 183 (1955).

[59] L. Kaufman and M. Cohen, Progress in Metal Physics **7**, 165 (1958).

[60] M. Zupan, M. Ashby, and N. Fleck, Advanced Engineering Materials **4**, 933 (2002).

[61] J.-Y. Gauthier, A. Hubert, J. Abadie, N. Chaillet, and C. Lexcellent, in *2007 IEEE/RSJ International Conference on Intelligent Robots and Systems* (IEEE, 2007), pp. 747–752.

[62] T. W. Duerig, K. Melton, and D. Stöckel, *Engineering aspects of shape memory alloys* (Butterworth-Heinemann, 2013).

[63] R. Velazquez, E. Pissaloux, M. Hafez, and J. Szewczyk, in *IEEE Symposium on Virtual Environments, Human-Computer Interfaces and Measurement Systems, 2005.* (IEEE, 2005), pp. 6–pp.

[64] V. Seetharaman, Bulletin of Materials Science **6**, 703 (1984).

[65] H. Ling and W. Owen, Acta Metallurgica **29**, 1721 (1981).

[66] J. Frenzel, E. George, A. Dlouhy, C. Somsen, M.-X. Wagner, and G. Eggeler, Acta Materialia **58**, 3444 (2010).

[67] G. Tadayyon, M. Mazinani, Y. Guo, S. M. Zebarjad, S. A. Tofail, and M. J. Biggs, Materials Science and Engineering: A **662**, 564 (2016).

[68] V. Krishnan, R. Manjeri, B. Clausen, D. Brown, and R. Vaidyanathan, Materials Science and Engineering: A **481-482**, 3 (2008), proceedings of the 7th European Symposium on Martensitic Transformations, ESOMAT 2006.

[69] T. H. Nam, T. Saburi, and K. Shimizu, Materials Transactions, JIM **31**, 959 (1990).

[70] P. Potapov, A. Shelyakov, and D. Schryvers, Scripta Materialia **44**, 1 (2001).

[71] K. Ramaiah, C. Saikrishna, Gouthama, and S. Bhaumik, Materials & Design (1980-2015) **56**, 78 (2014).

[72] O. Benafan, A. Garg, R. Noebe, G. Bigelow, S. Padula, D. Gaydosh, R. Vaidyanathan, B. Clausen, and S. Vogel, Journal of Alloys and Compounds **643**, 275 (2015).

[73] S. Wu and S. Hsieh, Journal of Alloys and Compounds **297**, 294 (2000).

[74] M. Ahlers, Progress in Materials Science **30**, 135 (1986).

[75] V. Recarte, R. Pérez-Sáez, J. San Juan, E. Bocanegra, and M. Nó, Metallurgical and Materials Transactions A **33**, 2581 (2002).

[76] K. Otsuka and K. Shimizu, Transactions of the Japan Institute of Metals **15**, 103 (1974).

[77] R. Toth and H. Sato, Acta Metallurgica **16**, 413 (1968).

[78] D. S. Lieberman, M. S. Wechsler, and T. A. Read, Journal of Applied Physics **26**, 473 (1955).

[79] T. Ohba, Y. Emura, S. Miyazaki, and K. Otsuka, Materials Transactions, JIM **31**, 12 (1990).

[80] H. Abe, M. Ishibashi, K. Ohshima, T. Suzuki, M. Wuttig, and K. Kakurai, Phys. Rev. B **50**, 9020 (1994).

[81] K. Enami and S. Nenno, Metallurgical Transactions **2**, 1487 (1971).

[82] S. Chakravorty and C. Wayman, Metallurgical Transactions A **7**, 569 (1976).

[83] Y. Au and C. Wayman, Scripta Metallurgica **6**, 1209 (1972).

[84] K. Otsuka, K. Oda, Y. Ueno, M. Piao, T. Ueki, and H. Horikawa, Scripta Metallurgica et Materialia **29**, 1355 (1993).

[85] S. Kajiwara and T. Kikuchi, Acta Metallurgica et Materialia **38**, 847 (1990).

[86] S. Kajiwara and T. Kikuchi, Philosophical Magazine A **48**, 509 (1983).

[87] A. Sato, E. Chishima, Y. Yamaji, and T. Mori, Acta Metallurgica **32**, 539 (1984).

[88] B. C. Maji and M. Krishnan, Scripta Materialia **48**, 71 (2003).

[89] T. Maki, S. Furutani, and I. Tamura, ISIJ International **29**, 438 (1989).

[90] M. Sugiyama, R. Oshima, and F. E. Fujita, Transactions of the Japan institute of metals **27**, 719 (1986).

[91] R. Oshima, Scripta Metallurgica **15**, 829 (1981).

[92] M. Sugiyama, R. Oshima, and F. E. Fujita, Transactions of the Japan institute of metals **25**, 585 (1984).

[93] R. Oshima, S. Sugimoto, M. Sugiyama, T. Hamada, and F. E. Fujita, Transactions of the Japan Institute of Metals **26**, 523 (1985).

[94] M. Umemoto and C. M. Wayman, Metallurgical Transactions A **9**, 891 (1978).

[95] J. H. Yang, H. Chen, and C. M. Wayman, Metallurgical Transactions A **23**, 1431 (1992).

[96] D. Vokoun and C. Hu, Journal of Alloys and Compounds **346**, 147 (2002).

[97] M. Ahlers and J. Pelegrina, Materials Science and Engineering: A **356**, 298 (2003).

[98] G. Scarsbrook, J. M. Cook, and W. M. Stobbs, Metallurgical Transactions A **15**, 1977 (1984).

[99] K. Otsuka and X. Ren, Intermetallics **7**, 511 (1999).

[100] X. Ren and K. Otsuka, Nature **389**, 579 (1997).

[101] T. Ohba, K. Otsuka, and S. Sasaki, in *Materials Science Forum* (Trans Tech Publ, 1990), vol. 56, pp. 317–322.

[102] R. Kainuma, K. Ishida, and T. Nishizawa, Metallurgical Transactions A **23**, 1147 (1992).

[103] A. Marder, Trans. ASM **60**, 651 (1967).

[104] C. Wayman, in *Materials Science Forum* (Trans Tech Publ, 1990), vol. 56, pp. 1–32.

[105] A. B. Greninger and V. Mooradian, Aime Trans **128**, 337 (1938).

[106] L. C. Chang and T. A. Read, Journal of Materials **3**, 47 (1951).

[107] M. W. Burkart and T. Read, Transactions of the American Institute of Mining and Metallurgical Engineers **197**, 1516 (1953).

[108] A. Higuchi, K. Suzuki, Y. Matsumoto, K. Sugimoto, S. Komatsu, and Y. Nakamura, Le Journal de Physique Colloques **43**, C4 (1982).

[109] K. Takezawa, T. Shindo, and S. Sato, Scripta Metallurgica **10**, 13 (1976).

[110] Y. Au and C. Wayman, Scripta Metallurgica **6**, 1209 (1972).

[111] S. Kajiwara, Materials Science and Engineering: A **273-275**, 67 (1999).

[112] S. Miyazaki and K. Otsuka, ISIJ International **29**, 353 (1989).

[113] C. M. Wayman, Journal of Materials **32**, 129 (1980).

[114] L. M. Schetky, Scientific American **241**, 74 (1979).

[115] G. B. Kauffman and I. Mayo, The Chemical Educator **2**, 1 (1997).

[116] T. B. Massalski, ASM international **3**, 2874 (1992).

[117] K. Otsuka and T. Kakeshita, MRS Bulletin **27**, 91 (2002).

[118] L. Orgéas and D. Favier, Acta Materialia **46**, 5579 (1998).

[119] G. Rondelli, B. Vicentini, and A. Cigada, Corrosion Science **30**, 805 (1990).

[120] D. Starosvetsky and I. Gotman, Biomaterials **22**, 1853 (2001).

[121] Y. Liang, S. Li, Y. Jin, W. Jin, and S. Li, Wear **198**, 236 (1996).

[122] J. V. Humbeeck, Journal of Alloys and Compounds **355**, 58 (2003).

[123] R. Dutta, K. Madangopal, H. Gadiyar, and S. Banerjee, British Corrosion Journal **28**, 217 (1993).

[124] O. Mercier, K. Melton, G. Gremaud, and J. Hägi, Journal of Applied Physics **51**, 1833 (1980).

[125] S. Miyazaki, K. Otsuka, and Y. Suzuki, Scripta Metallurgica **15**, 287 (1981).

[126] D. Stoeckel, Materials&Design **11**, 302 (1990).

[127] T. Duerig, A. Pelton, and D. Stöckel, Materials Science and Engineering: A **273**, 149 (1999).

[128] S. Saadat, J. Salichs, M. Noori, Z. Hou, H. Davoodi, I. Bar-on, Y. Suzuki, and A. Masuda, Smart Materials and Structures **11**, 218 (2002).

[129] Y. Liu and H. Xiang, Journal of Alloys and Compounds **270**, 154 (1998).

[130] G. Chen, K.-D. Liss, and P. Cao, Metallurgical and Materials Transactions A **46**, 5887 (2015).

[131] T. Philip and P. A. Beck, Trans AIME Journal of Metals **209**, 1269 (1957).

[132] N. Hatcher, O. Y. Kontsevoi, and A. J. Freeman, Phys. Rev. B **80**, 144203 (2009).

[133] N. Zhou, C. Shen, M.-X. Wagner, G. Eggeler, M. Mills, and Y. Wang, Acta Materialia **58**, 6685 (2010).

[134] J. Uchil, K. Kumara, and K. Mahesh, Materials Science and Engineering: A **332**, 25 (2002).

[135] P.Šittner, M. Landa, P. Lukáš, and V. Novák, Mechanics of Materials **38**, 475 (2006), shape Memory Alloys.

[136] T. Waitz, V. Kazykhanov, and H. Karnthaler, Acta Materialia **52**, 137 (2004).

[137] D. Chrobak and D. Stróż, Scripta Materialia **52**, 757 (2005).

[138] G. Airoldi, K. Otsuka, G. Riva, A. Sciacca, and J. Zhang, Materials Transactions, JIM **33**, 730 (1992).

[139] M. Sharma, B. C. Maji, and M. Krishnan, Physics Procedia **10**, 28 (2010).

[140] G. Airoldi, S. Besseghini, G. Riva, and T. Saburi, Materials Transactions, JIM **35**, 103 (1994).

[141] J. Khalil-Allafi, W. W. Schmahl, and D. Toebbens, Acta Materialia **54**, 3171 (2006).

[142] S. Miyazaki and K. Otsuka, Metallurgical Transactions A **17**, 53 (1986).

[143] X. Wang, B. Verlinden, and J. Van Humbeeck, Materials Science and Technology **30**, 1517 (2014).

[144] T. H. Nam, T. Saburi, and K. Shimizu, Materials Transactions, JIM **31**, 959 (1990).

[145] T. T. Sasaki, B. C. Hornbuckle, R. D. Noebe, G. S. Bigelow, M. L. Weaver, and G. B. Thompson, Metallurgical and Materials Transactions A **44**, 1388 (2013).

[146] K. Ramaiah, C. Saikrishna, Gouthama, and S. Bhaumik, Journal of Alloys and Compounds **554**, 319 (2013).

[147] H. Sehitoglu, I. Karaman, X. Zhang, A. Viswanath, Y. Chumlyakov, and H. Maier, Acta Materialia **49**, 3621 (2001).

[148] Y. Kudoh, M. Tokonami, S. Miyazaki, and K. Otsuka, Acta Metallurgica **33**, 2049 (1985).

[149] M. Nishida, C. M. Wayman, and T. Honma, Metallurgical and Materials Transactions A **17**, 1505 (1986).

[150] W. Tirry and D. Schryvers, Materials Science and Engineering: A **378**, 157 (2004), european Symposium on Martensitic Transformation and Shape-Memory.

[151] O. Bojda, G. Eggeler, and A. Dlouhý, Scripta Materialia **53**, 99 (2005).

[152] D. Holec, O. Bojda, and A. Dlouhý, Materials Science and Engineering: A **481-482**, 462 (2008), proceedings of the 7th European Symposium on Martensitic Transformations, ESOMAT 2006.

[153] D. Favier, Y. Liu, L. Orgéas, A. Sandel, L. Debove, and P. Comte-Gaz, Materials Science and Engineering: A **429**, 130 (2006).

[154] S. Nemat-Nasser and W.-G. Guo, Mechanics of Materials **38**, 463 (2006), shape Memory Alloys.

[155] X. Huang and Y. Liu, Scripta Materialia **45**, 153 (2001).

[156] R. R. Adharapurapu, F. Jiang, K. S. Vecchio, and G. T. Gray, Acta Materialia **54**, 4609 (2006).

[157] R. Hamilton, H. Sehitoglu, Y. Chumlyakov, and H. Maier, Acta Materialia **52**, 3383 (2004).

[158] J. van Vucht, Journal of the Less Common Metals **11**, 308 (1966).

[159] S. Civjan, E. F. Huget, and L. B. DeSimon, Journal of Dental Research **54**, 89 (1975).

[160] M. Nishida, C. Wayman, and T. Honma, Scripta Metallurgica **19**, 983 (1985).

[161] M. Nishida, C. Wayman, R. Kainuma, and T. Honma, Scripta Metallurgica **20**, 899 (1986).

[162] T. Tadaki, Y. Nakata, K. Shimizu, and K. Otsuka, Transactions of the Japan Institute of Metals **27**, 731 (1986).

[163] J. Khalil-Allafi, W. W. Schmahl, M. Wagner, H. Sitepu, D. Toebbens, and G. Eggeler, Materials Science and Engineering: A **378**, 161 (2004).

[164] D. Li and L. Chen, Acta Materialia **46**, 639 (1998).

[165] M. Mueller and H. Knott, Transactions of American Institute of Metallurgical Engineers **227** (1963).

[166] J. Bhagyaraj, K. Ramaiah, C. Saikrishna, S. Bhaumik, and Gouthama, Journal of Alloys and Compounds **581**, 344 (2013).

[167] G. Tadayyon, M. Mazinani, Y. Guo, S. M. Zebarjad, S. A. Tofail, and M. J. Biggs, Materials Characterization **112**, 11 (2016).

[168] W. Tang, B. Sundman, R. Sandström, and C. Qiu, Acta Materialia **47**, 3457 (1999).

[169] Y. Liu, X. Chen, and P. G. McCormick, Journal of Materials Science **32**, 5979 (1997).

[170] J. Khalil-Allafi, A. Dlouhy, and G. Eggeler, Acta Materialia **50**, 4255 (2002).

[171] Y. Zheng, F. Jiang, L. Li, H. Yang, and Y. Liu, Acta Materialia **56**, 736 (2008).

[172] J. Beyer and J. Mulder, MRS Proceedings **360** (1994).

[173] H. Hosoda, M. Tsuji, Y. Takahashi, T. Inamura, K. Wakashima, Y. Yamabe-Mitarai, S. Miyazaki, and K. Inoue, Materials Science Forum **426-432**, 2333 (2003).

[174] O. Benafan, D. J. Gaydosh, R. D. Noebe, S. Qiu, and R. Vaidyanathan, Shape Memory and Superelasticity **2**, 337 (2016).

[175] T. E. Buchheit, D. F. Susan, J. E. Massad, J. R. McElhanon, and R. D. Noebe, Metallurgical and Materials Transactions A **47**, 1587 (2016).

[176] P. Lindquist and C. Wayman, in *Engineering Aspects of Shape Memory Alloys* (Elsevier, 1990), pp. 58–68.

[177] D. Golberg, Y. Xu, Y. Murakami, K. Otsuka, T. Ueki, and H. Horikawa, Materials Letters **22**, 241 (1995).

[178] Y. Suzuki, Y. Xu, S. Morito, K. Otsuka, and K. Mitose, Materials Letters **36**, 85 (1998).

[179] O. Rios, R. Noebe, T. Biles, A. Garg, A. Palczer, D. Scheiman, H. J. Seifert, and M. Kaufman, in *Smart Structures and Materials 2005: Active Materials: Behavior and Mechanics*, edited by W. D. Armstrong (SPIE, 2005).

[180] G. Bigelow, Tech. Rep., NASA Glenn Research Center; Cleveland, OH, United States (2008).

[181] R. Noebe, S. P. II, G. Bigelow, O. Rios, A. Garg, and B. Lerch, in *Smart Structures and Materials 2006: Active Materials: Behavior and Mechanics*, edited by W. D. Armstrong (SPIE, 2006).

[182] R. Noebe, S. Draper, D. Gaydosh, A. Garg, B. Lerch, N. Penney, G. Begelow, S. Padula, and J. Brown, Tech. Rep., NASA Glenn Research Center; Cleveland, OH, United States (2006).

[183] S. Shimizu, Y. Xu, E. Okunishi, S. Tanaka, K. Otsuka, and K. Mitose, Materials Letters **34**, 23 (1998).

[184] G. S. Bigelow, S. A. Padula, A. Garg, D. Gaydosh, and R. D. Noebe, Metallurgical and Materials Transactions A **41**, 3065 (2010).

[185] F. Yang, L. Kovarik, P. J. Phillips, R. D. Noebe, and M. Mills, Scripta Materialia **67**, 145 (2012).

[186] L. Kovarik, F. Yang, A. Garg, D. Diercks, M. Kaufman, R. Noebe, and M. Mills, Acta Materialia **58**, 4660 (2010).

[187] G. A. Hudish, Ph.D. thesis, Colorado School of Mines. Arthur Lakes Library (2013).

[188] K. Eckelmeyer, Scripta Metallurgica **10**, 667 (1976).

[189] V. Sivokha and L. Meisner, Physica B: Condensed Matter **296**, 329 (2001).

[190] S. Hsieh and S. Wu, Journal of Alloys and Compounds **266**, 276 (1998).

[191] Z. Zhang, J. Frenzel, K. Neuking, and G. Eggeler, Materials Transactions **47**, 661 (2006).

[192] G. Firstov, J. V. Humbeeck, and Y. Koval, Scripta Materialia **50**, 243 (2004).

[193] A. Evirgen, I. Karaman, J. Pons, R. Santamarta, and R. Noebe, Materials Science and Engineering: A **655**, 193 (2016).

[194] A. Evirgen, I. Karaman, R. Santamarta, J. Pons, and R. Noebe, Scripta Materialia **81**, 12 (2014).

[195] A. Evirgen, I. Karaman, R. Noebe, R. Santamarta, and J. Pons, Scripta Materialia **69**, 354 (2013).

[196] A. Sandu, K. Tsuchiya, S. Yamamoto, Y. Todaka, and M. Umemoto, Scripta Materialia **55**, 1079 (2006).

[197] A. M. Sandu, K. Tsuchiya, M. Tabuchi, S. Yamamoto, Y. Todaka, and M. Umemoto, Materials Transactions **48**, 432 (2007).

[198] A. Evirgen, I. Karaman, R. Santamarta, J. Pons, C. Hayrettin, and R. Noebe, Acta Materialia **121**, 374 (2016).

[199] R. Santamarta, R. Arróyave, J. Pons, A. Evirgen, I. Karaman, H. Karaca, and R. Noebe, Acta Materialia **61**, 6191 (2013).

[200] A. Evirgen, J. Pons, I. Karaman, R. Santamarta, and R. Noebe, Shape Memory and Superelasticity **4**, 85 (2018).

[201] M. Carl, J. Smith, B. V. Doren, and M. Young, Metals **7**, 511 (2017).

[202] Y. Tong, F. Chen, B. Tian, L. Li, and Y. Zheng, Materials Letters **63**, 1869 (2009).

[203] P. E. Thoma and J. J. Boehm, Materials Science and Engineering: A **273-275**, 385 (1999).

[204] P. Potapov, A. Shelyakov, A. Gulyaev, E. Svistunov, N. Matveeva, and D. Hodgson, Materials Letters **32**, 247 (1997).

[205] M. Zarinejad, Y. Liu, and T. J. White, Intermetallics **16**, 876 (2008).

[206] H. Matsumoto, Journal of Alloys and Compounds **350**, 213 (2003).

[207] M.-X. Wagner, S. Dey, H. Gugel, J. Frenzel, C. Somsen, and G. Eggeler, Intermetallics **18**, 1172 (2010).

[208] A. Pérez-Sierra, J. Pons, R. Santamarta, I. Karaman, and R. Noebe, Scripta Materialia **124**, 47 (2016).

[209] P. E. Thoma and J. J. Boehm, MRS Online Proceedings Library Archive **604** (1999).

[210] S. Besseghini, E. Villa, and A. Tuissi, Materials Science and Engineering: A **273-275**, 390 (1999).

[211] X. Meng, Y. Zheng, Z. Wang, and L. Zhao, Materials Letters **45**, 128 (2000).

[212] Y. Wang, Y. Zheng, W. Cai, and L. Zhao, Scripta Materialia **40**, 1327 (1999).

[213] M. M. Javadi, M. Belbasi, M. T. Salehi, and M. R. Afshar, Journal of Materials Engineering and Performance **20**, 618 (2011).

[214] X. Meng, Y. Zheng, Z. Wang, and L. Zhao, Scripta Materialia **42**, 341 (2000).

[215] X.-L. Meng, Y.-F. Zheng, Z. Wang, and L. Zhao, Materials Letters **45**, 128 (2000).

[216] X. Meng, W. Cai, Y. Zheng, and L. Zhao, Materials Science and Engineering: A **438-440**, 666 (2006), proceedings of the International Conference on Martensitic Transformations.

[217] X. Meng, W. Cai, F. Chen, and L. Zhao, Scripta Materialia **54**, 1599 (2006).

[218] O. Benafan, G. Bigelow, and D. Scheiman, Scripta Materialia **146**, 251 (2018).

[219] H. Karaca, S. Saghaian, G. Ded, H. Tobe, B. Basaran, H. Maier, R. Noebe, and Y. Chumlyakov, Acta Materialia **61**, 7422 (2013).

[220] S. Saghaian, H. Karaca, M. Souri, A. Turabi, and R. Noebe, Materials & Design **101**, 340 (2016).

[221] O. Benafan, A. Garg, R. Noebe, G. Bigelow, S. Padula, D. Gaydosh, N. Schell, J. Mabe, and R. Vaidyanathan, Intermetallics **50**, 94 (2014).

[222] S. Saghaian, H. Karaca, H. Tobe, A. Turabi, S. Saedi, S. Saghaian, Y. Chumlyakov, and R. Noebe, Acta Materialia **134**, 211 (2017).

[223] F. Yang, D. Coughlin, P. Phillips, L. Yang, A. Devaraj, L. Kovarik, R. Noebe, and M. Mills, Acta Materialia **61**, 3335 (2013).

[224] B. Hornbuckle, M. Kapoor, and G. Thompson, Ultramicroscopy **159**, 346 (2015).

[225] B. Hornbuckle, T. Sasaki, G. Bigelow, R. Noebe, M. Weaver, and G. Thompson, Materials Science and Engineering: A **637**, 63 (2015).

[226] A. Evirgen, I. Karaman, R. Santamarta, J. Pons, and R. Noebe, Acta Materialia **83**, 48 (2015).

[227] F. Dalle, E. Perrin, P. Vermaut, M. Masse, and R. Portier, Acta Materialia **50**, 3557 (2002).

[228] M. Prasher and D. Sen, Journal of Alloys and Compounds **615**, 469 (2014).

[229] X. Meng, Y. Zheng, Z. Wang, and L. Zhao, Scripta Materialia **42**, 341 (2000).

[230] S. Shabalovskaya and J. Anderegg, in *Journal of Vacuum Science & Technology A: Vacuum, Surfaces, and Films CONF- 1* (AVS, 1995), vol. 13, pp. 2624–2632.

[231] C. A. Schneider, W. S. Rasband, and K. W. Eliceiri, Nature Methods **9**, 671 (2012).

[232] *Test method for transformation temperature of nickel-titanium alloys by thermal analysis*, URL https://doi.org/10.1520/f2004-05r10.

[233] G. Höhne, H. Cammenga, W. Eysel, E. Gmelin, and W. Hemminger, Thermochimica Acta **160**, 1 (1990).

[234] H. K. Cammenga, W. Eysel, E. Gmelin, W. Hemminger, G. W. Höhne, and S. M. Sarge, Thermochimica Acta **219**, 333 (1993).

[235] S. M. Sarge, E. Gmelin, G. W. Höhne, H. K. Cammenga, W. Hemminger, and W. Eysel, Thermochimica Acta **247**, 129 (1994).

[236] A. L. Bail, Powder Diffraction **20**, 316 (2005).

[237] J. R. Carvajal, Abstracts of the Satellite Meeting on Powder Diffraction of the XV Congress of the IUCr (1990).

[238] V. Siruguri, P. Babu, M. Gupta, A. Pimpale, and P. Goyal, Pramana **71**, 1197 (2008).

[239] P. Krishna, R. Chitra, R. Choudhury, and S. Mishra, Neutron News **25**, 18 (2014).

[240] S. Mazumder, D. Sen, T. Saravanan, and P. Vijayaraghavan, Current Science **81**, 257 (2001).

[241] S. Mazumder, D. Sen, T. Saravanan, and P. Vijayaraghavan, Journal of Neutron Research **9**, 39 (2001).

[242] S. Mazumder, D. Sen, T. Saravanan, and P. R. Vijayraghavan, Neutron News **13**, 25 (2002).

[243] G. D. Wignall, K. C. Littrell, W. T. Heller, Y. B. Melnichenko, K. M. Bailey, G. W. Lynn, D. A. Myles, V. S. Urban, M. V. Buchanan, D. L. Selby, et al., Journal of Applied Crystallography **45**, 990 (2012).

[244] P. E. Thoma and J. J. Boehm, Materials Science and Engineering: A **273-275**, 385 (1999).

[245] M. Sharma, B. C. Maji, and M. Krishnan, Physics Procedia **10**, 28 (2010).

[246] H. Hosoda, S. Hanada, K. Inoue, T. Fukui, Y. Mishima, and T. Suzuki, Intermetallics **6**, 291 (1998).

[247] J. Frenzel, E. P. George, A. Dlouhy, C. Somsen, M.-X. Wagner, and G. Eggeler, Acta Materialia **58**, 3444 (2010).

[248] X. Meng, W. Cai, Y. Zheng, Y. Tong, L. Zhao, and L. Zhou, Materials Letters **55**, 111 (2002).

[249] A. Evirgen, F. Basner, I. Karaman, R. D. Noebe, J. Pons, and R. Santamarta, Functional Materials Letters **5**, 1250038 (2012).

[250] B. Amin-Ahmadi, T. Gallmeyer, J. G. Pauza, T. W. Duerig, R. D. Noebe, and A. P. Stebner, Scripta Materialia **147**, 11 (2018).

[251] T. Umale, D. Salas, B. Tomes, R. Arroyave, and I. Karaman, Scripta Materialia **161**, 78 (2019).

[252] O. L. Semenova, L. O. Tret'yachenko, and V. M. Petyukh, Powder Metallurgy and Metal Ceramics **46**, 556 (2007).

[253] T. Waitz, V. Kazykhanov, and H. Karnthaler, Acta Materialia **52**, 137 (2004).

[254] K. Tsuchiya, M. Inuzuka, D. Tomus, A. Hosokawa, H. Nakayama, K. Morii, Y. Todaka, and M. Umemoto, Materials Science and Engineering: A **438-440**, 643 (2006).

[255] J. Frenzel, A. Wieczorek, I. Opahle, B. Maaβ, R. Drautz, and G. Eggeler, Acta Materialia **90**, 213 (2015).

[256] X. Ren and K. Otsuka, Scripta Materialia **38**, 1669 (1998).

[257] X. Ren, N. Miura, J. Zhang, K. Otsuka, K. Tanaka, M. Koiwa, T. Suzuki, Y. Chumlyakov, and M. Asai, Materials Science and Engineering: A **312**, 196 (2001).

[258] Q. M. Hu, R. Yang, J. M. Lu, L. Wang, B. Johansson, and L. Vitos, Phys. Rev. B **76**, 224201 (2007).

[259] O. Benafan, G. Bigelow, and D. Scheiman, Scripta Materialia **146**, 251 (2018).

[260] A. Evirgen, I. Karaman, R. Santamarta, J. Pons, C. Hayrettin, and R. Noebe, Acta Materialia **121**, 374 (2016).

[261] L. Vegard, Zeitschrift für Physik **5**, 17 (1921).

[262] J. Kim and S. Miyazaki, Acta Materialia **53**, 4545 (2005).

[263] J. S. Pedersen, Journal of Applied Crystallography **27**, 595 (1994).

[264] E. Orowan, Institute of Metals, London **451** (1948).

[265] G. Eggeler, E. Hornbogen, A. Yawny, A. Heckmann, and M. Wagner, Materials Science and Engineering: A **378**, 24 (2004).

[266] O. Benafan, A. Garg, R. Noebe, G. Bigelow, S. Padula Ii, D. Gaydosh, N. Schell, J. Mabe, and R. Vaidyanathan, Intermetallics **50**, 94 (2014).

[267] A. Evirgen, I. Karaman, R. Santamarta, J. Pons, and R. Noebe, Acta Materialia **83**, 48 (2015).

[268] F. De Geuser and A. Deschamps, Comptes Rendus Physique **13**, 246 (2012).

[269] J. William and R. Mehl, Transactions of the Metallurgical Society of AIME **135**, 416 (1939).

[270] M. Avrami, The Journal of Chemical Physics **7**, 1103 (1939).

[271] A. N. Kolmogorov, Bulletin of the Academy of Sciences, Math. Ser **1**, 355 (1937).

[272] I. Khan, M. Starink, and J. L. Yan, Materials Science and Engineering: A **472**, 66 (2008).

[273] H. Mirzadeh and A. Najafizadeh, Materials Chemistry and Physics **116**, 119 (2009).

[274] C. Capdevila, M. K. Miller, and J. Chao, Acta Materialia **60**, 4673 (2012).

[275] Y. Zheng, F. Jiang, L. Li, H. Yang, and Y. Liu, Acta Materialia **56**, 736 (2008).

[276] A. Dlouhy, J. Khalil-Allafi, and G. Eggeler, Philosophical Magazine **83**, 339 (2003).

[277] G. Fan, W. Chen, S. Yang, J. Zhu, X. Ren, and K. Otsuka, Acta Materialia **52**, 4351 (2004).

[278] J. Michutta, C. Somsen, A. Yawny, A. Dlouhy, and G. Eggeler, Acta Materialia **54**, 3525 (2006).

[279] M. Moshref-Javadi, S. H. Seyedein, M. T. Salehi, and M. R. Aboutalebi, Acta Materialia **61**, 2583 (2013).

[280] R. Wagner, R. Kampmann, and P. W. Voorhees, Materials Science and Technology (2006).

[281] C.-S. Tsao, C.-Y. Chen, U.-S. Jeng, and T.-Y. Kuo, Acta Materialia **54**, 4621 (2006).

[282] J. Miles, Adjusted R Squared Wiley StatsRef: Statistics Reference Online: John Wiley & Sons, Ltd (2014).

[283] M. Starink, Journal of Materials Science **32**, 4061 (1997).

[284] Y. Oh, P. Machmeier, T. Matuszewski, and R. Ayer, Journal of Materials Engineering and Performance **6**, 289 (1997).

[285] J. Bernardini, C. Lexcellent, L. Daróczi, and D. Beke, Philosophical Magazine **83**, 329 (2003).

[286] G. Erdelyi, Z. Erdelyi, D. Beke, J. Bernardini, and C. Lexcellent, Physical Review B **62**, 11284 (2000).

[287] I. M. Lifshitz and V. V. Slyozov, Journal of Physics and Chemistry of Solids **19**, 35 (1961).

[288] G. M. Novotny and A. J. Ardell, Materials Science and Engineering: A **318**, 144 (2001).

[289] J. Tiley, G. Viswanathan, R. Srinivasan, R. Banerjee, D. Dimiduk, and H. Fraser, Acta Materialia **57**, 2538 (2009).

[290] D. Bergner, Kristall und Technik **7**, 651 (1972).

[291] M. Behar, F. Dyment, R. Perez, J. R. Dos Santos, R. Maltez, and E. Savino, Philosophical Magazine A **63**, 967 (1991).

[292] A. D. LeClaire and G. Neumann, *3.2.10 Nickel group metals* (Springer Berlin Heidelberg, Berlin, Heidelberg, 1990), pp. 132–136.

[293] R. Pérez, F. Dyment, G. G. Bermúdez, H. Somacal, and D. Abriola, Journal of nuclear materials **207**, 221 (1993).

[294] W. Guo, I. Steinbach, C. Somsen, and G. Eggeler, Acta Materialia **59**, 3287 (2011).

[295] C. Ke, S. Cao, and X. Zhang, Modelling and Simulation in Materials Science and Engineering **22**, 055018 (2014).

[296] T. Saburi, S. Nenno, and T. Fukuda, Journal of the Less Common Metals **125**, 157 (1986).

[297] F. Jiang, L. Li, Y. Zheng, H. Yang, and Y. Liu, Intermetallics **16**, 394 (2008).

[298] A. Paula, J. Canejo, R. Martins, and F. B. Fernandes, Materials Science and Engineering: A **378**, 92 (2004).

[299] J. Uchil, K. G. Kumara, and K. Mahesh, Materials Science and Engineering: A **332**, 25 (2002).

[300] X. Liang, Y. Chen, H. Shen, Z. Zhang, W. Li, and Y. Wang, Solid State Communications **119**, 381 (2001).

[301] H. Matsumoto, Physica B: Condensed Matter **190**, 115 (1993).

[302] X. Wang, J. V. Humbeeck, B. Verlinden, and S. Kustov, Scripta Materialia **113**, 206 (2016).

[303] A. Pelton, G. Huang, P. Moine, and R. Sinclair, Materials Science and Engineering: A **532**, 130 (2012).

[304] T. Tadaki, Y. Nakata, and K. Shimizu, Transactions of the Japan Institute of Metals **28**, 883 (1987).

[305] M.-X. Wagner, S. Dey, H. Gugel, J. Frenzel, C. Somsen, and G. Eggeler, Intermetallics **18**, 1172 (2010).

[306] Y. Motemani, M. Nili-Ahmadabadi, M. Tan, M. Bornapour, and S. Rayagan, Journal of Alloys and Compounds **469**, 164 (2009).

[307] H. Fang, M. Wong, Y. Bai, and R. Luo, Construction and Building Materials **101**, 447 (2015).

[308] K. Nurveren, A. Akdoğan, and W. Huang, Journal of Materials Processing Technology **196**, 129 (2008).

[309] M. Prasher, D. Sen, J. Bahadur, R. Tewari, and M. Krishnan, Journal of Alloys and Compounds **779**, 630 (2019).

[310] L. Neelakantan, M. Valtiner, G. Eggeler, and A. W. Hassel, Physica Status Solidi (a) **207**, 807 (2010).

[311] H. Karaca, I. Karaman, D. Lagoudas, H. Maier, and Y. Chumlyakov, Scripta Materialia **49**, 831 (2003).

[312] H. Karaca, S. Saghaian, G. Ded, H. Tobe, B. Basaran, H. Maier, R. Noebe, and Y. Chumlyakov, Acta Materialia **61**, 7422 (2013).

[313] V. Pelosin and A. Riviere, Metallurgical and Materials Transactions A **29**, 1175 (1998).

[314] T. Simon, A. Kröger, C. Somsen, A. Dlouhy, and G. Eggeler, Acta Materialia **58**, 1850 (2010).

[315] A. N. Bucsek, G. A. Hudish, G. S. Bigelow, R. D. Noebe, and A. P. Stebner, Shape Memory and Superelasticity **2**, 62 (2016).

[316] P. Wollants, J. Roos, and L. Delaey, Progress in Materials Science **37**, 227 (1993).

[317] H. E. Kissinger, Analytical Chemistry **29**, 1702 (1957).

[318] T. H. Grgurić, D. Manasijević, S. Kožuh, I. Ivanić, I. Anžel, B. Kosec, M. Bizjak, E. G. Bajsić, L. Balanović, and M. Gojić, Journal of Alloys and Compounds **765**, 664 (2018).

[319] J. Fernández, A. Benedetti, J. Guilemany, and X. Zhang, Materials Science and Engineering: A **438-440**, 723 (2006).

[320] Z. Zhou, L. Yang, R. Li, J. Li, Q. Hu, and J. Li, Intermetallics **92**, 49 (2018).

[321] K. Inaekyan, V. Brailovski, S. Prokoshkin, A. Korotitskiy, and A. Glezer, Journal of Alloys and Compounds **473**, 71 (2009).

[322] X. Yi, H. Wang, W. Gao, B. Sun, X. Niu, X. Meng, J. Li, Z. Gao, W. Cai, and L. Zhao, Journal of Alloys and Compounds **802**, 181 (2019).

[323] R. Monzen, S. Okawara, and C. Watanabe, Philosophical Magazine **92**, 1826 (2012).

[324] I. Kaya, H. Tobe, H. E. Karaca, E. Acar, and Y. Chumlyakov, Acta Metallurgica Sinica (English Letters) **29**, 282 (2016).

[325] A. Nayak and R. Sinha, Progress in Nuclear Energy **49**, 486 (2007), ISSN 0149-1970.

[326] J. Ma, H. Shu, and J. Huang, Science and Technology of Nuclear Installations **2012**, 1 (2012).

[327] O. Benafan, W. U. Notardonato, B. J. Meneghelli, and R. Vaidyanathan, Smart Materials and Structures **22**, 105017 (2013).

[328] D. R. Gaskell and D. E. Laughlin, *Introduction to the Thermodynamics of Materials* (CRC Press, 2017).

[329] A. Baldan, Journal of Materials Science **37**, 2171 (2002).

[330] A. J. Ardell and V. Ozolins, Nature materials **4**, 309 (2005).

[331] A. Guinier, Nature **142**, 569 (1938).

[332] A. Guinier, G. Fournet, C. Walker, and K. Yudowitch, *Small Angle Scatterind of X-rays* (New York: Wiley, 1955).

[333] D. Sen, A. Das, and S. Mazumder, Journal of Applied Crystallography **47**, 712 (2014).

[334] I. Breßler, J. Kohlbrecher, and A. F. Thünemann, Journal of Applied Crystallography **48**, 1587 (2015).